

1-1-2007

Dynamic & CFD modeling of a continuous-flow mixer using fluids with yield stress

Salwan Emad Saeed

Ryerson University

Follow this and additional works at: <http://digitalcommons.ryerson.ca/dissertations>

 Part of the [Chemical Engineering Commons](#)

Recommended Citation

Saeed, Salwan Emad, "Dynamic & CFD modeling of a continuous-flow mixer using fluids with yield stress" (2007). *Theses and dissertations*. Paper 234.

This Thesis is brought to you for free and open access by Digital Commons @ Ryerson. It has been accepted for inclusion in Theses and dissertations by an authorized administrator of Digital Commons @ Ryerson. For more information, please contact bcameron@ryerson.ca.

TP
156
M5
S2C
2007

DYNAMIC & CFD MODELING OF A CONTINUOUS-FLOW MIXER USING FLUIDS WITH YIELD STRESS

by

SALWAN EMAD SAEED

M.Sc. Chemical Engineering, Baghdad University, Baghdad, Iraq, 1997
B.Sc. Chemical Engineering, Baghdad University, Baghdad, Iraq, 1993

A Thesis
Presented to Ryerson University
in Partial Fulfillment of the Requirements for the Degree of
Master of Applied Science
in the Program of Chemical Engineering

Toronto, Ontario, Canada, 2007
Copyright © 2007 by Salwan Emad Saeed

UMI Number: EC54191

INFORMATION TO USERS

The quality of this reproduction is dependent upon the quality of the copy submitted. Broken or indistinct print, colored or poor quality illustrations and photographs, print bleed-through, substandard margins, and improper alignment can adversely affect reproduction.

In the unlikely event that the author did not send a complete manuscript and there are missing pages, these will be noted. Also, if unauthorized copyright material had to be removed, a note will indicate the deletion.

UMI[®]

UMI Microform EC54191
Copyright 2009 by ProQuest LLC
All rights reserved. This microform edition is protected against
unauthorized copying under Title 17, United States Code.

ProQuest LLC
789 East Eisenhower Parkway
P.O. Box 1346
Ann Arbor, MI 48106-1346

ABSTRACT

Dynamic and CFD Modeling of a Continuous-Flow Mixer Using Fluids with Yield Stress

Sawlan Saeed
Chemical Engineering
MASc.
Ryerson University
Toronto, Ontario, Canada, 2007

A continuous-flow mixer was designed and built in the Mixing Technology Lab, Chemical Engineering Department at Ryerson University to study mixing of xanthan gum solutions in water, a pseudoplastic fluid possessing yield stress. The extent of flow non-ideality was quantified using a dynamic model that incorporated the extent of channeling and the effective mixed volume within the mixing vessel. Dynamic tests were made using a frequency-modulated random binary input of a brine solution. The same experiments were simulated using Fluent, a Computational Fluid Dynamics (CFD) Package. CFD flow fields were used to obtain the system dynamic response to a tracer injection applied at conditions identical to the experimental conditions. The extent of channeling and effective mixed volume were determined and then compared with the parameters obtained experimentally.

Experimental and CFD results show that the extent of non-ideal flow is significantly affected by impeller speed, impeller type, feed flow rate, fluid rheology, and exit location. The performance of continuous mixed vessels can be improved by increasing impeller speed, decreasing feed flow rate, and decreasing solution concentration. However, decreasing feed flow rate and solution concentration reduces the production capacity of the process. Increasing impeller speed may require modification to the motor and can cause air entrainment. Therefore, other remedies such as relocating the exit location and using the proper type of impeller may be taken into consideration. The results show that the extent of non-ideal flow was reduced using the bottom output and flow efficiency in the vessel was enhanced using A320 impeller.

ACKNOWLEDGEMENT

I would like to acknowledge my supervisor Dr. Farhad Ein-Mozaffari for his support, guidance and valuable comments to accomplish this thesis.

I would also like to thank the technologist and staff in Chemical Engineering Department at Ryerson University for the assistance provided during conducting this research.

Sincere thanks to all my friends in the Chemical Engineering Department at Ryerson University for their ultimate help.

I would also like to express my gratitude to my mother, father, sister and brother for their support and encouragement.

The financial support provided by Natural Science and Engineering Research Council of Canada (NSERC) for funding this research is greatly acknowledged.

DEDICATION

To "you" for all your love and support

Salwan
August, 2007

TABLE OF CONTENTS

AUTHOR DECLARATION	III
ABSTRACT.....	V
ACKNOWLEDGEMENT.....	VII
DEDICATION.....	IX
TABLE OF CONTENTS	XI
LIST OF TABLES	XVII
LIST OF FIGURES	XIX
1. INTRODUCTION.....	1
2. LITERATURE REVIEW	5
2.1 Introduction.....	5
2.2 Rheology of non-Newtonian Fluids	6
2.2.1 Time-Independent Fluids	7
2.2.2 Time-Dependent Fluids	9
2.2.3 Viscoelastic Fluids.....	9
2.2.4 Stimulant Time-Independent Yield Stress Fluids	10
2.3 Design Considerations of Mixing Vessels	11
2.3.1 Vessel Design	12
2.3.2 Shaft Design.....	13
2.3.3 Impeller Design.....	14
2.3.4 Mechanical Design.....	17
2.3.5 Other Design Considerations	17
2.4 Power Consumption in Agitated Vessels	18

2.4.1	Power in Agitated Vessels	18
2.4.2	Power Consumption for Newtonian Fluids	19
2.4.4	Power Consumption for non-Newtonian Fluids	21
2.4.5	Characteristics of Axial Flow Impellers	22
2.5	Cavern Region.....	27
2.6	Continuous-Flow Mixing Operation	31
2.6.1	Dynamic Modeling of Continuous-Flow Mixers	31
2.6.2	Continuous-Flow Mixers Literature Review.....	33
2.7	Computational Fluid Dynamics (CFD)	35
2.7.1	Mixing of non-Newtonian Fluids using CFD Literature Review.....	36
2.8	Research Objectives.....	36
3.	EXPERIMENTAL WORK	43
3.1	Experimental Setup.....	43
3.2	Impeller Specifications.....	47
3.3	Material Preparation	48
3.4	Xanthan Gum Physical & Rheological Properties.....	49
3.5	Experimental Test Procedure.....	53
3.6	Experimental Conditions	54
4.	DYNAMIC MODELING OF CONTINUOUS-FLOW MIXERS.....	55
4.1	Introduction.....	55
4.2	Dynamic Modeling of Mixing in Continuous-Flow Vessels	55
4.3	Estimation of Non-Ideal Flow Parameters in Continuous-Flow Mixers	56

4.4	Design of Input (Excitation) Signal	58
5.	COMPUTATION FLUID DYNAMICS (CFD)	65
5.1	Introduction.....	65
5.2	CFD Work Methodology.....	65
5.3	Property Transport Equations for Mixing Processes	66
5.4	Grid Generation	68
5.5	Discretization of Transport Equations.....	70
5.5.1	Spatial Discretization	70
5.5.2	Temporal Discretization.....	71
5.6	Finite Volume Spatial Discretization.....	72
5.6.1	Pressure Gradient Interpolation Schemes	73
5.6.2	Momentum Interpolation Schemes.....	75
5.6.3	Pressure-Velocity Coupling Schemes.....	79
5.7	Finite Volume Temporal Discretization.....	80
5.8	Solution of Discretized Equations.....	82
5.9	Checking CFD Solution.....	83
5.10	CFD Modeling of Mixing Vessels.....	86
5.10.1	Multiple Reference Frame (MRF) Model	86
5.10.2	Sliding Mesh (SM) Model.....	87
5.11	Scale Model of Continuous-Flow Mixing Vessel	88
5.11.1	Geometry.....	88
5.11.2	Material Definition	88
5.11.3	Selecting Boundary Conditions.....	90
5.11.4	Generating Meshing	91
5.11.5	Performing Numerical Simulations	93

5.11.6	Checking Grid Independency.....	94
5.11.7	Modeling Tracer Injection to Investigate Dynamics of Mixing Process ...	96
6.	RESULTS & DISCUSSION.....	101
6.1	Introduction.....	101
6.2	Impeller Characteristics.....	101
6.2.1	Power Number Estimation	102
6.2.1.1	Experimental Power Number Estimation.....	102
6.2.1.2	CFD Power Number Estimation.....	107
6.2.2	Average Shear Stress and Apparent Viscosity in the Mixing Vessel	111
6.2.3	Flow & Circulation Numbers Estimation	119
6.3	Dynamic Model Parameters	123
6.3.1	Dynamic Model Parameters Obtained from Experimental Data.....	126
6.3.1.1	Effect of Impeller Speed and Xanthan Gum Flowrate	126
6.3.1.2	Effect of Xanthan Gum Concentration	130
6.3.1.3	Effect of Output Location.....	134
6.3.1.4	Effect of Impeller Type.....	136
6.3.2	Dynamic Model Parameters Obtained from CFD.....	139
6.3.2.1	Effect of Impeller Speed and Xanthan Gum Flowrate	139
6.3.2.2	Effect of Xanthan Gum Concentration	146
6.3.2.3	Effect of Output Location.....	151
6.3.2.4	Effect of Impeller Type.....	155
6.4	Cavern Region & Flow Pattern in the Mixing Vessel.....	159
6.4.1	Cavern Region in the Mixing Vessel	159
6.4.2	Flow Pattern in the Mixing Vessel.....	176
7.	CONCLUSIONS & RECOMMENDATIONS FOR FUTURE WORK.....	185
7.1	Conclusions.....	185
7.2	Recommendations for Future Work	187

NOMENCLATURE	189
REFERENCES	195
APPENDIX EXPERIMENTAL & CFD DATA.....	221

LIST OF TABLES

<i>Table (2.1) Rheological Models for Fluids Possessing Yield Stress.....</i>	<i>7</i>
<i>Table (2.2) Rheological Models for Fluids without Yield Stress</i>	<i>8</i>
<i>Table (2.3) Power Consumption in Mixing of non Newtonian Fluid Literature Review</i>	<i>21</i>
<i>Table (2.4) Cavern Mathematical Models Literature Review.....</i>	<i>28</i>
<i>Table (2.5) Using CFD to Model Mixing Processes in non-Newtonian Fluids Literature Review</i>	<i>38</i>
<i>Table (3.1) Rheological Parameters of Xanthan Gum using Herschel Bulkley model.....</i>	<i>50</i>
<i>Table (3.2) Effect of Salt on Rheological Properties of Xanthan Gum Solutions.</i>	<i>51</i>
<i>Table (3.3) Density of Xanthan Gum Solutions.....</i>	<i>53</i>
<i>Table (4.1) Dynamic model Parameters obtained from Two Different Input Signals</i>	<i>64</i>
<i>Table (5.1) Xanthan Gum Rheological & Physical Properties</i>	<i>90</i>
<i>Table (6.1) Impeller Turbulent Power Number – Experimental Data.....</i>	<i>106</i>
<i>Table (6.2) Impellers Turbulent Power Numbers – CFD Simulations.....</i>	<i>108</i>
<i>Table (6.3) Impellers Turbulent Flow and Circulation Numbers – CFD Simulations</i>	<i>122</i>
<i>Table (6.4) Range of Operation Conditions used in Experimental Work</i>	<i>124</i>

<i>Table (6.5) Impeller Pumping and Circulation Efficiencies.....</i>	<i>138</i>
<i>Table (6.6) Effect of Impeller Speed on Dynamic Model Parameters Estimation from Experimental and CFD, 1.5% xanthan gum</i>	<i>142</i>
<i>Table (6.7) Effect of Xanthan Gum Concentration on Dynamic Model Parameters Estimation from Experimental and CFD Data, 896 L/hr.....</i>	<i>148</i>
<i>Table (6.8) Effect of Output Location on Dynamic Model Parameters Estimation from Experimental and CFD Data, 227 L/hr, 0.5% Xanthan Gum</i>	<i>151</i>
<i>Table (6.9) Effect of Impeller Type on Dynamic Model Parameters Estimation from Experimental and CFD Data, 897L/hr, 0.5% Xanthan Gum</i>	<i>157</i>
<i>Table (6.10) Width and Shape of Impellers Blades.....</i>	<i>157</i>
<i>Table (6.11) Cavern Diameter and Height in cm– A200 Impeller</i>	<i>169</i>
<i>Table (6.12) Summery of Cavern Dimensions for Axial Flow Impellers.....</i>	<i>171</i>
<i>Table (6.13) Cavern Diameter and Height in cm – A100, A200 & A310 Impellers</i>	<i>173</i>

LIST OF FIGURES

<i>Figure (2.1) Categories of non-Newtonian Fluids.....</i>	<i>6</i>
<i>Figure (2.2) Structure of Xanthan Gum Molecules (Jansson et al., 1975).....</i>	<i>11</i>
<i>Figure (2.3) Flow/Head (Shear) Spectrum of Impellers.....</i>	<i>15</i>
<i>Figure (2.4) Flow Pattern for an Axial and Radial Impeller.....</i>	<i>16</i>
<i>Figure (3.1) Detailed View in Mixing Vessel.....</i>	<i>44</i>
<i>Figure (3.2) Process Schematic Diagram.....</i>	<i>46</i>
<i>Figure (3.3) Impellers Shape.....</i>	<i>47</i>
<i>Figure (3.4) Xanthan Gum Rheograms.....</i>	<i>49</i>
<i>Figure (3.5) Xanthan Gum Rheograms Showing the Effect of Salt Addition.....</i>	<i>52</i>
<i>Figure (3.6) Vessel Configuration.....</i>	<i>54</i>
<i>Figure (4.1) Continuous-Time Domain Dynamic Model for Continuous-Flow Mixers (Ein-Mozaffari et al., 2002).....</i>	<i>56</i>
<i>Figure (4.2) Rectangular Pulse showing Input and Output Responses.....</i>	<i>60</i>
<i>Figure (4.3) Bode Plot of Partial Derivatives of Model Parameters.....</i>	<i>60</i>
<i>Figure (4.4) Procedure for Designing a Frequency-Modulated Random Binary Input Signal (Ein-Mozaffari et al., 2002).....</i>	<i>61</i>
<i>Figure (4.5) Frequency-Modulated Random Binary Input Signal.....</i>	<i>62</i>
<i>Figure (4.6) Model Validation Procedure (Ein Mozaffari, 2002).....</i>	<i>63</i>

<i>Figure (4.7) Model Validation Frequency-Modulated Random Binary Input Signal</i>	63
<i>Figure (5.1) 3D Cells Types</i>	69
<i>Figure (5.2) Grid Notation</i>	74
<i>Figure (5.3) Overview of the Segregated Solution Method (Fluent, 2006)</i>	84
<i>Figure (5.4) Method of Estimating Yielding Viscosity in Herschel Bulkley Model</i>	89
<i>Figure (5.5) 3D Mesh Generated by Gambit 2.2</i>	92
<i>Figure (5.6) Convergence History of Scaled Residuals</i>	93
<i>Figure (5.7) Axial, Radial and tangential Velocity Profiles at a below the Impeller showing Grid Independency</i>	96
<i>Figure (5.8) UDF Code Used to Model Tracer Injection for Frequency-Modulated Random Binary Input Signal</i>	99
<i>Figure (5.9) CFD Tracer Input Output Showing the Effect of Time Step</i>	100
<i>Figure (6.1) Experimental Power Curve for A200</i>	103
<i>Figure (6.2) Experimental Power Curve for all impellers</i>	104
<i>Figure (6.3) Impeller Turbulent Power Number Estimated using Mubaga and Bennington (1997) and Bubicco et al. (1997) method</i>	105
<i>Figure (6.4) Error Associated with Torque Measurements</i>	107
<i>Figure (6.5) Comparison between Experimental and CFD Torque – A200 Impeller</i>	110

<i>Figure (6.6) Comparison between Experimental and CFD Torque 0.5% Xanthan Gum Solution – A100 Impeller</i>	<i>110</i>
<i>Figure (6.7) Comparison between Experimental and CFD Torque 0.5% Xanthan Gum Solution – A310 Impeller</i>	<i>111</i>
<i>Figure (6.8) Average Shear Rate versus Impeller Speed – A200 Impeller</i>	<i>112</i>
<i>Figure (6.9) Average Shear Rate versus Impeller Speed – 0.5% Xanthan Gum Solution</i>	<i>113</i>
<i>Figure (6.10) Effect of Impeller Speed on Apparent Viscosity in Pa.s, 1.5% Xanthan Gum (a) 50, (b) 150, (c) 250 rpm.....</i>	<i>115</i>
<i>Figure (6.11) Effect of Xanthan Gum Concentration on Apparent Viscosity (Pa.s), 100 rpm, (a) 0.5%, (b) 1.0%, (c) 1.5% Xanthan Gum Solution.....</i>	<i>117</i>
<i>Figure (6.12) Flow Number & Circulation Number – A200 Impeller</i>	<i>121</i>
<i>Figure (6.13) Flow Number & Circulation Number for Different Impellers</i>	<i>122</i>
<i>Figure (6.14) System Reproducibility Examined using Channeling and $V/V_{\text{fully mixed}}$ Ratio</i>	<i>125</i>
<i>Figure (6.15) Effect of Impeller Speed & Input Flowrate on f and $V_{\text{fully mixed}}/V$....</i>	<i>129</i>
<i>Figure (6.16) Effect of Xanthan Gum Concentration on f and $V_{\text{fully mixed}}/V$</i>	<i>133</i>
<i>Figure (6.17) Effect of Output Location on f and $V_{\text{fully mixed}}/V$.....</i>	<i>135</i>
<i>Figure (6.18) Effect of Impeller Type on f and $V_{\text{fully mixed}}/V$.....</i>	<i>137</i>
<i>Figure (6.19) Effect of Impeller Speed on CFD Dynamic Response</i>	<i>141</i>

<i>Figure (6.20) Pathlines Predicted by CFD – Effect of Impeller Speed, 1.5% Xanthan Gum Solution</i>	<i>143</i>
<i>Figure (6.21) Effect of Xanthan Gum Flowrate on CFD Dynamic Response.....</i>	<i>145</i>
<i>Figure (6.22) Effect of Xanthan Gum Concentration on CFD Dynamic Response</i>	<i>147</i>
<i>Figure (6.23) Pathlines Predicted by CFD – Effect of Xanthan Gum Concentration.....</i>	<i>149</i>
<i>Figure (6.24) Effect of Output Location on CFD Dynamic Response.....</i>	<i>152</i>
<i>Figure (6.25) Pathlines predicted by CFD – Effect of Output Location</i>	<i>153</i>
<i>Figure (6.26) Effect of Impeller Type on CFD Dynamic Response.....</i>	<i>156</i>
<i>Figure (6.27) Vertical Velocity Contours in m/s showing Cavern Formation</i>	<i>161</i>
<i>Figure (6.28) Velocity Contours in m/s showing the Effect of Impeller Speed on Cavern Growth, 1.5% Xanthan Gum, (a) 50, (b) 250, (c) 500 rpm</i>	<i>163</i>
<i>Figure (6.29) Velocity Contours in m/s showing the Effect of Xanthan Gum Concentration on Cavern Growth, 300 rpm, (a) 0.5%, (b) 1.0%, (c) 1.5% xanthan gum.....</i>	<i>165</i>
<i>Figure (6.30) Velocity Contours in m/s showing the Effect of Impeller Type on Cavern Growth, 150 rpm, 0.5% Xanthan Gum, (a) A100, (b) A200, (c) A310...</i>	<i>167</i>
<i>Figure (6.31) D_o/D versus $Po_t.Re_y$– A200 Impeller</i>	<i>170</i>
<i>Figure (6.32) H_o/D_c versus Impeller Speed for A200 Impeller</i>	<i>172</i>
<i>Figure (6.33) D_o/D versus $Po_t.Re_y$ for A100 and A310 Impellers</i>	<i>173</i>

<i>Figure (6.34) H_0/D_c versus impeller speed for A100 and A310 Impellers.....</i>	<i>175</i>
<i>Figure (6.35) Effect of Impeller Speed on Flow Pattern, 1.5% Xanthan Gum....</i>	<i>177</i>
<i>Figure (6.36) Effect of Xanthan Gum Concentration on Flow Pattern, 150 rpm</i>	<i>179</i>
<i>Figure (6.37) Effect of Impeller Type on Flow Pattern, 150 rpm, 0.5% Xanthan Gum.....</i>	<i>181</i>

1. Introduction

Continuous-flow mixing is vital in many processes such as polymerization, fermentation, waste water treatment, and pulp and paper manufacturing because of its demonstrated ability to improve product uniformity and minimize shut down, loading and unloading times. Pseudoplastic or shear thinning fluids with yield stress such as paint, biological and polymer suspensions, pigment slurries, radioactive slurries, and paper and pulp suspension are commonly encountered in the aforementioned processes (Etchells et al., 1987).

Continuous-flow mixers have traditionally been designed based upon ideal flow assumption (Levenspiel, 1998); however, dynamic testing conducted on those mixing vessels (Ein-Mozaffari, 2002) predicted different non-ideality parameters quantified by channeling, recirculation and dead zones. Little information is available in the open literature on the effects of flow non-ideality on continuous-flow mixers for shear thinning fluids with yield stress. It is therefore highly desirable to investigate the dynamic behaviour of such vessels under realistic conditions, aiming to incorporate flow non-ideality parameters (channeling, recirculation and dead zones). Ein-Mozaffari's (2002) model successfully identified flow non-ideality in pulp suspension chest, and proved that conventional methods used to design such vessels under-predict the power required to achieve motion in the vessels.

A significant improvement in the design of mixing vessels can be obtained by developing models that take into account the actual flow fields in a mixing vessel. Computational Fluid Dynamics (CFD) made the development of those models possible by simulating impeller motion using models such as Multiple Reference Frame (MRF) and Sliding Mesh (SM) (Brucato et al., 1998).

Thus the objective of this study was (1) to apply the same dynamic model developed by Ein-Mozaffari (2002) to a scaled continuous-flow mixer for shear-thinning fluids with

yield stress, and (2) to use CFD to gain a better understanding of dynamic behaviour in the vessel.

Chapter two will provide a review of our current understanding of non-Newtonian fluid rheology, design consideration of mixing vessels, power consumption in agitated vessels, cavern formation, continuous-flow mixing in agitated vessels, and CFD application to the mixing process.

In chapter three, the specification of the scaled mixing vessel used in the experimental work will be described, and the experimental procedure will be detailed. Chapter four will provide a review of the dynamic model developed by Ein-Mozaffari (2002) to study the mixing dynamics in stock pulp chest. The numerical method used to quantify flow non ideal parameters, namely channeling and ratio of fully mixed volume in the vessel to the total volume of the vessel, will also be described. Excitation signal design will be examined because the choice of excitation signal has a substantial influence on parameter estimations.

Chapter five will begin with CFD work methodology and conventional transport equations used to model mixing processes. Spatial and time discretization will then be introduced with a special emphasis on pressure gradient, momentum and temporal interpolation schemes. CFD modeling for impeller rotation will then be reviewed, followed by the dynamic modeling of the continuous-flow vessel.

In chapter six, results obtained from experimental and CFD work will be presented. Specifically, the effect of impeller speed and type, feed flow rate, fluid rheology, and vessel configuration on the dynamic of the continuous-flow mixing vessel will be explored. The effect of the aforementioned operation parameters on channeling and ratio of fully mixed volume in the vessel to the total volume of the vessel will be investigated. Then, parameters obtained from CFD will be compared with those obtained from experimental data to test CFD ability to qualify and quantify flow non-ideality in a

vessel. CFD will be used to relate flow pattern, cavern dimension and pathlines to flow non-ideality parameters to provide a synopsis of the dynamics of continuous-flow mixers.

Chapter seven will present the conclusions drawn from this work and suggest recommendations for future research.

2. Literature Review

2.1 Introduction

Mixing refers to the induced motion of a material inside a vessel whereby the occurrence (degree or gradient) of non uniformities in composition and/or properties of the product is reduced to minimum (Ulbrecht and Patterson, 1985). Mixing is prevalent to almost every process industry, including oil and minerals processing, pulp and paper manufacturing, water and waste water treatment, and plastics manufacturing, and is considered to be the backbone of the infrastructure of the chemical, petrochemical, pharmaceutical and biochemical industries (Rushton and Oldshue, 1953).

The bulk of the research and development work done on mixing throughout several decades has focused on Newtonian materials like water and oil. Non-Newtonian fluids, however, can also be subjected to various mixing operations prevalent in polymerization, fermentation, waste water treatment, and pulp and paper industries. Uncertainties still exist in the interpretation of mixing in hydrodynamic complex systems to the extent that the mixer design of non-Newtonian fluids is often described as an “art” rather than a “science”, depending upon empirical correlations, working experience, and intuitive knowledge (Sue and Holland, 1968).

Following is a review of the literature pertaining to rheology of non-Newtonian fluids, design consideration of mixing vessels, power consumption in agitated vessels, cavern formation, continuous-flow mixing in agitated vessels, and CFD application in mixing processes.

2.2 Rheology of non-Newtonian Fluids

Rheology studies the relation between force and deformation in materials. The relationship between stresses acting at a point in a fluid and deformations occurring as a result of their action is called rheological equation of state or constitutive equation (Malkin, 1994).

Viscosity is usually defined as the ratio of shear stress (τ) to shear rate ($\dot{\gamma}$). Fluids having a constant viscosity for any shear rate are called Newtonian and their viscosity is called Newtonian viscosity. If the ratio of shear stress to shear rate is not constant, the fluid is called non-Newtonian, and their viscosity is called apparent or non-Newtonian viscosity (Morrison, 2001).

Non-Newtonian fluids can be grouped into three different classes (Chhabra and Richardson, 1999) as indicated in Figure (2.1).

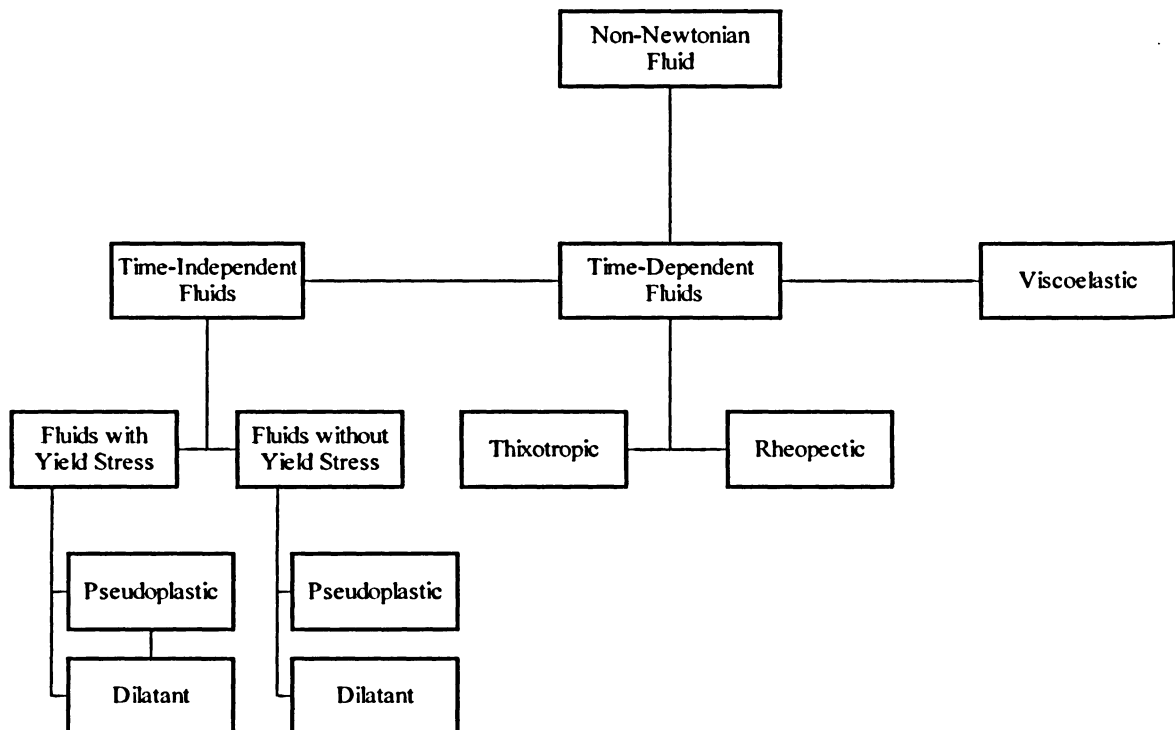


Figure (2.1) Categories of non-Newtonian Fluids

2.2.1 Time-Independent Fluids

Time-independent fluids are the most common type of non-Newtonian fluids. At any time, shear rate at any point in these fluids is determined only by the value of shear stress (Tanner, 2000). Under this category, two types of non-Newtonian fluids can be distinguished: fluids with yield stress and fluids without yield stress

Some non-Newtonian fluids show little or no deformation up to a certain level of stress. Such fluids behave like a solid below the level of stress and like a fluid above it. The stress at which such fluids start to flow is called yield stress, resulting in fluids often referred to as yield stress fluids (Barnes, 2000). The internal structure of yield stress fluids is capable of preventing movement below yield stress. However, the internal structure reforms to allow the fluid to move when shear stress exceeds yield stress (Macosko, 1994). Examples of fluids possessing yield stress can be found in plastic melts, coal, cement, margarine and shortenings, greases, chocolate mixtures, toothpaste, soap and detergent slurries, and paper and pulp suspension.

The rheological behaviour of fluids possessing yield stress can be described by many empirical models, as listed in Table (2.1), where τ_y is yield stress, K is consistency index, n is power law index, and η is apparent viscosity ($\tau/\dot{\gamma}$).

Table (2.1) Rheological Models for Fluids Possessing Yield Stress

Model Name	Model Equation	Reference
Bingham	$\eta = \frac{\tau_y + K\dot{\gamma}}{\dot{\gamma}}$	Malkin and Isayev, 2006
Herschel Bulkley	$\eta = \frac{\tau_y + K\dot{\gamma}^n}{\dot{\gamma}}$	Malkin and Isayev, 2006
Casson	$\eta^{1/2} = \frac{\tau_y^{1/2} + K\dot{\gamma}^{1/2}}{\dot{\gamma}^{1/2}}$	Casson, 1959

Non-Newtonian fluids without yield stress, conversely, can flow at any stress. Examples of non-Newtonian fluids without yield stress include starch suspensions, fruit juice concentrates and printer's ink. The rheology of non-Newtonian fluids without yield stress can be expressed using different rheological equations, as listed in Table (2.2), where τ_y is yield stress, K is consistency index, n is power law index, η_0 is viscosity at zero shear rate, η_∞ is viscosity at infinite shear rate, α is a constant, $\tau_{1/2}$ is shear stress at which viscosity drops to half of its value at zero shear, and η is apparent viscosity ($\tau/\dot{\gamma}$).

Table (2.2) Rheological Models for Fluids without Yield Stress

Model Name	Model Equation	Reference
Power Law (Ostwald de Waele)	$\eta = K(\dot{\gamma})^{n-1}$	Malkin and Isayev, 2006
Cross	$\frac{\eta - \eta_\infty}{\eta_0 - \eta_\infty} = \frac{1}{1 + (K \cdot \dot{\gamma})^n}$	Cross, 1968
Carreau	$\frac{\eta - \eta_\infty}{\eta_0 - \eta_\infty} = \left\{ 1 + (K \cdot \dot{\gamma})^2 \right\}^{(n-1)/2}$	Malkin and Isayev, 2006
Yasuada	$\frac{\eta - \eta_\infty}{\eta_0 - \eta_\infty} = \left\{ 1 + (K \cdot \dot{\gamma})^\xi \right\}^{(n-1)/\xi}$	Malkin and Isayev, 2006
Ellis	$\eta = \frac{\eta_0}{1 + (\tau_{yx} / \tau_{1/2})^{\xi-1}}$	Malkin and Isayev, 2006

Non-Newtonian fluids with and without yield stress can be further divided into pseudoplastic and dilatant fluids.

While pseudoplastic fluids thin at high shear rates, dilatant fluids thicken at high shear rates. Most of the non-Newtonian fluids encountered in industry are shear thinning. At zero shear rates, molecules in shear thinning non-Newtonian fluids are randomly oriented and coiled, imposing maximum resistance to the passage past each other. However, as shear rate is increased, the molecules tend to be “teased out” and aligned parallel to the

applied shear, forcing the viscosity to decrease (Ferguson and Kemblowski, 1991). Examples of pseudoplastic fluids are rubber solutions, adhesives, soap, detergents, paints, and paper and pulp suspension. Dilatant fluids are encountered in corn flour/sugar solutions, and many pigment dispersions containing high concentration of suspended solids such as mica and powdered quartz.

2.2.2 Time-Dependent Fluids

Shear rate in time-dependent fluids is a function of both magnitude and the duration of shear stress application to the fluid. Thixotropic and rheopectic or antithixotropic fluids are the most common kinds of time dependent non-Newtonian fluids.

In thixotropy, the longer the fluid is subjected to shear stress, the lower its viscosity. However, in rheopecty, the longer the fluid is subjected to shear stress, the higher its viscosity. Many gels, paints, and printing inks are thixotropic, exhibiting a stable form at rest but becoming fluid when agitated (subjected to shear stress). Some lubricants and gypsum suspension thicken or solidify when shaken and hence are considered rheopectic fluids (Barnes, 2000).

2.2.3 Viscoelastic Fluids

Viscoelastic fluids exhibit the characteristic of both fluids and elastic solids, showing partial elastic recovery after deformation (after applying shear stress).

In a purely elastic solid the shear stress corresponding to a given shear rate is independent of time, whereas for viscoelastic substances the shear stress will gradually dissipate with time. In contrast to purely viscous liquids, viscoelastic fluids flow when subjected to shear stress but part of their deformation is gradually recovered upon removal of shear stress (Macosko, 1994). Examples of viscoelastic fluids include bitumen, flour dough, and some polymer and polymer melts such as nylon.

2.2.4 Stimulant Time-Independent Yield Stress Fluids

Many materials have been used to simulate the mixing of time-independent yield stress fluids in mixing experiments such as sodium carboxymethylcellulose (CMC), carbopol, and xanthan gum (Edward et al., 2004).

Cellulose is the major component in the structure of the aforementioned materials; however, the properties and application of these materials differ. For instance, while the rheology of carbopol is very sensitive to pH variation, carbopol solution is transparent, permitting flow visualization applications. Xanthan gum and carboxymethylcellulose; however, are not suitable for flow visualization because they are opaque. Xanthan gum solution shows high shear thinning properties even at very low concentration, whereas similar concentrations of carboxymethylcellulose show totally Newtonian behaviour (Macosko, 1994, Barnes, 2000).

The remainder of this section focuses on structure, application and properties of xanthan gum as a time-independent yield stress fluid. Xanthan gum will be used to perform mixing experiments in this work.

Xanthan gum is a high molecular weight polysaccharide polymer produced by a fermentation process using *xanthomonas campestris* bacterium (Kennedy and Bradshaw, 1984). The structure of xanthan gum (Jansson et al., 1975) is shown in Figure (2.2).

Xanthan gum has widespread application; in foodstuff applications it has been used in salad dressings, creams, sauces, syrups, desserts, beverages, and prepared and frozen foods. In the cosmetics and pharmaceutical industry, xanthan gum has been used in lotions, creams, cough syrups, and toothpaste. Industrially it has been also employed in oils, hydraulic fluid, pesticides, animal fodder, cleaning products, dyes, and metal bathing (Kennedy & Bradshaw, 1984, Katzbauer, 1998).

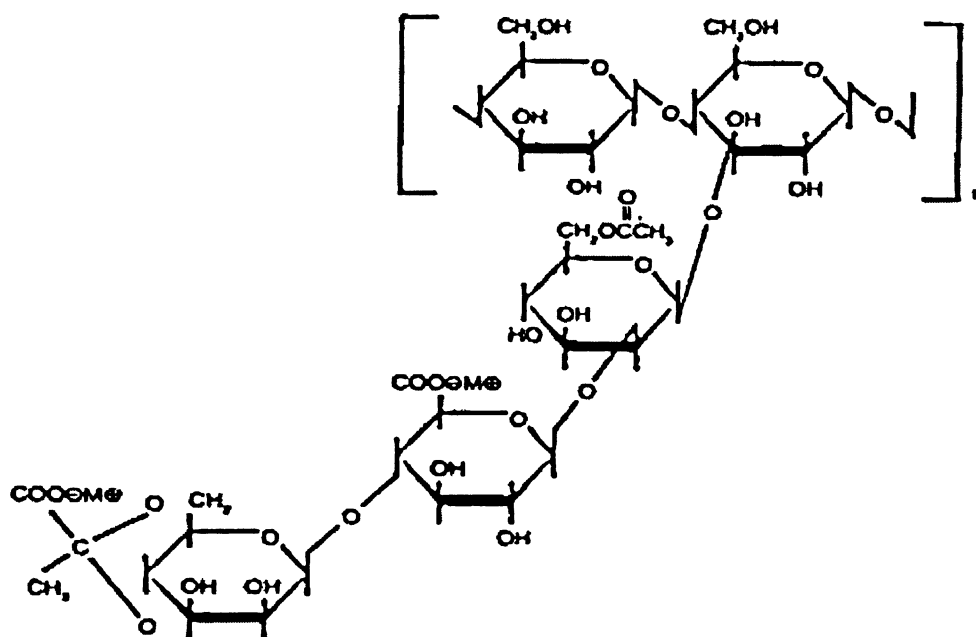


Figure (2.2) Structure of Xanthan Gum Molecules (Jansson et al., 1975)

Several studies have dealt with viscosity or rheology of xanthan gum solution. Most of the studies indicated that the rheology of xanthan gum can be described as a “pseudoplastic fluid with yield stress” (Whitcomb and Macosko, 1978, Galindo et al., 1989, Westra, 1989, Torees et al., 1993, Garcia-Ochoa and Casas, 1994, Xuewu, 1996, Podolsak et al., 1996, Renaud et al., 2005). Rheological models such as Herschel Bulkley (Galindo et al., 1989, Torees et al., 1993, Garcia-Ochoa and Casas, 1994) and Casson (Garcia-Ochoa and Casas, 1994) have been used to model xanthan gum properties. Cross (Renaud et al., 2005) and power law (Galindo et al., 1989, Torees et al., 1993, Xuewu, 1996) have also been used to model xanthan gum rheological properties at very low concentration when the values of yield stress could be neglected.

2.3 Design Considerations of Mixing Vessels

Optimal mixing can be achieved by minimizing mixer investment and operating costs in order to provide high-yield and high-productivity operation. A conventional stirred tank consists of a vessel equipped with a rotating mixer. The rotating mixer has several

components: an impeller, a shaft, flexible coupling, and a motor drive. Several others components, such as baffles and inlet/outlet, may be necessary to finalize stirred tank design and satisfy process objective. The design of a mixing vessel can thus be considered as a complex interaction of the factors listed below (Oldshue, 1983).

1. Vessel:
 - Shape (vertical or horizontal) & (rectangular, square, cylindrical, etc.)
 - Bottom shape (flat, dished, conical, etc.)
 - Height/diameter ratio
2. Shaft:
 - Shaft Entry (top, bottom or side)
 - Center (on or off)
3. Impeller:
 - Flow direction (axial or radial)
 - Number of impellers
 - Impeller design (blade width, blade height, blade twist, blade angle, blade thickness, number of blades, pitch ratio, etc.)
 - Clearance height
 - Impeller/vessel diameter ratio
4. Mechanical:
 - Variable frequency motor drive
 - Shaft support
5. Other:
 - Baffles
 - Input/output location

The following sections (2.3.1-2.3.5) aim to provide detailed insight about mixing vessel design.

2.3.1 Vessel Design

Mixing vessels are usually designed based upon proprietary data that have been refined through experimentation. A vertical cylindrical tank is often described as a standard mixing vessel; although, rectangular, square, or horizontal cylindrical vessels are also sometimes used (Rushton and Oldshue, 1959, Oldshue, 1983, Edward et al., 2004).

Tanks with height equal to diameter are ideal geometric proportions for top-entry agitators. Short tanks with height less than the diameter require multiple top-entry mixers or side entry mixer(s). However, tall tanks with height greater than diameter require a single top-entry mixer with multiple impellers or bottom-entry mixer(s) to reduce shaft length and provide mechanical stability (McDonough, 1992).

While conventional vessels use flat bottom tanks, dished bottom tanks such as ellipsoidal, conical, ASME, spherical or hemispherical can also be used (Rushton, 1947). The selection of bottom shape depends mainly on vessel use and required ease of cleaning and emptying (Harnby et al., 1997).

2.3.2 Shaft Design

Shaft configuration for a specific mixer application depends on the process requirements, tank geometry and drive unit (Ramsey and Zoller, 1976, Fasano et al., 1995). Shaft selection does not follow a specific design procedure.

The three most common mounting arrangements of shafts are top, side and bottom (AIChE, 2001). Although top-entry shafts can be used for many applications, side-entry units are best situated for blending homogenous fluids or slurries with low settling velocity solids (King, 1992). Bottom-entry shafts are not very common and are used mainly with dished-bottomed tanks. Top-mounted shafts are the most advantageous for three reasons (Bates, 1964, Tatterson, 1994). Firstly, top-entry shafts do not require a mechanical seal to prevent liquid leakage. Secondly, the top-entry mixer hangs straight in the vessel, allowing shaft and impeller weight to stabilize the shaft while in operation. Thirdly, compared with side-entry devices, pumping rates are higher in top-entry shafts, resulting in shorter blending times.

Mixers can be mounted in a number of different ways, including on-center, off-center, and angular. Top-entry mixers can be mounted off-center and at an angle in order to

avoid using baffles in the tank. Side-entry mixers must be angled approximately 7° to 10° from tank diameter to develop a top-to-bottom flow pattern in the vessel (Holland and Chapman, 1966).

2.3.3 Impeller Design

Hundreds of impellers are in commercial use in the industry. Generally, there is no one unique impeller that meets all process specifications (Oldshue and Tood, 1981). Determination of the most effective impeller should be based upon the understanding of process requirements and knowledge of physical properties of materials to be mixed (AIChE, 2001). Most of the impellers have three or four blades that are bolted or welded on a central hub that mounts to the shaft.

Impellers share many characteristic properties with pumps. The most fundamental of these properties is that impellers consume power to produce flow and velocity head (or shear). Accordingly, impellers can be grouped in a flow/head (shear) spectrum as shown in Figure (2.3) (Corpstein et al., 1979).

At the top of the impeller spectrum are hydrofoil impellers, propellers and axial flow impellers, such as pitched blade turbines. These impellers produce high flow and low shear rate, and are generally used for moderate viscosity, solid suspension, and heat transfer applications (McDonough, 1992). Following are radial impellers producing high power per unit volume (high shear). These impellers, including Rushton, bar and bladed turbines are often used for gas-liquid, liquid-liquid dispersion and other mass transfer applications (Harnby et al., 1997). Next are high efficiency impellers, such as paddle, anchors, helical and spirals. These impellers are suitable for very high viscosity mixing and slurries suspension applications. Extremely high shear rates may be obtained by using colloid mills, homogenizers and sawtooth impellers. These impellers have numerous applications in solid size reduction such as grinding, and in dispersing pigments and making emulsions (Oldshue, 1983).

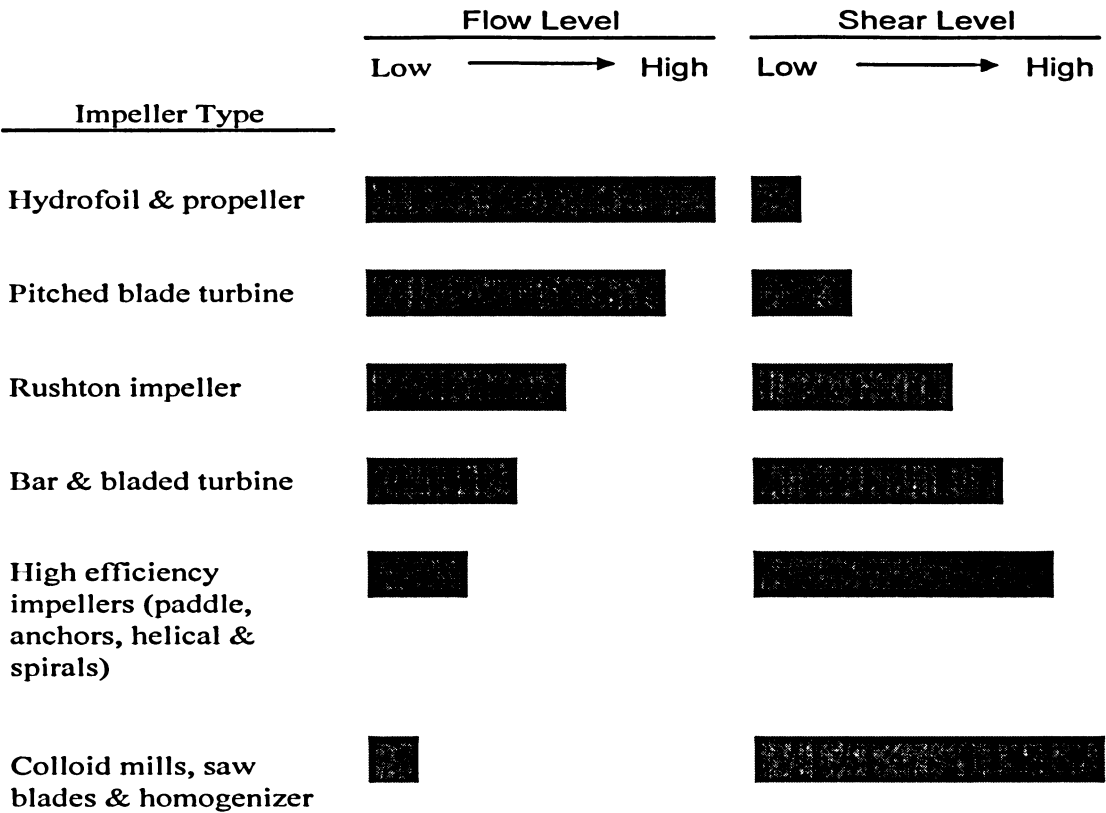
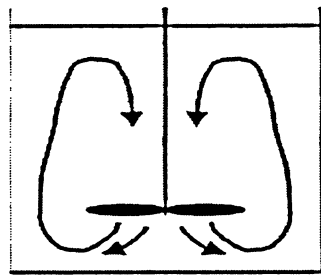
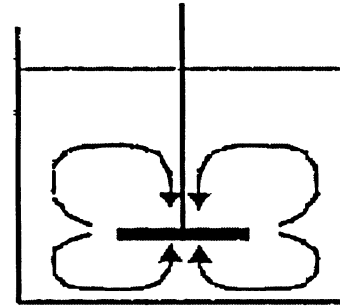


Figure (2.3) Flow/Head (Shear) Spectrum of Impellers

Due to their general multi-functions, axial and radial flow impellers are often used in mixing vessels. Axial flow impellers circulate the flow vertically up and down away from impeller blades, and parallel to the shaft axis. Radial flow impellers, on the other hand, discharge fluid horizontally away from the impeller toward the tank wall. Compared with radial flow impellers, axial flow impellers produce more flow per unit power (maximize flow and minimize shear rate), and are more cost effective (AIChE, 2001 and Oldshue, 1989). The flow pattern generated by an axial and a radial flow impeller is represented in Figure (2.4) below.



Axial Flow Impeller



Radial Flow Impeller

Figure (2.4) Flow Pattern for an Axial and Radial Impeller

Geometrical factors such as the number of impellers, pitch ratio, location of impeller in vessel and clearance, ratio of impeller to tank diameter, and blades geometry including blade width, blade height, blade twist, blade angle, blade thickness, and number of blades must be taken into consideration during the impeller design process.

For axial flow impellers, pitch ratio is equal to the distance in impeller diameter that an impeller would advance for each revolution when rotated in a fluid body (Oldshue, 1983). Impellers with a pitch ratio of 1.0 (or square pitch) would generate a path equal in length to impeller diameter for each revolution. Pitch ratio varies between 0.5 to 1.5 times impeller diameter. Variable-pitch, axial flow impellers have a constant blade angle while constant-pitch impellers have a variable blade angle. Variable pitch blades impellers produce a variable velocity discharge and variable shear rates across the impeller diameter (Bates, 1964).

The location of an impeller relative to other impellers, vessel bottom, and the static, free surface of liquid has an effect on mixing vessel performance. No formal rules are ascribed to these dimensions. The ratio between clearance (distance between vessel bottom to impeller blades) and liquid height in a mixing vessel is usually $1/3$ - $1/2$ (Perry & Green, 1997). A particularly important ratio in mixing vessel design is impeller to tank diameter ratio, which spans from $1/6$ to 0.98. A typical value of $1/3$ is recommended

(McCabe, 2005). Similarly, no rules are ascribed to blades geometrical dimension such as width, height, twist, angle, number of blades, etc.

2.3.4 Mechanical Design

Mixing vessel mechanical design contributes up to 60% of total mixer design cost (McDonough, 1992). One of the most important elements in mixing vessels is the variable speed device, an AC induction motor equipped with a control that varies the frequency of the alternating current and consequently the speed of the motor.

The primary function of the shaft is to transit torque from the drive to the mixing impellers. However, the shaft must perform other functions such as resisting the bending moments created by the impeller loads, limiting deflections, and supporting the weight of the impeller(s). Thus shaft support is crucial in mixing vessel design. Quill shaft support configuration (Oldshue, 1983) is a common arrangement isolating shaft from moments by connecting the shaft to a flexible coupling that accommodates misalignment accompanies shaft rotation.

2.3.5 Other Design Considerations

Baffles are generally used in transitional and turbulent mixing processes for the following reasons (Rushton, 1947):

- Promoting the flow pattern required for the process;
- Directing flow from the impeller producing the required vertical currents;
- Changing flow from a rotary pattern to a mixing pattern;
- Preventing excessive swirling, vortexing and air induction; and
- Assuring a stable consistent power draw.

Top-entry mixers mounted on a tank centerline require baffles, whereas side-entry mixers do not require baffles to achieve proper flow pattern. Baffles can also be eliminated from mixers mounted in an angular off-center position. Square or rectangular tanks do not require baffles as the tank walls act as baffles in providing vertical flow components for top-to-bottom turnover (Ulbrecht and Patterson, 1985).

The other important factor in mixing vessel design is input/output location required in continuous-flow mixing operation. The feed input should be pointed at an active surface away from the tank wall and impeller shaft. The outlet is generally located on the side of the vessel or in the bottom head.

2.4 Power Consumption in Agitated Vessels

2.4.1 Power in Agitated Vessels

Power (energy per time) is an integral quality required at all mixing processes to produce flow and/or shear (head). Power is added to the fluid by the mixing device (impeller) (Edward et al., 2004). An impeller operating at a specific speed and power produces torque. Impeller rotation imparts a mechanical force opposed by the fluid in the vessel. The fluid in turn produces a torque on the impeller transmitted through the shaft to the motor (Oldshue, 1983). Power is related to torque by the following equation:

$$P = 2\pi.N.M \quad (2.1)$$

where N is impeller velocity, M is torque and P is power.

Power determines utility costs and energy (power multiplied by time) determines mixer operating cost. Thus, a detailed analysis of power is essential to mixing vessel design (Su and Holland, 1968).

The following two sections aim to develop power relations for Newtonian fluids and non-Newtonian fluids. Some important characteristics of power consumption in axial impellers will be also reviewed in section 2.4.4.

2.4.2 Power Consumption for Newtonian Fluids

Impeller power consumption is a function of impeller speed, impeller diameter, physical properties of the fluid, vessel size and geometry, impeller location relative to vessel and fluid boundaries and relative to other impellers or obstructions in the mixing vessel, and the presence or absence of baffles (Holland and Chapman, 1966).

Using Buckingham's Pi Theorem, the following dimensional equation can be derived for power consumption in mixing vessels (Uhl and Gary, 1966, Dickey and Fenic, 1976):

$$f\left[\left(\frac{\rho.D^2.N}{\mu}\right),\left(\frac{D.N^2}{g}\right),\left(\frac{P}{\rho.D^5.N^3}\right),\left(\frac{D}{T}\right),\left(\frac{D}{Z}\right),\left(\frac{D}{C}\right),\left(\frac{D}{p}\right),\left(\frac{D}{w}\right),\left(\frac{D}{l}\right),\left(\frac{b_2}{b_1}\right)\right] = 0 \quad (2.2)$$

where D , T , Z , C , w , p , b , l , ρ , μ , P , N and g are impeller diameter, tank diameter, liquid depth, clearance off the vessel bottom, blade width, pitch of blades, number of blades, blade length, fluid density, fluid viscosity, power, impeller rotational speed and gravitational acceleration, respectively.

For geometrically similar systems, Equation (2.2) can be reduced to the following equation:

$$f\left[\left(\frac{\rho.D^2.N}{\mu}\right),\left(\frac{D.N^2}{g}\right),\left(\frac{P}{\rho.D^5.N^3}\right)\right] = 0 \quad (2.3)$$

where

$$Re = \frac{\rho.D^2.N}{\mu} \quad \text{is Reynolds number (the ratio of inertial to viscous force)}$$

$$Fr = \frac{D.N^2}{g} \quad \text{is Froude number (the ratio of inertial to gravitational force)}$$

$$Po = \frac{P}{\rho.D^5.N^3} \quad \text{is Power number}$$

Equation (2.3) can be rewritten in terms of the dimensionless numbers defined above:

$$Po = c(Re)^a (Fr)^b \quad (2.4)$$

where c , a and b are equation constants.

For a fully baffled tank, where the surface waves and vortices are absent, the exponent (b) is usually zero and the power number is solely a function of Reynolds number (McDonough, 1992).

Depending on viscosity, mixing processes involve three different flow regions, namely laminar, transition and turbulent. Turbulent flow prevails when Reynolds number is greater than 10^3 or 10^4 (Tatterson, 1994). Plotting Power number versus Reynolds number on log-log coordinates yields power curve. Important influencing factors for the characteristics of such curves are the type of mixer, tank geometry (especially the presence of baffles), and the rheology of mixing material.

In the laminar mixing regime, density has no influence on power draw. In the transition region, both density and viscosity can be significant. In turbulent region, viscosity is not important. Accordingly, in the turbulent range, Power number is almost constant. At laminar range; however, power number is inversely proportional to Reynolds number (Holland and Chapman, 1966).

2.4.4 Power Consumption for non-Newtonian Fluids

While predicting power number poses no problems for Newtonian fluids, the situation is more complicated for non-Newtonian fluids. Reynolds number is required to estimate the region of mixing process, i.e., laminar or turbulent, and then to estimate power number. Viscosity is necessary to calculate Reynolds number, but viscosity in non-Newtonian fluids is a function of shear rate, which itself is a function of the flow parameters (Knoch, 1999, Shekhar and Jayanti, 2003).

Two approaches have been used in the literature to tackle power curve estimation in non-Newtonian fluids:

- Modification of Reynolds number; and
- Modification of viscosity definition.

Modification of Reynolds number yields a power curve that is fluid and geometry dependent (Foresti and Liu, 1959, Calderbank and Moo-Young, 1961). However, the power curve obtained from modifying viscosity definition is efficient to describe all Newtonian and non-Newtonian fluids. The pioneering work of Metzner and Otto (1957) addressed the second approach based on the assumption that the fluid motion in the vicinity of the impeller can be characterized by an average shear rate ($\dot{\gamma}_{avg}$) which is linearly related to the impeller rotational speed.

$$\dot{\gamma}_{avg} = k_s \cdot N \quad (2.5)$$

The proportionality constant (k_s) is independent of tank-to-diameter ratio and dependent only on impeller geometry. This approach has been cited by many researchers to estimate power in fermentation broths, biological systems, foods, slurries, and concrete mixture (Doraiswamy et al, 1994). Value of k_s has been reported at 10-12 for many impellers (Calderbank and Moo-Young, 1959 and 1961).

Due to the importance of power in optimizing the configuration of stirred vessels, thousands of published studies are available in the open literature. Table (2.3) briefly reviews the work done on power consumption in non-Newtonian fluids using axial impellers.

2.4.5 Characteristics of Axial Flow Impellers

The characteristic of any impeller can be usually quantified by two numbers, namely, power number and flow number (King et al., 1988).

Power consumed by an impeller can be obtained by multiplying pumping capacity, Q_p by head H . A particular agitator imparts power at a rate dependent on its type, and this power is characterized by power number.

$$P \propto [Q_p][H] \rightarrow P \propto [\rho.N.D^3][N^2.D^2] \quad (2.6)$$

The proportionality constant is called power number, Po , accordingly:

$$Po = \frac{P}{\rho.D^5.N^3} \quad (2.7)$$

The other important characteristic of agitators is pumping capacity, which relates the agitator ability to pump and circulate fluid in a vessel. Pumping capacity, Q_p , is proportional to impeller speed and impeller diameter.

$$Q_p \propto [N^3][D] \quad (2.8)$$

The proportionality constant is called flow number, Fl, accordingly:

$$Fl = \frac{Q_P}{ND^3} \quad (2.9)$$

Table (2.3) Power Consumption in Mixing of non Newtonian Fluid Literature Review

Author	Fluid	Impeller	Power Correlation
Calderbank and Moo-Young, 1959	Perspex in toluene, oil based paint, clay suspension in water, CMC*, paper pulp suspension	A100 & various radial impellers	$k_s = 10$
Foresti and Liu, 1959	Silicon fluid, CMC*, clay suspension in water, solution of polyisobutene	A100 & various radial impellers	$\frac{P}{D^5 N^3 \rho} = 160 \times 50^{n-1} \left(\frac{D^2 N^{2-n} \rho}{K} \left(\frac{Z}{C} \right)^n \left(\frac{D}{D+T} \right) \right)^{-1}$ <p>P power, D impeller diameter, N impeller speed, ρ fluid density, K power law consistency index, Z liquid depth, C impeller off vessel bottom clearance, T vessel diameter</p>
Metzner et al, 1961	CMC*, Attasol, Carbopol, Permangel	A100 & various radial impellers	$k_s = 10 \pm 0.9$
Calderbank and Moo-Young, 1961	Perspex in toluene, oil based paint, clay suspension in water, CMC*, paper pulp suspension	A100 & various radial impellers	$\frac{P}{N^3 D^5 \rho} \left(\frac{4N_s L_e + D_e}{N_s D_e} \right) \left(\frac{\Delta w^{0.5}}{(b.N_s)^{0.67}} \right) = 6.3 \left(\frac{D^2 N \rho (BN)^{1-n}}{K} \left(\frac{4n}{3n+1} \right)^n \right)^{-1}$ <p>P power, D impeller diameter, N impeller speed, ρ fluid density, N_s effective number of blade edge (=1 for axial flow impellers), L_e and D_e impeller equivalent height and diameter ,respectively, Δw vessel wall proximity factor (=3.33 for axial flow impellers), s ratio of impeller to vessel diameter, b number of impeller blades, B constant depends on impeller type (=11±0.1 for axial flow impellers), n is power law exponent, K power law consistency index</p>

Table (2.3) Power Consumption in Mixing of non Newtonian Fluids Literature Review – Cont (1)

Author	Fluid	Impeller	Power Correlation
Blasinski and Ryzski, 1976	non-Newtonian power law fluids	A100 & various radial impellers	Review of Power number-Reynolds number relationship
DucLa et al, 1983	Alginate & CMC*	A200	Graphs of Power number-Reynolds number relationship
Nouri and Hockey, 1988	CMC*	A200	$k_s=12$
Zappenfeld and Mersmann, 1988	CMC* & xanthan gum	A200 & various radial impellers	$\frac{P}{N^3 D^5 \rho} = \frac{K_R}{D^2 N^{2-n} \rho} \left[\left(\frac{U_{tur}}{U_{lam}} - 1 \right) \phi + 1 \right]^n + Po_t \phi^3$ $\frac{K_R}{K \cdot k_s^{n-1}}$
<p>P power, D impeller diameter, N impeller speed, ρ fluid density, K_R power number at Reynolds number equals 1, Po_t impeller turbulent power number, n is power law exponent, K power law consistency index, k_s proportionality constant in Metzner and Otto correlation, Φ constant depends on flow region in vessel (=0 for laminar and 1 for turbulent), U_{tur}/U_{lam} ratio of laminar to turbulent impeller speed</p>			
Galindo and Nienow, 1992	Xanthan gum broths	A315	$\frac{P}{N^3 D^5 \rho} = a \left(\frac{D^2 N^{2-n} \rho}{K \cdot k_s^{n-1}} \right)^{-1} \quad 1 < Re < 30,$ $\frac{P}{N^3 D^5 \rho} = a \left(\frac{D^2 N^{2-n} \rho}{K \cdot k_s^{n-1}} \right)^{-0.33} \quad 30 < Re < 100$ $\frac{P}{N^3 D^5 \rho} = a \left(\frac{D^2 N^{2-n} \rho}{K \cdot k_s^{n-1}} \right)^{-0.50} \quad 100 < Re < 300$

Table (2.3) Power Consumption in Mixing of non Newtonian Fluids Literature Review – Cont (2)

Author	Fluid	Impeller	Power Correlation
Galindo and Nienow, 1992			P power, D impeller diameter, N impeller speed, ρ fluid density, K power law consistency index, n is power law exponent, k_s proportionality constant in Metzner and Otto correlation, a constant depends on solution concentration
Kelly and Gigas, 2003	Carbopol	A315 & A200	$k_s=8.58$

*CMC is Carboxymethylcellulose

2.5 Cavern Region

An important characteristic of the rheology of pseudoplastic fluids possessing yield stress is that viscosity decreases with increasing shear rate. Therefore, fluid flows easily in high shear regions near the rotating impeller but is subjected to high shear flow resistance in low shear regions remote from the impeller. In particular, the fluid motion ceases where shear stresses are below the yield stress of the fluid. This leads to the formation of a well mixed region of fluid around the impeller with the remaining fluid appearing stagnant (Nienow, 1984, Nienow and Elson, 1988, Galindo et al., 1988, Galindo and Nienow, 1993, Nienow, 1998). The term “cavern” was first introduced by Wichterle and Wein (1975 and 1981) to describe this region.

In the laminar flow region, the ratio of cavern diameter/impeller diameter is constant (independent of impeller speed) and approximately equal to unity. Thus, mixing of a yield stress fluid in the laminar region requires an impeller which has a diameter equal to that of the tank to avoid stagnant regions (Solomon et al. 1981, Elson et al. 1986, Galindo & Nienow, 1992, Galindo et al., 1996, Serraano-Carreón and Galindo, 1997).

In the transition and turbulent region, cavern diameter increases with increasing impeller speed. Cavern diameter becomes constant when the cavern reaches the vessel wall. As impeller speed continues to increase, cavern gains vertical circulation and increases in height until it fills the whole of the vessel (Elson, 1990 B, Galindo & Nienow, 1992, Galindo et al., 1996, Serraano-Carreón and Galindo, 1997).

Different mathematical models have been proposed to estimate cavern diameter (Wichterle and Wein, 1975 & 1981, Solomon et al., 1981, Elson et al., 1986, Elson, 1988, Hirata & Aoshima, 1995 & 1996, Amanullah et al., 1998, Wilkens et al., 2005). The details of those models are provided in Table (2.4).

Table (2.4) Cavem Mathematical Models Literature Review

Author	Cavem Measurements Technique	Correlation Proposed	Remarks
Witchterle and Wein, 1975 & 1981	Coloring with a dye	Centrifugal forces generated by the impeller were balanced by the retarding shear forces on the cavem surface	D_c cavem diameter, D impeller diameter, N impeller speed, ρ fluid density, τ_y is fluid yield stress
		$\left(\frac{D_c}{D}\right)^2 = \frac{\rho \cdot N^2 \cdot D^2}{\tau_y}$	
Solomon et al. , 1981	Streak photographs in carbolol solution & hot film anemometry in opaque xanthan gum solution	Spherical cavem centered upon the impeller assuming that the shear stress at the cavem boundary equals to the fluid yield stress	P_{ot} impeller turbulent power number, and Re_y is yield stress Reynolds number defined as follows $Re_y = \frac{\rho \cdot N^2 \cdot D^2}{\tau_y}$
		$\left(\frac{D_c}{D}\right)^3 = \frac{4}{\pi^3} \cdot P_{ot} \cdot \frac{\rho \cdot N^2 \cdot D^2}{\tau_y} = \frac{4}{\pi^3} \cdot P_{ot} \cdot Re_y$	
Elson et al., 1986	X-ray in xanthan gum solution	Modification to Solomon et al. (1981) model to a right circular cylinder centered upon the impeller	
		$\left(\frac{D_c}{D}\right)^3 = \frac{1.36}{\pi^2} \cdot P_{ot} \cdot \frac{\rho \cdot N^2 \cdot D^2}{\tau_y} = \frac{1.36}{\pi^2} \cdot P_{ot} \cdot Re_y$	
Elson, 1988	X-ray flow visualization	Modification to Elson et al. (1986) model to include the ratio of cavem height to diameter assuming a cylindrical cavem	H_c cavem height When $D_c < D_{Tank}$, $H_c/D_c = 0.4$ $H_c \propto N^{0.88}$ for two-blade paddle impeller
		$\left(\frac{D_c}{D}\right)^3 = \frac{P_{ot} \cdot Re_y}{\left(\frac{H_c}{D_c} + \frac{1}{3}\right)^2 \pi^2}$	

Table (2.4) Cavern Mathematical Models Literature Review – Cont (2)

Author	Cavern Measurements Technique	Correlation Proposed	Remarks
Elson., 1990 A & B.	X-ray flow visualization	Elson model (Elson, 1988)	When $D_c < D_{Tank}$, $H_c/D_c = 0.75$ $H_c \propto N^{0.76}$ for marine propeller
Hirata et al., 1991 & 1994	Laser Doppler Anemometry	Elson model (Elson, 1988)	When $D_c < D_{Tank}$, $H_c/D_c = 0.50$ $H_c \propto N^{2/3}$ for Scaba impeller
Galindo and Nienow, 1992	Visualization techniques in carbopol solution	Assuming a toroidal cavern. No clear agreement was found with cavern cylindrical model (Elson, 1988) and a slope of 0.25 was suggested (instead of 1/3) when D_c/D was plotted against power number	When $D_c < D_{Tank}$, $H_c/D_c = 0.58$ $H_c \propto N^p$ where p is equal to 0.39 and 0.52 for forward and reverse modes of pumping, respectively, for A315 Lighnin impeller
Hirata and Aoshima, 1995 & 1996	Laser Doppler Anemometry	Redevelopment to Elson et al. model (1988) under the assumption that the fluid motion ceases if the shear stress in a dissipation zone is smaller than the fluid yield stress. $\left(\frac{D_c}{D}\right)^3 = \frac{4\alpha^2}{\pi} \cdot P_{ot} \cdot \frac{Re_y^2}{Re} \cdot \frac{H_c}{D_c}$	where α is the proportional constant between shear stress in the dissipating zone and average shear stress responsible for the dissipation rate in the cavern. α was found to be equal to 0.43

Table (2.4) Cavern Mathematical Models Literature Review – Cont (3)

Author	Cavern Measurements Technique	Correlation Proposed	Remarks
Amanullah et al., 1997 & 1998	Laser Doppler Anemometry	$\left(\frac{Dc}{D}\right)^2 = \frac{1}{\pi} \left\{ \frac{\rho \cdot N^2 \cdot D^2}{\tau_y} \right\} \sqrt{N_f^2 + \left(\frac{4 \cdot P_{ot}}{3\pi} \right)^2}$	Assuming a toroidal cavern and equating the total momentum imparted by the impeller to the sum of both tangential and axial shear components. These forces transported to the cavern boundary by the pumping action of the impeller
		<p>Here $N_f = F_a / N^2 D^4$ is the dimensionless axial force number and F_a is the axial force imparted by the impeller</p>	
Wilkens et al., 2005	Injecting glitter, freezing the solution, and dissecting the frozen solid	$Dc = \alpha \cdot \left(\frac{P_{ot} \cdot N^2 \cdot D^5}{2\pi} \right)^{1/3}$ $Hc = \beta \cdot \left(\frac{P_{ot} \cdot N^2 \cdot D^5}{2\pi} \right)^{1/3}$	<p>Elliptical torus cavern derived under the assumption that the torque imparted by the impeller equals to the torque dissipated at the cavern boundary</p> <p>For radial flow impellers α is 1.08 and β is 0.85. For axial flow impellers α is 0.98 β is 1.13</p>

2.6 Continuous-Flow Mixing Operation

In batch mixing, material to be mixed is loaded into the mixer, the mixer is operated, and the final product is unloaded so that another batch can be loaded into the vessel. By contrast, continuous-flow mixing allows material to flow steadily from an upstream process into the mixing vessel, is retained in the vessel for a specified mixing time, and discharges for downstream handling. Continuous-flow mixing operation has numerous advantages over the batch operation as the continuous operation allows high production rates, improves process control, and decreases operation time by eliminating pump-out, filling, and between-cycle cleaning.

In continuous-flow mixers, the mixing process depends not only upon the type of stirrer and speed of stirring, but also upon mean residence time and vessel geometry, including the input and output location. The outlet may be positioned either at the bottom of the tank to drain vessel contents by gravity, or at the side of the vessel. The inlet position may also vary, with the tip of the inlet pipe located at the top of the vessel or at some place inside the stirred liquid close to the impeller. Although submerged inlets are recommended for efficient mixing, they may generate operational problems such as mechanical vibrations, corrosion, and clogging. Thus, bottom outlet and surface input are often preferred.

The remainder of this section will be devoted to first developing the dynamic response of a continuous-flow mixer, and then summarizing the work done in the open literature on mixing in continuous-flow vessels.

2.6.1 Dynamic Modeling of Continuous-Flow Mixers

Continuous-flow agitated vessels have always been designed based on perfect (or ideal) mixing assuming (Oldshue, 1983): (1) input stream is instantaneously dispersed throughout the vessel, (2) input and output flowrate are equal, (3) composition of outlet

stream is equal to the uniform composition throughout the tank, and (4) fully mixed volume is equal to the total volume of solution in the vessel.

A mass balance on continuous-flow vessel yields the following:

$$\rho Q C_{m,in} - \rho Q C_{m,out} = \rho V \frac{dC_{m,out}}{dt} \quad (2.10)$$

$$C_{m,in} - C_{m,out} = \tau_m \frac{dC_{m,out}}{dt} \quad (2.11)$$

where C_m , t , ρ , Q , V and $\tau_m = V/Q$, represent solution mass concentration, time, solution density, solution flowrate, solution volume and vessel residence time.

At steady state, $C_{m,in,ss} = C_{m,out,ss}$ and Equation (2.11) can be written as follows:

$$(C_{m,in} - C_{m,in,ss}) - (C_{m,out} - C_{m,out,ss}) = \tau_m \frac{dC_{m,out}}{dt} \quad (2.12)$$

$$C'_{m,in} - C'_{m,out} = \tau_m \frac{dC'_{m,out}}{dt} \quad (2.13)$$

where $C'_{m,in} = C_{m,in} - C_{m,in,ss}$ and $C'_{m,out} = C_{m,out} - C_{m,out,ss}$ are deviation variables.

Taking Laplace transform of both sides of Equation (2.13) yields the following:

$$\tau_m s C'_{m,out}(s) = C'_{m,in}(s) - C'_{m,out}(s) \quad (2.14)$$

$$G(s) = \frac{C'_{m,out}(s)}{C'_{m,in}(s)} = \frac{1}{\tau_m s + 1} \quad (2.15)$$

Equation (2.15) indicates the behaviour of a perfectly mixed-flow mixer represented by a first order transfer function.

2.6.2 Continuous-Flow Mixers Literature Review

Works examining mixing in continuous-flow vessels is relatively limited to few publications, although continuous-flow stirred tanks have been described by Agricola in 1556. In his state of the art book *De Re Metallica* (1556), Agricola provided drawings of continuous-flow stirred tanks utilized in mining and metallurgical applications.

Johnson and Hubbard (1974) obtained response data for negative step changes in input tracer concentration for a continuous-flow mixing vessel under different impeller speeds and polysaccharide dilution rates. Comparing experimental measurements with the ideal residence time distribution, Johnson and Hubbard concluded that using ideal mixing concept in scaling mixing vessels may lead to serious errors because bulk motion does not dominate the mixing vessel.

In a typical continuous-flow mixer, the feed enters at the top of the tank, circulates in the vessel and then exits at the bottom. The choice of feed rate, and thus mean residence time ($\tau_m = V/Q$, where V is vessel volume and Q is feed flowrate) is often related to the mixing time (t_m), in batch vessels. Typically, a value of the ratio $\tau_m/t_m \approx 10$ is often recommended for an effective operation of continuous-flow mixers (Mavros et al., 1997, Zannoud et al., 1991).

Using Laser Doppler Velocimetry, several investigators observed fully mixed volume in agitated vessels. Height of fully mixed region was considered the height at which the impeller jet diminishes in front of the baffles or the height at which slope of axial velocity gradient approaches zero. Bittorf and Kresta (2000) investigated the effect of impeller off bottom clearance on the size and location of fully mixed volume in a stirred vessel. Under

fully turbulent flow conditions, the size of the active volume was found to be independent of operation conditions (i.e., impeller diameter, impeller type, impeller rotational speed and off bottom clearance). Active volume was approximately two-thirds of the tank volume and the location of active volume was dependent upon the clearance for A200 impeller, but not for A310 impeller. This was attributed to the discharge angle of A200 and subsequent impingement of the discharge stream on vessel wall.

Mavros et al. (1997 & 2002 A&B) investigated the flow structure in a continuous-flow stirred vessel agitated by a Rushton turbine and a Mixel TT using Laser Doppler Velocimetry. Velocity measurements were obtained for two inlet locations: a surface input located above the impeller and a submerged input facing the impeller. Mavros et al. concluded that the flow disruption caused by incoming liquid stream in both configurations was noticeable only in the first vessel quarter, which followed the plane where the input tube was located. The disruption of the flow gradually attenuated and velocity measurements taken in a plane rotated 90° clockwise from the input indicated a flow pattern similar to that obtained in a batch mixing vessel.

Khopkar et al. (2004) studied the flow fields generated by agitating water using a Mixel TT impeller in a stirred vessel. CFD was used to simulate the flow structure and the results were verified using Laser Doppler Velocimetry. The influence of impeller speed and inlet and outlet location was studied. Even when $\tau_m/t_m=9.6$, short circuiting and bypassing were observed in the vessel as long as the input was from top.

Ein-Mozaffari et al. (2001 & 2005) studied the dynamics of agitated pulp stock chest under controlled conditions of impeller speed, pulp suspension concentration, input pulp suspension flowrate and vessel input and output locations. They attributed the deviations from ideal mixing to a number of factors including bypassing, recirculation and the presence of dead zones in the chest. Such zones can arise from the interaction between the circulation patterns generated by the impellers, the suspension flow through the vessel and chest geometry (Ein-Mozaffari et al. 2004). Dynamic tests conducted on a pilot stock chest by Ein-Mozaffari et al. (2003) showed that the extent of non-ideal flow can be

significant. The percentage of channeling was as high as 90% of pulp feed at high input flowrates and low impeller speed. Even when eye observations show that the whole suspension was in motion, the channeling and dead volume remained 26% and 16% respectively (Ein-Mozaffari et al. 2002 A&B).

Samaras et al. (2006 A&B) studied the effect of continuous water flow and agitator type (Mixel TT and Rushton turbine) on vessel hydrodynamics and flow non ideality using residence time distribution analysis and Computational Fluid Dynamics. They concluded that the amount of perfectly mixed volume in the vessel reached only 60%-80% of the total vessel volume, and noted that up to 25% of the total vessel volume behaved liked dead zones, and up to 14% corresponds to plug flow.

Aubin et al. (2006) studied the effect of pumping direction of a Mixel TT impeller, feeding rate and the number of feed inlets on the operation of a continuously stirred tank using CFD. They concluded that the mixing quality in such vessels can be improved, without problems of short circuiting, by employing up-pumping impellers coupled with multiple surface feed inlets. Using up-pumping impellers decreases mixing time, leading to higher τ_m / t_m ratios. Adding additional inputs intensifies total feed flowrate without short circuiting problems caused by high velocity streams.

Ford (2004) and Ford et al. (2006) simulated the flow dynamics in a pulp chest previously measured experimentally by Ein Mozaffari (2002) using Computational Fluid Dynamics (CFD). Although CFD was able to capture the mixing dynamics in the vessel fairly well, it underestimated flow non-ideality.

2.7 Computational Fluid Dynamics (CFD)

Computational Fluid Dynamics (CFD) techniques are capable of providing very detailed information in mixing vessels. CFD has been effectively utilized to investigate flow fields (Bkker and Fasano, 1993, Wikstrom and Rasmuson, 1998, Kelly and Humphrey,

1998, Ford et al., 2006, Moilanen et al., 2006), measure turbulence and energy dissipation (Sahu et al., 1999), validate Metzner-Otto concept and locate regions of high shear stress (Torrez and Andre, 1998 & 1999, Shekhar and Jayanti, 2003, A & B, Kelly and Gigas, 2003), provide a visual depiction of pressure distribution on impeller blades (Vlaev et al., 2004), observe cavern formation (Adams and Barigou, 2006, Arratia et al., 2006), and measure mixing time (Iranshai et al., 2006, Ihejirika and Ein-Mozaffari, 2007). In conjunction with the results of laboratory and pilot-scale tests, CFD flow simulations of mixing vessels are desirable as a supplement to the poorly established scale-up criteria traditionally used to design such vessels (Daskopoulos & Harris, 1996). The numerical details of CFD development will be examined in chapter 5.

2.7.1 Mixing of non-Newtonian Fluids using CFD Literature Review

Based on Computational Fluid Mechanics (CFD), many packages have been developed and used in the last few years to simulate complex processes, including mixing. The rest of this section (Table (2.5)) will briefly review CFD studies on the mixing of non-Newtonian fluids.

2.8 Research Objectives

It is evident from the literature review that mixing dynamics in continuous-flow vessels are not well understood, especially for non-Newtonian fluids. This study aims to identify important criteria for mixing in continuous-flow vessels that will improve the mixing efficiency in those vessels. Thus the research objectives are:

- To improve the understanding of mixing dynamics in continuous-flow mixers,
- To identify sources of flow non-ideality in continuous-flow mixers,
- To study the effect of impeller speed, impeller type, fluid rheological properties, fluid flowrate, and vessel configuration on the dynamics of continuous-flow mixers,

- To develop a CFD model for a scaled continuous-flow mixer,
- To use CFD to introduce further avenues for improvement of continuous-flow mixing operation, and
- To recommend remedies to rectify flow performance in continuous-flow mixers.

Table (2.5) Using CFD to Model Mixing Processes in non-Newtonian Fluids Literature Review

Authors	CFD Code	Impeller Model	Impeller & Fluid	Objective	Findings/Comments
Bkker & Fasano, 1993	Fluent	Black box	Chemineer HE-3/ pulp suspension	Simulate the flow fields in a tank with a side entering mixer	CFD gave satisfactory agreement with experimental data
Roberg, 1997	PHONICS & - FLOW 3D		A100/ pulp suspension	Check if the flow fields can be predicted using only Newtonian model for rheology of pulp suspension	Newtonian CFD predications can only be used as an initial guess for the non-Newtonian fields
Wikstrom & Rasmuson, 1998	CFX	Boundary conditions imposed on flow	Jet nozzle/ pulp suspension	Simulate the flow fields in a mixing vessel	CFD flow fields deviated from experimental fields (measured using Laser Doppler Velocimetry) as distance from impeller increased
Kelly & Humphrey, 1998	Fluent	MRF	A315/ Power law fluid	Study the effect of impeller speed & power law index (n) on flow patterns in a fermentor	Flow patterns in fermentor did not appreciably change with changing n

Table (2.5) Using CFD to Model Mixing Processes in non-Newtonian Fluids Literature Review – Cont (1)

Authors	CFD Program	Impeller Model	Impeller & Fluid	Objective	Findings/Comments
Torrez & Andre, 1998 & 1999	Fluent	MRF	A200/ fluids modeled by Bingham and Herschel Bulkley	Study the influence of impeller location and speed on local average shear stress	At any fixed position in the vessel, shear stress was proportional to impeller speed. Metzner-Otto constant was 8.5
Shekhar & Jayanti, 2003 A & B	CFX	Sliding Mesh	Anchor impeller/ Power law fluid	Investigate Metzner-Otto concept	Shear near the impeller varied linearly with impeller speed. The proportionality constant in this relationship was independent of either the clearance ratio or power law index (n)
Kelly & Gigas, 2003	Fluent	MRF	A200 and A315/ Carpobol	Predict the dependence of power number & average shear stress near the impeller on Reynolds number and power law parameters (K and n)	Power number increased with increasing impeller speed and n. Power number, on the other hand, was not affected by K

Table (2.5) Using CFD to Model Mixing Processes in non-Newtonian Fluids Literature Review – Cont (2)

Authors	CFD Program	Impeller Model	Impeller & Fluid	Objective	Findings/Comments
Vlaev et al., 2004	Fluent	MRF	Rushton and Scaba impeller/ Xantahn gum	Investigate the effect of blade shape on pressure distribution	Rushton turbine showed high pressure non-uniformity while Scaba exhibited a uniform pressure distribution. Uniform pressure distribution resulted in higher power draw effectiveness and thus maximized mixing efficiency
Ford et al., 2006	Fluent	MRF	Maxflo/ Paper & Pulp suspension	Simulate the flow in a pulp chest using the experimental data of Ein-Mozaffari (2002)	CFD was able to capture the mixing dynamics in the vessel fairly well. However, it underestimated flow non- ideality in the vessel
Adams & Barigou, 2006	CFX	MRF	Rushton turbine/ Herschel Bulkley fluid	Observe cavern formation around impeller	At low Reynolds number, CFD predictions of cavern diameters agreed well with experimental measurements

Table (2.5) Using CFD to Model Mixing Processes in non-Newtonian Fluids Literature Review – Cont (3)

Authors	CFD Program	Impeller Model	Impeller & Fluid	Objective	Findings/Comments
Moilanen et al., 2006	CFX	MRF & Sliding Mesh	Rushton Turbine/ Xanthan gum	Simulate hydrodynamics in a gas-liquid aerated fermentor	CFD predicted the formation of cavern region and poor mixing at the bottom of the fermenter. Inhomogeneity was observed in gas-liquid mass transfer rate
Iranshahi et al., 2006	POLY3D	MRF	Ekato Paravisc	Observe flow pattern, power consumption, pumping capacity, mixing time and mixing efficiency of Ekato Paravisc impeller	
Arratia et al., 2006	ICEM	MRF	Rushton turbine/ Carbopol	Investigate in 3D the mixing of a shear-thinning fluids with yield stress	Strong compartmentalization characterized by segregation between adjacent caverns was observed when multiple impellers were used. Mixing efficiency was improved by moving the shaft-off center

Table (2.5) Using CFD to Model Mixing Processes in non-Newtonian Fluids Literature Review – Cont (4)

Authors	CFD Program	Impeller Model	Impeller & Fluid	Objective	Findings/Comments
Saeed et al., 2007	Fluent	MRF	A310/ Paper & Pulp suspension	Investigate the flow field in a cylindrical pulp mixing chest equipped with a side- entering impeller	CFD predictions picked up details of flow fields, and computed velocities agreed well with experimental data measured using Ultrasonic Doppler Velocimetry. CFD provided a variable tool to measure cavern dimensions and mixing time in vessel
Ihejirika & Ein-Mozaffari, 2007	Fluent	MRF	Helical ribbon/ Xanthan gum	Investigate the effect of pumping direction on flow fields and mixing time	Although power consumption were the same for both pumping direction; mixing times were considerably longer for downward pumping mode

3. Experimental Work

3.1 Experimental Setup

A complete system was designed to simulate the continuous-flow mixing process, consisting of four major parts: mixing, flow, tracer and data acquisition systems.

The major component of the mixing system is the mixing vessel. A flat-bottomed, cylindrical, glass tank with a volume of 0.075 m^3 was used (internal diameter 40 cm and height 60 cm). The tank was equipped with four 4 cm wide and 1.2 cm thick PVC baffles whose lengths were equal to the tank height. The tank was further equipped with PVC input and output tubes of an inner diameter of 2.5 cm. Input was positioned in the plane $\theta=90^\circ$ (at the baffles). The tube was located at the top of the vessel, immersed 3 cm into the liquid. The tank was equipped with two outputs, the first of which was located at tank bottom in the plane $\theta=315^\circ$ (between two adjacent baffles), and the second located at tank side at an elevation of 35 cm from tank bottom also in the plane $\theta=315^\circ$ (between two adjacent baffles). The tank was also equipped with a bottom drainage pipe. A detailed view of the tank is provided in Figure (3.1).

The tank was supplied with a top-entry, 2.5 cm diameter, stainless steel shaft driven by a 2 hp mixer (Neptune Chemical Pump Co., USA).

Impeller torque was measured with a torque meter (Staiger Mohilo, Germany) equipped with an encoder disk to measure impeller speed. Impeller speed was also checked with a tachometer. Two flexible couplings were mounted above and below the torque meter to accommodate radial, angular, and axial misalignment that accompany shaft rotation (Quill shaft configuration, section 2.3.2).

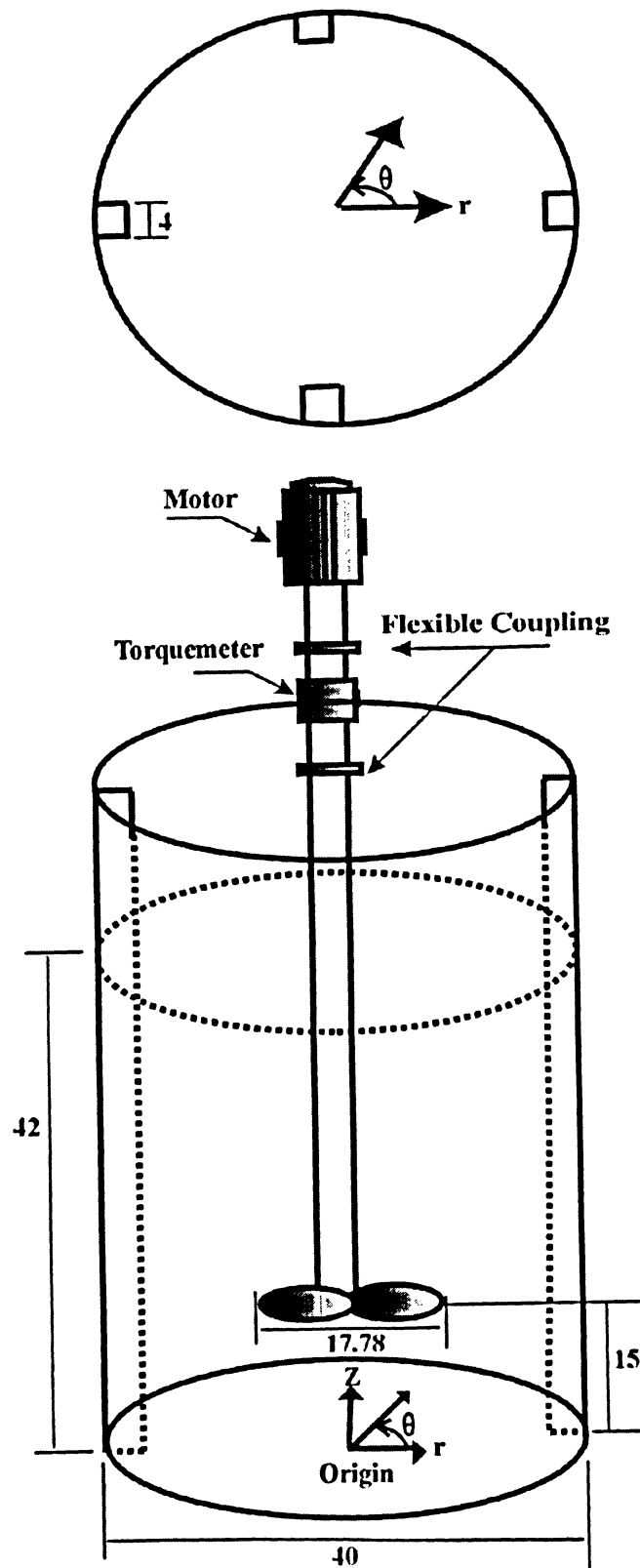


Figure (3.1) Detailed View in Mixing Vessel
(Dimension in cm)

The second part of the experimental setup was flow system, consisting of feed section and discharge section. Each section contains a plastic 0.3 m³ cylindrical tank and a progressive cavity pump (Moyno Industrial Products, USA).

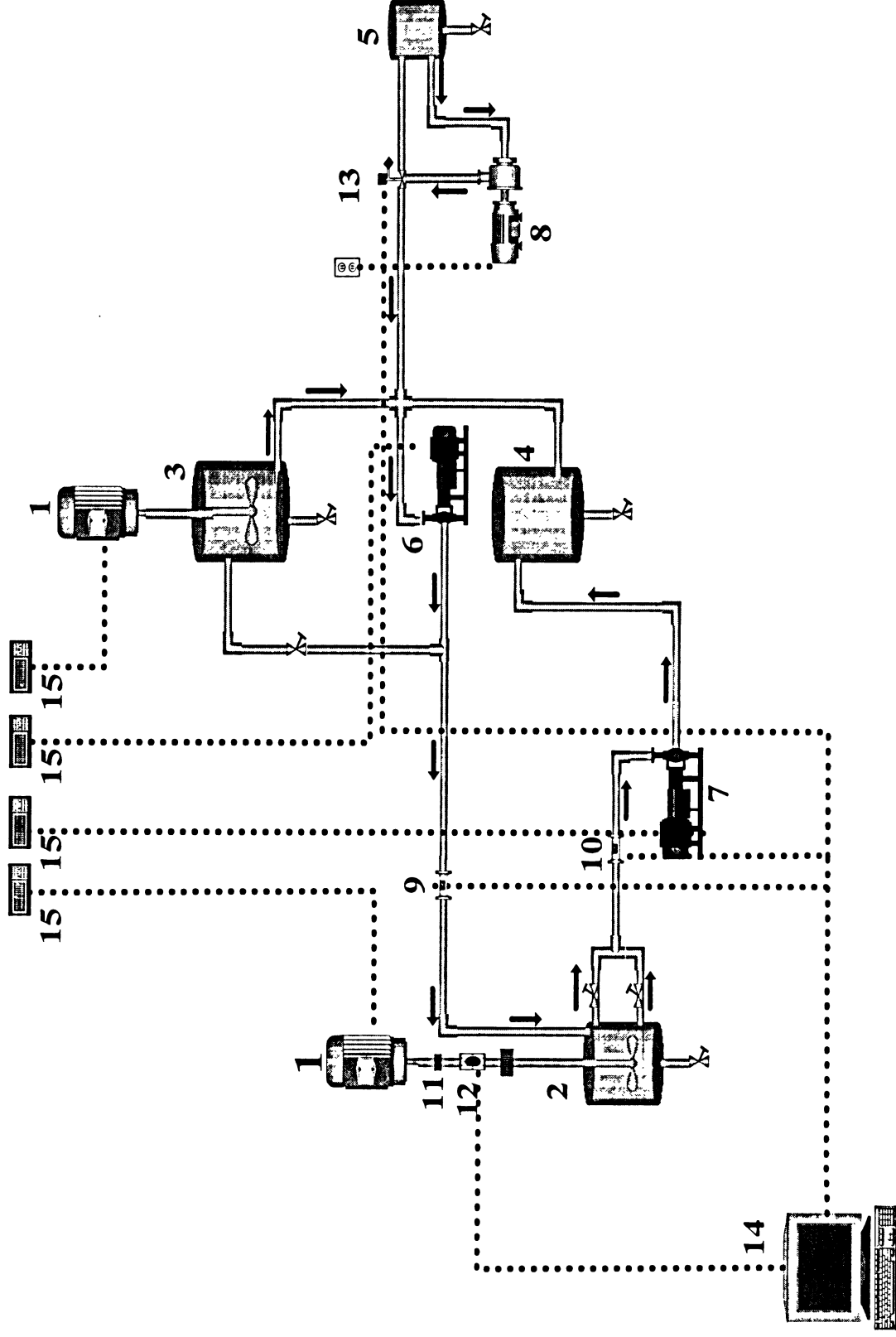
A feed tank, supplied with a top entry shaft driven by a 3 hp mixer (Neptune Chemical Pump Co., USA) and equipped with a marine propeller, was used to prepare fresh feed at each experiment. A discharge tank was used to collect material during experiment runs.

Both feed and discharge pumps were equipped with a variable frequency drive to control operation and maintain a constant liquid flowrate through the mixing tank. Tank liquid level was kept constant at 41±1cm. To maintain this constant level, inlet flowrate was kept constant and the outlet flowrate was manipulated to adjust liquid level in the tank.

The third part of the experimental system was the tracer injection unit. To study the dynamic of continuous mixing, a tracer was injected in the system using a metering pump (Milton Roy, USA). The tracer was prepared in a 0.06 m³ plastic tank. The injection of the tracer was controlled by a solenoid valve (Ascoelectric Ltd., Canada).

Two flow-through conductivity meters (Rosement Analytical, USA) were supplied to measure conductivity variations in the output and input of the mixing tank.

The last part of the experimental setup was the data acquisition system. This system was able to record impeller torque and both input and output conductivity readings with the corresponding temperatures. Data acquisition was made using LABVIEW[®] software (National Instruments, USA). Figure (3.2) represents a schematic diagram of the experimental setup.

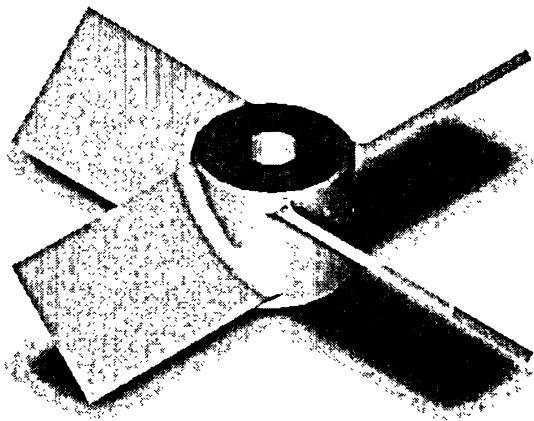


(1)-Mixer, (2)-Feed Tank, (3)-Discharge Tank, (4)-Tracer Tank, (5)-Progressive Cavity Feed Pump, (6)-Progressive Cavity Discharge Pump, (7)-Progressive Cavity Meter, (8)-Coupling, (9)-Input Conductivity Meter, (10)-Output Conductivity Meter, (11)-Flexible Coupling, (12)-Torque Meter, (13)-Solenoid Valve, (14)-Variable Frequency Drive Control Panel, (15)-Variable Frequency Drive Control Panel

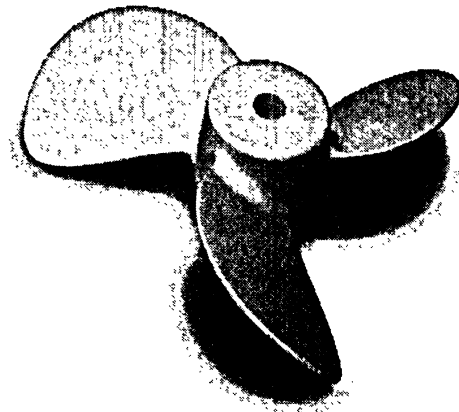
Figure (3.2) Process Schematic Diagram

3.2 Impeller Specifications

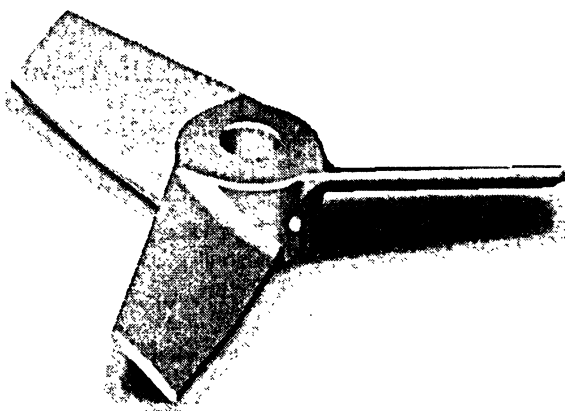
Four axial flow impellers, each with a 17.8 cm diameter, were used. A200 (equivalent to a pitched blade turbine) was used as the main impeller in the current study. A100 (equivalent to a marine propeller), A310 and A320 Lightning impellers were also employed. Clearance between impeller and tank bottom was 15 cm. Figure (3.3) shows the shape of those impellers.



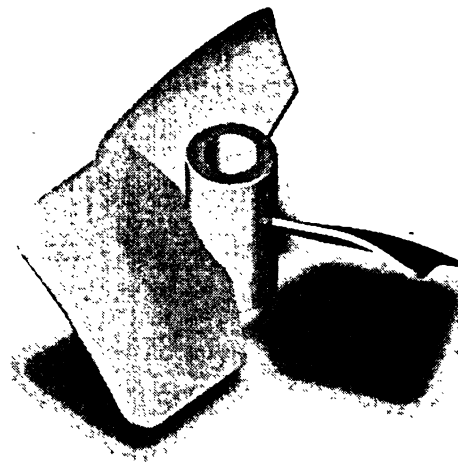
A200 (equivalent to pitched blade turbine)



A100 (equivalent to marine propeller)



A310



A320

Figure (3.3) Impellers Shape

A200 impellers (pitched blade turbine) produce an axial flow pattern with a balance between shear and pumping. Standard A200 impellers consist of four blades welded on a central hub at a 45° pitch. A200 impellers are recommended for low- to medium-viscosity, flow-controlled applications (Bates, 1964).

A100 impellers (marine propeller) produce a downward axial flow towards the bottom of the tank, and are most effective in low viscosity applications requiring moderate pumping (McDonough, 1992). A100 impellers are characterized by high discharge capacity with low head. The twisted skewness of the blades creates a constant blade pitch. A100 impeller used in this experimental work has a square pitch.

Hydrofoil impellers (like A310 and A320) have 3 curved, twisted, and sometimes (like A320) rounded edged blades. The blades are tapered more on width from impeller hub to blades tip. Blade tip in these impellers eliminate any tendency for the flow to recirculate around the tips, producing a uniform velocity across the entire discharge area. While A310 is recommended for low-viscosity flow-controlled applications, A320 is advised for higher-viscosity applications requiring high flow (Corpstein et al., 1979).

Material Preparation

Food grade xanthan gum 60 mesh size supplied by ADM (ADM, USA) was used throughout the experiment cycle. Each batch was prepared by adding the appropriate amount of xanthan gum to tap water. One third of the feed tank was filled with water. The impeller in the feed tank was started first and then xanthan gum was poured gradually into the water in the feed tank. Each batch was mixed for approximately 5-6 hours. Water was then added to complete the required solution volume, and the whole solution was mixed for an additional 1-2 hours.

Saline tracer solution was prepared by dissolving table salt in distilled water. The concentration of salt varied from 20 to 60 g/L, depending on xanthan gum flowrate.

3.4 Xanthan Gum Physical & Rheological Properties

The rheological properties of xanthan gum solutions were measured with a computer controlled C-VOR rheometer (Bohlin Instruments, USA). A cone and plate geometry was used. The diameter of the cone was 4 cm with a 2° angle. The temperature at which these measurements were made was the same as that of the bulk solution in the mixing tank. As the mixing vessel temperature varied slightly with daily room temperature, all measurements were made at $23 \pm 1^\circ\text{C}$. Rheograms were obtained at controlled shear rate in the range of $0.14\text{--}130\text{S}^{-1}$.

Rheological data were fitted to Herschel Bulkley model. Regression coefficient (R^2) and Chi-square non-parametric test of statistical significance (χ^2) were used to evaluate the fitted curves. Rheograms were obtained for three different concentrations, namely, 0.5, 1.0, and 1.5% mass concentration xanthan gum solutions in water. The results are shown graphically with the best fitting obtained using Herschel Bulkley model in Figure (3.4).

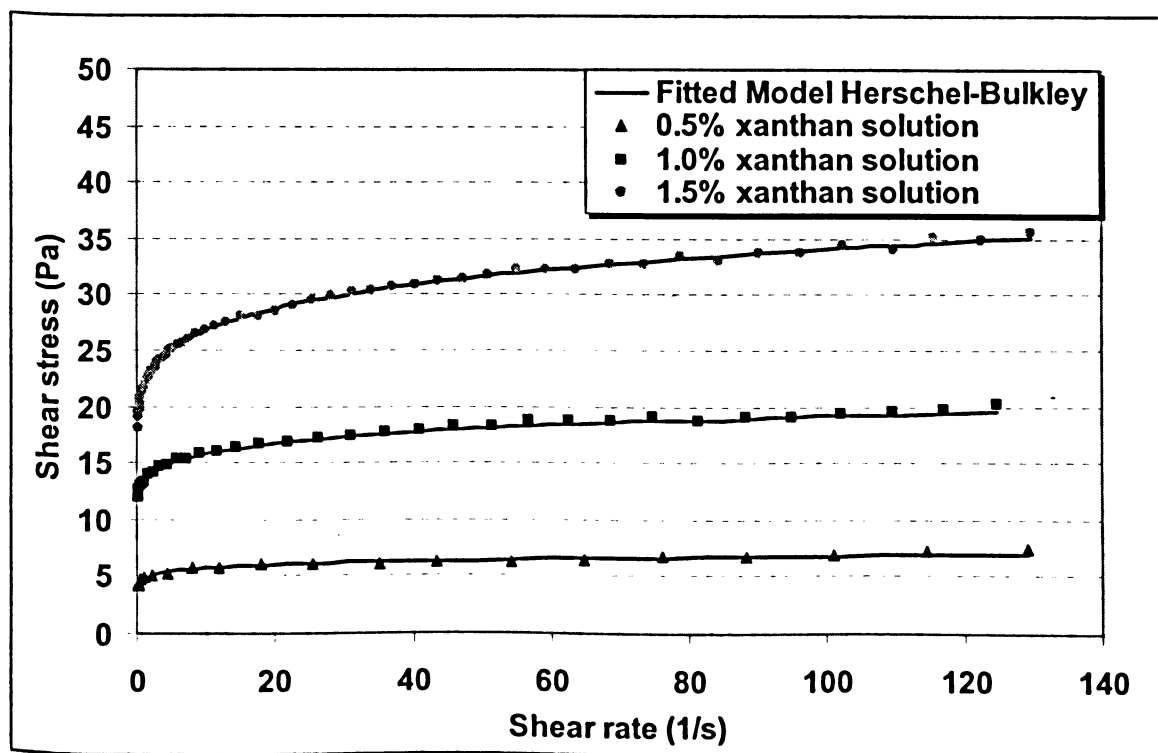


Figure (3.4) Xanthan Gum Rheograms

The rheological parameters of Herschel Bulkley model, yield stress (τ_y), consistency index (K), and power law index (n), are shown in Table (3.1).

Table (3.1) Rheological Parameters of Xanthan Gum using Herschel Bulkley model

Xanthan Gum Concentration, %	Yield stress (τ_y , Pa)	Consistency index (K, Pa.s ⁿ)	Power law index (n)	Regression coefficient (R^2)	Chi-square parameter (χ^2)
0.5	1.789	3	0.11	0.9905	0.0885
1.0	5.254	8	0.12	0.9985	0.1111
1.5	7.455	14	0.14	0.9992	0.0460

Xanthan gum is a polyelectrolyte polymer and its molecular structure depends primarily upon the ionic strength of the side chains and the presence of free ions in the solution.

In an aqueous xanthan gum solution with no added ions, xanthan gum molecules are extended due to electrostatic repulsion of the negatively trisaccide charged side chains. When a salt like sodium or potassium chloride is added to dilute xanthan gum solution of mass concentration <0.05% (Muller et al., 1986, Somlka and Belmonte, 2006) and semi dilute solution of mass concentration <0.5% (Rocheftort and Middleman, 1987, Ferguson and Kemblowski, 1991, Carrington et al., 1996), charge screening causes the side chains to collapse down to the backbone. The salt will thus induce a disorder→order (random→helix) transition in the backbone conformation. This transformation will lead to a substantial decrease in molecular size and a corresponding decrease in solution viscosity. No study has been made to verify the effect of salt on xanthan rheology at high concentration (mass concentration >0.5%). Once the transitions in xanthan gum molecular structure from a disordered to an ordered state occurs, the molecules in ordered state becomes relatively insensitive to further increases in salt level. The critical value of salt concentration beyond which no change in xanthan rheological properties is $[\text{NaCl}] \approx 10^{-2} \text{ M}$ (0.05% mass concentration) (Muller et al., 1986, Somlka and Belmonte, 2006).

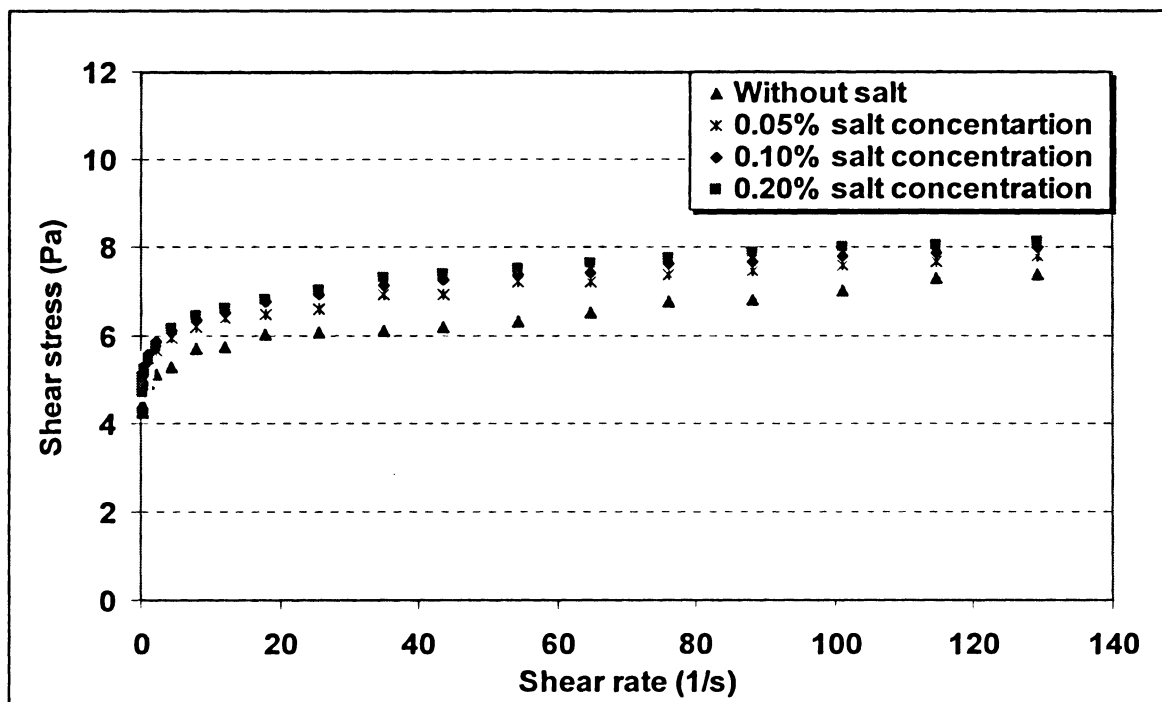
The effect of salt on behaviour of xanthan gum rheological parameters was investigated by many investigators. It was observed that the addition of salt for dilute and semi-dilute xanthan gum concentration increases consistency index (K) and decreases power law index (n) (Torres et al., 1993). Yield stress was observed to increase with increasing salt concentration (Hannote et al., 1991, Torres et al., 1995). Viscosity, consistency index, and power law index were found to be constant when salt concentration reaches a critical value ($>0.3\%$ mass concentration).

Each sample of prepared xanthan gum was used 1-3 times, till the maximum amount of salt accumulated in the solution reached approximately 0.17%. The rheological properties of xanthan gum solutions were measured with 0.17% Sodium Chloride salt. Figure (3.5) shows the effect of adding salt on 0.5% and 1.5% xanthan gum solutions. Table (3.2) shows Herschel Bulkley rheological parameters obtained for all xanthan gum solutions at 0.2% salt.

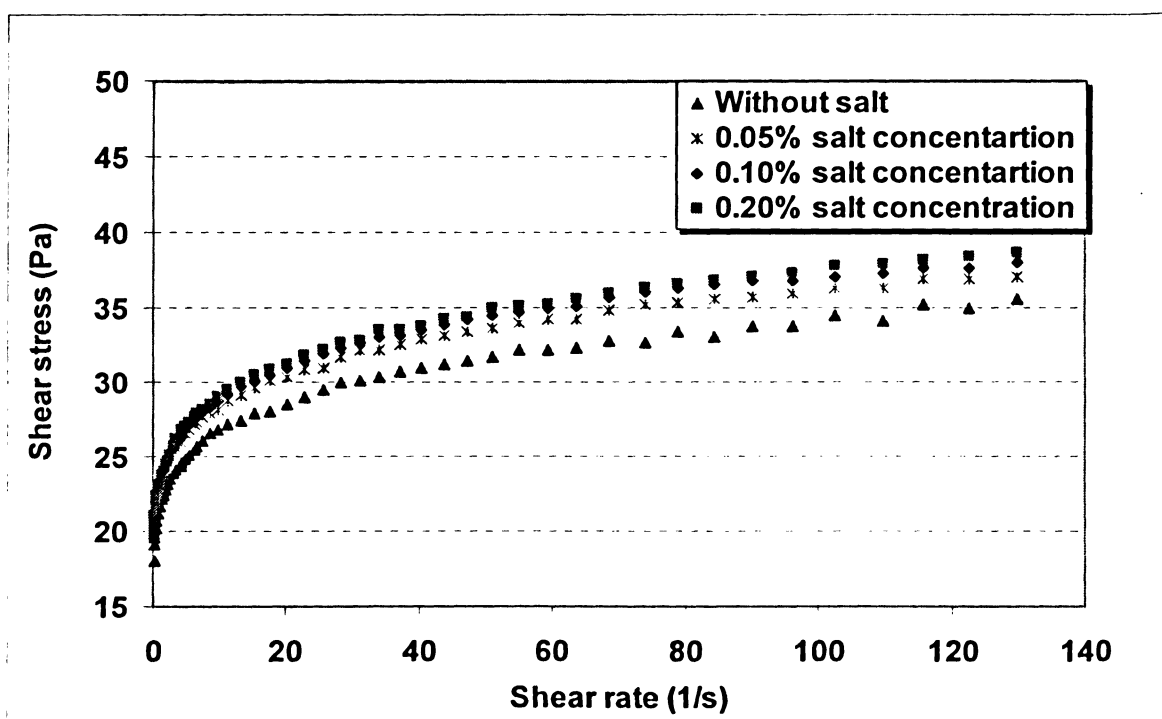
Figure (3.5) & Table (3.2) clearly demonstrates that adding 0.17% of salt did not appreciably change the rheological properties of xanthan gum solutions.

Table (3.2) Effect of Salt on Rheological Properties of Xanthan Gum Solutions

Xanthan Gum Solution	Yield stress (τ_y , Pa)	Consistency index (K, Pa.s ⁿ)	Power law index (n)
0.5% Without Salt	1.789	3.00	0.110
0.5%, with 0.2% salt	1.910	3.47	0.116
1.0% Without Salt	5.254	8.00	0.120
1.0%, with 0.2% salt	5.783	8.65	0.127
1.5% Without Salt	7.455	14.00	0.140
1.5%, with 0.2% salt	7.564	14.90	0.149



(a)-0.5% Xanthan Gum Solution



(b)-1.5% Xanthan Gum Solution

Figure (3.5) Xanthan Gum Rheograms Showing the Effect of Salt Addition

Density was also estimated for 0.5, 1.0, and 1.5% mass concentration xanthan gum solutions using a 25 ml pycnometer. Measurements were made at 23 °C. Data are shown in Table (3.3).

Table (3.3) Density of Xanthan Gum Solutions

Xanthan Gum Solution Concentration, %	Density Kg/m ³
0.5	997.36
1.0	991.80
1.5	989.76

3.5 Experimental Test Procedure

Xanthan gum solution was pumped from the feed tank to the mixing tank via the feed progressive cavity pump. The solution was agitated in the mixing vessel and discharged to the discharge tank by the discharge progressive cavity pump. Xanthan gum solution was allowed to gather during test time in the discharge tank, where it could either be pumped back to the feed tank via feed progressive cavity pump, or drained.

Dynamic testing was performed by exciting the system and observing its input and output over a specified time interval. For this purpose, saline solution was pumped from tracer tank through the metering pump at specified periods of injection. Tracer injection was controlled by a solenoid valve and the tracer was mixed with a fresh feed solution in the feed pump prior to being pumped to the mixing vessel.

The input and output conductivity signals were measured by flow-through conductivity meters and data were recoded by a data acquisition system controlled by LABVIEW software.

3.6 Experimental Conditions

The effect of operation conditions and design criteria on the dynamic and performance of the continuous-flow mixing vessel was studied by varying the following parameters:

- Impeller velocity (50-700 rpm),
- Xanthan gum solution mass concentration (0.5-1.5%),
- Xanthan gum flowrate through the mixing vessel (227-896 L/hr),
- Impeller type A200 (pitched blade turbine), A100 (marine propeller), A310 and A320 Lightnin impellers, and
- Tank geometry, including output location (bottom and side) as indicated in Figure (3.6).

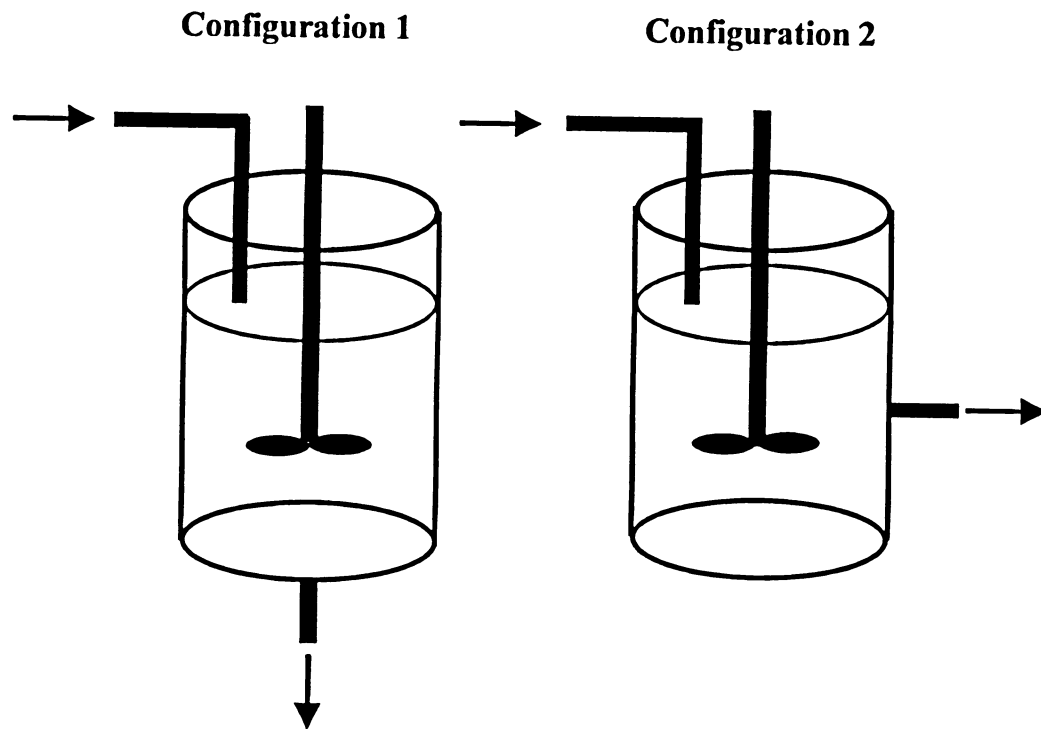


Figure (3.6) Vessel Configuration

4. Dynamic Modeling of Continuous-Flow Mixers

4.1 Introduction

The main objective of this experiment was to identify flow non-ideality encountered in a continuous-flow mixing vessel under different working conditions. For this purpose, a model that describes the dynamics of a mixing vessel, incorporating non-ideal flow parameters, i.e., channeling, recirculation and dead zones, should be adopted. The dynamic model developed by Ein-Mozaffari (2002) is used here to describe the behaviour of mixing in a continuous-flow vessel. Flow non-ideal parameters are estimated by the method developed by Kammer et al. (2005).

This chapter briefly introduces Ein-Mozaffari (2002) and Ein-Mozaffari et al. (2002 A) dynamic model, then explains the procedure for obtaining model parameters. The design of excitation input signal is also discussed in the last section of this chapter.

4.2 Dynamic Modeling of Mixing in Continuous-Flow Vessels

Ein-Mozaffari (2002) and Ein-Mozaffari et al. (2002 A) developed a dynamic model for an agitated pulp stock chest that included a well-mixed zone, within the possibility of stock recirculation with the mixing zone and short-circuiting past the mixing zone. In this model (shown in Figure (4.1)), (f) represents the portion of stock that bypasses the mixing zone. A limited amount of mixing can occur in the bypass flow and is presented by a first order transfer function (G_1) . On the other hand, $(1-f)$ is the fraction of stock that enters the mixing zone and has a first order transfer function of G_2 . A portion of stock, R , exiting the mixing zone can be recirculated within the mixing zone. τ_1 and τ_2 are the time constants for the bypassing and agitated zones, respectively. T_1 and T_2 are the time delays for the bypassing and agitated zones, respectively.

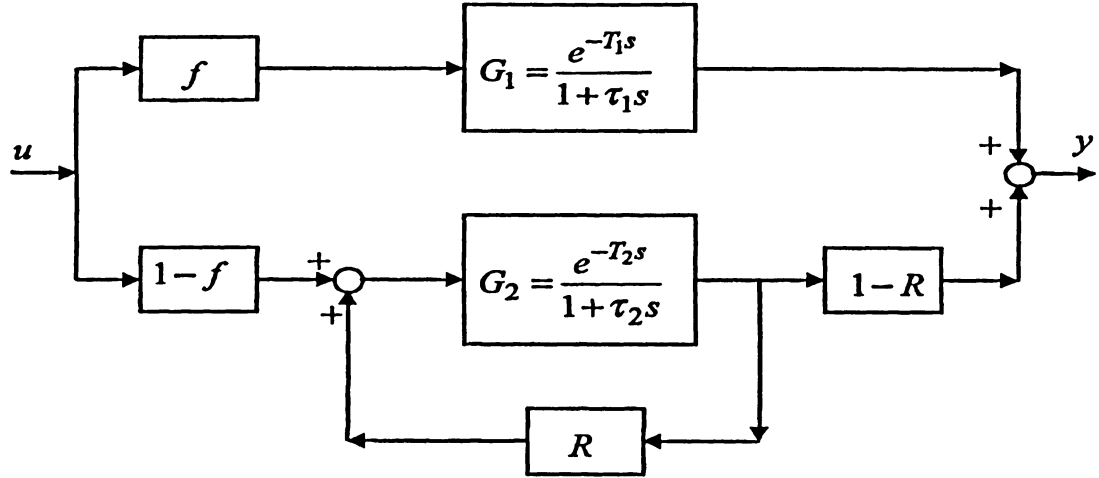


Figure (4.1) Continuous-Time Domain Dynamic Model for Continuous-Flow Mixers
(Ein-Mozaffari et al., 2002)

The combined transfer function for the above system in a continuous time domain is given as follows:

$$G_{\text{mixing vessel}} = \frac{f e^{-T_1 s}}{1 + \tau_1 s} + \frac{(1-f)(1-R) \frac{e^{-T_2 s}}{1 + \tau_2 s}}{1 - \frac{R e^{T_2 s}}{1 + \tau_2 s}} \quad (4.1)$$

To estimate flow non-ideal parameters, i.e., channeling, recirculation and dead zones, the mixing vessel has to be excited by an input signal in order to observe system response (output signal).

4.3 Estimation of Non-Ideal Flow Parameters in Continuous-Flow Mixers

Because experimental data will be obtained at fixed time intervals, Kammer et al. (2005) transformed the continuous-time model into a simple discrete-time model using zero-

order hold (Seborg et al., 1989). The discrete-time domain transfer function equivalent to Equation (4.1) is given below:

$$\hat{G}(q) = \frac{\rho_1 q^{-d_1} + \rho_2 q^{-(d_1+1)} + \rho_3 q^{-d_2} + \rho_4 q^{-(d_2+1)} + \rho_5 q^{-(d_1+d_2)}}{1 + \rho_6 q^{-1} + \rho_7 q^{-2} + \rho_8 q^{-d_2} + \rho_9 q^{-(d_2+1)}} \quad (4.2)$$

where: $\rho_1 = f(1-a_1)$, $\rho_2 = -f(1-a_1)a_2$, $\rho_3 = (1-f)(1-R)(1-a_2)$, $\rho_4 = -(1-f)(1-R)(1-a_2)a_1$, $\rho_5 = -fR(1-a_1)(1-a_2)$, $\rho_6 = -a_1 a_2$, $\rho_7 = a_1 a_2$, $\rho_8 = -R(1-a_2)$, $\rho_9 = Ra_1(1-a_2)$, $a = e^{-t_s/\tau}$, $d_i = 1 + T_i/t_s$, $d_2 \geq d_1$, T_i is i^{th} time delay, t_s and q^{-1} are the sampling time and backward shift operator, respectively. Backward shift operator is defined as $q^{-1}f(K) = f(K-1)$.

The model parameters (f , R , a_1 , a_2 , d_1 , and d_2) can be estimated by minimizing the cost function as follows:

$$J_L = \frac{1}{L} \sum_{t=1}^L [y_t^b - \hat{G}(q)u_t^b]^2 \quad (4.3)$$

where L , y_t^b , u_t^b are length of data set, measured output and measured input, respectively.

Two distinct stages were used during the minimum search process: an efficient but less accurate least squares minimization for the optimal delays, followed by an accurate gradient search for all parameters using Sequential Quadratic Programming (SQP) method (Fletcher, 1987, Edager et al., 2001). This method is iterative optimization technique and used to solve constrained nonlinear problems. A code written in MATLAB based on SQP by Kammer et al. (2005) was used to estimate model parameters.

Recently, Upreti and Ein-Mozaffari (2006) developed a hybrid genetic multi-parameters optimization algorithm with gradient search to estimate flow non-ideal parameters in agitated pulp chest previously studied by Ein-Mozaffari (2002). The non-ideal flow

parameters identified by this algorithm agreed very well with Ein-Mozaffari's (2002) experimental data.

SQP is not guaranteed to converge to the global minimum because it is very sensitive to the initial guesses. Hybrid genetic algorithm, by contrast, enables users to initiate the search with any suboptimal points. The disadvantage of using Hybrid genetic algorithm is that it is much more time consuming than SQP, requiring 10 hours to reach optimal in comparison to 30min. with SQP.

Two parameters were used here to quantify flow non-ideality: f , the degree of channeling in the vessel, and $V_{\text{fully mixed}}/V$, the ratio of fully mixed volume in the vessel to the total volume of the vessel. To calculate fully mixed volume, the effect of recirculation will be eliminated by setting $R=0$ (Ein-Mozaffari, 2002). This assumption is very reasonable, because dynamic response obtained experimentally (Figure (4.2), Figure (4.5) and Figure (4.7)) did not show any effect of recirculation distinguished by a series of first order exponential responses.

For $R=0$, the time constant for the agitated zone (τ_2) is given by the following equation:

$$\frac{V_{\text{fully mixed}}}{V} = \frac{Q \cdot \tau_2 \cdot (1 - f)}{V} \quad (4.4)$$

where Q is solution flowrate through the mixing vessel, and V is total volume of vessel.

4.4 Design of Input (Excitation) Signal

The choice of input signal has a substantial influence on the observed output. The same procedure suggested by Ein-Mozaffari (2002) will be used here. This procedure consists of the following steps:

- Exciting the system by a rectangular pulse,
- Designing a frequency-modulated random binary exciting signal based on rectangular pulse,
- Exciting the system by the frequency-modulated random binary exciting signal, and
- Validating the use of frequency-modulated random binary exciting signal.

The excitation was performed by injecting the saline solution through a computer controlled solenoid valve into the feed stream. The conductivity variations in input and output streams were measured using the flow-through conductivity sensors. These signals were recorded in a computer using data acquisition system to estimate flow non-ideal parameters.

In the first experiment, the input signal was a rectangular pulse (two steps change). Figure (4.2) shows a typical rectangular pulse and the corresponding output signal. It is believed that the input signal should be persistently exciting, implying that all the modes of the system should be excited (Ljung, 1999). Thus, a simple input such as two steps change will not provide enough excitation to identify model parameters (Ein-Mozaffari, 2002). However, the quality of parameter estimation can be improved by using this simple rectangular pulse to design a frequency-modulated random binary exciting signal by concentrating the excitation energy at frequencies where the Bode plot for model parameters is sensitive to parameter variations (Ljung, 1999).

For rectangular pulse input, Bode plot for partial derivatives of transfer function with respect to model parameters (f , R , a_1 , a_2) was obtained. The partial derivatives of the model were calculated using MATLAB to generate Bode plots of these partial derivatives. The result is shown in Figure (4.3).

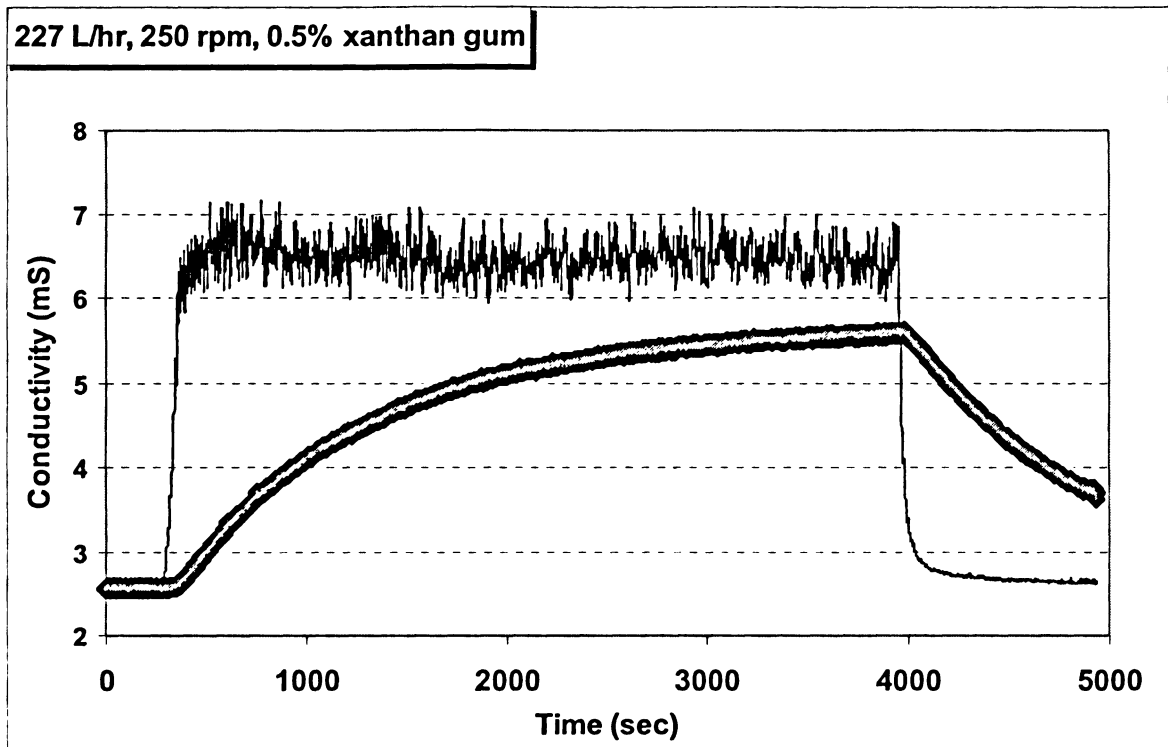


Figure (4.2) Rectangular Pulse showing Input and Output Responses
Experimental Output in Black and Model Output in Gray

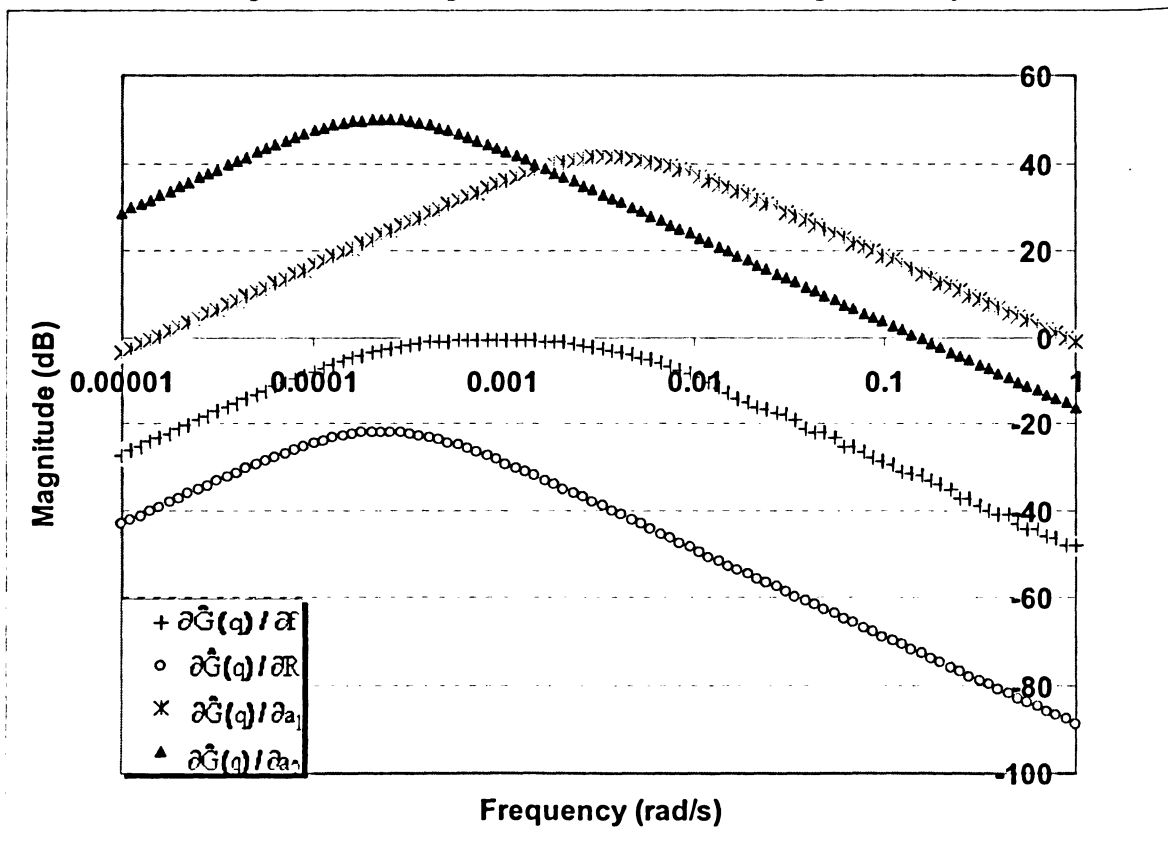


Figure (4.3) Bode Plot of Partial Derivatives of Model Parameters

The excitation energy for random exciting signal must be chosen at frequencies where the magnitude of Bode plot is sensitive to model parameter variations (Ljung, 1999). From Figure (4.3), model parameters exhibited maxima at the following frequencies: $\omega_f = 0.00105$ rad/s, $\omega_R = 0.00023$ rad/s, $\omega_{a1} = 0.00420$ rad/s, $\omega_{a2} = 0.00026$ rad/s. Therefore, the excitation energy for the second experiment was concentrated at frequencies from $\min \{\omega_f, \omega_R, \omega_{a1}, \omega_{a2}\} = 0.00023$ rad/s to $\max \{\omega_f, \omega_R, \omega_{a1}, \omega_{a2}\} = 0.00420$ rad/s.

A zero-mean white noise signal was filtered by a band-pass filter with cut-off frequencies 0.00023 rad/s to 0.00420 rad/s, as indicated in Figure (4.4). Then, the filtered signal was converted into a binary sequence using:

$$u_t^b = \begin{cases} 0 & \text{if } e_t^f \leq 0 \\ 1 & \text{if } e_t^f > 0 \end{cases} \quad (4.5)$$

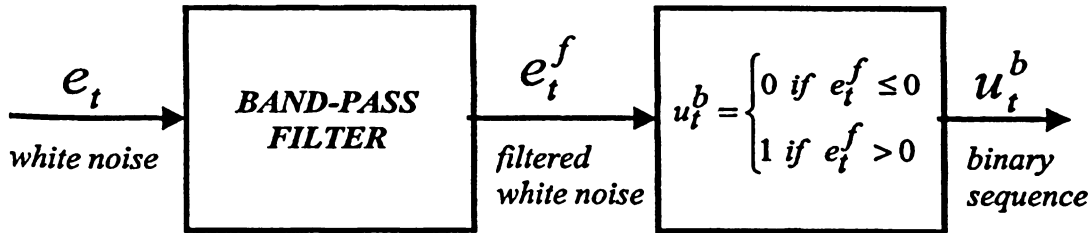


Figure (4.4) Procedure for Designing a Frequency-Modulated Random Binary Input Signal (Ein-Mozaffari et al., 2002)

The new input and output signals (black line) are shown in Figure (4.5). In this figure the response of the model to the given excitation is in gray line.

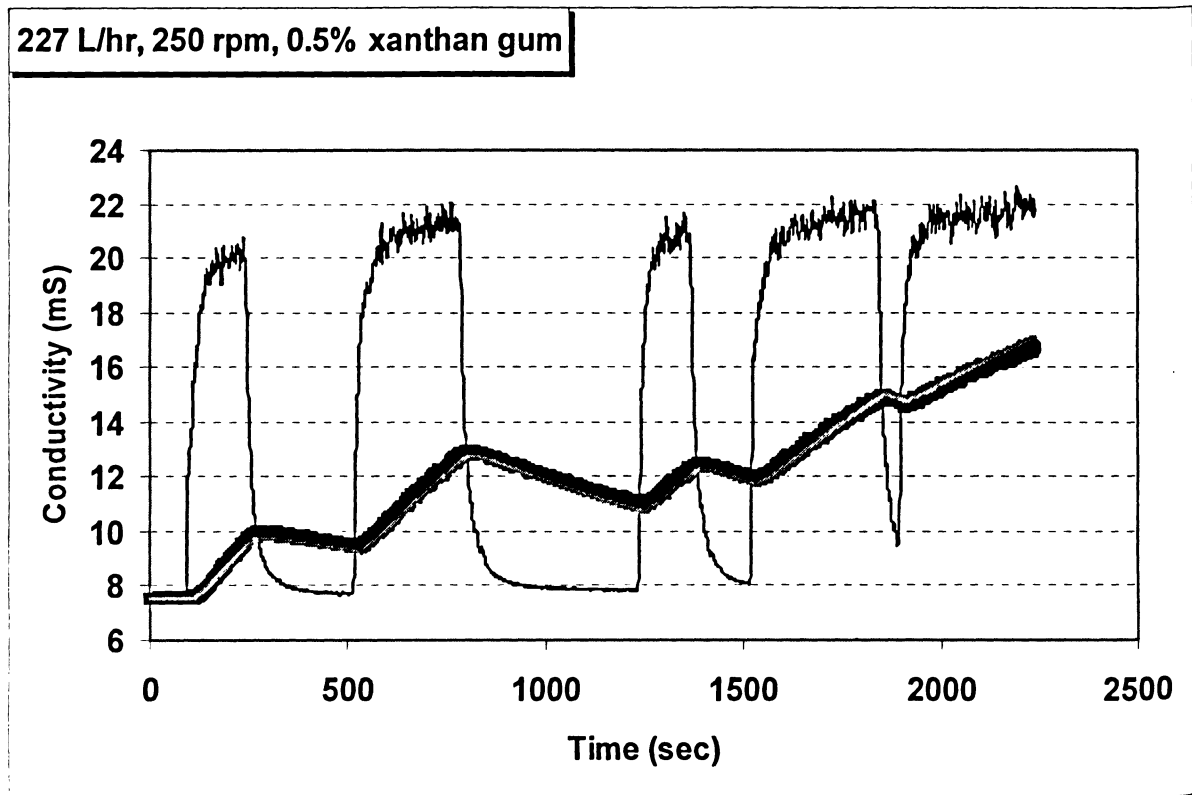


Figure (4.5) Frequency-Modulated Random Binary Input Signal
Experimental Output in Black and Model Output in Gray

The random exciting signal employed in these experiments was validated by using a second random exciting signal applied to the system under identical operation conditions. The same validation procedure (Figure (4.6)) suggested by Ein-Mozaffari (2002) was implemented here.

Figure (4.7) shows the details of the second random exciting signal. The model parameters, f & $V_{\text{fully mixed}}/V$, obtained from the first random exciting signal were used together with the input signal imposed by the second random exciting signal to generate a new output. The generated output was compared with measured output.

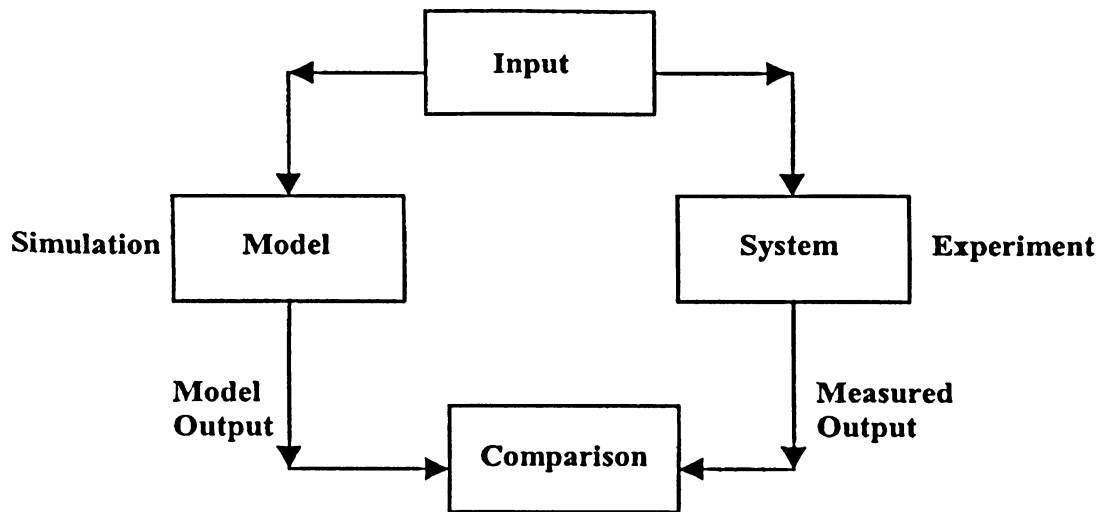
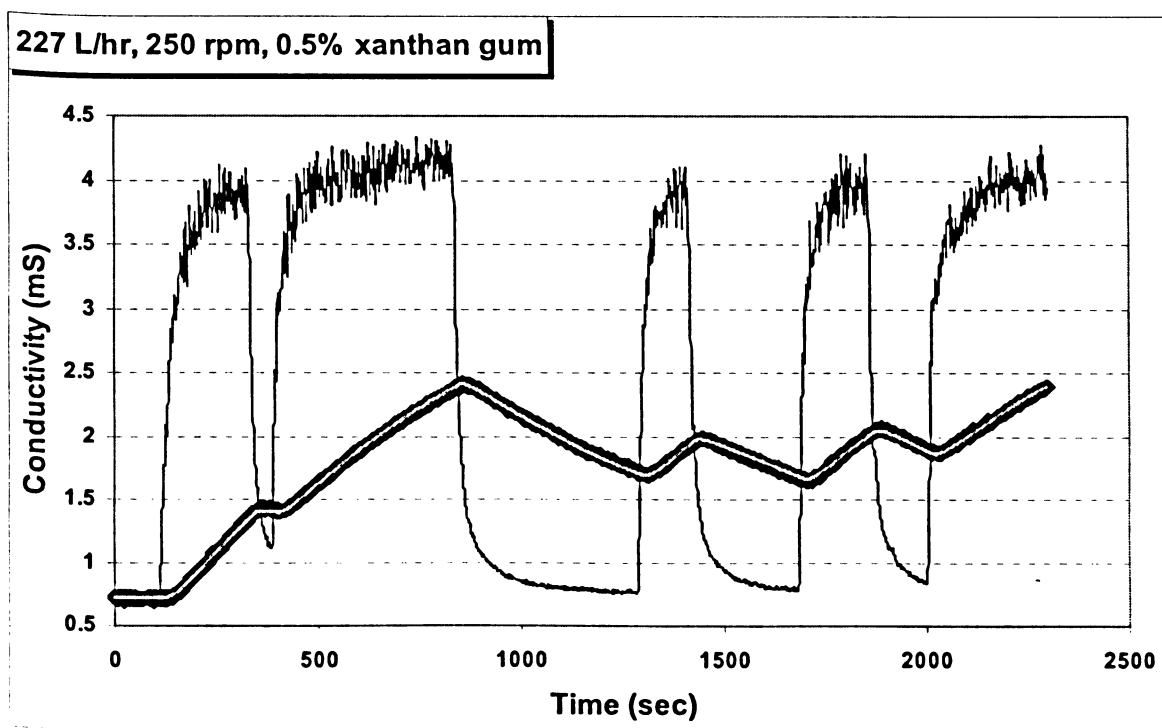


Figure (4.6) Model Validation Procedure (Ein Mozaffari, 2002)

Figure (4.7) Model Validation Frequency-Modulated Random Binary Input Signal
Experimental Output in Black and Model Output in Gray

The first and second dynamic model parameters obtained from both experiments were compared against each other and shown in Table (4.1). The parameters completely

matched, implying that the first exiting input signal was able to identify dynamic model parameters, and that the estimated parameters are unique characteristics of the system under specified operation conditions.

Table (4.1) Dynamic model Parameters obtained from Two Different Input Signals

First Input Signal (Figure (4.5))		Second Input Signal (Figure (4.7))	
f	$V_{\text{fully mixed}}/V$	f	$V_{\text{fully mixed}}/V$
0.2330	0.7550	0.2331	0.7549

5. Computation Fluid Dynamics (CFD)

5.1 Introduction

Computational Fluid Dynamics (CFD) solves transport equations (fluid flow, heat transfer, mass transfer) numerically using various algorithms. In this work, commercial packages Fluent 6.3 and Mixsim 2.1 (Fluent Inc., Lebanon, NH) were used to perform CFD modeling. Fluent 6.3 and Mixsim 2.1 use a finite-volume approach to tackle CFD problems. The remainder of this section focuses on CFD principles and its application to model mixing process. Only finite-volume approach is discussed due to its relevancy to the packages used in this work.

5.2 CFD Work Methodology

CFD packages consist of three main elements: (i) a preprocessor, (ii) a solver and (iii) a post processor (Versteeg & Malalasekera, 1995).

CFD Preprocessor accepts the inputs from the user(s) and transforms them into a form suitable for use by the solver. The preprocessor activities involve the following:

- Defining system geometry (computational domain),
- Defining fluid properties,
- Selecting physical and chemical phenomena to be modeled,
- Dividing domain into a number of smaller sub domains, called grid (mesh) of cells, and
- Specifying appropriate boundary conditions.

The CFD solver performs the following functions: (1) discretizing the domain, (2) transforming the governing transport differential equations into algebraic equations, and (3) solving the algebraic equations.

CFD postprocessors are equipped with data visualization techniques to display grid, vector plots, contours, 2D and 3D surface plots and many other output capabilities.

The following sections highlight the most important parts of CFD principles, following the work methodology described above.

5.3 Property Transport Equations for Mixing Processes

After specifying system geometry and fluid properties, selecting the physical and chemical phenomena to be modeled becomes essential. This step is usually performed by choosing the appropriate transport equation(s) that represent the model under study. Classical transport phenomena include continuity, motion, energy, and species transport equations. Modeling an isothermal, non-reacting mixing vessel requires adopting continuity and motion equations.

Transport equation for any system for any property can be written as follows (Bird et al., 2002):

$$\text{Rate of accumulation in property} = \text{Rate of property in} - \text{Rate of property out} + \text{Forces acting on the system} \quad (5.1)$$

In mixing process, the general transport equation represents mathematical statements of two conservation laws: 1) mass of a fluid is conserved; 2) the rate of change of momentum equals the sum of forces acting on the fluid. These statements represent continuity and momentum equations, respectively. These two equations can be written as follows (Bird et al., 2002):

$$\frac{\partial \rho}{\partial t} + \text{div}(\rho \mathbf{u}) = 0 \quad (5.2)$$

$$\frac{\partial}{\partial t}(\rho \mathbf{u}) = -\text{div}(\rho \mathbf{u} \mathbf{u}) + \text{div}(\boldsymbol{\tau} \boldsymbol{\tau}) + \rho \mathbf{g} - \text{grad}(\mathbf{p}) \quad (5.3)$$

where ρ is fluid density, $\rho \mathbf{u}$ is mass velocity vector, $\rho \mathbf{u} \mathbf{u}$ is connective momentum tensor, $\boldsymbol{\tau} \boldsymbol{\tau}$ is stress tensor, \mathbf{g} is gravitational acceleration vector, and \mathbf{p} is fluid pressure vector.

The first term on the right hand side of Equation (5.3) represents the rate of momentum gained by convection, while the second term represents the rate of momentum gained by diffusion. The last two terms, $\rho \mathbf{g} - \text{grad}(\mathbf{p})$, symbolizes forces acting on fluid due to gravity and pressure, respectively.

In CFD textbooks, a “generic transport equation” is used that defines all the individual transport equations as follows:

$$\frac{\partial}{\partial t}(\rho \Phi) = -\text{div}(\rho \mathbf{u} \Phi) + \text{div}(\Gamma_{\Phi} \nabla \Phi) + S_{\Phi} \quad (5.4)$$

where Φ is general transport property ($\Phi=1$ in continuity equation and $\Phi=\mathbf{u}$ in momentum equation), Γ_{Φ} is diffusion coefficient of Φ ($\Gamma_{\Phi} = \text{zero}$ in continuity equation and $\Gamma_{\Phi} = \text{viscosity}$ in momentum equation), and S_{Φ} represents the source term ($S_{\Phi} = \text{zero}$ in continuity equation and $S_{\Phi} = \rho \mathbf{g} - \text{grad}(\mathbf{p})$ in momentum equation).

Stress tensor, $\boldsymbol{\tau} \boldsymbol{\tau}$, can be expressed as follows (Bird et al., 2002):

$$\boldsymbol{\tau} \boldsymbol{\tau} = -\eta \left[\text{grad} \mathbf{u} + \text{grad}(\mathbf{u}^T) - \frac{2}{3} \text{div}(\mathbf{u} \cdot \mathbf{I}) \right] \quad (5.5)$$

$$\boldsymbol{\tau} \boldsymbol{\tau} = -\eta \left[\overline{\overline{D}} - \frac{2}{3} \text{div}(\mathbf{u} \cdot \mathbf{I}) \right] \quad (5.6)$$

where η is non-Newtonian (apparent) fluid viscosity, I is identity matrix and $\overline{\overline{D}}$ is rate of deformation (or strain) tensor. Non-Newtonian fluid viscosity is a function of all three invariants of rate of deformation tensor. However, for non-Newtonian incompressible fluids, η is a solely function of shear rate, $\dot{\gamma}$ (Bird et al., 2002). $\dot{\gamma}$ is related to rate of deformation tensor as follows:

$$\dot{\gamma} = \sqrt{\frac{1}{2}(\overline{\overline{D}} : \overline{\overline{D}})} \quad (5.7)$$

Thus, Equation (5.6) can be rewritten for non-Newtonian, incompressible fluids as follows:

$$\tau \tau = -\eta \left[\overline{\overline{D}} \right] \text{ with } \eta = \eta(\dot{\gamma}) \quad (5.8)$$

5.4 Grid Generation

After selecting physical and chemical phenomena to be modeled for a specified geometry (computational domain), the domain has to be broken into sub domains usually called grid (or mesh) of cells.

The computational cells can have a variety of shapes. Triangular or quadrilateral cells are generally used for two dimensional problems, while tetrahedral, prisms, pyramids or hexahedral cells are used for three dimensional geometries. Figure (5.1) below shows the kinds of cells produced in Fluent 6.3 for 3D geometries (Fluent Inc., 2006). The grid elements used in Fluent 6.3 and Mixsim 2.1 are mainly tetrahedral and hexahedral, with pyramids between differently meshed zones. Tetrahedral and hexahedral cells produce a good quality grid. However, they can result in a very large grid for small-dimension elements such as baffle (Fluent Inc., 2006).

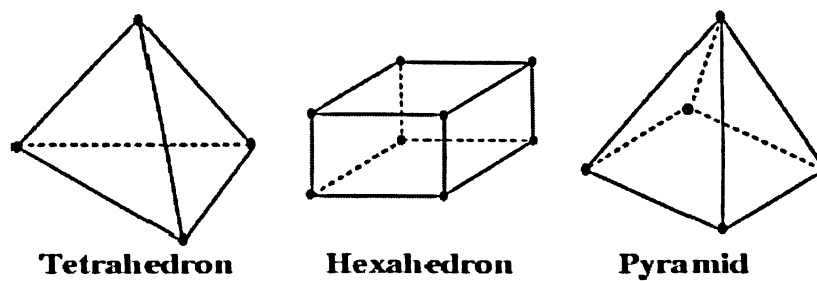


Figure (5.1) 3D Cells Types

The density of the cells in a computational grid needs to be fine enough to capture flow details, but not so fine that the overall number of cells in the domain is excessively large to require large computational time (Edward et al., 2004). The most important requirements placed on a grid generation are that there must be no holes between the grid cells, grid cells do not overlap, the grid is smooth with no abrupt changes in the volume of grid cells, and the grid elements are as regular as possible (Blazek, 2005).

Basically, two different types of grids exist:

- Structured grids – grid points are placed at the intersections of co-ordinates lines, and interior grid points have a fixed number of neighboring grid points. Grid cells are quadrilaterals in 2D and hexahedra in 3D geometries.
- Unstructured grids – grid cells and nodes have no particular order. Grid cells are quadrilaterals and triangles in 2D and hexahedra, tetrahedral, prisms and pyramids in 3D geometries.

Evaluation of gradients and fluxes on structured grids is greatly simplified, because each grid can be accessed quickly and easily. The price paid for the enhanced flexibility in structured grid is a prolonged time (often weeks or months) required to generate grids for complex geometries. Unstructured grids, on the other hand, offer very flexible treatment of complex geometries. Quadrilaterals and triangles grids (in 2D) and hexahedra, tetrahedral, prisms and pyramids grids (in 3D) can be placed independent of the

complexity of the domain. This mixed grids results in a reduction in the number of grid cells, edges, faces and possibly nodes. Time required to build an unstructured, mixed grid for a complex configuration is significantly lower than that for a structured grid (Blazek, 2005, Versteeg and Malalasekera, 2007). Fluent 6.3 and Mixsim 2.1 uses Gambit 2.2 to generate unstructured grids.

5.5 Discretization of Transport Equations

To apply CFD, the transport equations, which describe the continuous movement of a fluid in space and time, must be discretized or changed from a continuous to a discontinuous formulation. Discretization is the method of approximating the differential equations from continuous domain to a discrete domain (Chung, 2002).

Discretization has to be applied to each term in transport equations; accordingly, discretization can be divided into spatial (convective, diffusion and source) and temporal (time).

5.5.1 Spatial Discretization

After generating a grid, the CFD solver implements the numerical technique to discretize convective, viscous and source terms in transport equations. Three numerical techniques are known for spatial discretization: (i) finite difference, (ii) finite element, and (iii) finite volume.

Finite difference approach uses truncated Taylor series expansions to generate finite difference approximations of derivatives at each grid point for each term in the transport differential equation. While finite difference method is an approximation of the transport differential equation, the finite element method is an approximation of the transport differential equation solution. Applying finite element method involves using weighted residuals. An approximate functional behaviour of field variables that satisfies

differential equations and boundary conditions is assumed. Substitution of this approximation into the original differential equations and boundary conditions results in an error called residual. Weighted residuals formulation seeks to determine the function behaviour in such a way that the residuals vanish over the solution domain. Finite element method uses simple piecewise approximation functions (e.g. linear or quadratic) to describe the local variations of property in the transport differential equation. The approximating functions, also known as shape or interpolation function, are defined in terms of the value of the variables at nodes (Chung, 2002).

Finite volume method on the other hand is usually considered the classical or standard approach to performing spatial discretization (Ranade, 2002). This method is widely used in CFD packages, such as Fluent 6.3 and Mixsim 2.1. Finite volume technique consists of integrating the transport governing equations about each cell (or control volume) yielding discrete equations that conserve each quantity on a control volume basis. Volume integrals in partial transport differential equations that contain a divergence term are converted to surface integrals, using the Gauss' divergence theorem (Date, 2005).

The remainder of this chapter will focus on finite volume discretization techniques.

5.5.2 Temporal Discretization

CFD solver implements two techniques to perform temporal discretization: (i) explicit, and (ii) implicit approach.

Explicit time discretization scheme evaluates field variables at the current time level only. Although explicit time discretization schemes are numerically cheap, stability and convergence are hard to achieve using these schemes. Implicit time discretization scheme, on the other hand, evaluates field variables at different time levels. Larger time steps can be utilized with explicit time scheme without hampering the stability of the time

discretization. Another important advantage of implicit schemes is their superior robustness and convergence speed (Blazek, 2005).

5.6 Finite Volume Spatial Discretization

The steady state continuity and motion equations can be expressed as follows in terms of an integral form for an arbitrary three dimensional control volume (CV):

$$\int_{CV} \text{div}(\rho \mathbf{u}) dv = 0 \quad (5.9)$$

$$\int_{CV} -\text{div}(\rho \mathbf{u} \mathbf{u}) dv + \int_{CV} \text{div}(\Gamma_{\Phi} \nabla \Phi) dv + \int_{CV} S_{\Phi} dv = 0 \quad (5.10)$$

The divergence terms can be rewritten as integrals over the entire bounding surface of the control volume using Gauss' divergence theorem (Bird et al. 1002), resulting in the following equation:

$$\int_A (\rho \mathbf{u}) dA = 0 \quad (5.11)$$

$$\int_A -(\rho \mathbf{u} \mathbf{u}) dA + \int_A (\Gamma_{\Phi} \nabla \Phi) dA + \int_{CV} S_{\Phi} dv = 0 \quad (5.12)$$

If the above equations are applied to all control volumes or cells in the computational domain, and summed up for all the cells of computational domain the following equations will result:

$$\sum_f^{N_{\text{faces}}} \rho_f \cdot \bar{\mathbf{u}}_f \cdot \bar{\mathbf{A}}_f = 0 \quad (5.13)$$

$$\sum_f^{N_{\text{faces}}} -\rho_f \bar{u}_f \bar{u}_f \bar{A}_f + \sum_f^{N_{\text{faces}}} \Gamma_\Phi (\nabla \Phi)_n \bar{A}_f + \bar{S}_\Phi \Delta v = 0 \quad (5.14)$$

where subscript (f) refers to cell face, N_{faces} is the number of faces enclosing the cell, \bar{S}_Φ is average value of S_Φ over control volume, $(\nabla \Phi)_n$ is magnitude of $\nabla \Phi$ normal to face (f), and superscript arrows indicate vector of transport property.

The real difficulty encountered in calculating velocity fields lies in the unknown pressure field. The pressure gradient forms a part of the source term for the momentum equation. Yet, there is no obvious equation for obtaining pressure. The unknown pressure field can be indirectly specified from the continuity equation. If the correct pressure field is substituted into the momentum equation, the resulting velocity field should satisfy the continuity equation. Such coupling between pressure and velocity introduces a constraint on flow field, and is usually called pressure-velocity coupling (Patankar, 1980).

Transport field variables are usually stored at the cell centers (nodes). Nodes are usually placed between control volumes such that the faces of control volume are positioned mid-way between adjacent nodes. However, face values of field variables are required to perform the calculations and must be interpolated from the cell values (Abbott and Basco, 1989).

Section 5.6.1 shows the interpolation schemes for pressure gradient, and section 5.6.2 focuses on interpolation schemes for momentum. The diffusion term in Fluent 6.3 is always centre-differenced and hence second order accurate. Section 5.6.3 intends to shed light on the possible methods for solving pressure-velocity coupling.

5.6.1 Pressure Gradient Interpolation Schemes

The pressure gradient appears in the momentum equation in terms of $-dp/dx$, $-dp/dy$ and $-dp/dz$. Different schemes can be used to interpolate the pressure at the nodes of the cells

to the interface or faces of cells. Figure (5.2) intends to show the grid notation in a one-dimensional geometry (Versteeg & Malalasekera, 2007) where capital letters denote cell nodes and small letters denote cell faces.

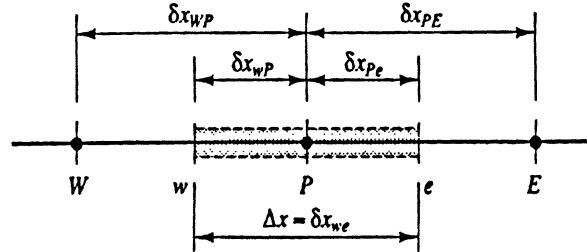


Figure (5.2) Grid Notation

Fluent 6.3 and Mixsim 2.1 use the following pressure interpolation schemes:

- Linear scheme;
- Standard (First Order) scheme;
- Second-Order scheme; and
- PRESTO scheme.

Linear interpolation scheme assumes a piecewise linear profile for pressure between nodes of adjacent cells, computing face pressure as the average of the pressure values between two adjacent cells. At one-dimensional grid, the pressure gradient at face (e) can be expressed as follows (Fluent Inc, 2006):

$$\left(\frac{\partial p}{\partial x} \right)_e = \frac{\frac{P_E + P_W}{2}}{\delta_{XPE}} = \frac{(P_E + P_W)}{\frac{\delta_{XPE}}{2}} \quad (5.15)$$

Having first order accuracy, the first order scheme deals with smooth uniform pressure fields. Under this scheme, the pressure at face (e) can be expressed as follows (Fluent Inc, 2006):

$$\left(\frac{\partial P}{\partial x}\right)_e = \frac{(P_E - P_e)}{\frac{\delta_{XPE}}{2}} \quad (5.16)$$

Second order pressure interpolation scheme (central difference scheme) has a second degree of accuracy. Under this scheme, the pressure at face (e) can be expressed as follows (Versteeg & Malalasekera, 1995):

$$\left(\frac{\partial P}{\partial x}\right)_e = \frac{(P_E - P_P)}{\delta_{XPE}} \quad (5.17)$$

The above schemes store the transport properties at the nodes. Discretizing highly non-smooth pressure fields using standard, linear and/or second order schemes may lead to zero discretize gradient because velocity and pressure are both defined at the same nodes. Staggered grid, first defined by Harlow and Welch (1965), leads to the development of PRESTO (PREssure Stagging Option) scheme. This scheme can be used for high swirling flows, such as flows involving a porous medium. PRESTO is second order accurate.

As the second order scheme provides improvement over first order and standard schemes, and as PRESTO is recommended for high swirling flow, second order scheme is used in this work to discretize pressure.

5.6.2 Momentum Interpolation Schemes

The following different schemes can be used to interpolate the momentum term defined at the nodes of the cells to the interface or faces of cells:

1. First-Order Upwind Scheme;
2. Second-Order Upwind Scheme;
3. Quadratic Upwind Scheme (QUICK); and
4. Power Law Scheme.

The first order scheme was first put forward by Courant et al., (1952) and subsequently developed by Gentry et al. (1966), Barakat and Calrk (1966) and Runchal and Wolfshtein (1969). In this scheme, quantities at cell faces are determined by assuming that the cell-center values of any field variable represent a cell-average value and hold throughout the entire cell; the face quantities are identical to the cell quantities. Thus face value is set equal to the cell-center value of the upstream cell.

$$u_e = u_P \quad \text{if} \quad u_w > 0 \text{ and } u_e > 0 \quad (5.18)$$

$$u_e = u_E \quad \text{if} \quad u_w < 0 \text{ and } u_e < 0 \quad (5.19)$$

Higher orders schemes, such as second order scheme developed by Barth & Jespersen (1989), involve more neighbor points and reduce the interpolation errors as indicated below:

$$u_e = u_P + \nabla u_P \cdot \vec{r}_L \quad \text{if} \quad u_w > 0 \text{ and } u_e > 0 \quad (5.20)$$

$$u_e = u_E + \nabla u_E \cdot \vec{r}_R \quad \text{if} \quad u_w < 0 \text{ and } u_e < 0 \quad (5.21)$$

where ∇u is gradient of u in upstream cell center, and \vec{r} is displacement vector pointed from upstream cell center to the face midpoint (center). Gradients at the cell centers can be estimated using Green-Gauss theorem. Barth & Jespersen second order upwind corresponds to a Taylor series expansion around the centers of cell face, where only linear term in Taylor series is retained.

The quadratic upstream interpolation scheme of Leonard (1979) and Leonard & Mokhtari (1990), usually called QUCIK, uses a three-point upstream-weighted quadratic interpolation for cell face values. The face value for any transport property can be obtained from a quadratic function passing through two bracketing nodes (on each side of the face) and a node on the upstream side as follows:

$$u_e = \frac{6}{8}u_P + \frac{3}{8}u_E - \frac{1}{8}u_W \quad \text{if} \quad u_W > 0 \text{ and } u_e > 0 \quad (5.22)$$

$$u_e = \frac{6}{8}u_E + \frac{3}{8}u_P - \frac{1}{8}u_{EE} \quad \text{if} \quad u_W < 0 \text{ and } u_e < 0 \quad (5.23)$$

where EE is the node upstream of node E.

In Patankar's power law scheme (1980), the value of transport property at any face is related to the value of Peclet number, a dimensionless number that shows the strength of convection to diffusion. The power law expression for cell-face value can be expressed as follows (Patankar, 1981):

$$\text{For } Pe < -10 \quad \frac{de - \frac{Fe}{2}}{de} = -Pe \quad (5.24)$$

$$\text{For } 10 \leq Pe < 0 \quad \frac{de - \frac{Fe}{2}}{de} = (1 + 0.1Pe)^5 - Pe \quad (5.25)$$

$$\text{For } 0 \leq Pe < 10 \quad \frac{de - \frac{Fe}{2}}{de} = (1 - 0.1Pe)^5 \quad (5.26)$$

$$\text{For } Pe > 10 \quad \frac{de - \frac{Fe}{2}}{de} = 0 \quad (5.27)$$

where de is momentum conductance expressed as μ/δ_x , Fe is strength of convection expressed as $\rho \cdot u_e$, Pe is $\rho \cdot u_e \cdot \delta_x / \mu$, μ is fluid viscosity, ρ is fluid density, and δ_x is element length as indicated in Figure (5.2).

Although first order schemes preserve conservativeness, boundedness and transportiveness of transport equation, this scheme is first order accurate and is numerically diffusive (Ranade, 2002). Second order scheme is unbounded, and physical oscillations may appear in systems of strong convection (Versteeg & Malalasekera, 2007). Although QUICK scheme has a third order error and preserves transportiveness of transport equation, it is unbounded and sometimes unstable (Ranade, 2002). Schemes like Power Law combine the benefit of first and second order schemes. Peclet number is used in this scheme to differentiate the use of first order scheme when diffusion dominates the process ($Pe < 2$) and second order upwind when convection dominates the process ($Pe > 2$). Power law is bounded and stable (Patankar, 1980, Ranade, 2002).

Few works have been published on the effect of momentum discretization schemes on CFD results (Sahu & Joshi, 1995, Brucato et al., 1998, Joshi et al., 1998, Sahu et al., 1998, Aubin et al., 2004, Deglon & Meyer, 2006). Power law scheme was found to be superior to upwind schemes in predicting flow fields (Sahu & Joshi, 1995, Joshi et al., 1998). Even when numerical simulations converged faster using upwind schemes, power law scheme was preferred (Sahu & Joshi, 1995, Sahu et al., 1998, Joshi et al., 1998). Brucato et al. (1998) compared numerical simulations of QUICK and Hyperid scheme (a scheme less accurate than Power law, Patankar, 1980), and concluded that the numerical predictions (flow fields and power consumption) do not differ appreciably except that QUICK predicted higher recirculation rates in the top and bottom of the mixing vessel. Aubin et al. (2004) observed that first order upwind scheme compared with second order upwind scheme and QUICK, underpredicts a region of liquid swirling under the impeller. Surprisingly, both first order upwind scheme and QUICK underpredicts power consumption in the vessel. Deglon & Meyer (2006) observed that numerical scheme did not affect CFD predictions for mean velocity profiles in the vessel. However, both flow fields and power number were affected by numerical schemes. The accuracy of QUICK was dominant over upwind schemes.

Power law scheme was used to discretize momentum in this work due to its accuracy, robustness, conservativeness, boundedness and transportiveness (Patankar, 1980).

5.6.3 Pressure-Velocity Coupling Schemes

Pressure-velocity coupling stems from the fact that the pressure field is required to estimate the velocity field, yet there is no equation that describes pressure field. Iterative strategies are used to encounter this problem based on the following approach: 1) Guess initial pressure and velocity field, 2) Use those guessed fields to solve momentum equation, a pressure correction, and velocity correction equations, and 3) Check if the updated velocity field satisfies continuity equation (Wesseling, 2001).

The most frequently used velocity-coupling schemes are:

1. Semi-Implicit Method for Pressure-linked Equations (SIMPLE);
2. Semi-Implicit Method for Pressure-linked Equations Consistent (SIMPLEC); and
3. Pressure Implicit with Splitting of Operators (PSIO).

SIMPLE algorithm, originally developed by Patankar and Spalding (1972), Caretto et al. (1972) and Patankar (1975), is essentially a guess-and-correct procedure for the calculating of pressure on staggered grid arrangement. SIMPLE omits the implicit velocity corrections at the neighboring nodes. Neglecting velocity corrections has detrimental consequences on the overall performance of SIMPLE. Under-relaxation factors (see section 5.9) have to be used to control the change of velocity and pressure during the iterative process in order to maintain the stability of SIMPLE. Using relaxation factors reduces the rate of convergence of SIMPLE algorithm (Ranade, 2002). Depending on the value of under-relaxation factors, SIMPLE may not achieve convergence (Xu and Zhang, 1999).

A number of modifications have been proposed to SIMPLE algorithm to improve convergence properties. SIMPLEC algorithm of Van Doormal and Raithby (1984) and PISO algorithm of Issa (1986) are examples of such modifications.

SIMPLEC assumes that the velocity corrections at the neighboring nodes will be the same as that of the node under consideration (Ranade, 2002). No restrictions on under-relaxations are needed when SIMPLEC is applied due to the consistent assumption made by this algorithm (Xu and Zhang, 1999). It was observed that the convergence and robustness of SIMPLEC was superior to SIMPLE. SIMPLEC was recommended to be used for computation of incompressible fluids at fine grids (Zeng and Tao, 2003).

PISO algorithm was originally developed for the non-iterative computation of unsteady compressible flow (Fluent Inc., 2006). PISO involves two corrector steps; the first of which is the same as that of SIMPLE algorithm. The corrected velocity and pressure fields are used to derive the second correction step. Several researchers also observed that PISO is more computationally expensive to use than SIMPLE and SIMPLEC (Jang et al., 1986, Moukalled and Darwish, 2002 & 2004 A).

The convergence, robustness and stability of SIMPLEC were observed to be dominating over the other algorithm (Darwish et. al., 2004 and Moukalled and Darwish, 2004 B). SIMPLEC algorithm was thus used in this work for pressure-velocity coupling.

5.7 Finite Volume Temporal Discretization

For transient simulations, the governing transport equations must be discretized in both space and time. Temporal discretization involves the integration of every term in the differential equations over time step (Δt).

A generic expression for the time evolution of a variable Φ is given by the following equation:

$$\frac{\partial \Phi}{\partial t} = F(\Phi) \quad (5.28)$$

where the function $F(\Phi)$ incorporates any spatial discretization.

Fluent 6.3 and Mixsim 2.1 discretize time derivative using the following schemes:

- Backward first order differences; and
- Backward second order differences.

First-order accurate temporal discretization is calculated as:

$$\frac{\Phi^{m+1} - \Phi^m}{\Delta t} = F(\Phi) \quad (5.29)$$

and the second-order discretization is calculated as:

$$\frac{3\Phi^{m+1} - 4\Phi^m + \Phi^{m-1}}{2\Delta t} = F(\Phi) \quad (5.30)$$

where Φ is any scalar quantity (like concentration), Δt is time step, $m+1$ is the value of scalar quantity at next time step ($t + \Delta t$), m is the value of scalar quantity at current time step and $m-1$ is the value of scalar quantity at previous time step ($t - \Delta t$).

Once the time derivative has been discretized, a choice remains for evaluating $F(\Phi)$; in particular, which time level values of Φ should be used in evaluating F ? Fluent 6.3 uses the following time integration schemes to evaluate $F(\Phi)$:

- Implicit Time Integration; and
- Explicit Time Integration.

While implicit time integration evaluates $F(\Phi)$ at the future time level, explicit time integration evaluates $F(\Phi)$ at the current time level. Implicit scheme is unconditionally stable with respect to time step size. The use of explicit time stepping is fairly restrictive

because of sensitivity of this integration scheme to time step, and is used primarily to capture the transient behaviour of moving waves (e.g., shocks).

By default, Fluent 6.3 disables the user to utilize explicit time integration for incompressible flow simulations, because for such applications solutions must be iterated to convergence within each time step (Fluent Inc., 2007). First order, implicit scheme was used for temporal discretization in this work.

5.8 Solution of Discretized Equations

Discretization yields a set of algebraic equations that have to be solved simultaneously in every cell in the domain under investigation. The linearized form of the discretized equation can be written as follows (Versteeg & Malalasekera, 2007):

$$a_p \Phi_p = \sum_{nb} a_{nb} \Phi_{nb} + b \quad (5.31)$$

where Φ is any transport property, subscript “nb” refers to the neighbor cells, and a_p and a_{nb} are the linearized coefficients for Φ_p and Φ_{nb} .

Fluent 6.3 and Mixsim 2.1 solve transport equations using segregated and coupled solvers (Fluent Inc., 2006). The segregated approach solves the governing equations sequentially (i.e., segregated from one another). Coupled solver, on the other hand, solves the governing equation simultaneously (i.e., coupled together). Both solvers yield a system of equations represented by Equation (5.31) for dependent variables in every computational cell.

The segregated approach solves for a single variable field (e.g. velocity) by considering all cells at a specific time. It then solves again solves for the next variable field by considering all cells at the same time, and so on. The segregated approach, therefore, solves each discretized governing equation implicitly with respect to the equation's

dependent variable, resulting in a system of linear equations with one equation for each cell in the domain (Abbott and Basco, 1989). A point implicit (Gauss-Seidel) linear equation solver is used in conjunction with an algebraic multigrid (AMG) method (Greenbaum, 1997, Versteeg & Malalasekera, 2007) to solve the equations for all dependent variables in each cell.

Coupled solution method allows using both implicit and explicit solvers. Coupled implicit approach solves for all variables in all the cells at the same time. Each equation in the coupled set of governing equations under the implicit coupled solver is solved implicitly with respect to all dependent variables in the set. This results in a system of linear equations for each cell in the domain. A point implicit (block Gauss-Seidel) linear equation solver is used in conjunction with an algebraic multigrid (AMG) method to solve the resultants system of equations for all dependent variables in each cell. The coupled explicit approach, on the other hand, solves for all variables in one cell at a specific time. Each equation in the coupled set of governing equations under explicit coupled solver is solved explicitly, resulting in a system of equations for each cell in the domain. A multi-stage Runge-Kutta solver is used to solve the resultants system of equations (Greenbaum, 1997, Fluent Inc., 2006).

Segregated implicit scheme, as indicate in Figure (5.3), was used to solve linearized discretized equations in this work.

5.9 Checking CFD Solution

Iterative numerical solutions, such as CFD, are approximations to the exact solution of the governing equations, depending on the appropriateness of numerical schemes used, initial guesses, and iterations.

The solution of each governing equation at each iterative step is based on orientation from the initial guesses that are refined through repeated iterations. Therefore, the right

hand side of Equation (5.31) is a non-zero value, representing the error or residuals in the solution. The total residual, often called unscaled residual, is the sum over all cells in the computational domain of the residuals in each cell and expressed as follows (Fletcher, 1991):

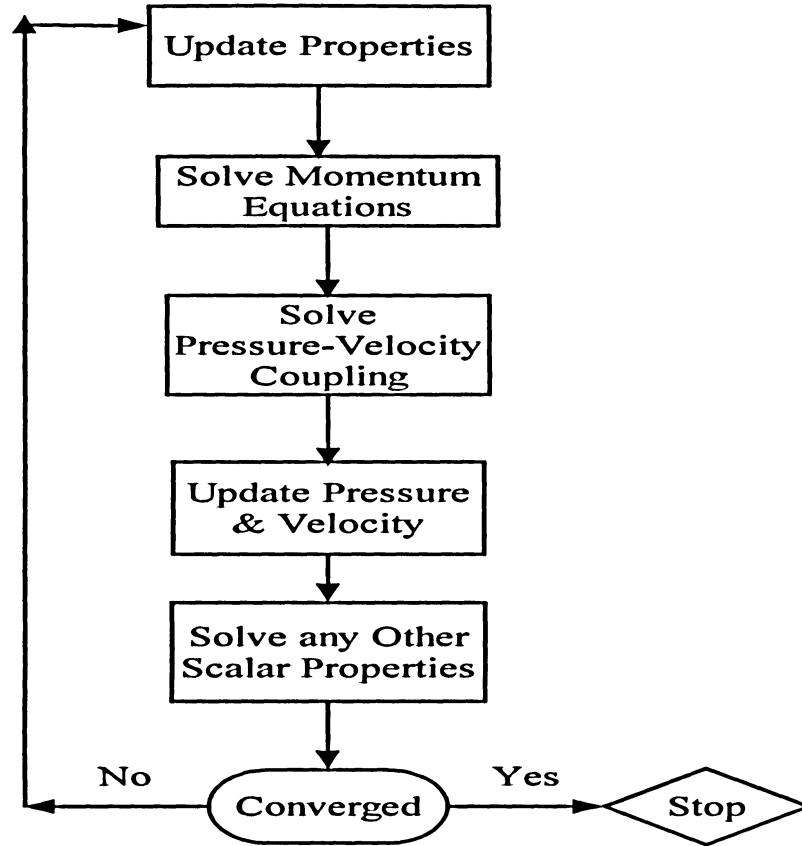


Figure (5.3) Overview of the Segregated Solution Method (Fluent, 2006)

$$R^{\Phi} = \sum_{\text{Cells}} \left| \sum_{nb} a_{nb} \Phi_{nb} + b - a_p \Phi_p \right| \quad (5.32)$$

Since the total residual defined above depends upon the magnitude of the variable being solved, it is customary to either normalize or scale the total residual to gauge its change during the solution process. Using a scaling factor representative of the total flow rate of Φ through the domain, the unscaled residual can be expressed as follows:

$$R^{\Phi}_C = \frac{\sum_{\text{Cells}} \left| \sum_{\text{nb}} a_{\text{nb}} \Phi_{\text{nb}} + b - a_p \Phi_p \right|}{\sum_{\text{Cells}} |a_p \Phi_p|} \quad (5.33)$$

Convergence and stability are two mathematical concepts that are used to determine the success or failure of a CFD solution.

Convergence is the property of a numerical method to produce a solution that approaches the exact solution as the control volume size is reduced to zero. Convergence criteria are preset conditions for the normalized or scaled residuals that determine when an iterative solution is converged and the solution is no longer changing. Stability is associated with the damping errors as the numerical method proceeds. When unstable or divergent behaviour is obtained, “under relaxation” factors can be used to control the computed variables.

The solution of a single differential equation, solved iteratively, makes use of information from the preceding iteration so that the new value is expressed as follows:

$$\Phi_{\text{new}} = \Phi_{\text{old}} + \Delta\Phi \quad (5.34)$$

Rather than using the full computed change in the variable ($\Delta\Phi$) and in order to make the convergence process stable, it is often necessary to use a fraction of the computed range (Edward et al., 2004) so that:

$$\Phi_{\text{new}} = \Phi_{\text{old}} + \alpha \Delta\Phi \quad (5.35)$$

where α is called under relaxation factor and usually takes a value from 0 to 1.0.

Small under relaxation factors facilitate convergence, but they require longer computational time (Fletcher, 1991).

5.10 CFD Modeling of Mixing Vessels

To model the geometry of the impeller in a mixing vessel, fully predictive simulation methodologies were developed to explicitly present impeller rotation in a vessel. An impeller in a mixing vessel induces a periodic flow field associated with separations behind the blades and vortexes production, which are transported into the bulk flow of the vessel by convection and turbulent transport. Fluent 6.3 uses the following two methods to model impeller rotation in a mixing vessel: Multiple Reference Frame (MRF) Model and Sliding Mesh (SM) Model.

5.10.1 Multiple Reference Frame (MRF) Model

A multiple reference frame model (MRF) is a steady state approach allowing for the modeling of baffled tanks with complex (rotating or stationary) internals (Luo et al., 1994).

A rotating frame is used for the region containing the rotating components while a stationary frame is used for regions that are stationary. In the rotating frame containing the impeller, the impeller is at rest. In the stationary frame containing the tank walls and baffles, the walls and baffles are also at rest.

Momentum equation inside the rotating frame is solved in the frame of the enclosed impeller while those outside the rotating frame are solved in the stationary frame. A steady transfer of information is made at the MRF interface as the solution progresses. While the solution of the flow field in the rotating frame in the region surrounding the impeller imparts the impeller rotation to the region outside this frame, the impeller itself does not move during simulations. Impeller position is static, implying that the orientation of impeller blades relative to the baffles does not change. MRF is recommended for simulations in which impeller-baffle interaction is weak.

With this model, rotating frame section extends radially from the centerline or shaft out to a position that is about midway between the blade's tip and baffles. Axially, rotating frame section extends above and below the impeller. In the circumferential direction, it extends throughout the entire angle of the vessel (Fluent Inc., 2006).

5.10.2 Sliding Mesh (SM) Model

The sliding mesh (Luo et al., 1993) model provides a time-dependent description of the periodic interaction between impellers and baffles.

In this model, the grid surrounding the rotating component(s) physically moves during the simulations, while the stationary grid remains static. The velocity of the impeller and shaft relative to the moving mesh region is zero as is the velocity of the tank, baffles, and other internals in the stationary mesh region.

The motion of the impeller is realistically modeled because the grid surrounding it moves as well, giving rise to a time accurate simulation of the impeller-baffle interaction. The motion of the grid is not continuous, but it is in small discrete steps. After each such motion, the set of transport equations is solved in an iterative process until convergence is reached. The grid moves again, and convergence is once again obtained from another iterative calculation. During each of these quasi-steady calculations, information is passed through an interface from the rotating to the stationary regions back again.

Sliding mesh model is the most rigorous and informative solution method for stirred tank simulations. Upon comparing numerical predictions obtained from applying different impeller modeling methodologies, several investigators observed that steady state approaches, like MRF, can provide reasonable predictions to flow field features and power consumption. About one-seventh of the CPU-time can be saved using steady state approaches (MRF) (Brucato et al., 1998, Marshall et al., 1999). Instead of performing a single calculation to obtain a converged result, as is the case with steady state flows,

sliding mesh simulations advance forward in time using small time steps. This requires some level of convergence at each of the time steps. The goal of the sliding mesh model is a solution for the final, periodic steady-state condition.

MRF was successfully used in modeling stirred baffles vessels (Harvey et al., 1997, Naude et al., 1998, Jaworski et al., 2001, Bujalski et al., 2002, Kelly & Gigas, 2003, Khopkar et al., 2004, Aubin et al., 2004, Sommerfeld & Decker, 2004, Jian et al., 2005, Kukukova et al., 2005, Lane et al., 2005, Deglon & Meyer, 2006, Khopkar et al., 2006, Kerdouss et al., 2006, Yue-Lan et al., 2007). MRF was used in this work to simulate impeller rotation in the mixing vessel.

5.11 Scale Model of Continuous-Flow Mixing Vessel

5.11.1 Geometry

A mixing tank with identical geometry to the one used in the experiments was modeled using Mixsim 2.1. The same dimensions for tank, baffles, shaft, input and output mentioned in section 3.1 were used to model the tank.

Impellers geometry was imported from Mixsim 2.1 impeller library. Unfortunately, A320 geometry is not available in Mixsim 2.1 impeller library, and for this reason A320 was excluded from CFD modeling.

5.11.2 Material Definition

Xanthan gum was defined as a new material in Mixsim 2.1 material library. The rheological properties of xanthan gum solutions were defined using Herschel Bulkley model (section 2.2.1). An inherent difficulty in Herschel Bulkley model is that the model is discontinuous because at vanishing shear stress rates, the non-Newtonian viscosity becomes unbounded. To overcome this continuity problem, a two-viscosity model is

used: at low shear stress rate ($\dot{\gamma} \leq \tau_y/\mu_0$), xanthan gum solutions will act like a very viscous "rigid" material with viscosity μ_0 . As the shear stress rate is increased and yield stress, τ_y , is passed, xanthan gum behavior will be described by a power law. Therefore the apparent viscosities of xanthan gum solutions were described as follows.

$$\eta = \mu_0 \quad \text{for } \tau \leq \tau_y \quad (5.36)$$

$$\eta = \frac{\tau_y + K \left[\dot{\gamma}^n - \left(\frac{\tau_y}{\mu_0} \right)^n \right]}{\dot{\gamma}} \quad \text{for } \tau > \tau_y \quad (5.37)$$

where η is apparent viscosity, μ_0 is viscosity up to yielding point (yielding viscosity), $\dot{\gamma}$ is the shear rate, τ_y is the yield stress, K is the consistency index, and n is the flow behaviour index.

Consistency index, K , power law index, n , and yield stress, τ_y , were estimated for xanthan gum solutions from rheological measurements (Table (3.1)). Yielding viscosity was estimated from experimental rheological curves. Yielding viscosity was assumed to be the slope of the line of shear stress versus shear rate curve before yielding, as indicated in Figure (5.4) (Barnes et al., 1989). Density was measured using a pycnometer, as indicated in section 3.4, and the data are given in Table (3.3).

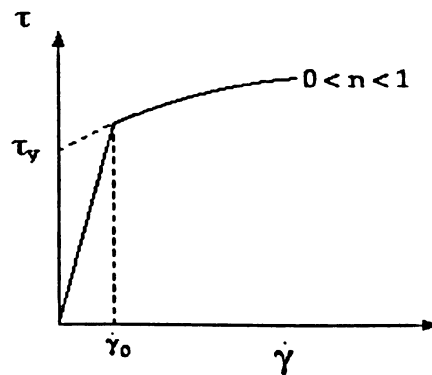


Figure (5.4) Method of Estimating Yielding Viscosity in Herschel Bulkley Model

Table (5.1) Xanthan Gum Rheological & Physical Properties

Xanthan Gum Concentration, %	Yield stress (τ_y , Pa)	Consistency index (K, Pa.s ⁿ)	Power law index (n)	μ_o , Pa.S	Density, Kg/m ³
0.5	1.789	3	0.11	13.300	997.36
1.0	5.254	8	0.12	22.613	991.80
1.5	7.455	14	0.14	32.360	989.76

5.11.3 Selecting Boundary Conditions

Inlet Boundary Condition

At inlet boundaries, velocity (or pressure), and composition of the incoming fluid stream are known. The inlet velocity can be calculated from volumetric flowrate specified from experimental condition, i.e, $v=4Q/\pi d^2$ where Q is volumetric flowrate and d is pipe inlet diameter. All other scalar, except pressure, can be set equal to input values. When velocity is known, the boundary condition for pressure is not required since the pressure-velocity coupling schemes depend on the pressure gradient and not on the absolute pressure. CFD codes usually fix the absolute pressure at one inlet node (atmospheric pressure for open tanks), and set the pressure correction to zero at that node (Versteeg & Malalasekera, 1995 and Ranade, 2002).

Outlet Boundary Condition

Output boundary condition implies that gradients normal the outlet boundary are zero for all the variables except pressure. This boundary condition means that the conditions downstream of the outlet boundary should not influence the flow within the solution domain. This condition approached physically in fully developed flows, thus the exit pipe was modeled with a length/diameter ratio=10 (Versteeg & Malalasekera, 2007). For

pressure boundary condition, static pressure (atmospheric pressure for open tanks) is defined. For outflow through the exit, the static pressure is used to calculate the outflow velocities (Ranade, 2002).

Walls Boundary Condition

At the impermeable wall boundaries, normally a “no slip” boundary condition is employed. For velocity, this boundary condition implies that the traverse fluid velocity is equal to that of the surface and setting the normal velocity equal to zero. For species concentration, a zero flux boundary condition is applied at the wall of the vessel, implying that the wall is impermeable and that the species can not penetrate the wall (Versteeg & Malalasekera, 1995 and Ranade, 2002).

Symmetry (Free Surface) Boundary Condition

A symmetry surface is one across which the flux of all quantities is zero. The tank surface is considered as a symmetry surface. At symmetry surface the normal velocity and concentration are set equal to zero to ensure that there is no connective or diffusive flux across the tank surface (Versteeg & Malalasekera, 1995 and Ranade, 2002).

5.11.4 Generating Meshing

A three dimensional mesh was generated in Mixsim 2.1 using Gambit 2.2, a meshing tool package works under Fluent 6.3 and Mixsim 2.1.

The most critical part of the mesh was around the impeller where velocity gradients prevail. Very fine mesh is required in the vicinity of the blades to define the blades curvature. Mixsim 2.1 uses impeller mesh growth factor function to control mesh density and generate unstructured grid. This function allows the mesh elements to grow slowly as a function of the distance from impeller blades. A fine mesh was also generated for other

curved bodies such as input, output, and tank walls to capture the geometrical features of those elements. Mixsim 2.1 uses mesh normal angle, short edge factor, and maximum growth factor function to control mesh density in curved objects (Fluent Inc, 2006). The final three dimensional mesh of the model generated by Gambit 2.2 is presented in Figure (5.5).

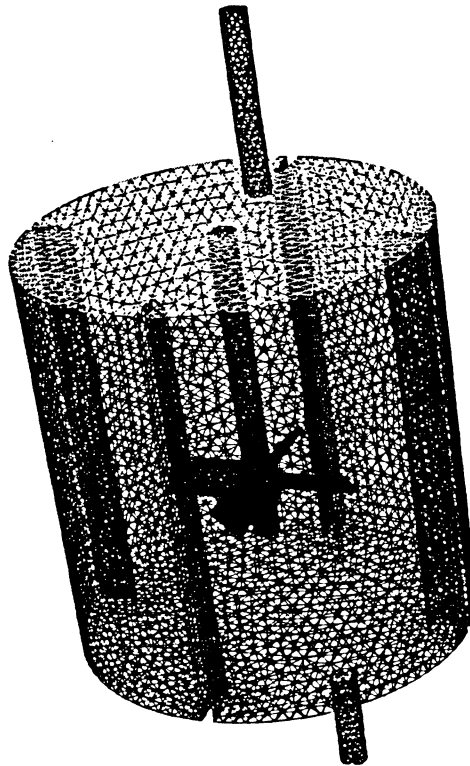


Figure (5.5) 3D Mesh Generated by Gambit 2.2

The grid quality was assessed using skewness of the cells (an indication of how close cells are to a perfect equilateral element, i.e., skewness=0 describes perfect equilateral and skewness=1 describes poorly shaped element). 98% of the cells generated had a skewness smaller than 0.6, indicating an excellent mesh formation (Fluent Inc, 2006), and 78% of the cells were tetrahedral.

5.11.5 Performing Numerical Simulations

The discretized equations were solved using a segregated implicit scheme. CFD simulation carried using the followings schemes: (1) Second Order for pressure interpolation, (2) Power Law for momentum interpolation, (3) First Order for temporal discretization, (4) SIMPLEC for Pressure-Velocity Coupling, and (5) Multiple Reference Frame (MRF) for impeller modeling. The under relaxation factors were left to the default values (0.7 for pressure and 0.3 for momentum) as SIMPLEC impose no restrictions on under relaxation. Convergence, as depicted in Figure (5.6), was monitored during CFD simulations. Convergence history was monitored for mass, x-,y- and z- velocities. The solution was considered converged when the scaled residuals were smaller than 1×10^{-5} for continuity and momentum equations.

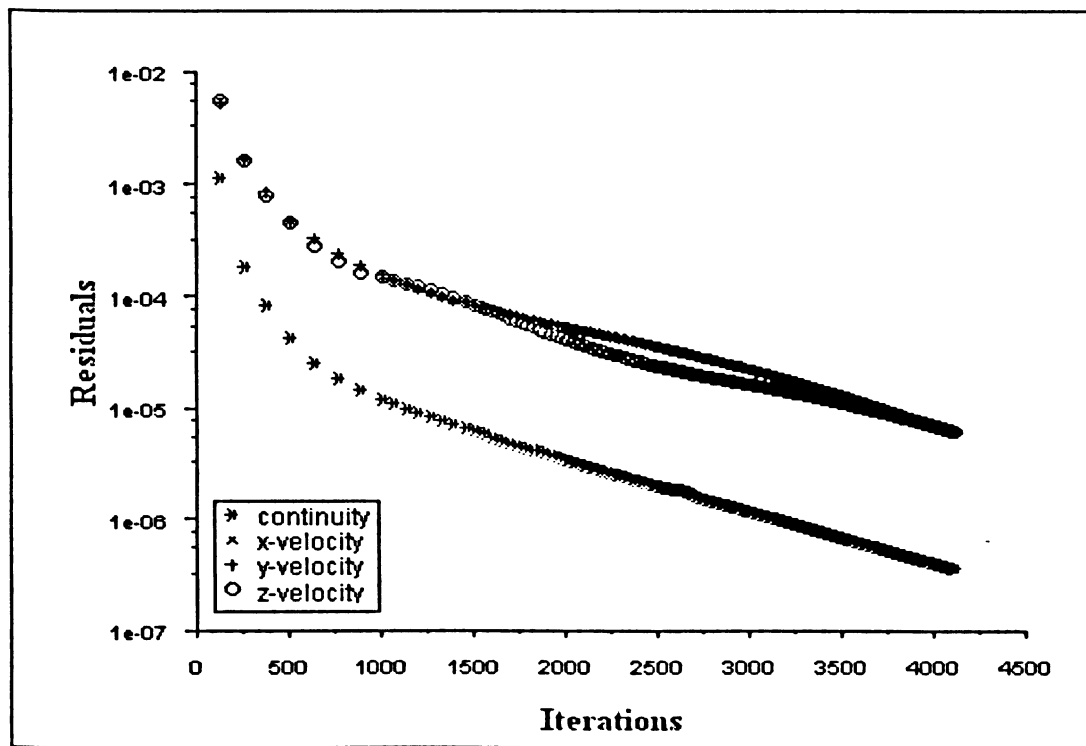


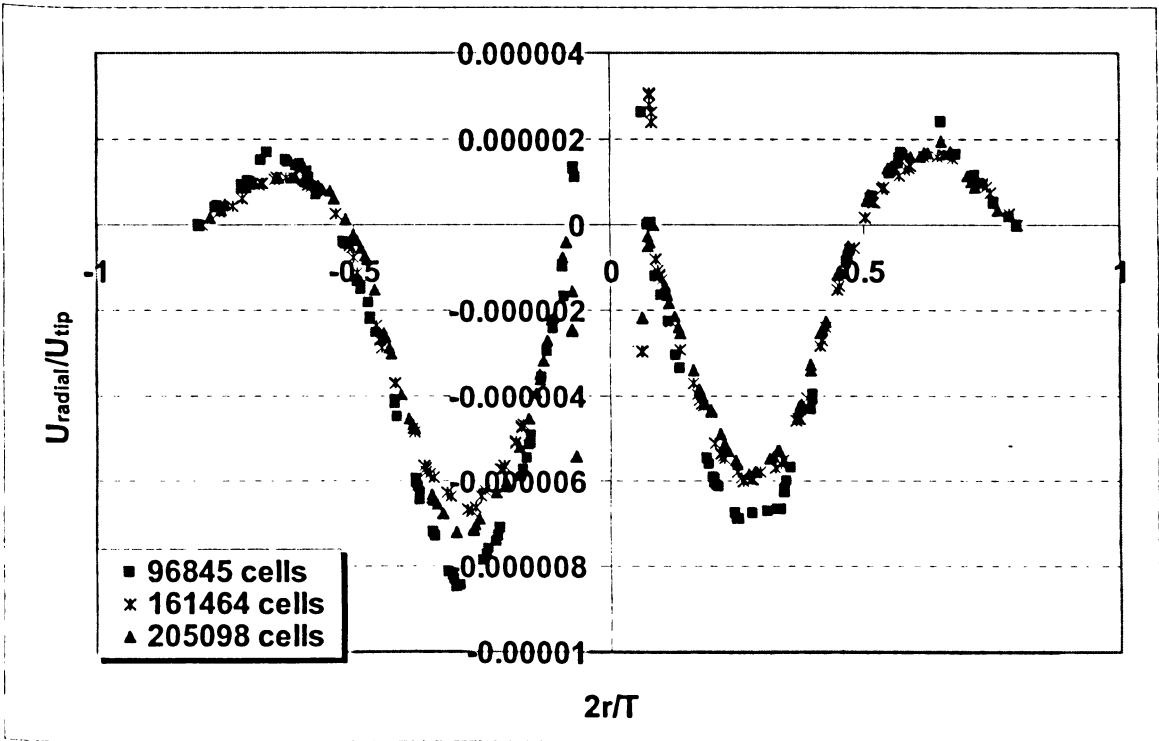
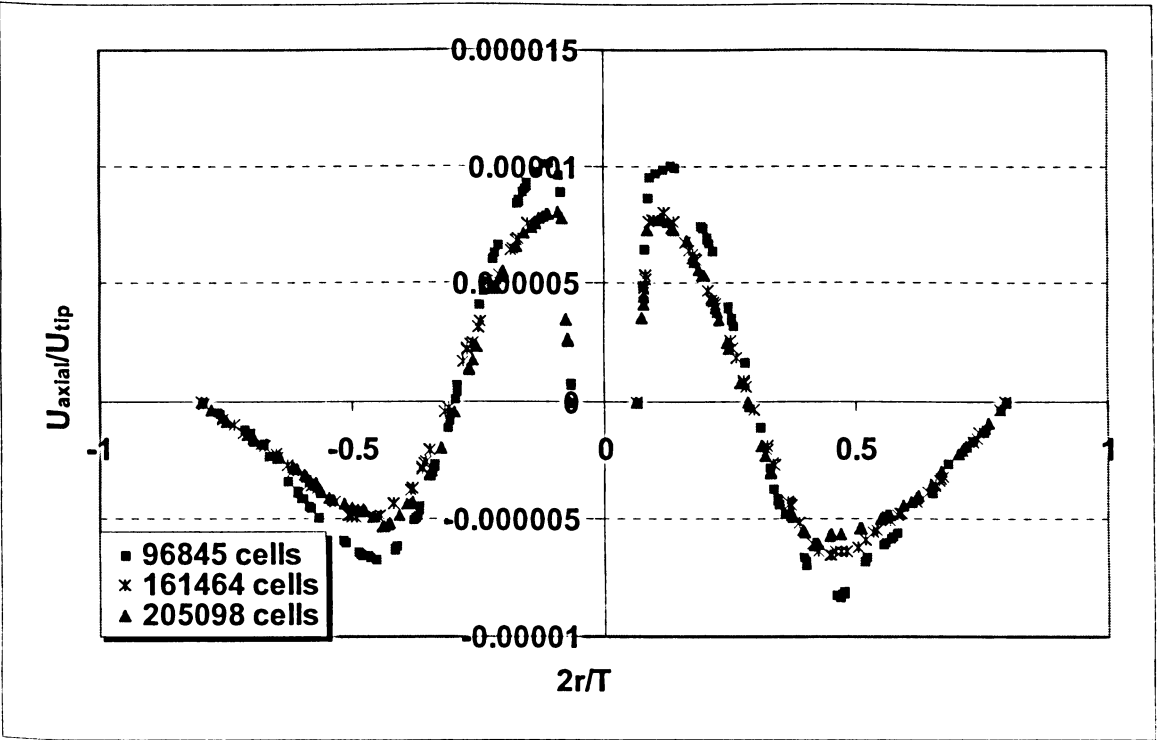
Figure (5.6) Convergence History of Scaled Residuals

5.11.6 Checking Grid Independency

The accuracy of the CFD simulations depends on mesh resolution. Adding more cells to a mesh enables the features of the flow to be better resolved. Grid independency can be verified by demonstrating that adding grid cells to the computational domain can not change flow fields appreciably; however, it is widely believed that no numerical solution is grid independent (Sahu & Joshi, 1995, Joshi et al., 1998, Sommerfeld and Decker, 2004, Kukukova et al., 2005).

To verify the grid independency of the solution, additional cells were added to the default mesh produced by Gambit 2.2. The default mesh has 96845 cells. Number of cells was increased by 67% (161464 cells) and by 100% (205098 cells) by increasing global mesh resolution factor and decreasing impeller mesh growth factor in Mixsim 2.1. Velocity magnitudes were obtained at a plane located midway between impeller blades and bottom of tank. This location was selected because high velocity gradients exist below the impeller. Axial, radial and tangential velocities were plotted at this location for the meshes indicated above and the results are shown in Figure (5.7). Values of the velocities were dimensionalized using impeller tip speed, viz πND , where N is impeller speed and D is impeller diameter and the corresponding locations (r) were normalized using tank radius ($T/2$), where T is vessel diameter.

All velocity profiles show that the first mesh of 96845 cells (Gambit 2.2 default) was unable to predict the flow fields in the vessel accurately, as velocity magnitudes calculated by this mesh differ substantially from the predictions of the second and third mesh. CFD prediction for velocity profiles for the other two meshes was almost identical as depicted in Figure (5.7). The second grid was used for the rest of the calculation in this work as the Central Processing Unit (CPU) time required to achieve convergence was approximately 5-6 hrs, compared to 8-10 hrs for the third grid.



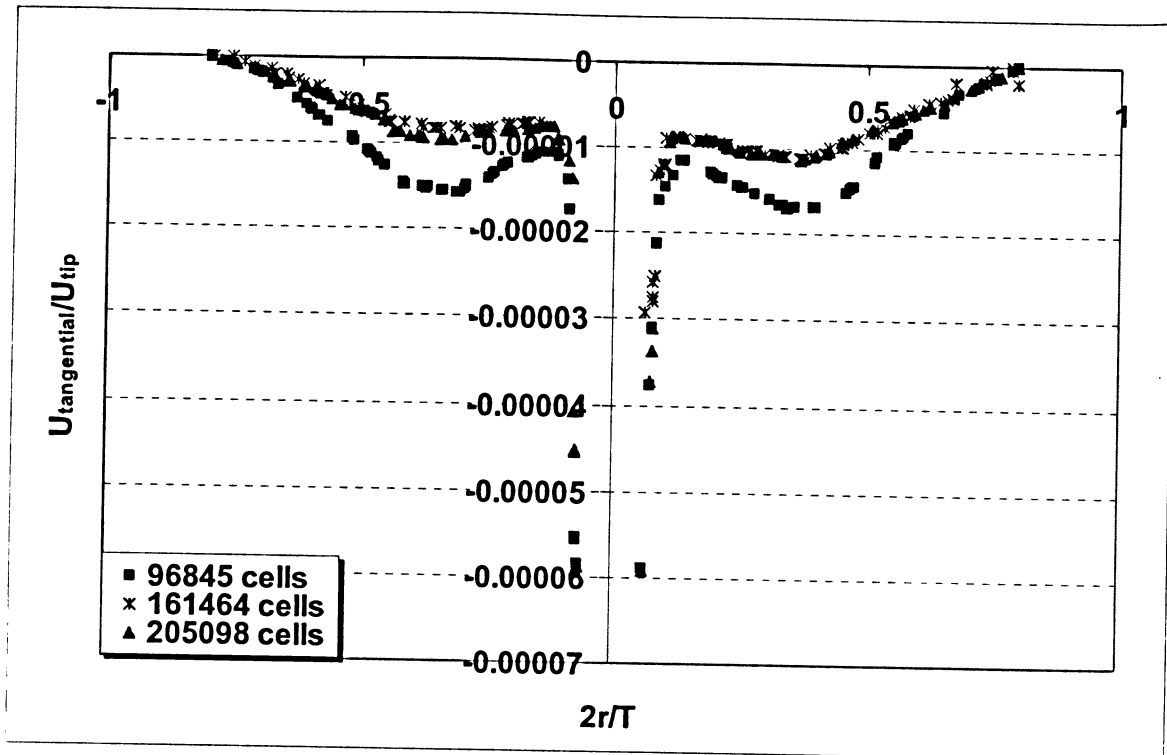


Figure (5.7) Axial, Radial and tangential Velocity Profiles at a below the Impeller showing Grid Independency

5.11.7 Modeling Tracer Injection to Investigate Dynamics of Mixing Process

The flow fields obtained using Mixsim 2.1 were used to simulate the system dynamic response to a tracer injection. When a tracer is added to a fluid in a mixing tank, the transient calculation can be exclusive of the flow field simulations, provided that the properties of the tracer and the background flow in the vessel are the same. Once the flow field of the background fluid is satisfactorily converged, the tracer can be introduced and transient species solution for the tracer can be performed. The properties of background fluid (xanthan gum) will not be changed during tracer addition as the tracer was added in very small amount to the vessel.

The convection-diffusion species transport equation solved by Fluent 6.3 takes the general form (Brid et al., 2002).

$$\frac{\partial}{\partial t}(\rho Y_i) + \text{div}(\rho \mathbf{u} \cdot Y_i) = -\text{div}(J_i) + R_i + S_i \quad (5.38)$$

where Y_i is local mass fraction of species i , R_i is net rate of production of species i by chemical reaction, S_i is rate of creation by addition from the dispersed phase plus any other sources, and J_i is concentration gradient diffusion flux of species i .

In laminar flows, diffusion flux can be calculated from the following equation.

$$J_i = -\rho D_{i,m} \cdot \text{grad}(Y_i) \quad (5.39)$$

where $D_{i,m}$ is diffusion coefficient of species i in mixture m . Convection dominates mixing vessel. In order to neglect diffusion term, diffusion coefficient was set to a very small value ($1 \times 10^{-45} \text{ cm}^2/\text{s}$).

No chemical reaction occurred between tracer and xanthan gum solution in the mixing vessel and since no generation of tracer was possible in the vessel, both R_i and S_i are set equal to zero.

In order to simulate transient species transport, species conservation equation must be solved in a time-dependent form and species conservation equation must be discretized in time and space. Temporal discretization involves the integration of every term in Equation (5.38) over a time step Δt . First order scheme was used for temporal discretization (section 5.7), and second order upwind scheme was used for concentration interpolation (section 5.6.2). Implicit scheme was used for temporal discretization of species transport equation (section 5.7).

The time step was chosen so that the number of iterations needed to reach convergence at each time step was about 20-30. The solution was considered converged when the scaled residuals of tracer concentration were smaller than 1×10^{-6} .

In order to specify tracer injection, a User Defined Function (UDF), written in C programming language (Ford, 2004) was linked to Fluent 6.3 solver. A typical UDF can be shown in Figure (5.8). This UDF defines the time at which the tracer was continuously injected in the mixing vessel. The UDF was linked to the inlet as a boundary condition that specifies the tracer concentration in the inlet stream. Outlet concentration was monitored with time to obtain the response.

Mass fraction of tracer in UDF was set to values analogous to the conductivity of the random binary excitation signal used in the experimental work. Time step was set at first to be equal to 0.1 sec, and the mass fraction of tracer was obtained with time. Then the time step was increased to 1 sec, and the predicted dynamic responses (tracer concentration) from the first and second runs were compared with each other to verify the effect of time step on discretization process. The dynamic responses, as shown in Figure (5.9), were overlapping, indicating temporal independency. The time required to obtain full response using a time step of 0.1 sec was 24 hrs, while the time required to obtain full response using a time step of 1 sec was 3-4 hrs. The time step used in simulating tracer injection was thus set to 1 sec.

```
#include "udf.h"
DEFINE_PROFILE(tracer_mf_profile,t,i)
{
    real flow_time=CURRENT_TIME;
    face_t f;
    begin_f_loop(f,t)
    {
        if(flow_time>1854)
            F_PROFILE(f,t,i)=0.1504;
        else if(flow_time>1806)
            F_PROFILE(f,t,i)=0.0598;
        else if(flow_time>1486)
            F_PROFILE(f,t,i)=0.1491;
        else if(flow_time>1338)
            F_PROFILE(f,t,i)=0.0481;
        else if(flow_time>1212)
            F_PROFILE(f,t,i)=0.1393;
        else if(flow_time>764)
            F_PROFILE(f,t,i)=0.0456;
        else if(flow_time>500)
            F_PROFILE(f,t,i)=0.1386;
        else if(flow_time>230)
            F_PROFILE(f,t,i)=0.0457;
        else if(flow_time>58)
            F_PROFILE(f,t,i)=0.1350;
        else
            F_PROFILE(f,t,i)=0.0442;
    }
    end_f_loop(f,t)
}
```

Figure (5.8) UDF Code Used to Model Tracer Injection for Frequency-Modulated Random Binary Input Signal

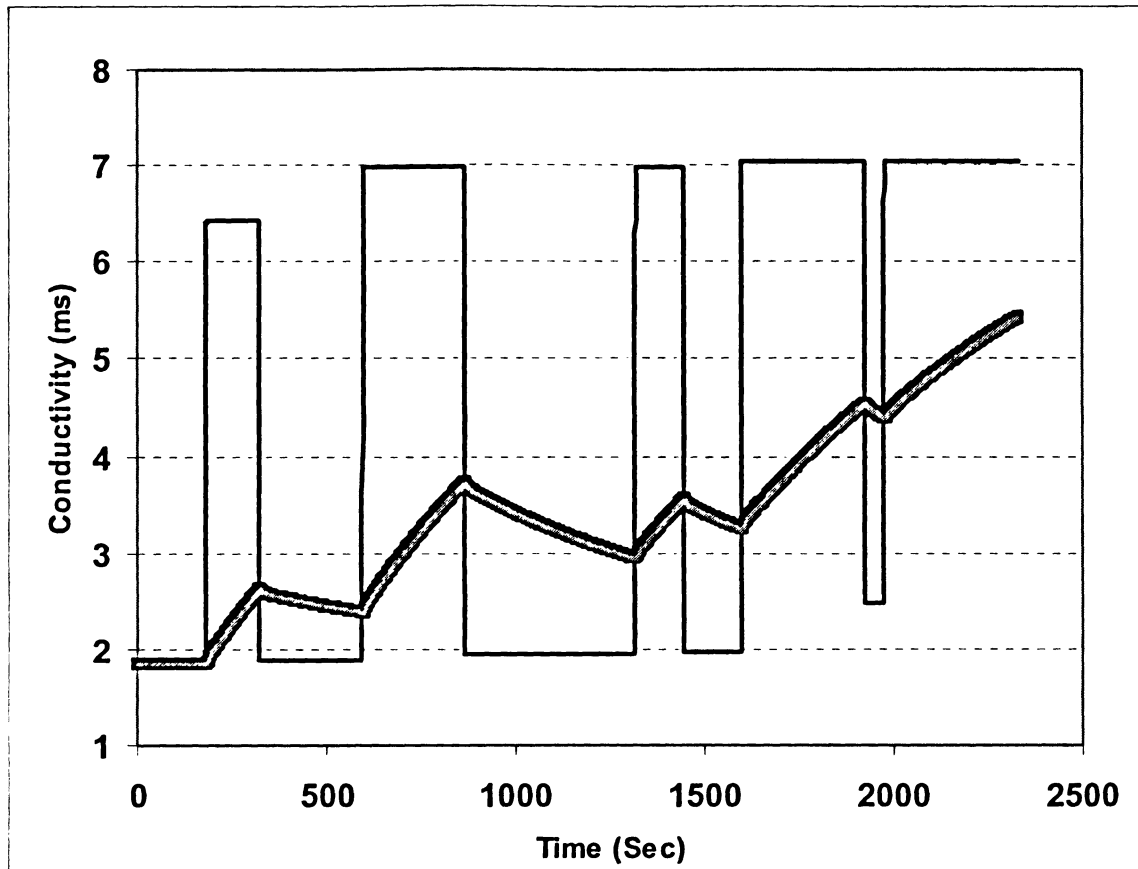


Figure (5.9) CFD Tracer Input Output Showing the Effect of Time Step
Time Step 0.1 sec in Black and Time Step 1.0 sec in Gray

6. Results & Discussion

6.1 Introduction

In this chapter, the results collected from the experimental work and CFD modeling is presented. Comparative analysis between experimental work and CFD is provided where appropriate.

The chapter begins with identifying impeller characteristics, including power number and flow number. In order to validate CFD, experimental values of torque are compared with torque values obtained from CFD. Dynamic model parameters, f and $V_{\text{fully mixed}}/V$, obtained from experimental dynamic response utilizing Ein-Mozaffari model (2002) are presented. CFD predictions for dynamic response is compared with the response obtained experimentally. Dynamic model parameters estimated from CFD dynamic response using Kammer et al. method (2005) is then presented and compared with parameters calculated experimentally.

CFD is then used to capture the other important mixing characteristics, such as cavern, and flow patterns. In order to obtain the whole picture that controls mixing behaviour in continuous-flow mixing vessels, system non-ideal parameters is then related to cavern and flow patterns.

6.2 Impeller Characteristics

Four impellers were used in this work, namely: A200, A100, A310 and A320. Power, flow and circulation numbers are among the most important impeller characteristics. In this section, torque and power number measurements obtained from experimental data are compared with CFD predictions in order to validate CFD. CFD is then utilized to estimate flow and circulation numbers and average shear stress near the impeller.

6.2.1 Power Number Estimation

Power input to the impeller was obtained from torque and impeller speed using the following relation:

$$P = 2\pi.N.M \quad (6-1)$$

where N is impeller velocity, M is torque and P is power.

A torque meter and a tachometer were used to measure impeller torque and speed, respectively. The torque that was lost due to bearing friction, or residual torque, was subtracted from all torque measurements. Residual torque was obtained by operating the mixing vessel when empty.

Power number was estimated from the following relationship using calculated values of power obtained from measured torque:

$$Po = \frac{P}{\rho.D^5.N^3} \quad (6-2)$$

where ρ is fluid density and D is impeller diameter.

6.2.1.1 Experimental Power Number Estimation

Values of power numbers for A200 impeller were plotted against Reynolds numbers at different xanthan gum concentrations, as presented in Figure (6.1). Modified Reynolds number definition for non-Newtonian fluids using Metzner-Otto (1957) definition of effective viscosity was used as follows:

$$Re = \frac{\rho.N.D^2}{\eta} = \frac{\rho.N.D^2}{\tau/\dot{\gamma}_{avg}} = \frac{\rho.N.D^2}{\tau/(k_s.N)} = \frac{\rho.N^2.D^2.k_s}{\tau} \quad (6-3)$$

where η is apparent viscosity, $\dot{\gamma}_{avg}$ is average shear stress close to the impeller ($\dot{\gamma}_{avg} = k_s.N$). Value of Metzner-Otto proportionality constant, k_s , was selected to be 10 (Metzner and Otto, 1957 and Metzner et al., 1961).

Shear stress, τ , defined using Herschel Bulkley model, was inserted in Equation (6-3). Values of τ_y , K , and n presented in Table (5.1) were used for these calculations. The final expression of Reynolds number is as follows:

$$Re = \frac{\rho.N^2.D^2.k_s}{[\tau_y + K(k_s.N)^n]} \quad (6-4)$$

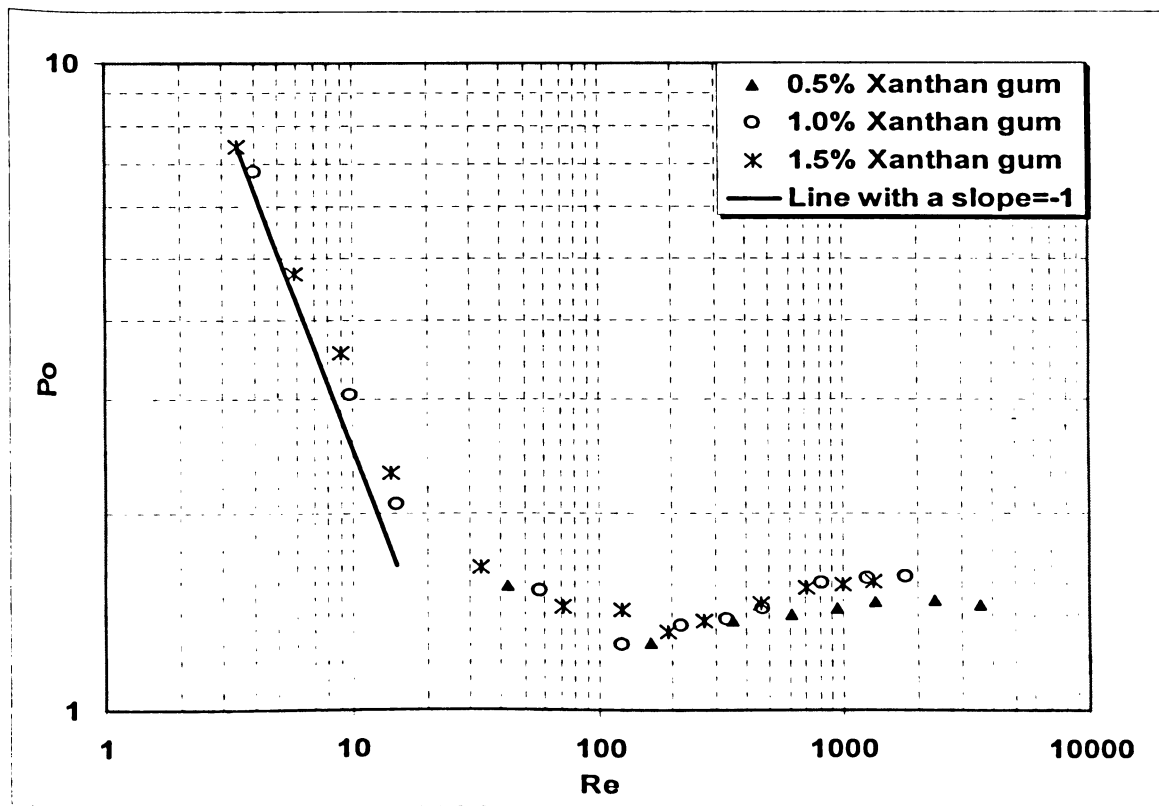


Figure (6.1) Experimental Power Curve for A200

Figure (6.1) shows that power consumption depends upon xanthan gum concentration. The higher the xanthan gum concentration, the higher the energy consumed by the impeller to induce motion in the vessel. At low impeller speed (in the laminar region), power number was inversely proportional to Reynolds number. To compare the behaviour of all impellers, power curves for other impellers are plotted together in Figure (6.2). A200 consumes the largest amount of power at a specific speed, while A310 consumes the smallest amount of power, as similarly observed by Ibrahim and Nienow (1995).

In order to calculate turbulent power number for each impeller, water was used in the mixing vessel instead of xanthan gum to achieve turbulent flow. Impeller turbulent flow number is a characteristic of the impeller geometry and does not depend upon the rheological properties of the material (Tatterson, 1994).

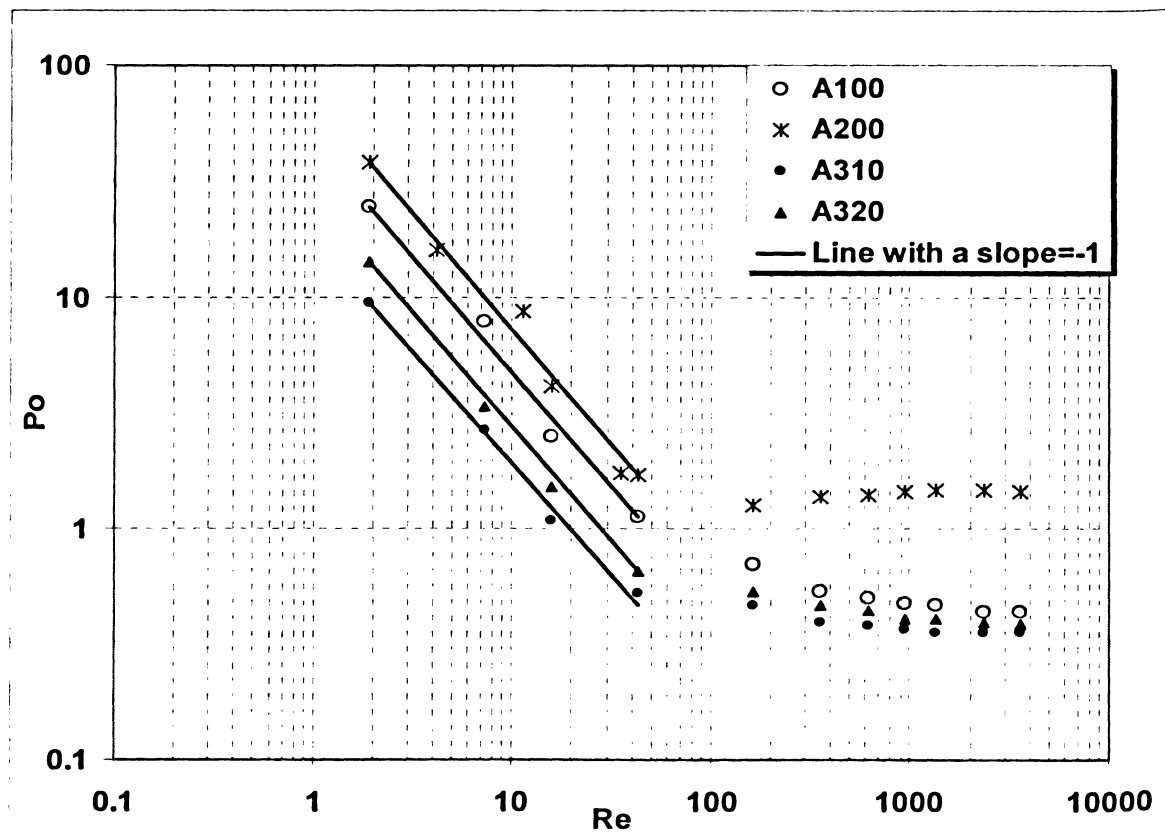


Figure (6.2) Experimental Power Curve for all impellers
0.5% xanthan gum solution

Impeller turbulent flow number, Po_t , was estimated using Mubaga and Bennington (1997) and Bubicco et al. (1997) method. Impeller turbulent flow number can be related to the power input per unit mass via the following relation:

$$\xi_{av} = \frac{P}{\rho V} = Po_t \frac{D^5 N^3}{V} \quad (6-5)$$

where ξ_{av} is power input per unit mass of material and V is solution volume in the vessel.

A plot of $P/\rho V$ versus $D^5 N^3/V$ (as indicated in Figure (6.3)) under turbulent flow conditions can provide impeller turbulent flow number. Table (6.1) shows impeller turbulent power number.

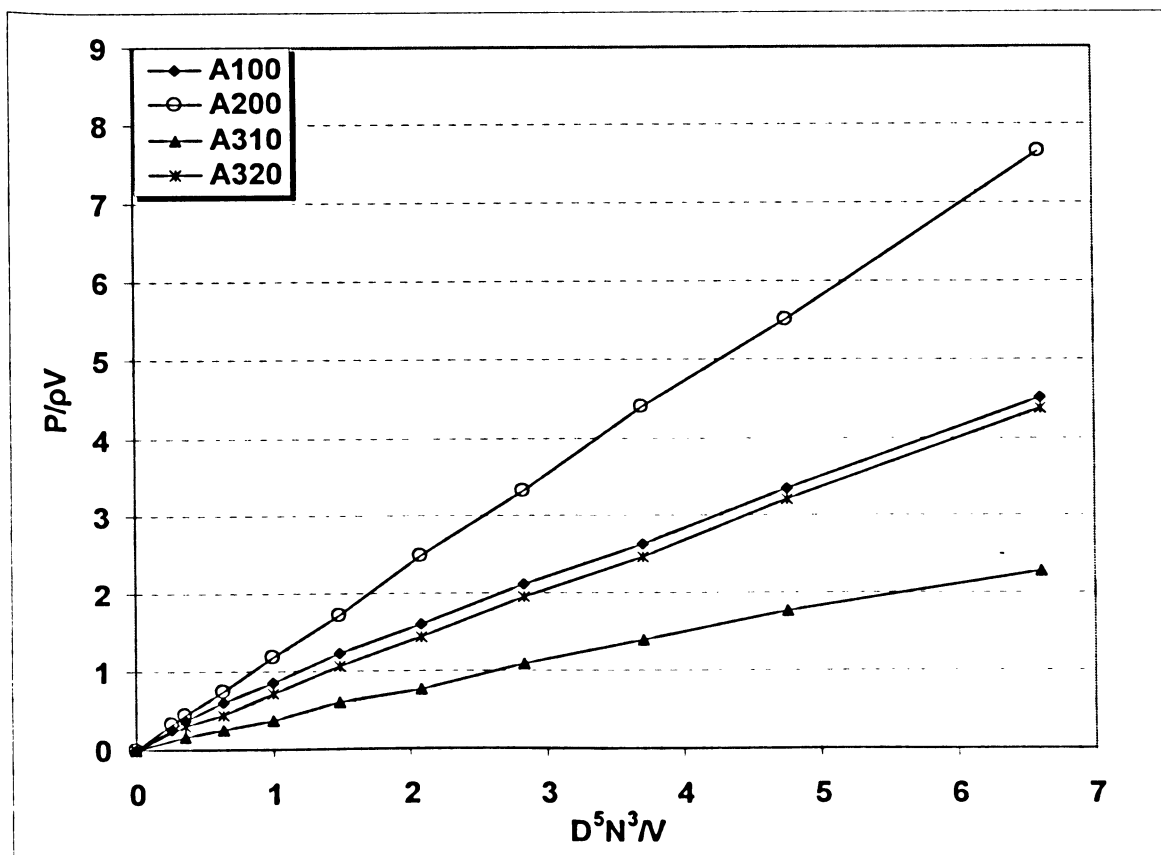


Figure (6.3) Impeller Turbulent Power Number Estimated using Mubaga and Bennington (1997) and Bubicco et al. (1997) method

Table (6.1) Impeller Turbulent Power Number – Experimental Data

	A100	A200	A310	A320
Power Number Turbulent	0.66	1.16	0.40	0.63

For an A100 impeller, the following power number is given: 0.87 (Oldshue, 1983), 0.89 (Mishra et al., 1998), 0.23 (Nienow, 1990), 0.89 (Ranade et al., 1992), 0.89 (Sahu et al., 1999), and 0.34 (Edward et al., 2004).

For an A200 impeller, the following power number is given: 1.27 (Oldshue, 1983), 2.21 (Ranade & Joshi, 1989), 1.27 (Nienow, 1990), 2.1 (Ranade et al., 1992), 1.7 (Jaworski et al., 1996), 1.8 (Ranade and Dommeti, 1996), 2.1 (Mishra et al., 1998), 2.2 (Sahu et al., 1999), 1.93 (Patwardhan and Joshi, 1999), 1.26 (Houcine et al., 2000), 1.93 (Aubin et al., 2001), 1.22 (Wu et al., 2001), 1.6 (Wyczalkowski, 2004), 1.27 (Edward et al., 2004), 1.6 (Kukukova et al., 2005), and 1.3 (Kumaresan & Joshi, 2006).

For an A310 impeller, the following power number is given: 0.29 for A310 impeller (Ibrahim & Nienow, 1995), 0.40 (Mavros et al., 1996), 0.34 (Patwardhan and Joshi, 1999), 0.33 (Wu and Pullum, 2000), 0.32 (Wu et al., 2001), 0.37 (Wyczalkowski, 2004), 0.3 (Edward et al., 2004), 0.28-0.35 (Kumaresan et al., 2005), 0.3-0.4 (Kumaresan & Joshi, 2006), and 0.31 (Wu et al., 2006 A).

For an A320 impeller, power number was reported to be 0.64 (Weetman and Coyle, 1989).

Power numbers for all impellers obtained from experimental measurements were in very good agreement with values reported in the literature.

Experimental torque measurement accuracy was checked by performing a set of 6 experiments at 6 different speeds. Each experiment was repeated 4 times and the torque

measurements were averaged. Error bars were plotted to include standard deviation in each measurement.

Data presented in Figure (6.4) demonstrate that the maximum standard deviation observed in torque measurements was 0.0175 N.m, indicating an excellent reproducibility of torque measurements.

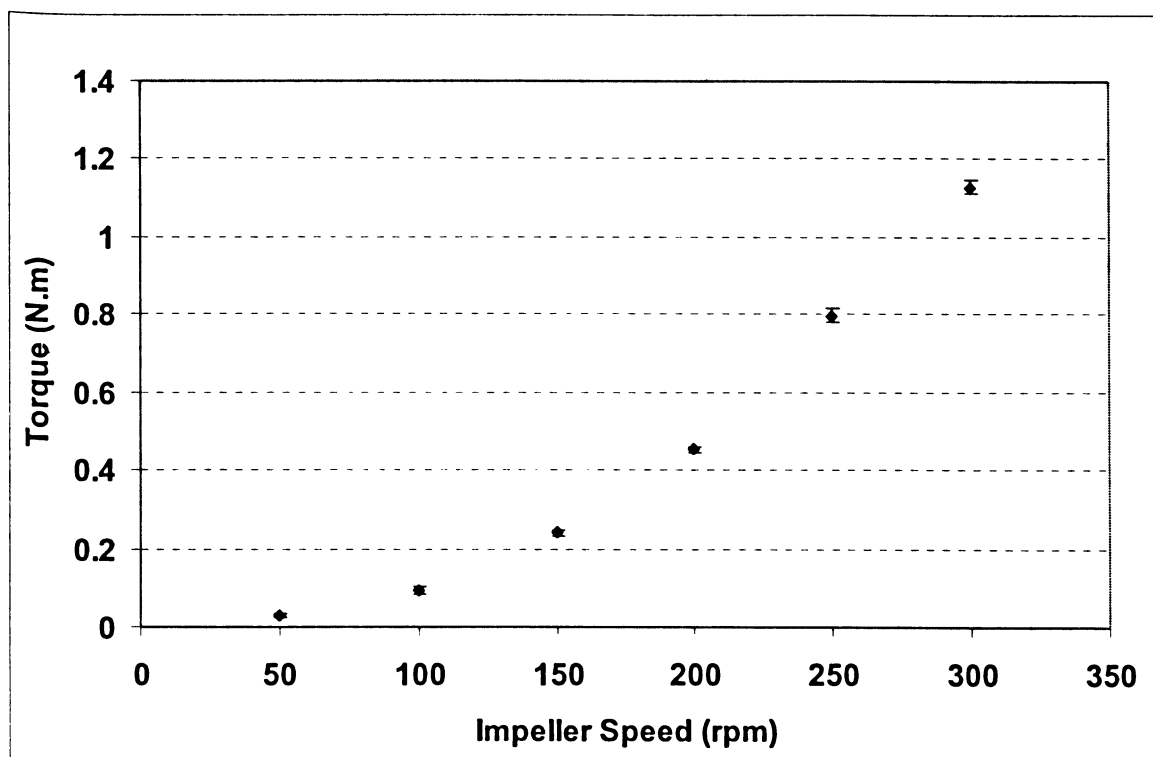


Figure (6.4) Error Associated with Torque Measurements
0.5% Xanthan Gum Solution – A200 Impeller

6.2.1.2 CFD Power Number Estimation

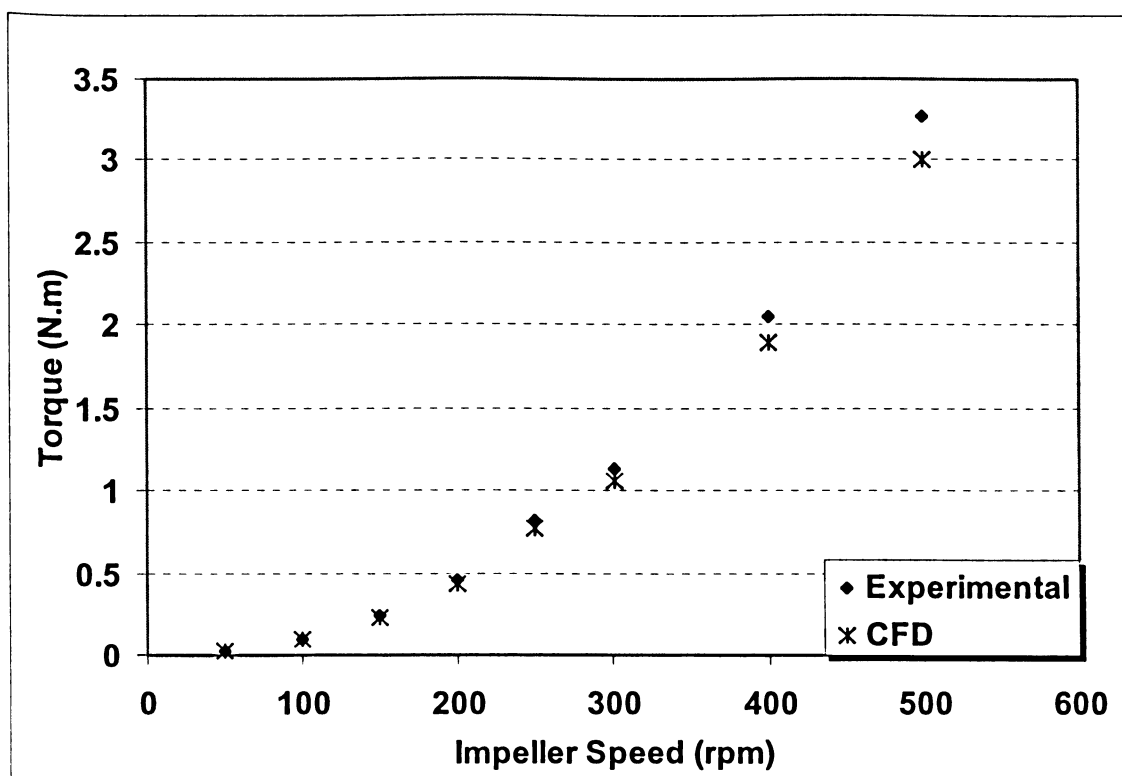
Mixsim 2.1 estimates power from torque imparted by the impeller using Equation (6-1). The flow fields were simulated using conditions identical to the experimental flow fields. Unfortunately, the geometry of A320 impeller was unavailable in the impellers library provided by Mixsim 2.1, and for this reason the A320 impeller was excluded from the simulations.

The experimental torque measurements were compared with CFD predictions and the data are presented in Figure (6.5) to Figure (6.7) for A200, A100 and A310 impellers. The data demonstrate excellent agreement between CFD and experimental torque measurement for all impellers, indicating CFD's ability to predict power consumption in the vessel. Values of torque measured experimentally exceeded CFD predictions. The deviation between CFD and experimental torque became notable (maximum 8%) at high impeller speed. Flow conditions in the mixing vessel became turbulent at high impeller speed, violating the laminar flow assumption imposed on CFD simulations.

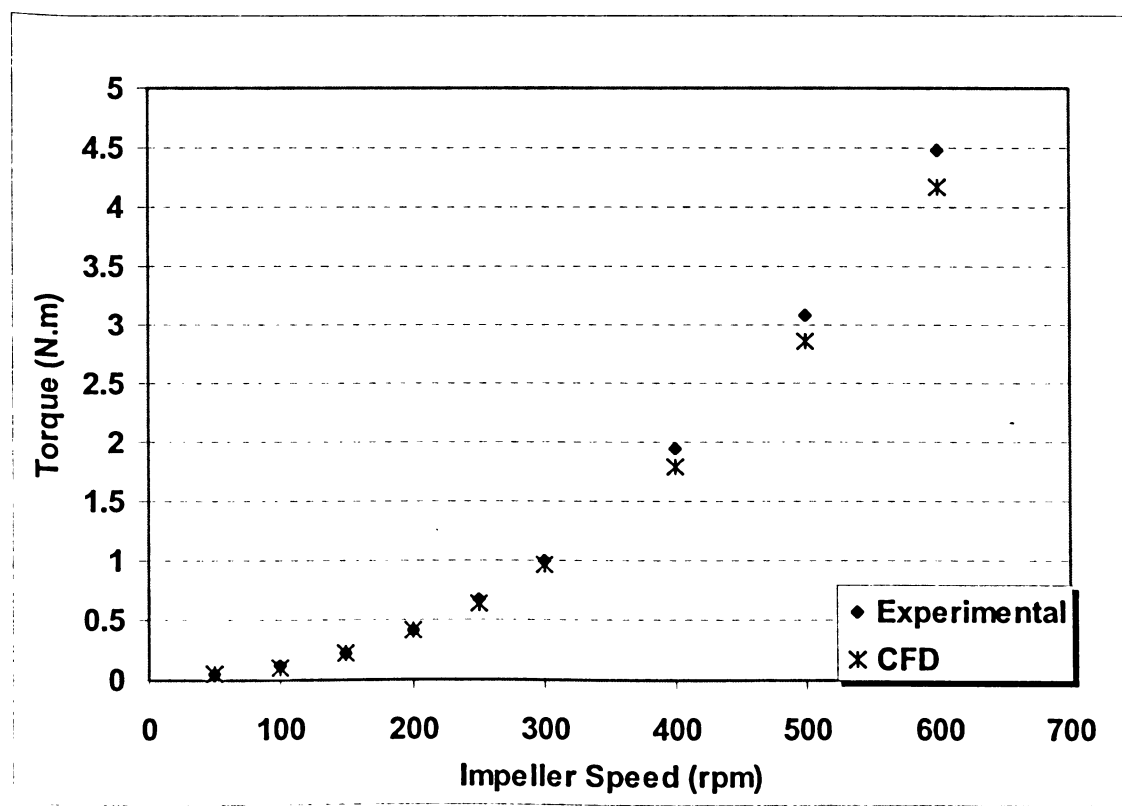
Water was used instead of xanthan gum to obtain impeller turbulent power number. The data presented in Table (6.2) show very good agreement with experimental data presented in Table (6.1).

Table (6.2) Impellers Turbulent Power Numbers – CFD Simulations

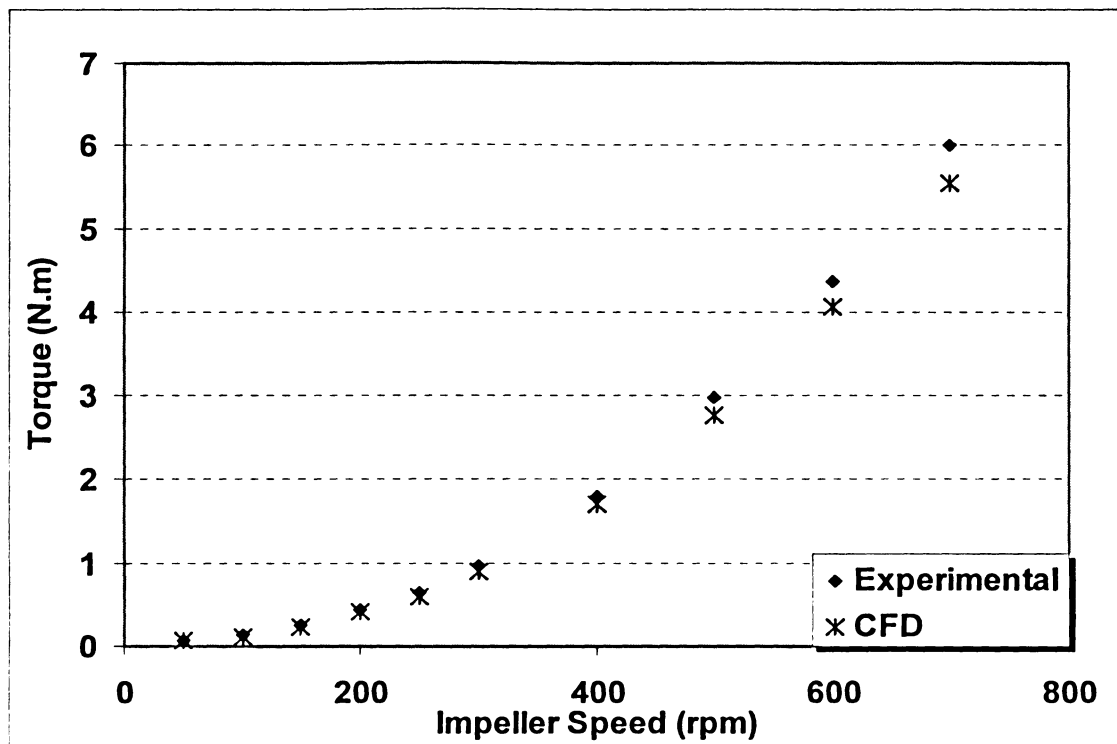
	A100	A200	A310
Power Number Turbulent	0.68	1.14	0.42



(a) 0.5% Xanthan Gum Solution



(b) 1.0% Xanthan Gum Solution



(c) 1.5% Xanthan Gum Solution

Figure (6.5) Comparison between Experimental and CFD Torque – A200 Impeller

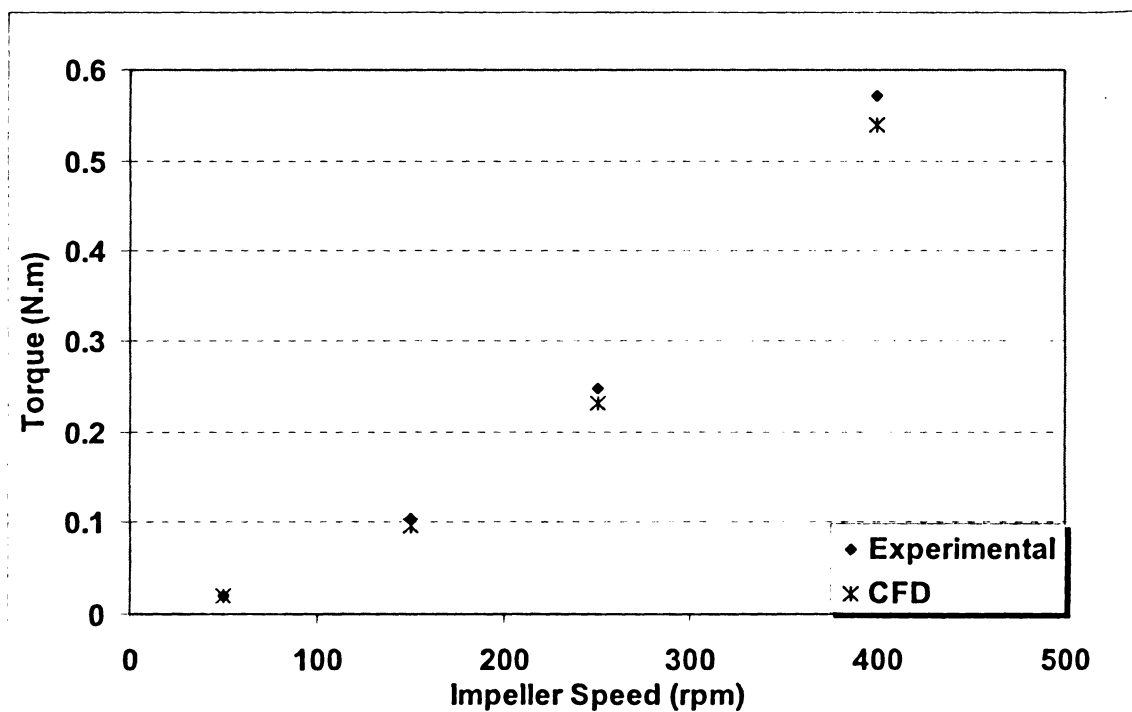


Figure (6.6) Comparison between Experimental and CFD Torque 0.5% Xanthan Gum Solution – A100 Impeller

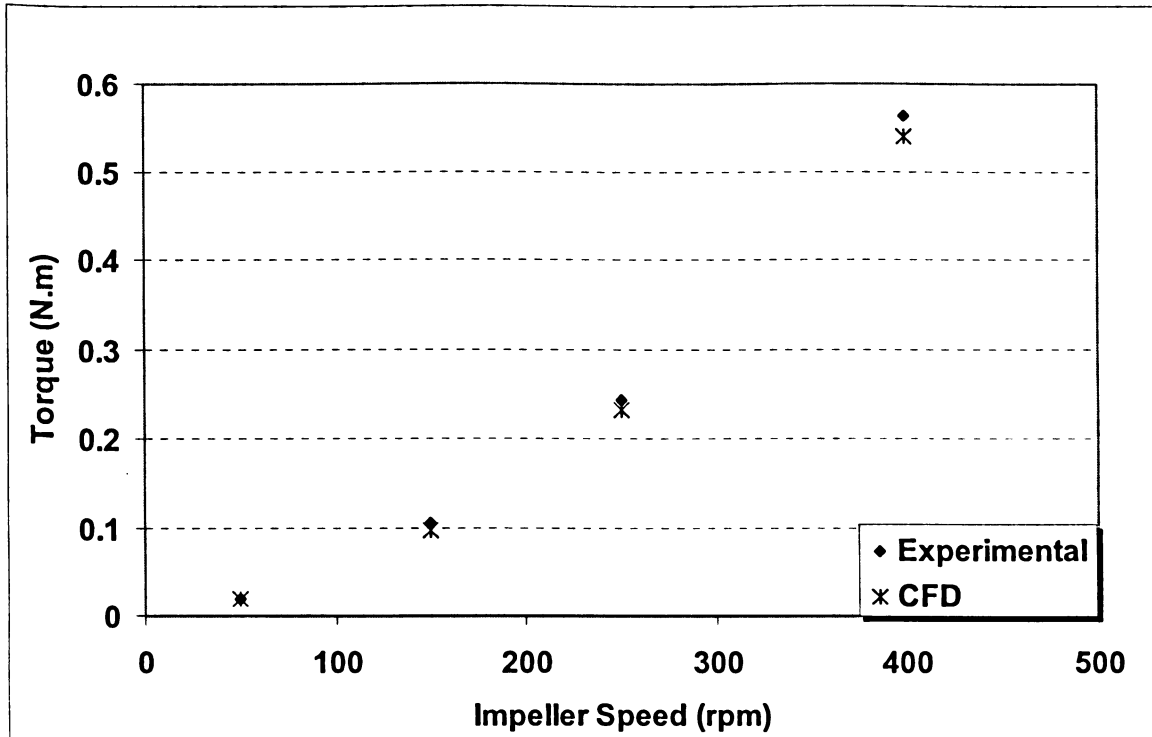


Figure (6.7) Comparison between Experimental and CFD Torque 0.5% Xanthan Gum Solution – A310 Impeller

6.2.2 Average Shear Stress and Apparent Viscosity in the Mixing Vessel

Metzner and Otto's (1959) study of impeller power consumption pattern for power law fluids suggests that the shear rate near the impeller is directly proportional to the impeller speed, and that this proportionality constant, k_s , is largely independent of geometric and fluid rheology. Shear stress influences the average apparent viscosity of non-Newtonian fluids and hence affects power consumption and mixing characteristics.

CFD can be used to examine whether or not a value of k_s derived from the local shear rate near the impeller is constant. Area weighted average shear rate for region around the impeller was calculated from CFD flow fields. The region around the impeller extended 2.5 cm beyond the impeller blades both horizontally and vertically. This approach has been used by many investigators to validate the authenticity of the Metzner-Otto concept (Torrez and Andre, 1998 & 1999, Shekhar and Jayanti, 2003 A & B, Kelly and Gigas, 2003, Vlaev et al., 2006).

Using CFD flow fields, average shear stress was estimated for all xanthan gum solutions at all impeller speeds. Values k_s were then estimated as the slope of average shear stress-versus-impeller speed line following Metzner and Otto's (1959) equation:

$$\dot{\gamma} = k_s \cdot N \quad (6-6)$$

Resulting data are presented in Figure (6.8). The dependency of near-impeller average shear rate on impeller speed and xanthan gum concentration was evident. Similar observations were reported by Kelly and Gigas (2003), Wu et al. (2006 A & B), and Vaev et al. (2006). However, an average value of $k_s = 8.5$ was extracted for A200. Value of k_s for A100 has been reported to be 5.4 (Weetman and Oldshue, 1988), 11 (Bakker and Gates, 1995), 8.58 (Kelly & Gigas, 2003), and 9.2 (Rudolph, 2006).

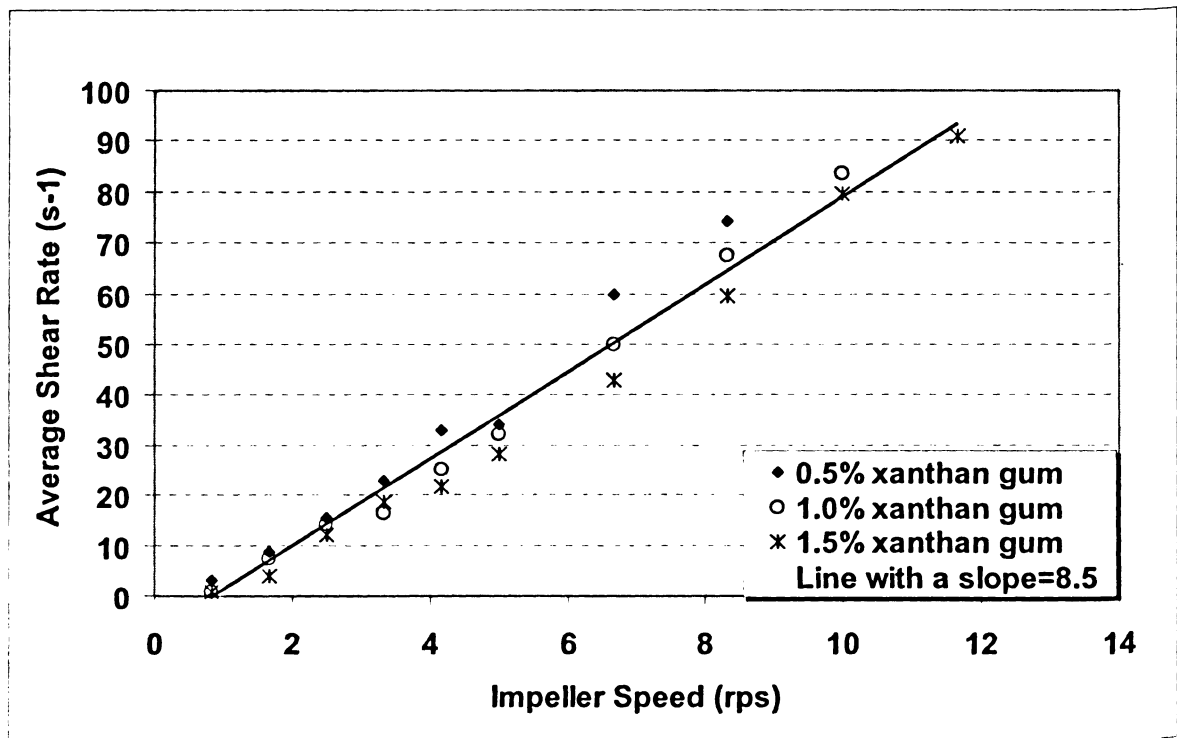


Figure (6.8) Average Shear Rate versus Impeller Speed – A200 Impeller

To allow for comparison of the impellers, Metzner-Otto relationship was plotted for all impellers following the same approach explained above for A200. The results are presented in Figure (6.9). Values of k_s have been reported to be 3.42 for A310 (Weetman

and Oldshue, 1988), 11 for A100 (Metzner et al., 1961), 10 (Skelland, 1983), and 5.4 (Weetman and Oldshue, 1988).

The maximum average value of shear rate was 60 s^{-1} . The rheological properties were measured at controlled shear rate in the range of $0\text{-}130 \text{ S}^{-1}$, proposing that the rheological measurements were made at the same range of average shear stress prevailing in the mixing vessel.

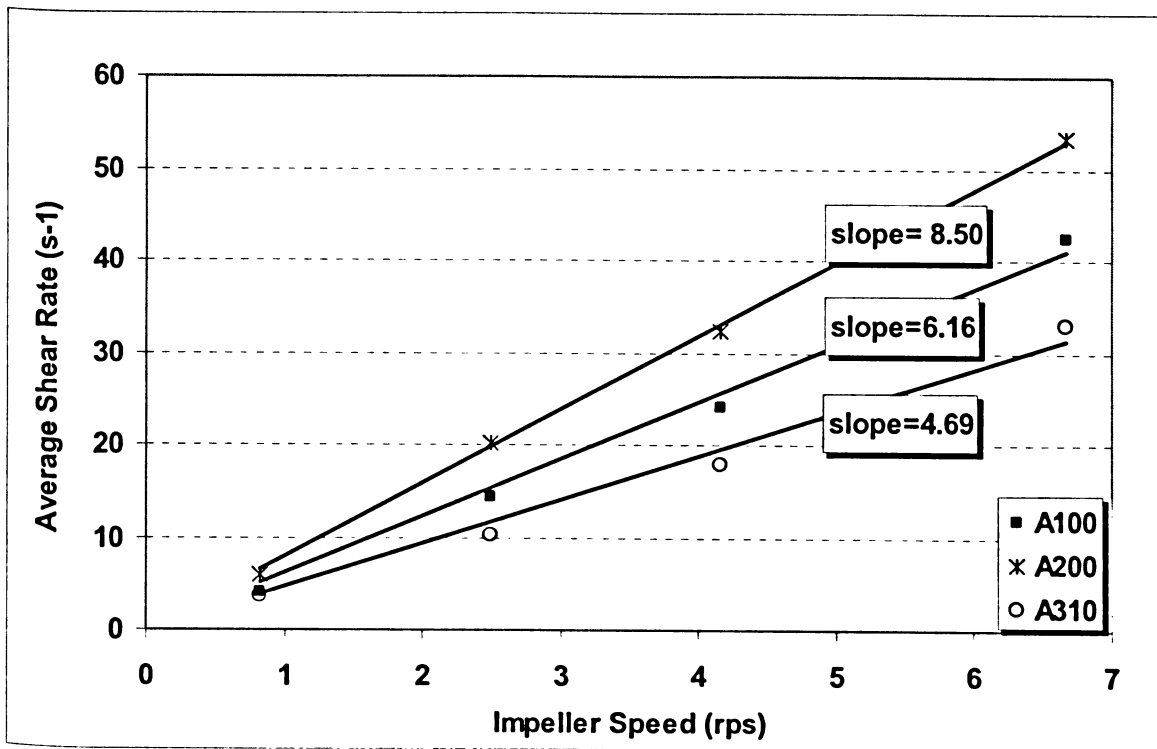


Figure (6.9) Average Shear Rate versus Impeller Speed – 0.5% Xanthan Gum Solution

Apparent viscosity (η) in the mixing vessel was monitored by extracting vertical and horizontal apparent viscosity contours from CFD. Figure (6.10) shows the effect of impeller speed on vertical and horizontal contours for the A200 impeller and Figure (6.11) shows the effect of xanthan gum concentration on the same contours. Horizontal apparent viscosity planes were obtained on planes cutting the impeller surface, while vertical apparent viscosity contours were obtained on planes parallel to the shaft and perpendicular to the impeller.

It is clear that increasing impeller speed and reducing xanthan gum concentration reduce viscosity in the mixing vessel. Viscosity was high except near the impeller region. The minimum viscosity was 0.038 Pa.s and the maximum viscosity was 0.324 Pa.s.

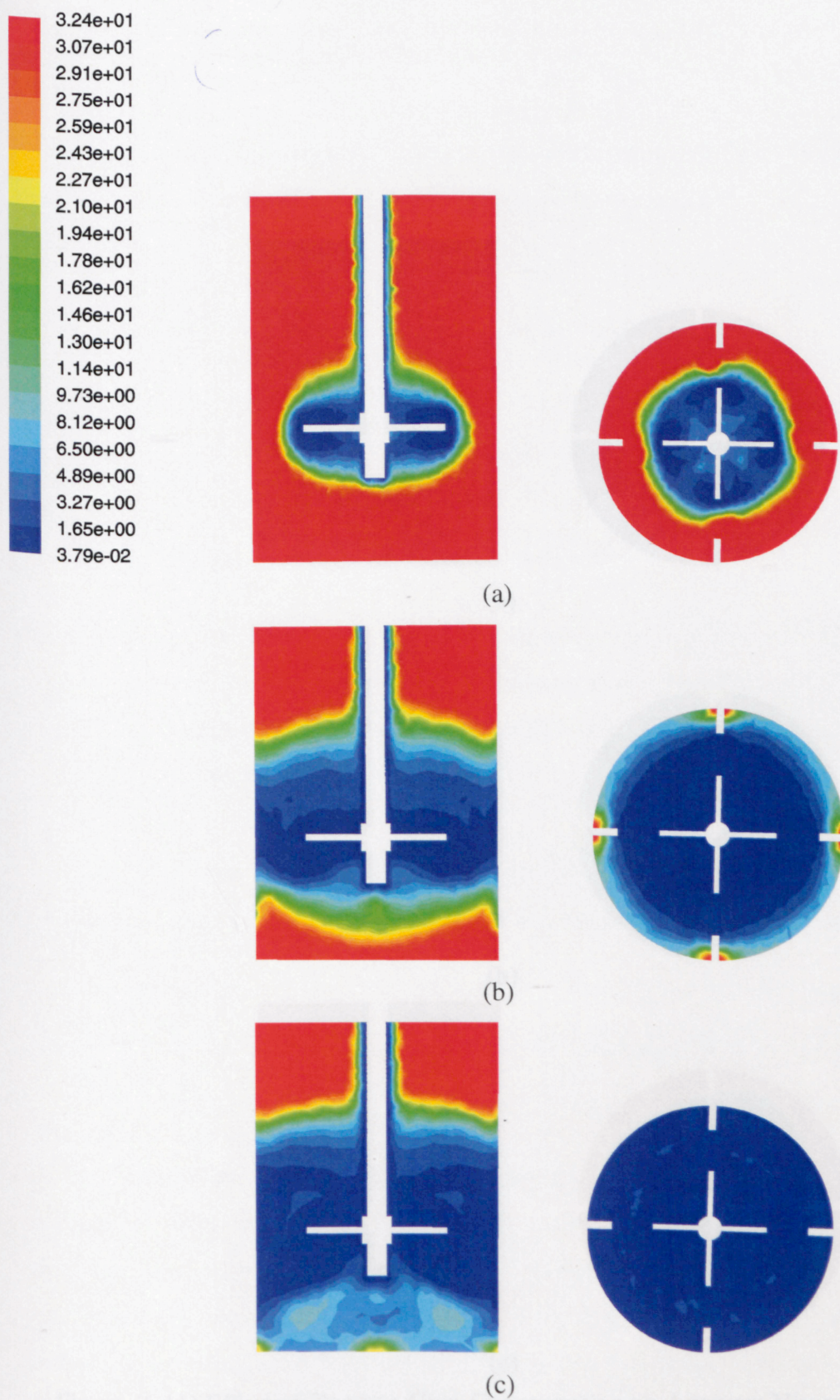


Figure (6.10) Effect of Impeller Speed on Apparent Viscosity in Pa.s, 1.5% Xanthan Gum (a) 50, (b) 150, (c) 250 rpm

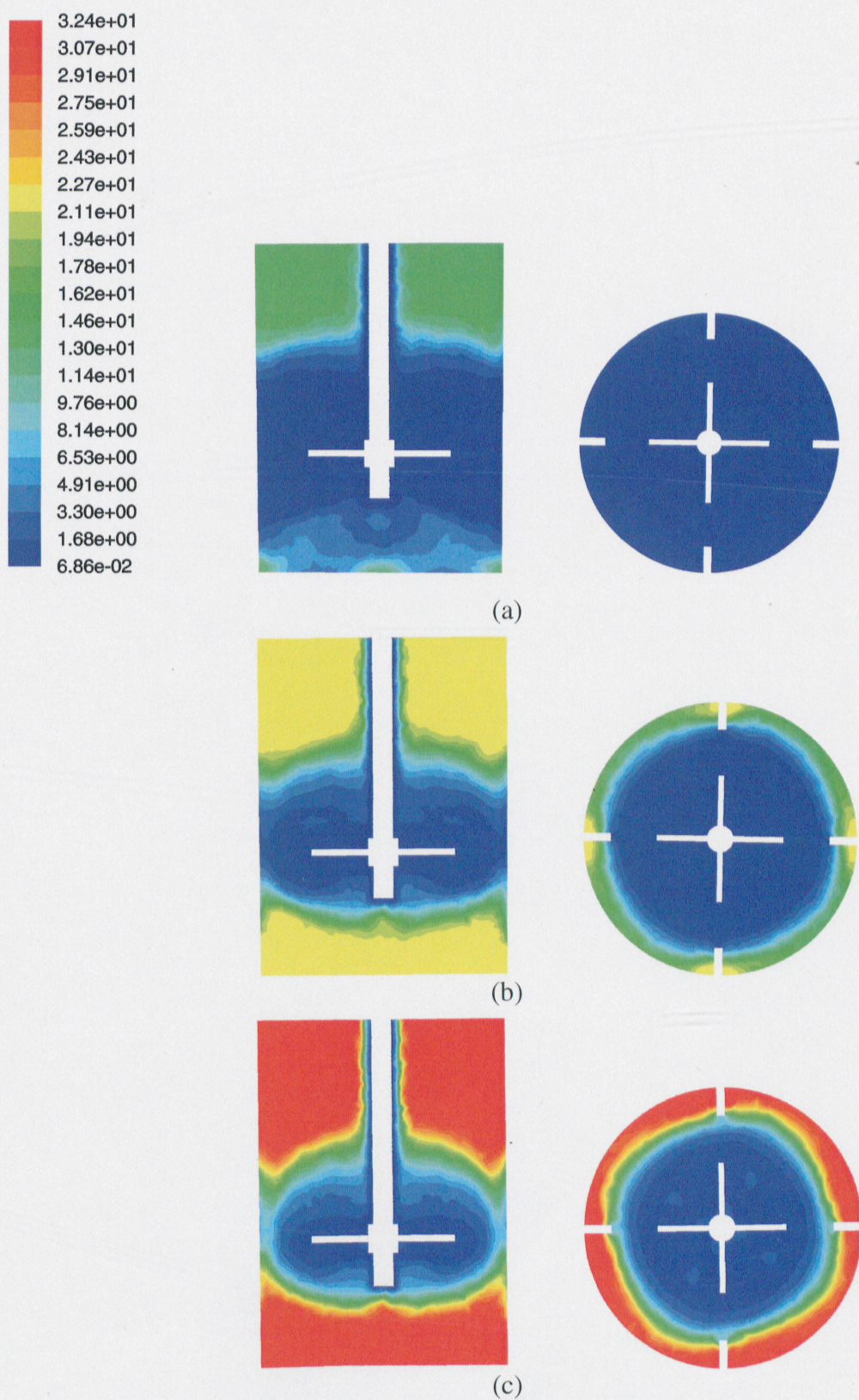


Figure (6.11) Effect of Xanthan Gum Concentration on Apparent Viscosity (Pa.s), 100 rpm, (a) 0.5%, (b) 1.0%, (c) 1.5% Xanthan Gum Solution

6.2.3 Flow & Circulation Numbers Estimation

Flow number measures impeller ability to generate convective flow. The higher the flow number, the higher the convective flow generated by the impeller.

Flow number (sometimes called primary flow number) can be estimated from the following relationship using impeller pumping flowrate, Q_P :

$$Fl = \frac{Q_P}{ND^3} \quad (6-7)$$

where N is impeller speed and D is impeller diameter.

Impeller pumping flowrate can be estimated by integrating velocity profiles in planes surrounding impeller swept volume. Experimentally, obtaining velocity profiles was beyond the scope of this research. Instead, CFD velocity profiles were used to estimate flow numbers.

Pumping flowrate that encompasses impeller swept volume can be estimated mathematically as follows (Tatterson, 1991, Jaworski et al., 1996, Mishra et al., 1998):

$$Q_P = 2\pi \int_0^{D/2} (rU_{axial})|_{z_1} dr + \pi D \int_{z_1}^{z_2} U_{radial}|_{D/2} dz \quad (6-8)$$

where r is radial coordinates, U_{axial} and U_{radial} is axial and radial velocities, respectively, D is impeller diameter, and z_1 & z_2 are boundaries of impeller swept volume in axial direction. Two planes define the location of the impeller swept volume in axial direction, one below the impeller (z_1) and one above the impeller (z_2). These planes have been defined to be touching impeller blades (Armenante and Chou, 1996, Mavros et al., 1996 & 1997, Mishra et al., 1998). Since axial velocity dominates, the second term in Equation

(6-8) is negligible (Ranade et al., 1992, Ranade, 1997, Patwardhan and Joshi, 1999, Kumaresan and Joshi, 2006).

The motion of an impeller induces a pumping effect as the liquid is drawn towards the agitator and then pumped away from it. The outgoing flow may have an axial or radial direction depending upon the impeller. The high velocity outgoing flow entrains the neighboring fluid into motion, thus the overall circulating fluid combines both the pumped out and the entrained fluid. Accordingly, another flow number called circulation number or secondary flow number (Fl_c), can be defined so as to include flow entrained by impeller discharge stream (Ranade and Dommeti, 1996, Aubin et al., 2001, Kumaresan, 2005).

$$Fl_c = \frac{Q_c}{ND^3} \quad (6-9)$$

where Q_c is overall liquid circulation generated in impeller swept volume and including flow entrained by impeller discharge. Mathematically, Q_c can be estimated as follows:

$$Q_c = 2\pi \int_0^{r|_{U_{axial\ turn}}} (rU_{axial})|_{z_1} dr \quad (6-10)$$

where $r|_{U_{axial\ turn}}$ is the radius where axial flow velocity reversal (from downward to upward in downward pumping impellers) occurs (Jaworski et al., 1996, Mishra et al., 1998).

Axial velocity profiles calculated at a plane exactly below impeller blades ($z_1=13.5$ cm) were integrated to calculate flow number. For circulation numbers the whole velocity profile was integrated to include pumping and circulation. The results are shown for A200 impeller in Figure (6.12) for different concentrations of xanthan gum solution. Both flow and circulation numbers exhibit a decrease when xanthan gum concentration

increased, indicating that an increase in xanthan gum concentration not only causes a loss in pumping capacity, but also reduces circulation number. Both flow and circulation numbers become independent of xanthan gum concentration and impeller speed at high impeller speed.

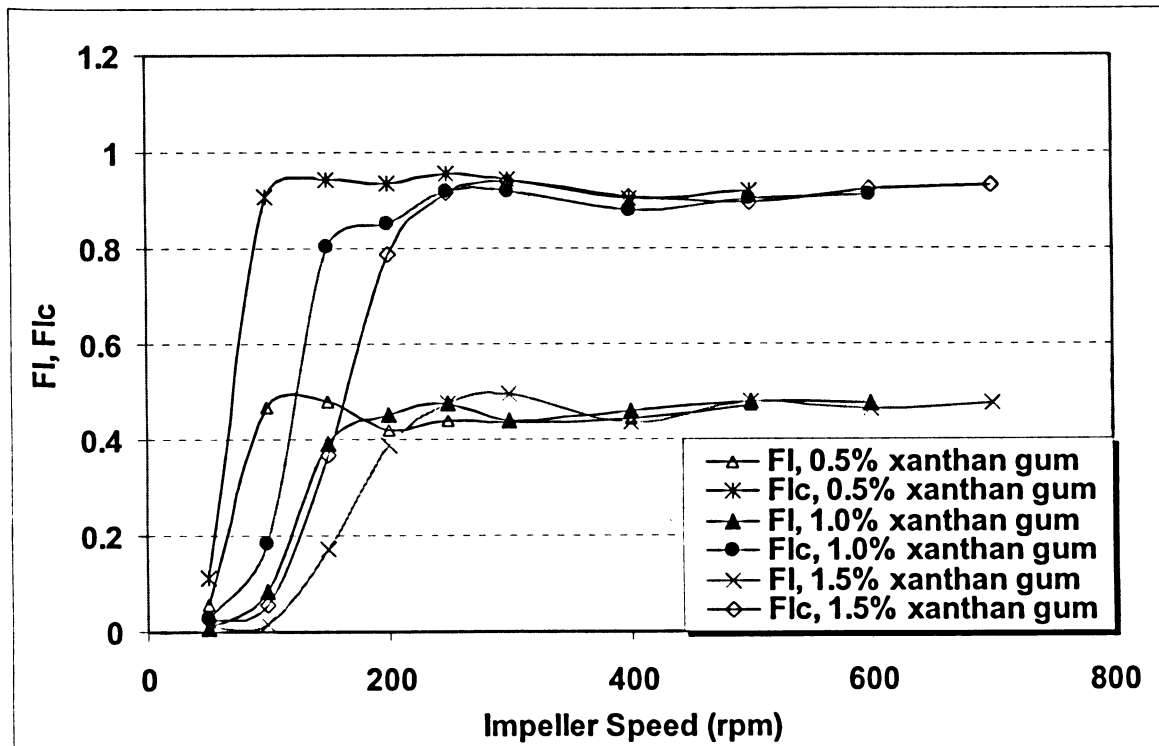


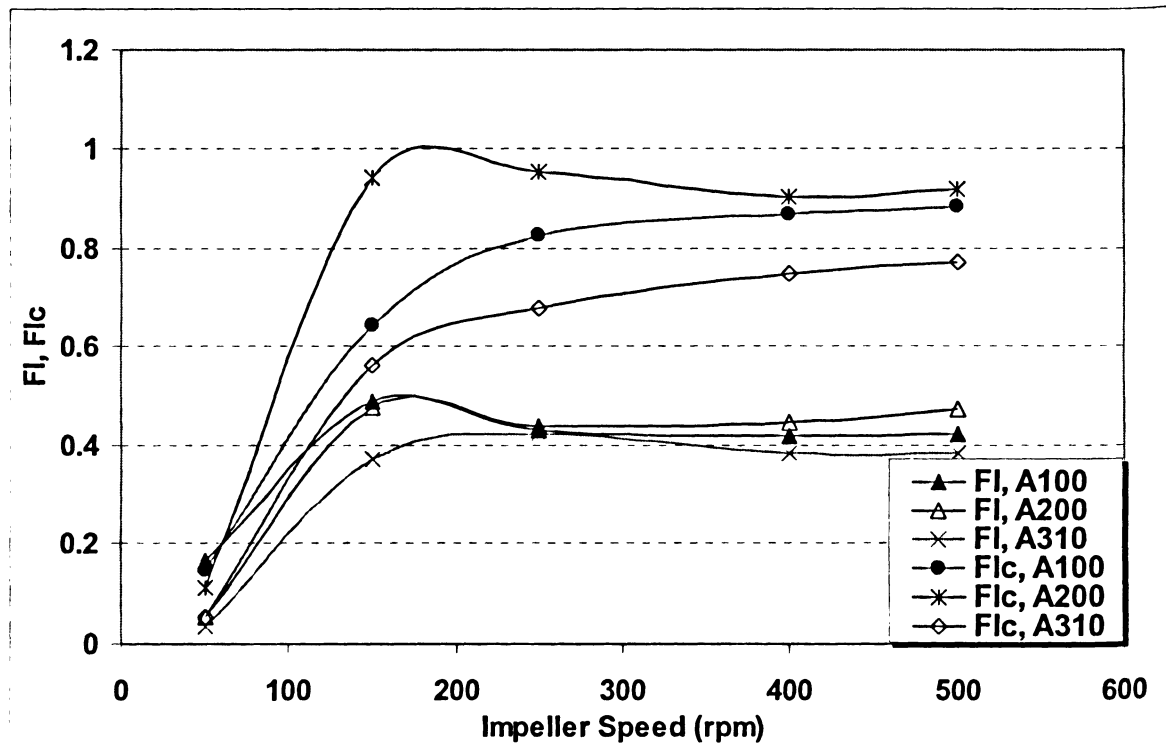
Figure (6.12) Flow Number & Circulation Number – A200 Impeller

Figure (6.13) shows the effect of impeller type on flow and circulation numbers. While A310 has the highest flow and circulation number, flow and circulation numbers for A200 were very close to those of A100.

Table (6.3) summarizes flow and circulation numbers obtained from CFD for all impellers at turbulent flow condition.

Table (6.3) Impellers Turbulent Flow and Circulation Numbers – CFD Simulations

	A100	A200	A310
Turbulent Flow Number	0.42	0.47	0.37
Turbulent Circulation Number	0.89	0.92	0.77

Figure (6.13) Flow Number & Circulation Number for Different Impellers
0.5% Xanthan Gum Solution

For an A100 impeller, the following flow number is given: 0.73 (Mishra et al., 1998), 0.56 (Nienow, 1990), 0.79 (Ranade et al., 1992), 0.72 (Sahu et al., 1999).

For an A200 impeller, the following flow number is given: 0.75-0.79 (Oldshue, 1983), 0.85 (Ranade & Joshi, 1989), 0.79 (Nienow, 1990), 0.94 (Ranade et al., 1992), 0.753 (Kresta & Wood, 1993), 0.85 (Ranade and Dommeti, 1996), 0.71 (Jaworski et al., 1996), 0.91 (Mishra et al., 1998), 0.98 (Sahu et al., 1999), 0.98 (Patwardhan and Joshi, 1999), 0.75 (Aubin et al., 2001), 0.76 (Wu et al., 2001), 0.83 (Kukukova et al., 2005), 0.88 (Kumaresan & Joshi, 2006).

For an A310 impeller, the following flow number is given: 0.41 for A310 (Mavros et al., 1996), 0.49 (Patwardhan and Joshi, 1999), 0.56 (Wu and Pullum, 2000), 0.56 (Wu et al., 2001), 0.31-0.35 (Kumaresan et al., 2005), 0.58-0.70 (Kumaresan & Joshi, 2006), 0.57 (Wu et al., 2006 A).

For an A320 impeller, flow number was reported to be 0.64 (Weetman and Coyle, 1989).

Flow numbers obtained for all impellers are smaller than most of the values reported in the literature. Most of the studies conducted on flow number employed Newtonian fluids such as water. However, it is believed that fluid viscosity affects flow number measurements. Mavros et al. (1996) observed that flow number for A310 and Mixel TT decreased by almost 50% when water was replaced with 1% carboxymethylcellulose. Koutsakos et al. (1999) reported the flow number for Rushton turbine impeller decreased from 0.455 to 0.072 when water was replaced with 0.28% carboxymethylcellulose solution.

6.3 Dynamic Model Parameters

In order to improve the performance of continuous-flow mixers the effect of various operating parameters was explored. Operation conditions examined included impeller speed and type, xanthan gum solution flowrate and concentration, and vessel configuration. Table (6.4) summarizes these experimental conditions.

To describe the performance of the continuous-flow mixer, two parameters will be examined here, namely, f , the degree of channeling in the vessel, and $V_{\text{fully mixed}}/V$, ratio of fully mixed volume in the vessel to the total volume of the vessel.

Table (6.4) Range of Operation Conditions used in Experimental Work

Variable	Range
Impeller velocity	50-700 rpm
Xanthan gum mass concentration	0.5-1.5%
Xanthan gum flowrate	227-896 L/hr
Impeller type	A200 (main impeller), A100, A310 and A320
output location	bottom and side

The reproducibility of the system was examined by repeating a set of 4 experiments 4 times each. The data were then analyzed to estimate f and $V_{\text{fully mixed}}/V$. Standard deviation was used to plot the error bar graph in Figure (6.14) based on the averaged values of f and $V_{\text{fully mixed}}/V$. The maximum standard deviation observed was 0.0115, indicating excellent reproducibility of the measurements.

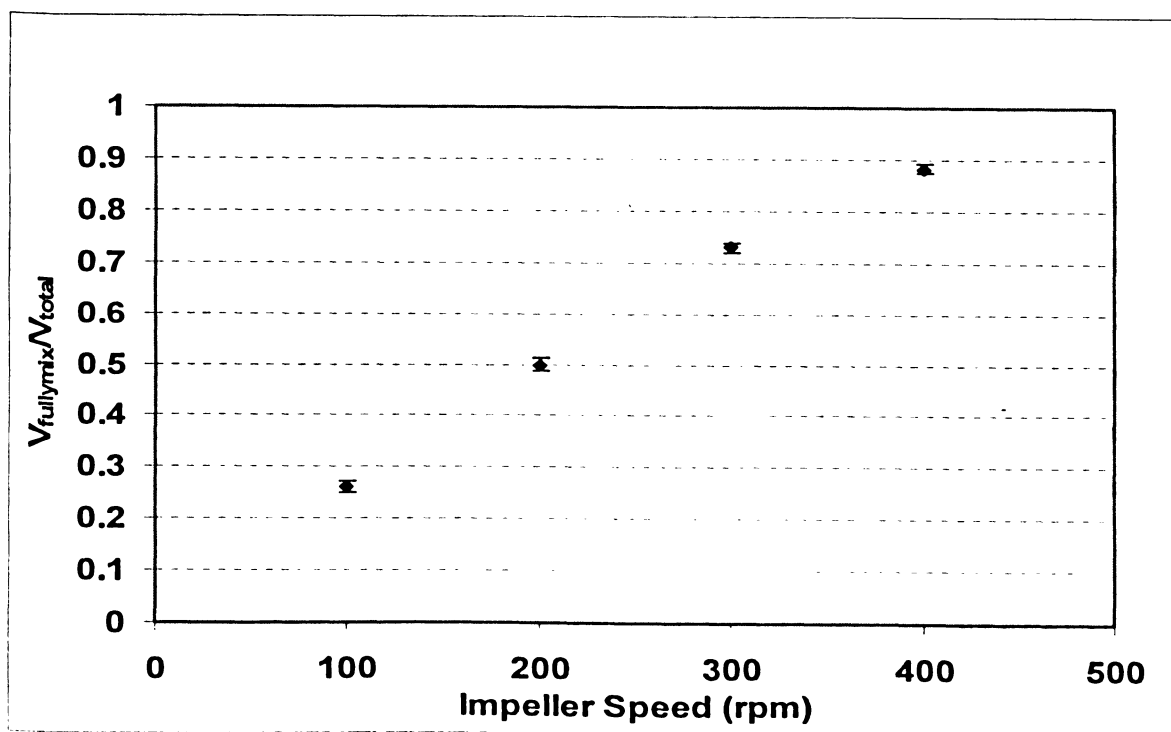
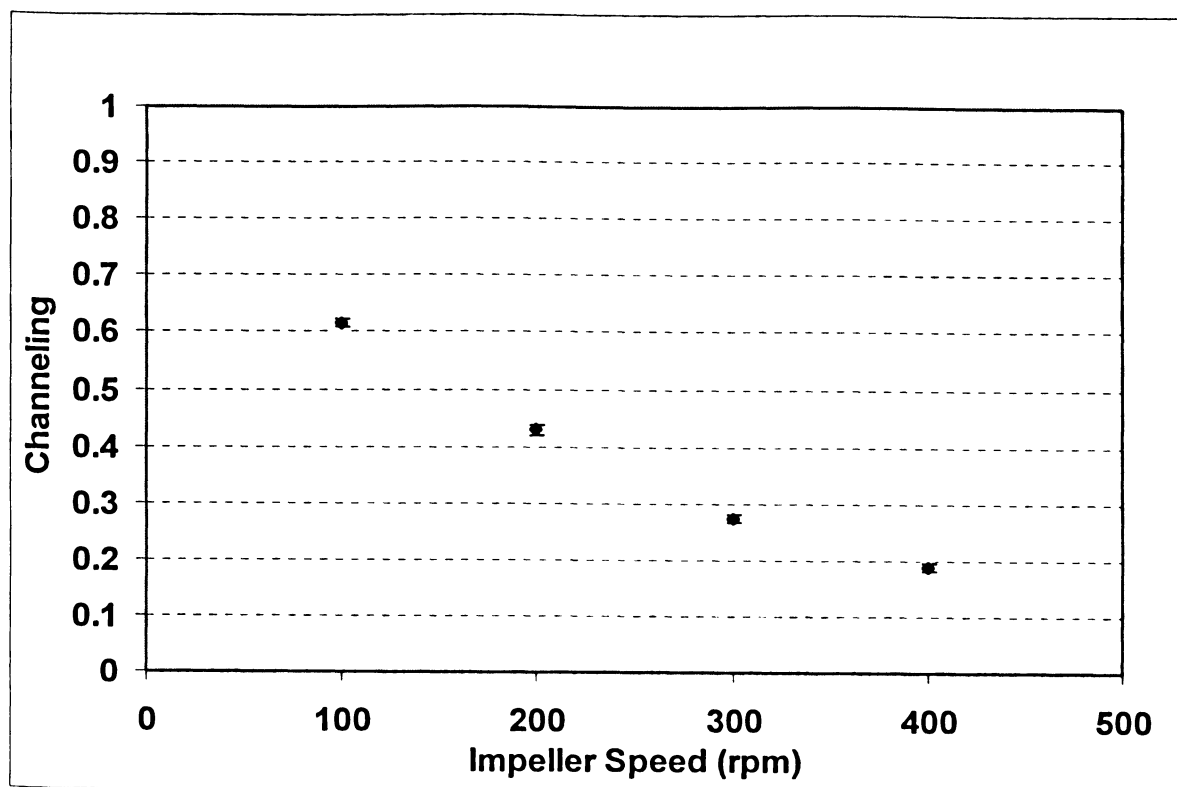


Figure (6.14) System Reproducibility Examined using Channeling and $V/V_{fully\ mixed}$ Ratio

6.3.1 Dynamic Model Parameters Obtained from Experimental Data

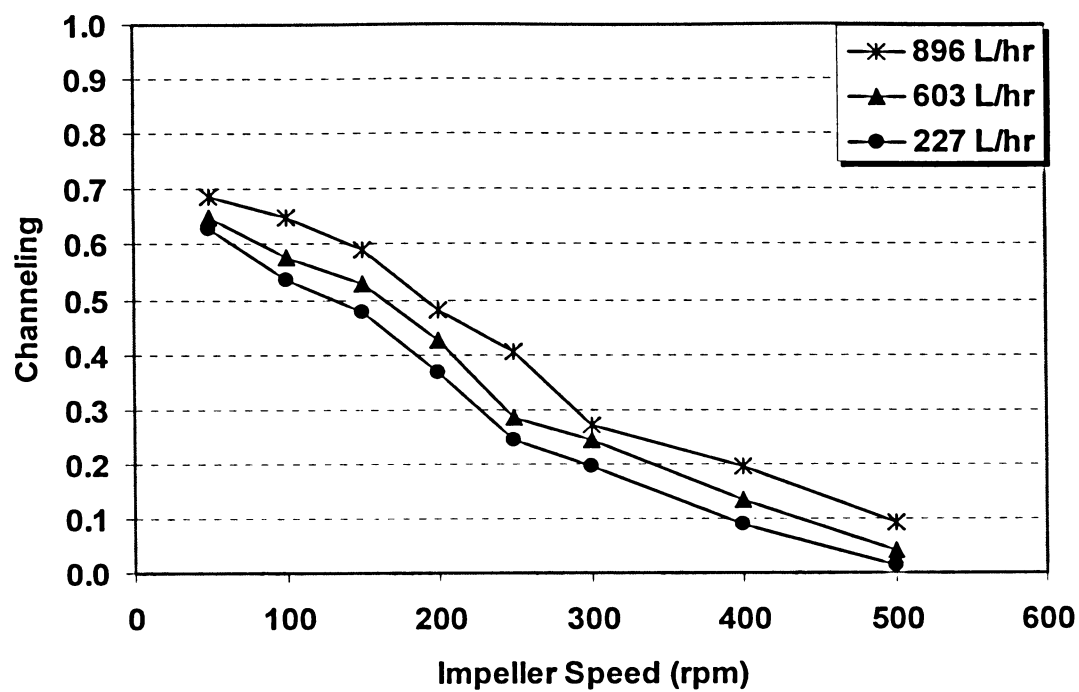
Channeling and fully mixed volume in the mixing vessel was obtained from experimental data by minimizing cost function associated with the system transfer function using a MATLAB code developed by Kammer et al. (2005) based on Sequential Quadratic Programming (SQP) method. Values of channeling and fully mixed volume obtained from experimental data are documented in Appendix A.

6.3.1.1 Effect of Impeller Speed and Xanthan Gum Flowrate

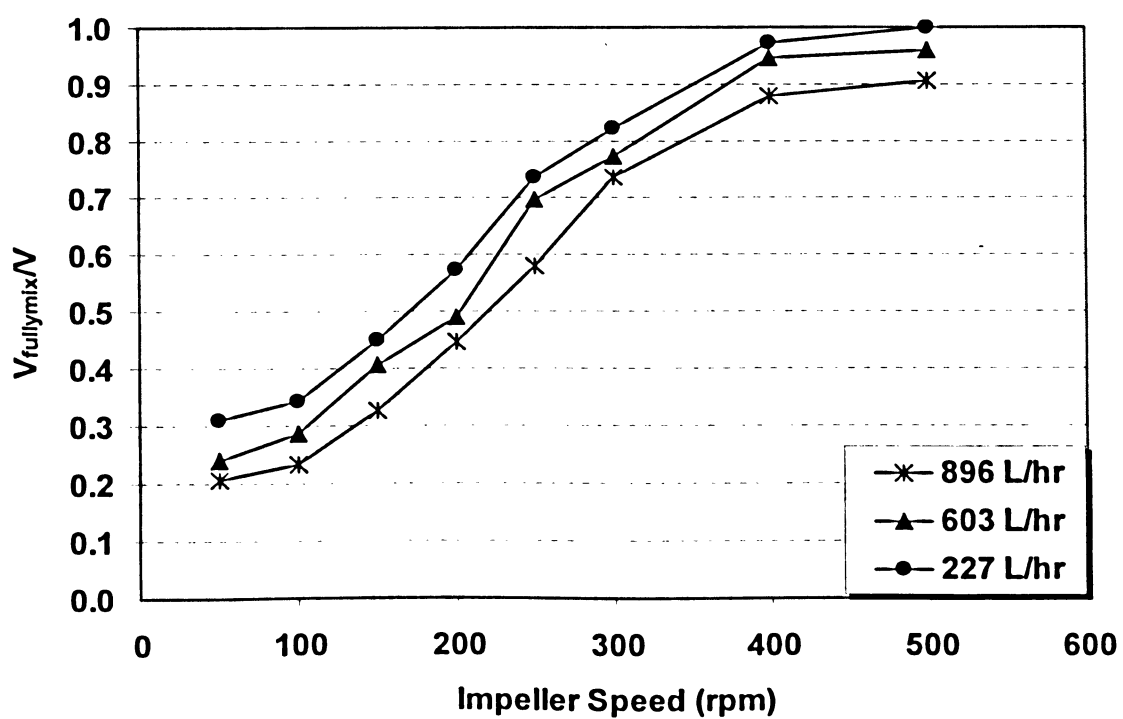
For A200, data for channeling and ratio $V_{\text{fully mixed}}/V$ for different impeller speeds and different xanthan gum flowrate are presented in Figure (6.15). Channeling decreased and ratio $V_{\text{fully mixed}}/V$ increased as impeller speed increased. The high impeller speed disturbs the fluid in the vessel, resulting in reducing dead zones and channeling. Higher feed flowrate in the mixing vessel produces higher channeling and lower $V_{\text{fully mixed}}/V$ ratio. Increasing the flowrate reduces mean residence time in the vessel, forcing the material to leave the vessel faster without going into the well-mixed region close to the impeller.

The same observations have been reported by Mavros et al. (2002 A & B), Ein-Mozaffari (2002), Khopkar et al. (2004) and Samaras et al. (2006 A). Ein-Mozaffari et al. (2004) found that the ratio of flow induced by the impeller to the flow through the mixing tank affects the extent of channeling. This was attributed to competition between the pumping action of the impeller (which entrains the fluid in the mixing flow) and the discharge flow (which removes fluid from the vessel).

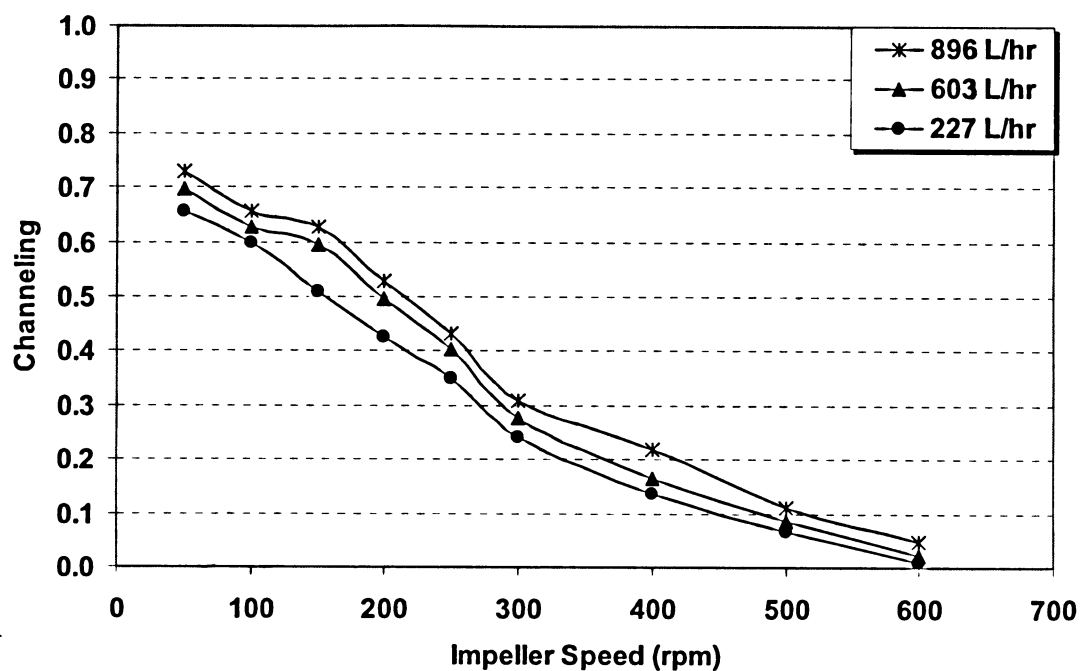
Experimental Data - 0.5% Xanthan Gum



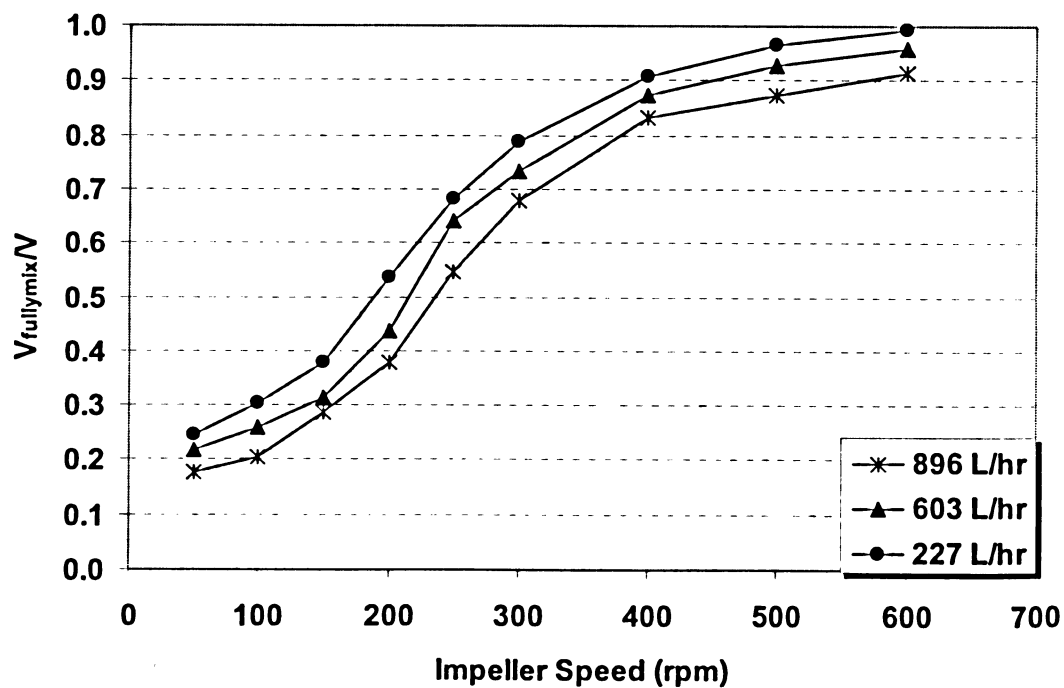
Experimental Data - 0.5% Xanthan Gum



Experimental Data - 1.0% Xanthan Gum



Experimental Data - 1.0 % Xanthan Gum



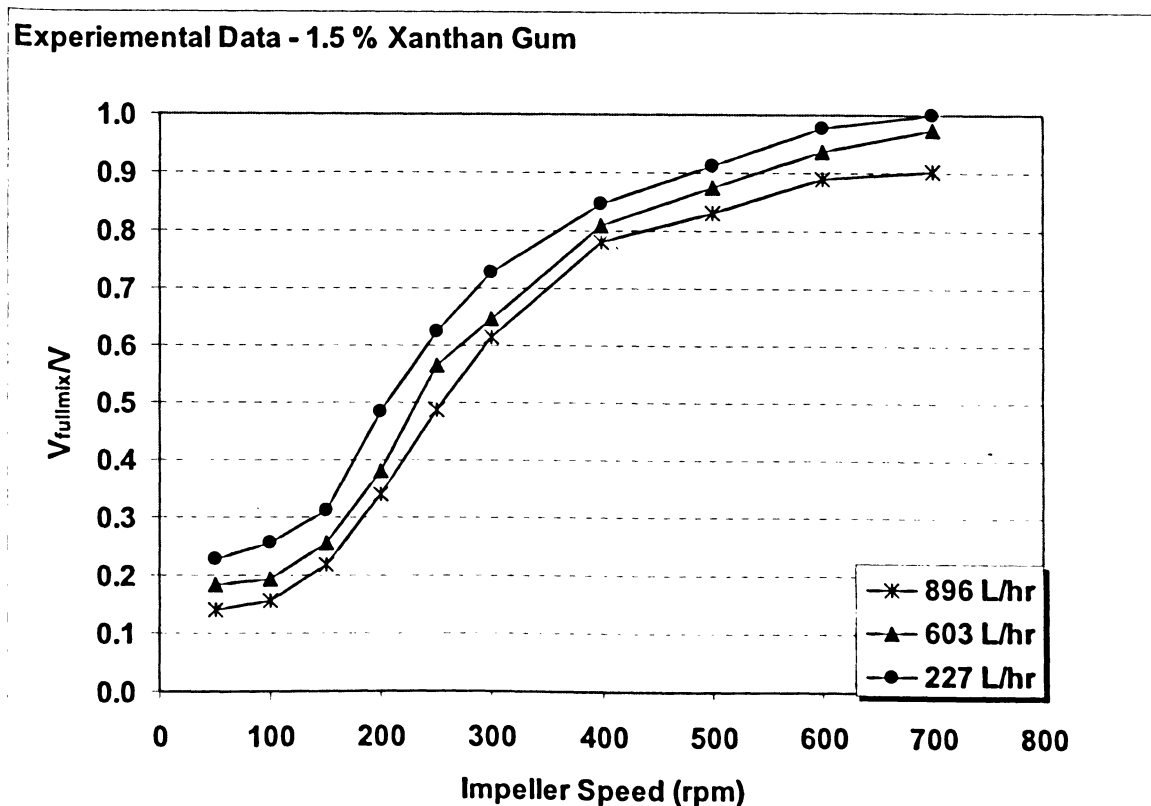
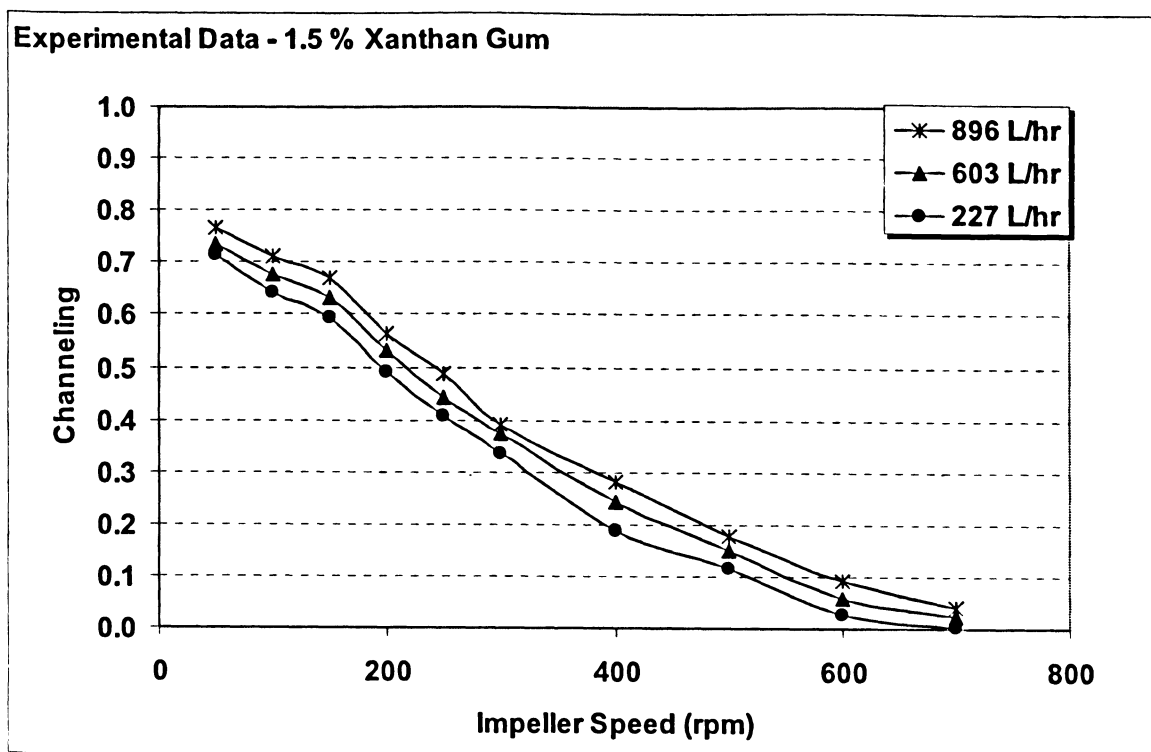
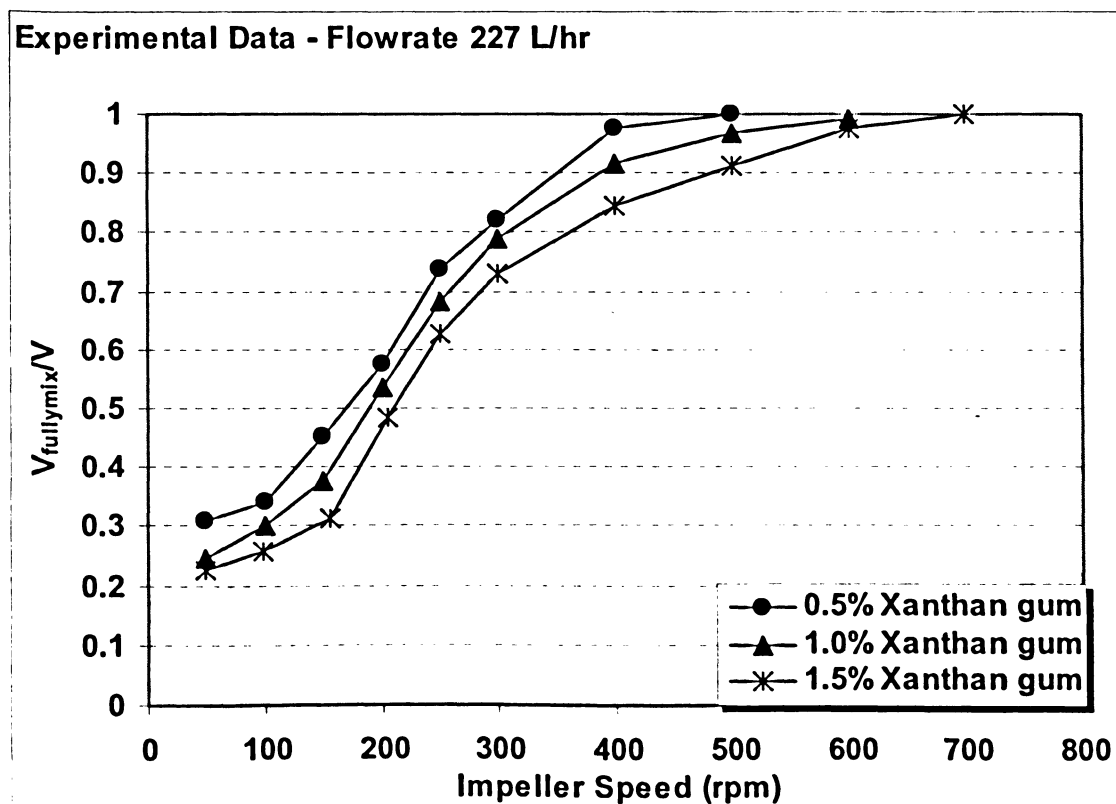
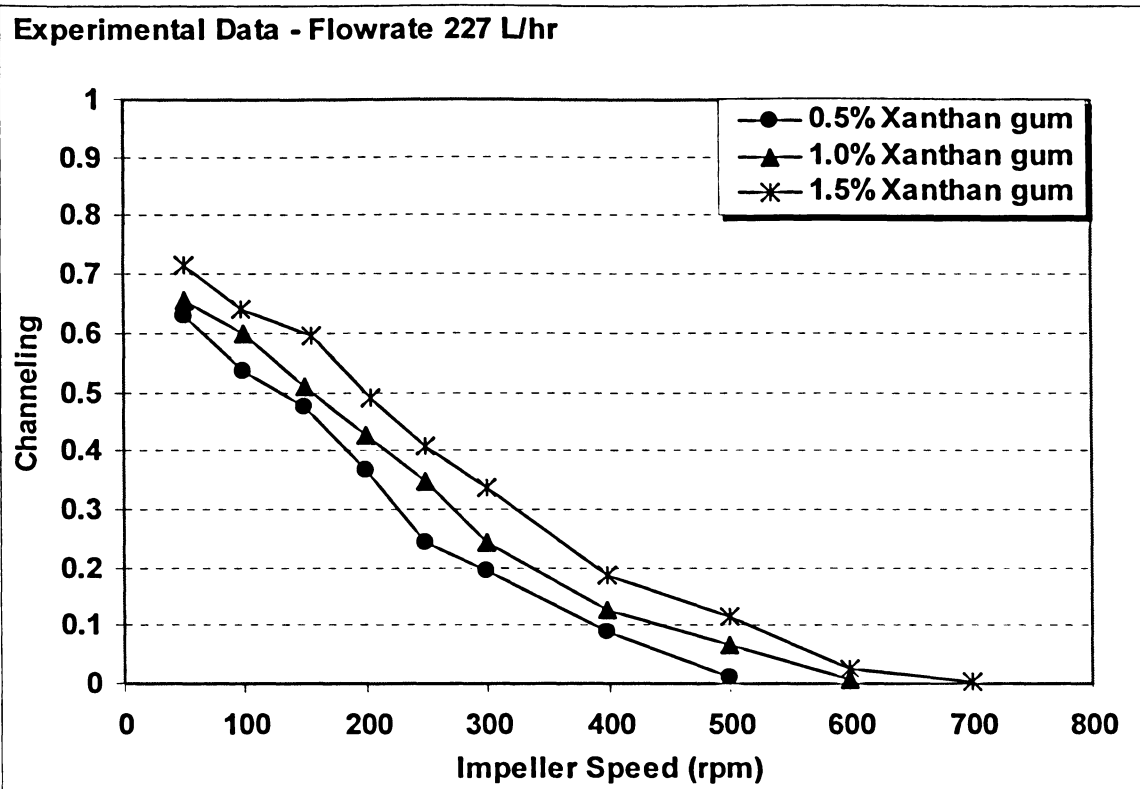


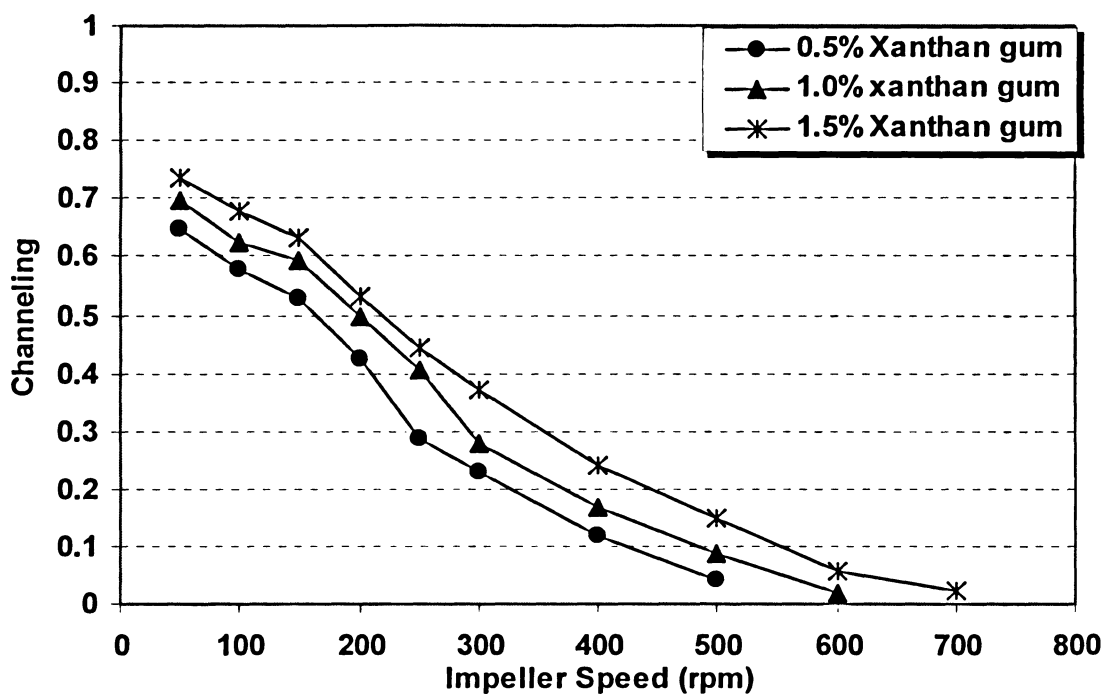
Figure (6.15) Effect of Impeller Speed & Input Flowrate on f and $V_{fully\ mixed}/V$
A200 Impeller

6.3.1.2 Effect of Xanthan Gum Concentration

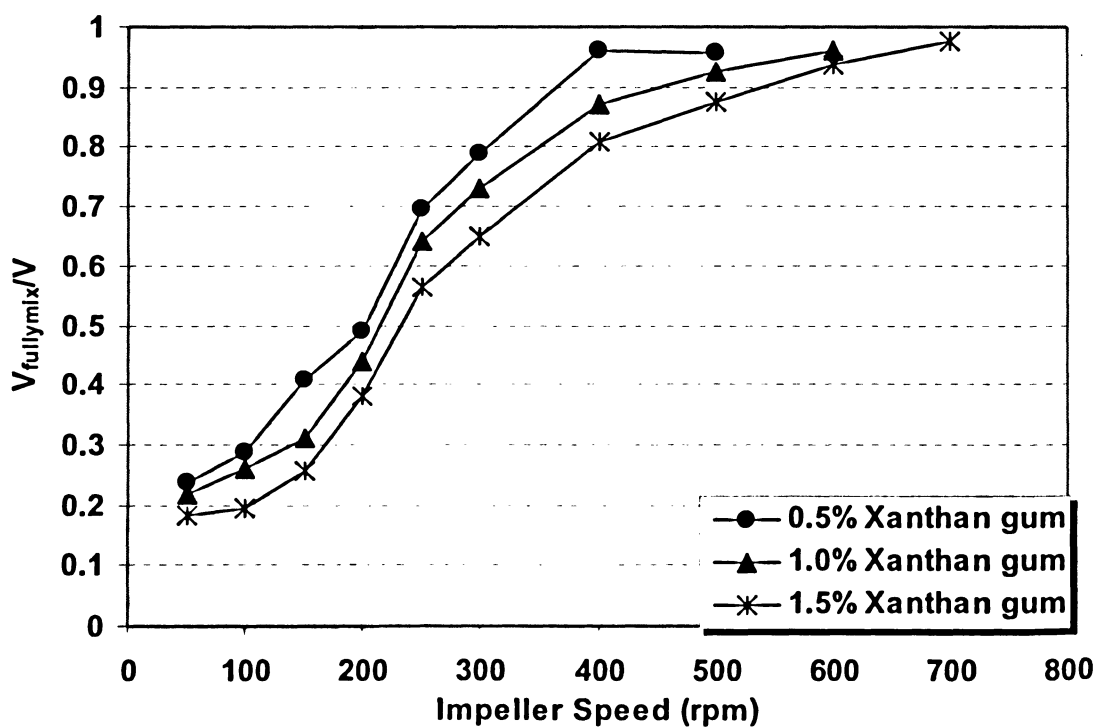
The extent of channeling increases and the fraction of fully mixed volume decreases as suspension concentration increases at a fixed impeller speed. Figure (6.16) shows channeling and $V_{\text{fullymixed}}/V$ ratio for A200 at three different xanthan gum concentrations. In order to avoid channeling and stagnant regions within the vessel, the minimum impeller speed must be 500 rpm at 0.5% xanthan gum solution, 600 rpm at 1.0% xanthan gum solution, and 700 rpm at 1.5% xanthan gum solution. The rheology of the fluid significantly affects the dynamic performance of the continuous mixing process. Energy delivered by the impeller will be dissipated in the concentrated xanthan gum solution without producing enough mixing in the vessel, leading to high channeling and dead zones. The same observations have been reported by Ein-Mozaffari (2002).



Experimental Data - Flowrate 603 L/hr



Experimental Data - Flowrate 603 L/hr



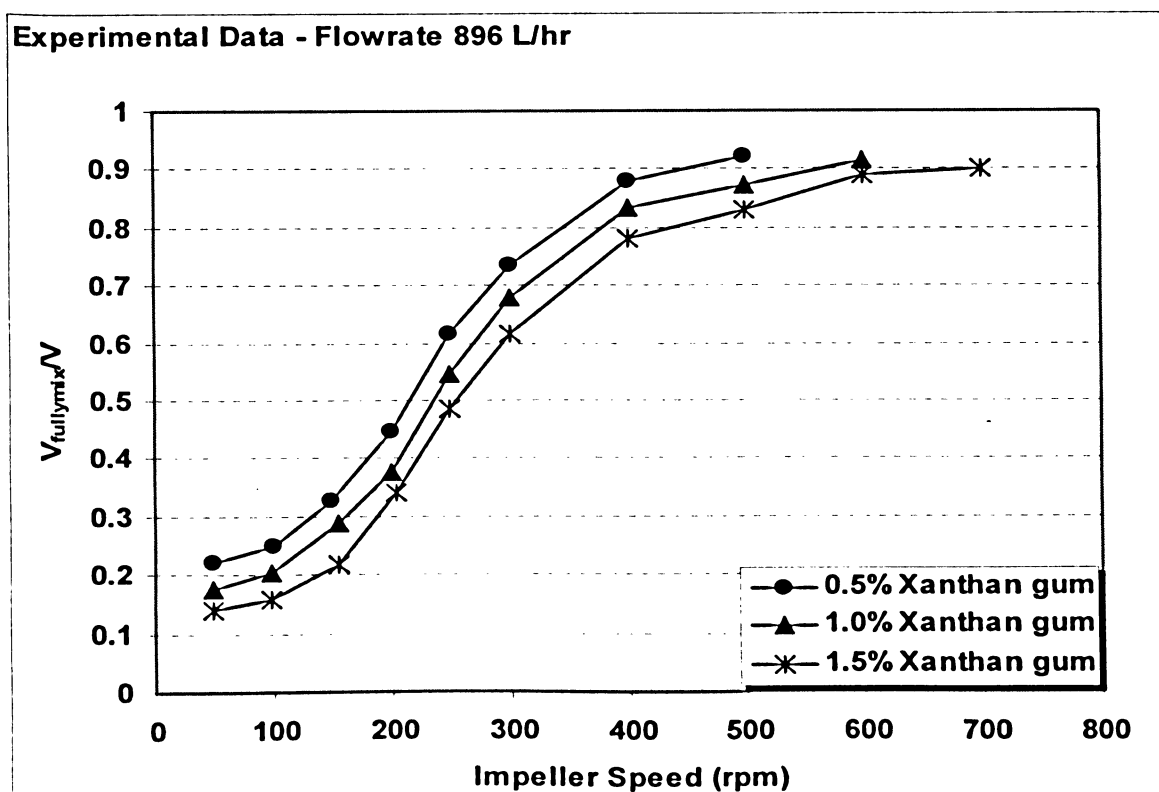
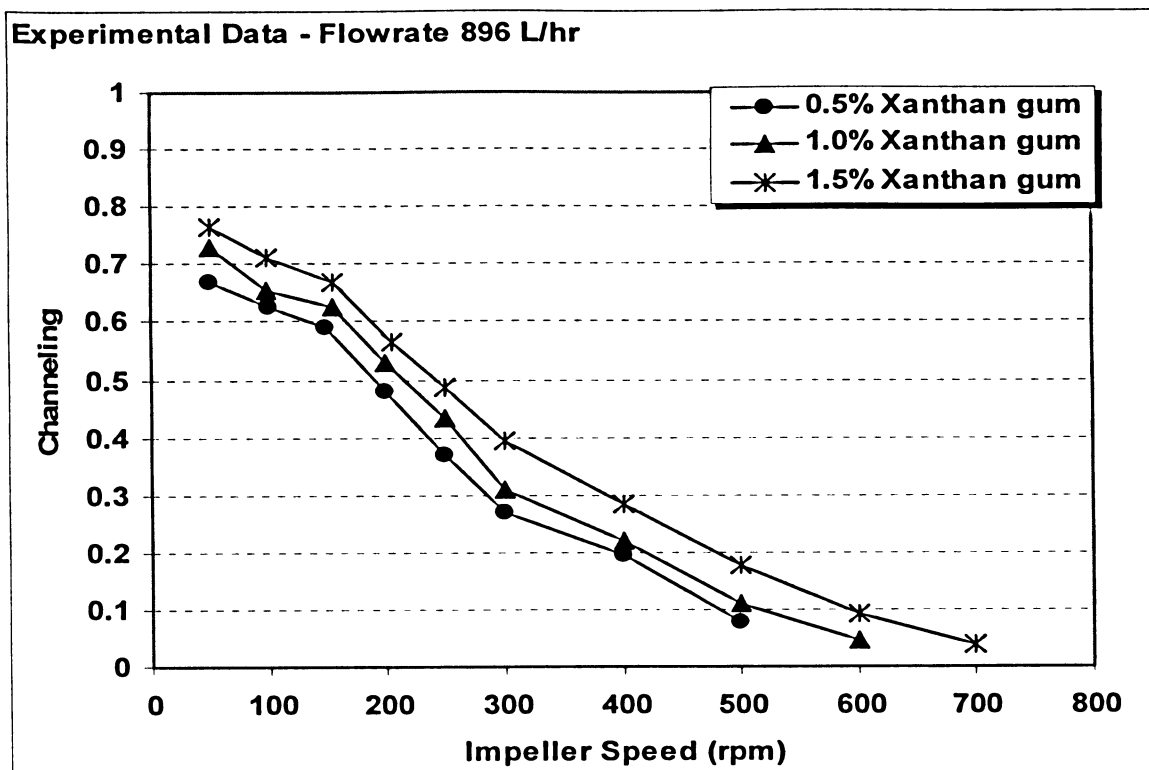


Figure (6.16) Effect of Xanthan Gum Concentration on f and $V_{full\ mixed}/V$
A200 Impeller

6.3.1.3 Effect of Output Location

Ein-Mozaffari et al. (2005) found that the input/output location has a significant effect on flow non-ideality in continuous mixing processes. Hence, we investigated the effect of output location on the extent of non-ideal flow for two configurations Figure (3.6). From Figure (6.17) it can be seen that for identical operating conditions, while Configuration 1 gave superior mixing response, Configuration 2 was more prone to a high degree of channeling and stagnant zones. Configuration 2 (where the exit location is on the side of the vessel) enables a large percentage of feed to be conveyed directly to the exit location without being drawn into the mixing zone. In Configuration 1, however, the feed is forced to flow through the mixing zone before leaving the chest.

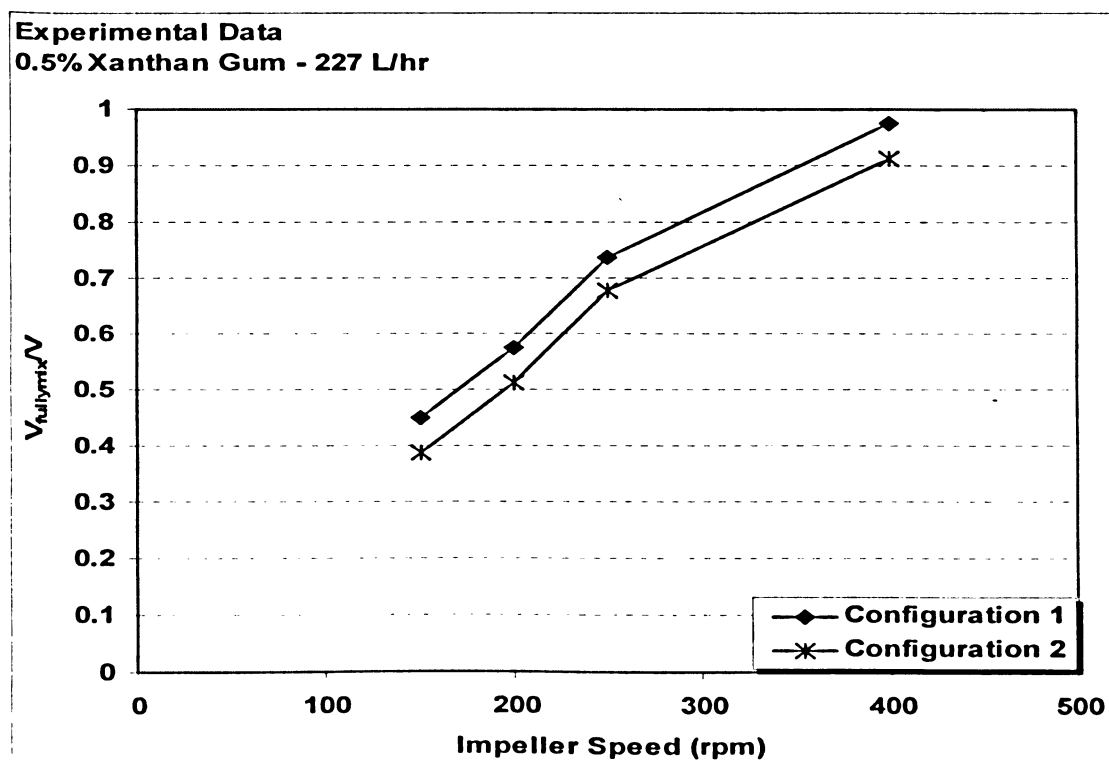
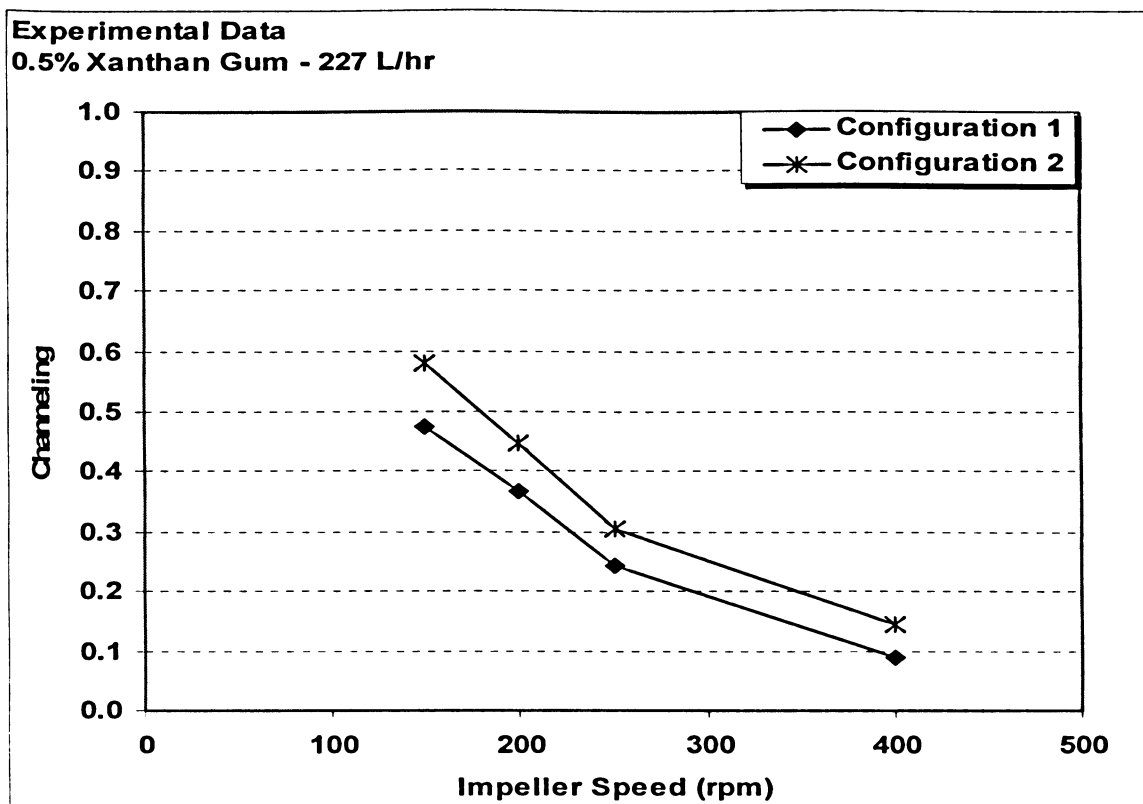


Figure (6.17) Effect of Output Location on f and $V_{full\ mixed}/V$
0.5% xanthan gum, 227 L/hr, A200 Impeller

6.3.1.4 Effect of Impeller Type

Impellers share characteristics attributed to pumps, such as the ability to produce flow and velocity head (or shear). Determining the most effective impeller for a specific mixing application should be based on the understanding of process requirements (AIChE, 2001). Figure (6.18) demonstrates the crucial role impellers play in determining channeling and $V_{\text{fully mixed}}/V$ ratio. In summary, A100 impeller was the least effective, while A320 impeller was the most effective.

Many attempts have been made to define impeller efficiency. The following two efficiencies are usually encountered when distinguishing between impellers:

- Pumping efficiency

Pumping efficiency takes into consideration the impeller's ability to pump fluid in the mixing vessel. The following definitions have been frequently used in the literature to define pumping efficiency at constant D/T (impeller diameter/vessel diameter) ratio.

1. $E_1 = Fl^3 / Po_t$ (Medek and Fort, 1985).
2. $\eta_p = Fl / Po_t$ average pumping rate per unit power consumption (Mishra et al., 1998, Aubin et al., 2001, Wu et al., 2001, Wu et al., 2006 A).

- Circulation efficiency

Circulation efficiency takes into consideration the impeller's ability to circulate the fluid in the mixing vessel. The following definitions have been frequently used in the literature to define circulation efficiency at constant D/T (impeller diameter/vessel diameter) ratio.

1. $E_2 = Fl_c^3 / Po_t$ (Medek and Fort, 1985).
2. $\eta_c = Fl_c / Po_t$ average circulation rate per unit power consumption (Jawoski et al. 1996, Mishra et al., 1998, Aubin et al., 2001, Wu et al., 2001, Wu et al., 2006 A).

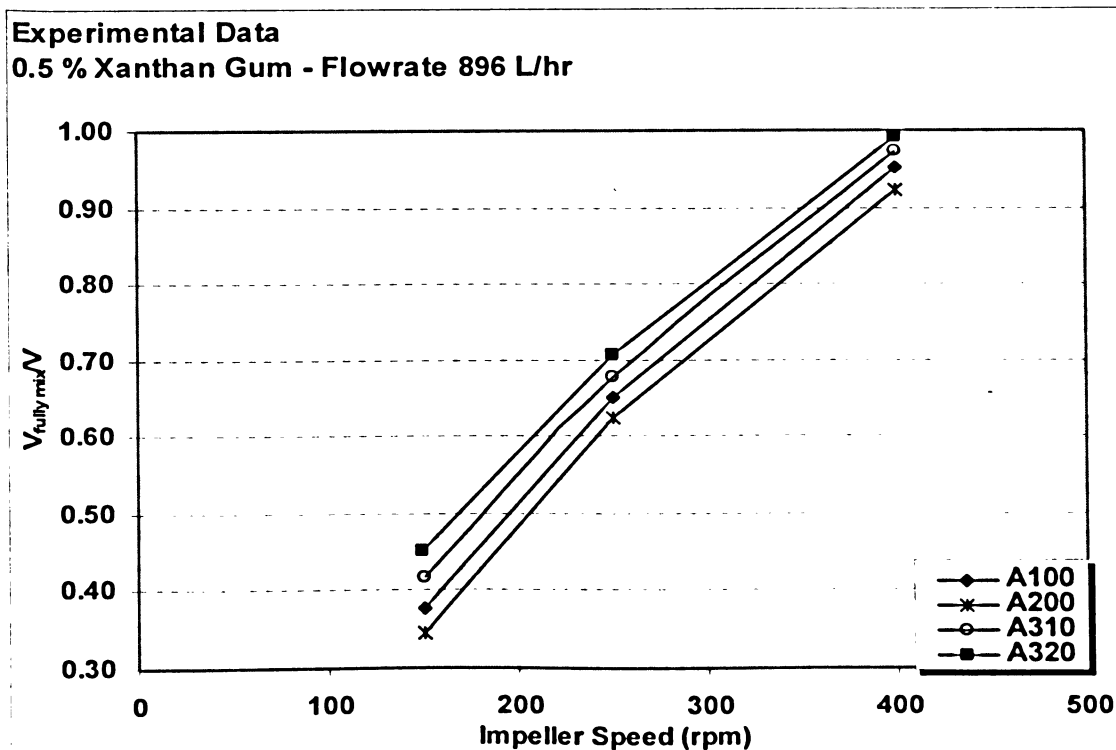
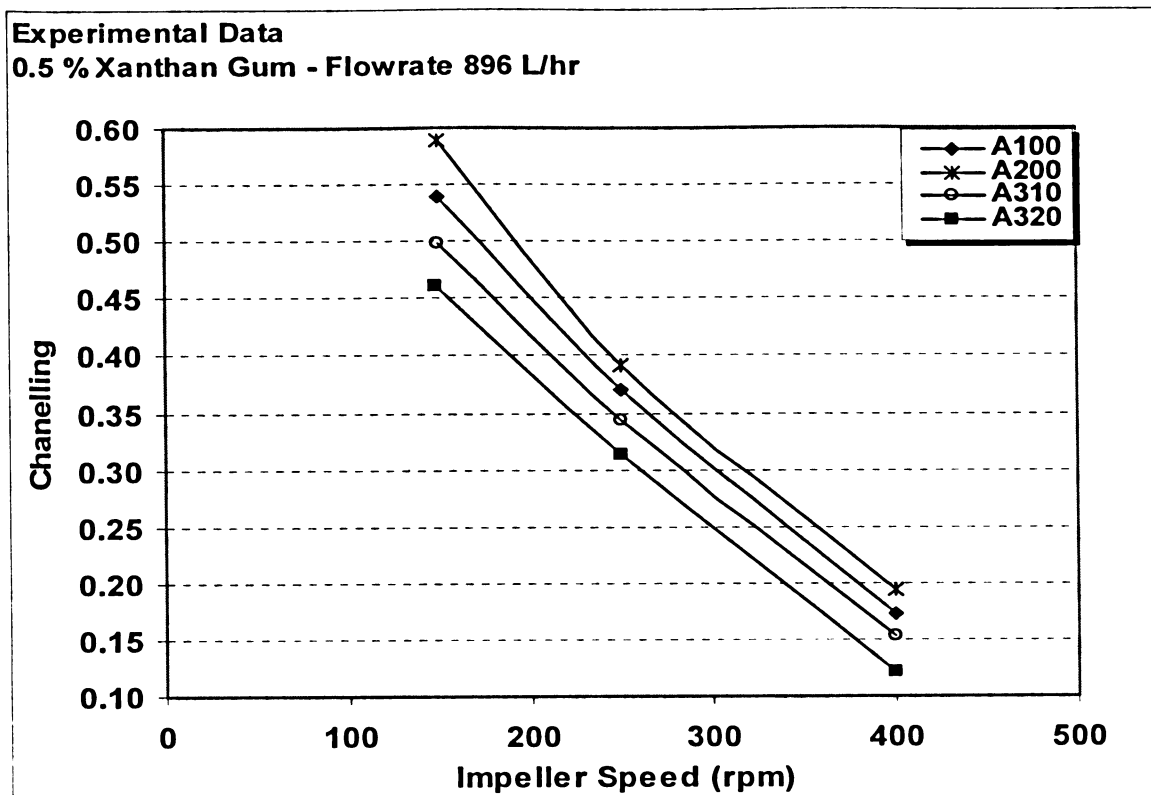


Figure (6.18) Effect of Impeller Type on f and $V_{\text{fully mixed}}/V$
0.5% xanthan gum, 896 L/hr

Impellers turbulent power number (Table (6.1)) was used along with the flow and circulation (Table (6.3)) to compare the performance of A100, A200, and A310. In order to accomplish impeller evaluation and because A320 geometry was not available in the Fluent 6.3 impeller library, flow number for A320 was selected to be 0.64 (Weetman and Coyle, 1989). For A320 impeller, no published value for circulation number could be located in the literature.

Data obtained from calculating pumping and circulation efficiencies are tabulated in Table (6.5). The data clearly show that A200 provides the lowest pumping and circulation efficiency, and A320 provides the best pumping efficiency. Circulation efficiency also shows the same trend. A100 was reported to be superior to A200 by many investigators (Elson, 1990 B, Ranade et al., 1992), while A310 was found to be better than A200 (Lighnin Mixing Equipment Co., 1981, Weetman and Oldshue, 1988, Kubera and Oldshue, 1992, Zhou and Kresta, 1996, Wu and Pullum, 2000) and better than A100 (Lighnin Mixing Equipment Co., 1985). A320 was found to provide better mixing performance when compared against A200 (Weetman and Coyle, 1989, Oldshue et al., 1989).

The comparison presented above coupled with the calculations presented in Table (6.5) support the idea that A320 is superior to all other impellers. A320, also called fluidfoil, has been developed to operate in the viscous flow regime, and to continually operate as an axial flow impeller into the transition region (Weetman and Coyle, 1989).

Table (6.5) Impeller Pumping and Circulation Efficiencies

		A100	A200	A310	A320
Pumping Efficiency	$E_1 = Fl^3 / Po_t$	0.112	0.090	0.127	0.436
	$\eta_p = Fl / Po_t$	0.636	0.405	0.925	1.032
Circulation Efficiency	$E_2 = Flc^3 / Po_t$	1.068	0.671	1.268	-
	$\eta_c = Flc / Po_t$	1.348	0.793	2.139	-

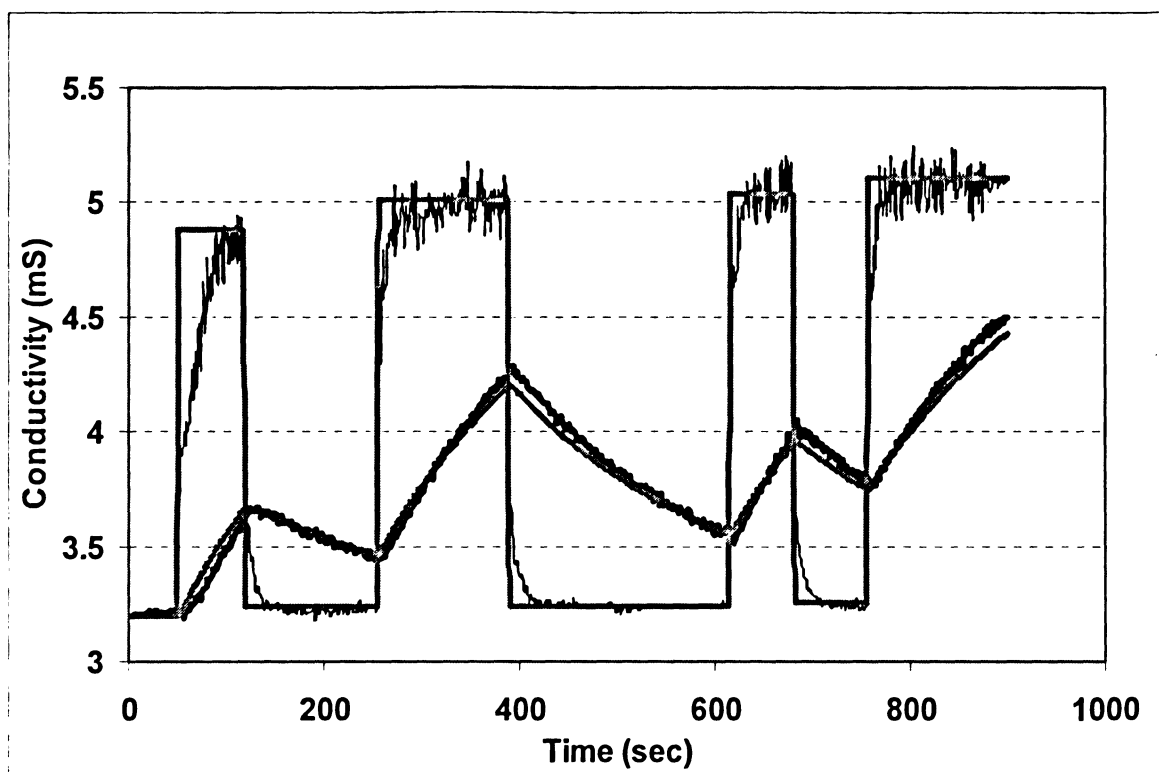
6.3.2 Dynamic Model Parameters Obtained from CFD

Once the flow fields were generated using Mixsim 2.1, a User-Defined Function (UDF) was linked to Fluent 6.3 solver to define the time at which the tracer was continuously injected in the mixing vessel. UDF was linked to the inlet as a boundary condition and outlet concentration was monitored with time. Channeling and fully mixed volume in the mixing vessel were obtained from CFD input-output conductivity data in a manner similar to that used in the experimental section. Values of channeling and fully mixed volume obtained from experimental data are documented in Appendix A.

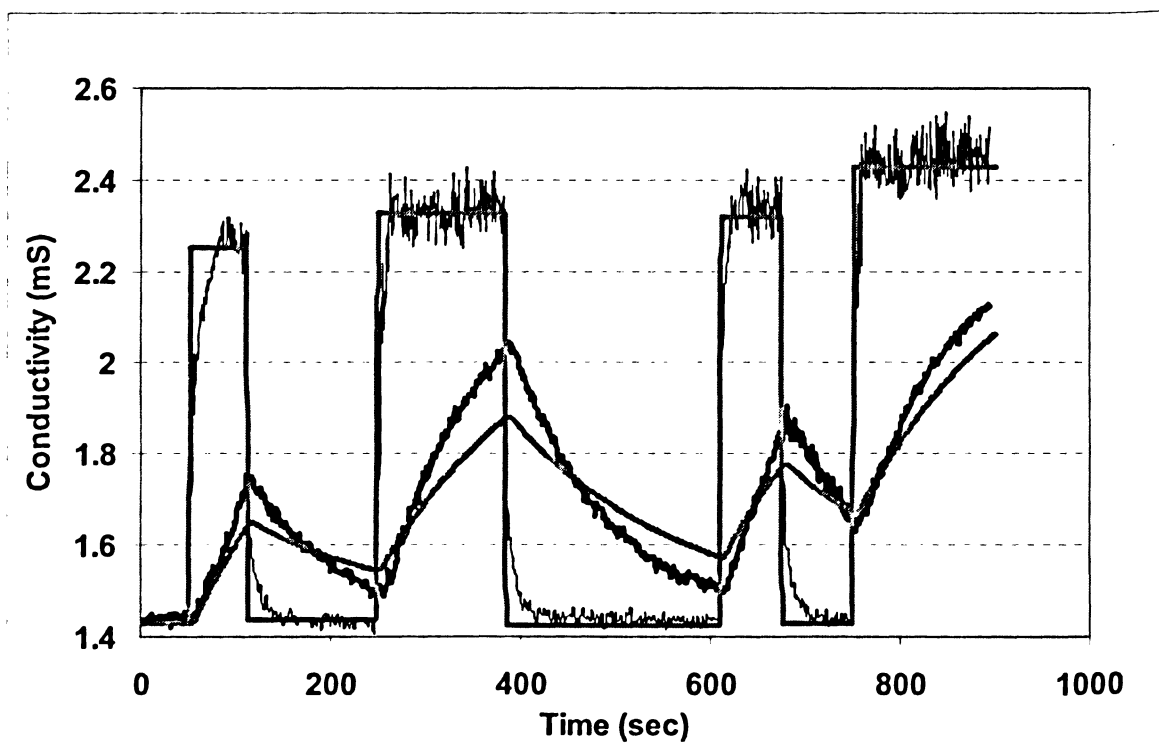
6.3.2.1 Effect of Impeller Speed and Xanthan Gum Flowrate

In order to evaluate CFD ability to estimate model parameters, experimental and CFD input-output conductivity curves for tracer injections were compared against each other at different impeller and xanthan gum flowrates. A200 impeller data are presented in Figure (6.19).

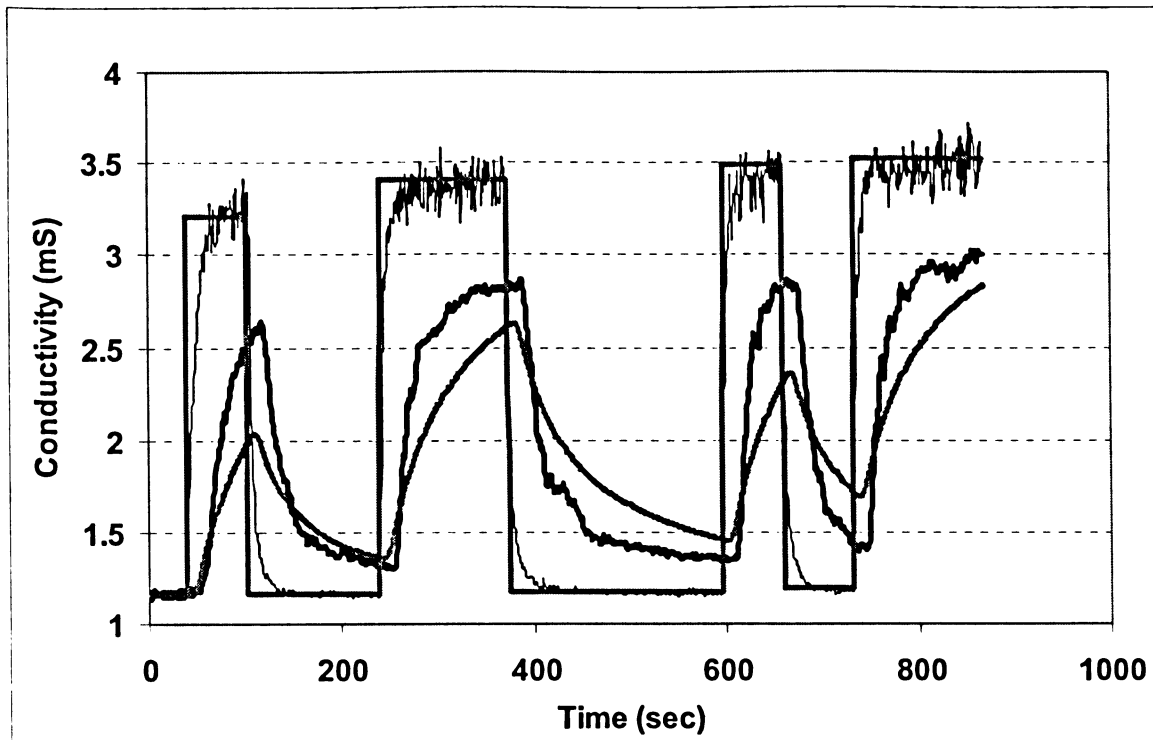
Noise associated with experimentally measured input signals were excluded from input signals used in CFD simulations. Output response predicted by CFD shows excellent agreement with experimental response at high impeller speed (Figure (6.19, a). However, CFD predictions of output signal deviates substantially from experimental measurements with decreasing impeller speed. This can be depicted at low impeller speed (Figure (6.19, c) where CFD was totally unable to predict the severe channeling occurring in the mixing vessel, quantified by the sudden bump (sudden sharp increase in conductivity). Figure (6.19) shows that CFD can predict the dynamic response for mixing vessel when the vessel performance becomes close to ideal. The same observations have been reported by Ford (2004) and Ford et al. (2006).



(a)- 898 L/hr, 500 rpm, and 0.5% xanthan gum



(b)- 898 L/hr, 200 rpm, and 0.5% xanthan gum



(c)- 898 L/hr, 50 rpm, and 0.5% xanthan gum

Figure (6.19) Effect of Impeller Speed on CFD Dynamic Response
Experimental Data in Black and CFD Data in Gray

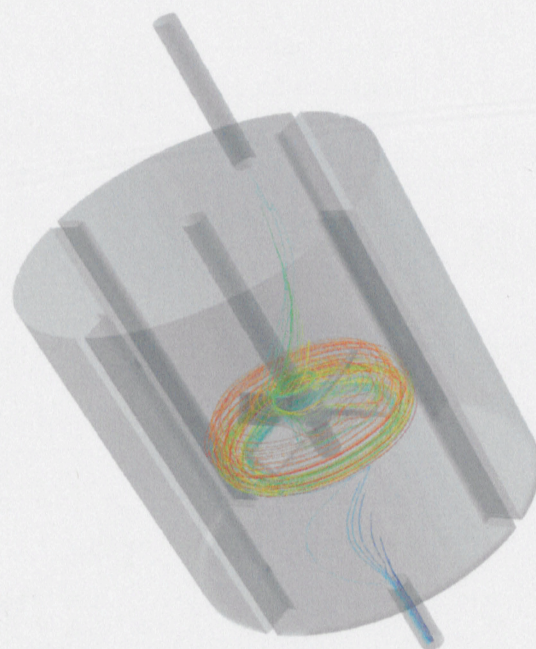
In order to investigate CFD ability to distinguish the channeling in the mixing vessel, pathlines obtained by releasing tracer particles from the inlet to the outlet were generated in CFD. Data are presented in Figure (6.20).

Pathlines generated in Figure (6.20) indicate that the flow generated by the impeller at 50 rpm was not sufficient to disperse the injected tracer homogenously within the vessel. Particle pathlines are not distributed all over the vessel, suggesting the possibility of the existence of dead zones. The same behaviour was observed regarding water by Khopkar et al. (2004). Experimental and CFD predictions of dynamic model parameters were compared against each other in Table (6.6). CFD always predicted less channeling and accordingly, higher mixed volume in the vessel.

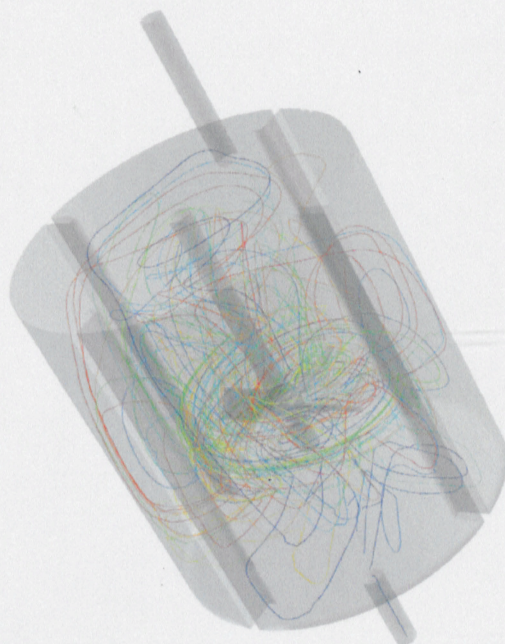
Table (6.6) Effect of Impeller Speed on Dynamic Model Parameters Estimation from Experimental and CFD, 1.5% xanthan gum

Dynamic Parameters	Experimental	CFD	Experimental	CFD
	<u>50 rpm</u>		<u>700 rpm</u>	
<u>896 L/hr</u>				
f	0.766	0.680	0.040	0.028
$V_{\text{fully mixed}}/V$	0.14	0.22	0.91	0.92
<u>227 L/hr</u>				
f	0.715	0.612	0.003	0.001
$V_{\text{fully mixed}}/V$	0.23	0.32	0.91	1.00

Decreasing flowrate reduces the extent of channeling and increases the fraction of fully-mixed volume. Figure (6.21) compares CFD and experimental dynamic response at the same concentration of xanthan gum and same impeller speed, but at different xanthan gum flowrates. CFD prediction of dynamic responses became closer to the experimental results as xanthan gum flowrate decreased. This result was similarly attributed to CFD inability to predict channeling in the mixing vessel.

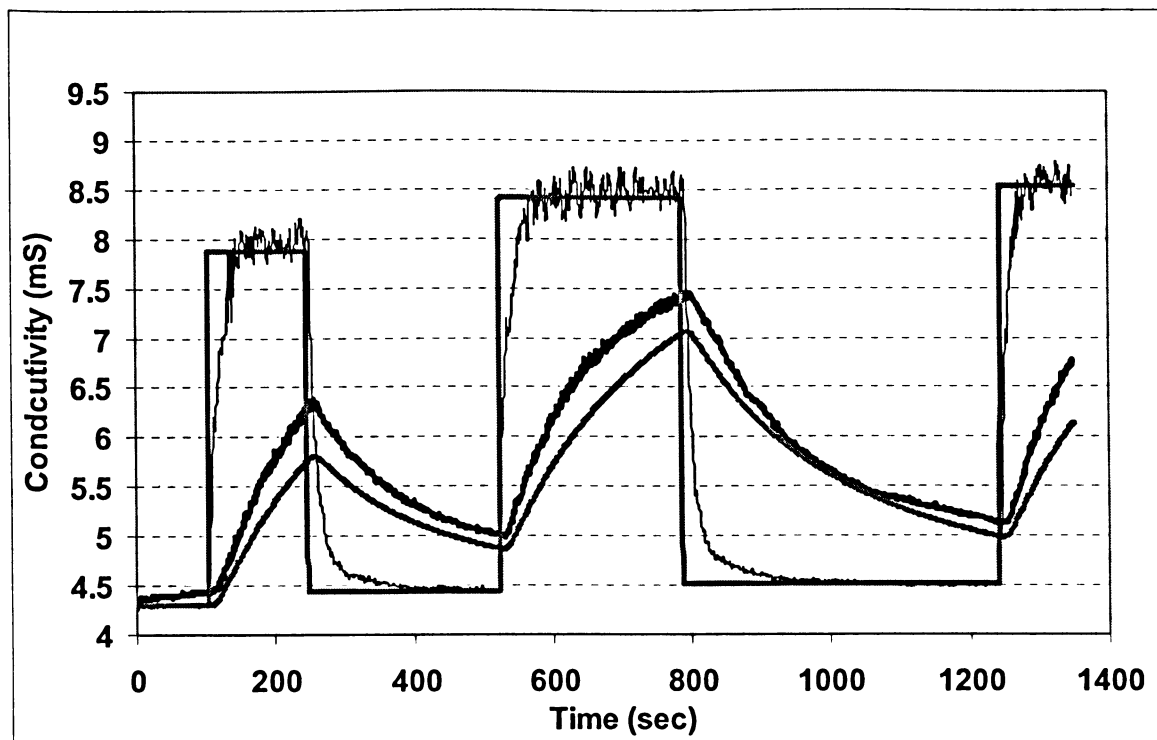


(a)-50 rpm

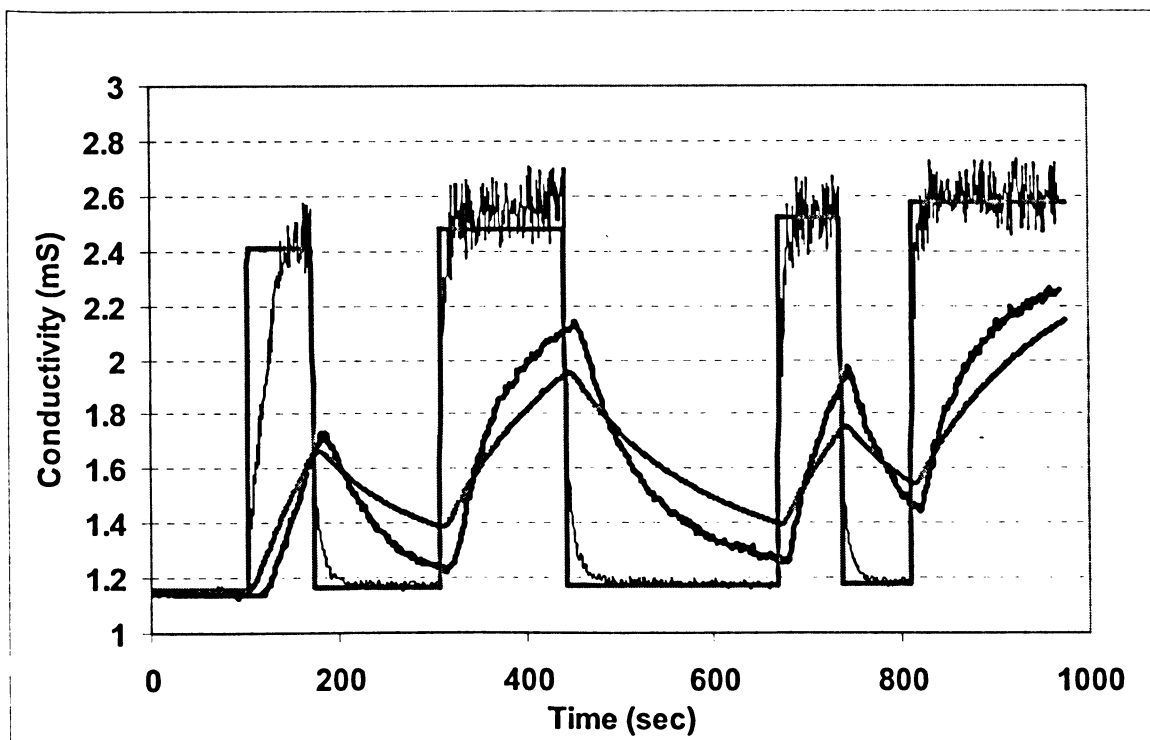


(b)-700 rpm

Figure (6.20) Pathlines Predicted by CFD – Effect of Impeller Speed, 1.5% Xanthan Gum Solution



(a)-608 L/hr, 150 rpm, and 0.5% xanthan gum



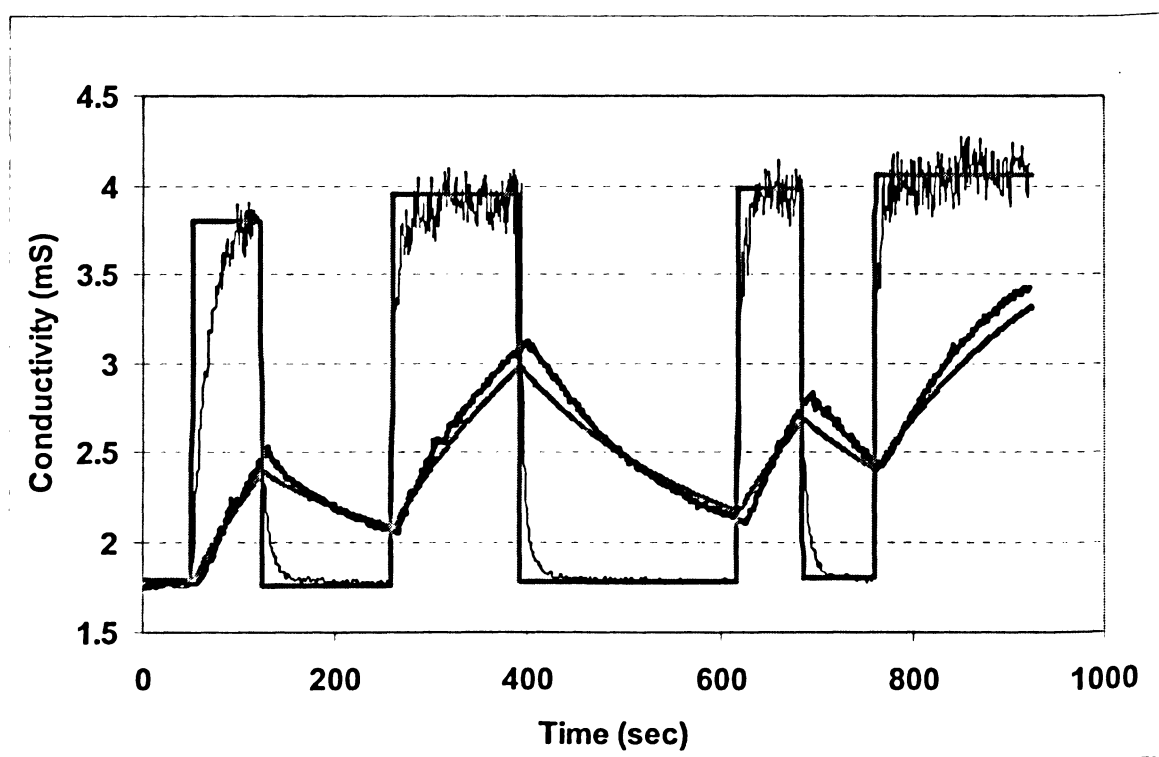
(b)- 898 L/hr, 150 rpm, and 0.5% xanthan gum

Figure (6.21) Effect of Xanthan Gum Flowrate on CFD Dynamic Response
Experimental Data in Black and CFD Data in Gray

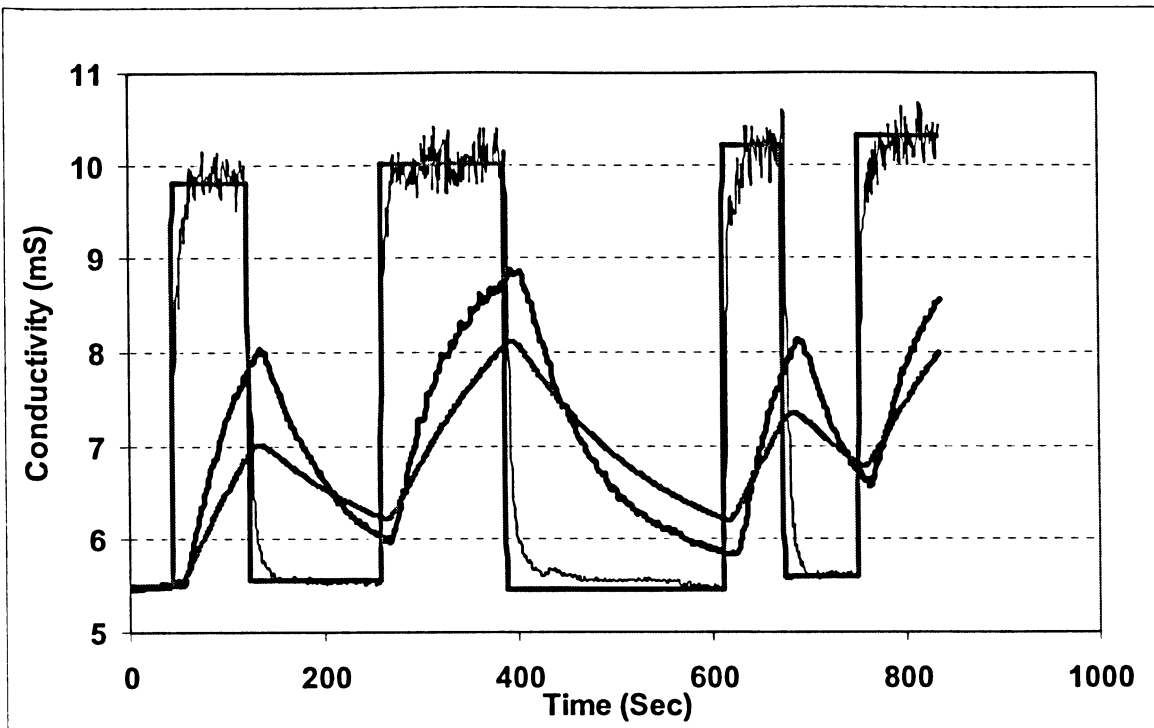
6.3.2.2 Effect of Xanthan Gum Concentration

Channeling increased with increasing xanthan gum concentration. Dynamic response data presented in Figure (6.21) show that CFD ability to predict channeling deteriorated as xanthan gum concentration increased.

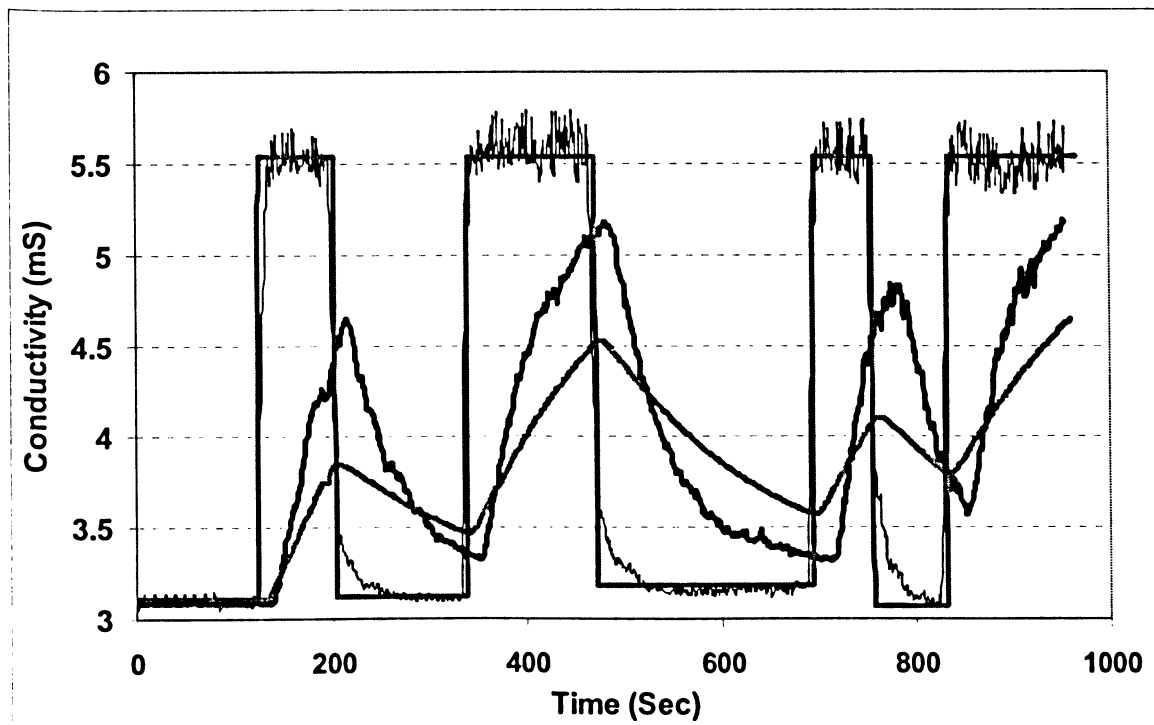
Table (6.7) shows a comparison between non-ideal flow parameters, channeling and $V_{\text{fullymixed}}/V$ ratio, obtained from experimental work and CFD modeling for an A200 impeller at different xanthan gum concentrations. Channeling predicted by CFD was always smaller when compared with the data obtained experimentally under identical operation conditions. Both experimental findings and CFD predicted that increasing xanthan gum concentration results in increased channeling and reduced volume of the totally mixed region in the vessel, as depicted in pathlines shown in Figure (6.23). Dysfunction in vessel performance at high xanthan gum concentration can be attributed to the interaction between input and output, forcing the material to leave the vessel without entering the well-mixed region.



(a)- 898 L/hr, 250 rpm, and 0.5% xanthan gum



(b)- 898 L/hr, 250 rpm, and 1.0% xanthan gum

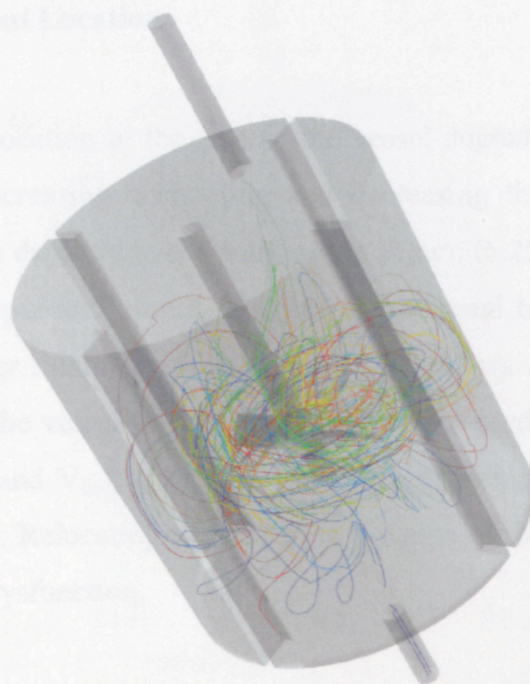


(c)- 898 L/hr, 250 rpm, and 1.5% xanthan gum

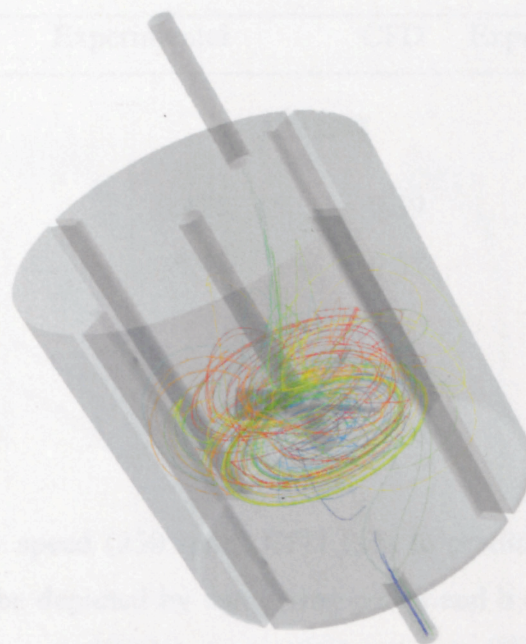
Figure (6.22) Effect of Xanthan Gum Concentration on CFD Dynamic Response
Experimental Data in Black and CFD Data in Gray

Table (6.7) Effect of Xanthan Gum Concentration on Dynamic Model Parameters
Estimation from Experimental and CFD Data, 896 L/hr

Dynamic Parameters	Experimental	CFD	Experimental	CFD
	<u>50 rpm</u>		<u>500 rpm</u>	
<u>0.5% xanthan gum</u>				
f	0.687	0.580	0.093	0.073
$V_{\text{fully mixed}}/V$	0.21	0.33	0.91	0.94
<u>1.5% xanthan gum</u>				
f	0.766	0.680	0.178	0.148
$V_{\text{fully mixed}}/V$	0.14	0.22	0.83	0.87



(a)-0.5 xanthan gum solution



(b)-1.5% xanthan gum solution

Figure (6.23) Pathlines Predicted by CFD – Effect of Xanthan Gum Concentration
Impeller speed 150 rpm

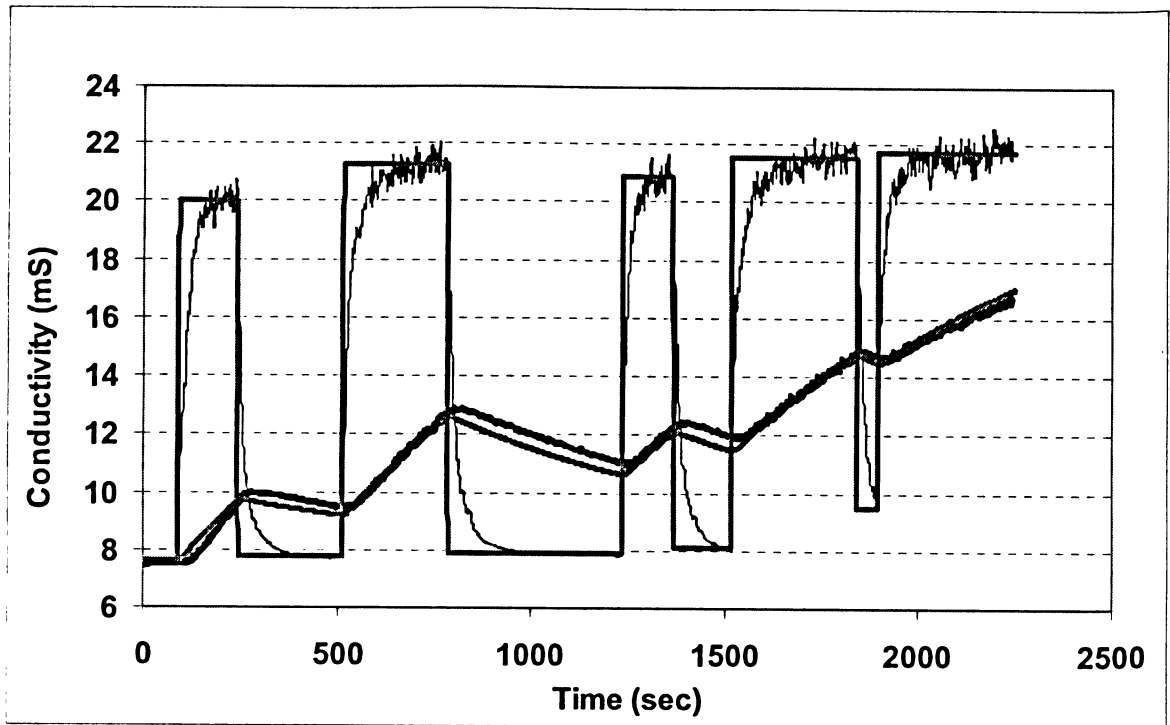
6.3.2.3 Effect of Output Location

Changing the output location to the side of the vessel degrades the performance of the mixing process by increasing channeling and decreasing the volume of fully mixed region in the vessel, as depicted in the pathlines in Figure (6.25) generated by CFD. The interaction between input and output provokes the material to leave the vessel without going into the impeller mixing region. Figure (6.24) shows the effect of changing the location of output in the vessel on the dynamic response predicted by CFD. Table (6.8) compares channeling and $V_{\text{fully mixed}}/V$ ratio between experimental and CFD predictions for the A200 impeller. Relocating the output to the side of the vessel may lead to short circuiting and vessel dysfunction.

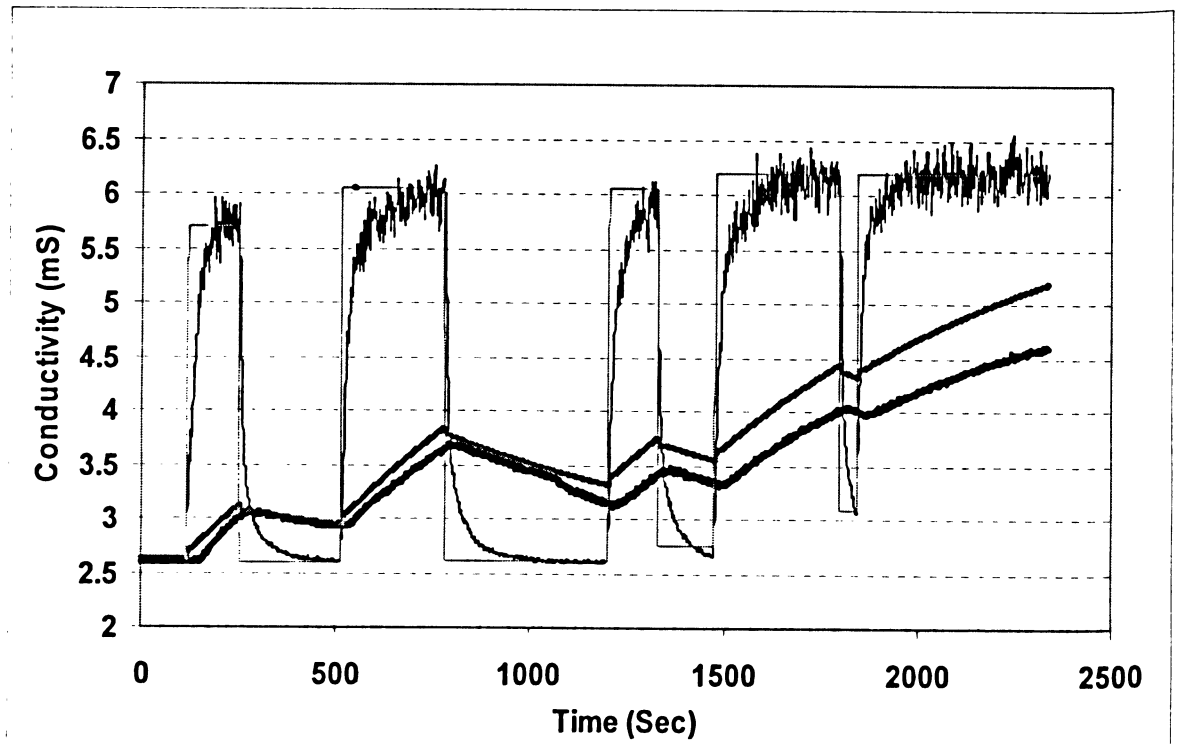
Table (6.8) Effect of Output Location on Dynamic Model Parameters Estimation from Experimental and CFD Data, 227 L/hr, 0.5% Xanthan Gum

Dynamic Parameters	Experimental	CFD	Experimental	CFD
	<u>150 rpm</u>		<u>400 rpm</u>	
<u>Configuration 1</u>				
f	0.476	0.39	0.089	0.073
$V_{\text{fully mixed}}/V$	0.45	0.57	0.97	0.99
<u>Configuration 2</u>				
f	0.580	0.513	0.145	0.126
$V_{\text{fully mixed}}/V$	0.39	0.50	0.91	0.94

Even at high impeller speed (250 rpm), CFD fails to predict dynamic response in the mixing vessel as can be depicted by comparing part a and b of Figure (6.24). Changing the location of the output can be a very valuable alternative that can enhance the performance of continuous-flow mixers. The performance of the vessel can be further improved by using an outflow-type outlet. Also, changing the location of input to the bottom of the vessel forces the material to go into the impeller mixing region and accordingly reduce channeling in continuous-flow mixers (Khopkar et al., 2004).

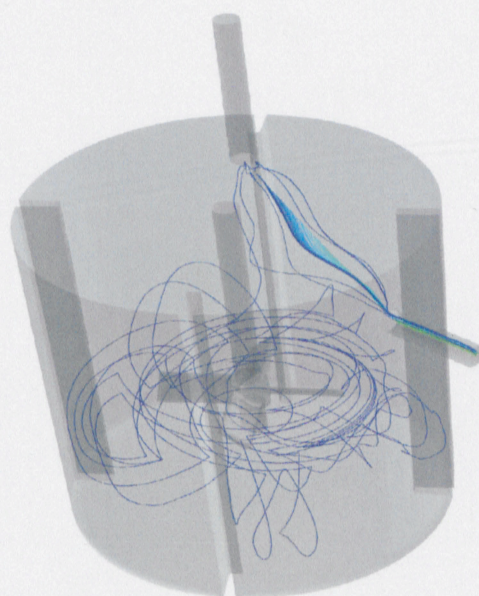


(a)- 227 L/hr, 250 rpm, 0.5% xanthan gum, bottom output



(b)- 227 L/hr, 250 rpm, 0.5% xanthan gum, side output

Figure (6.24) Effect of Output Location on CFD Dynamic Response
Experimental Data in Black and CFD Data in Gray



150 rpm

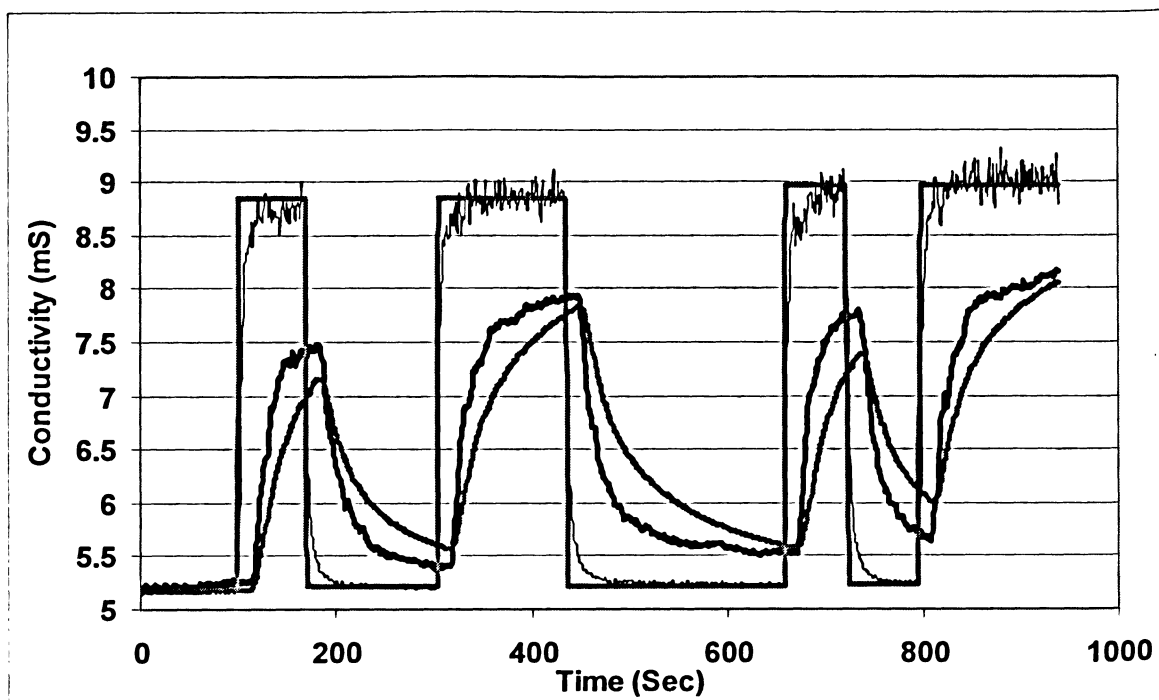
Figure (6.25) Pathlines predicted by CFD – Effect of Output Location
0.5% Xanthan Gum Solution

6.3.2.4 Effect of Impeller Type

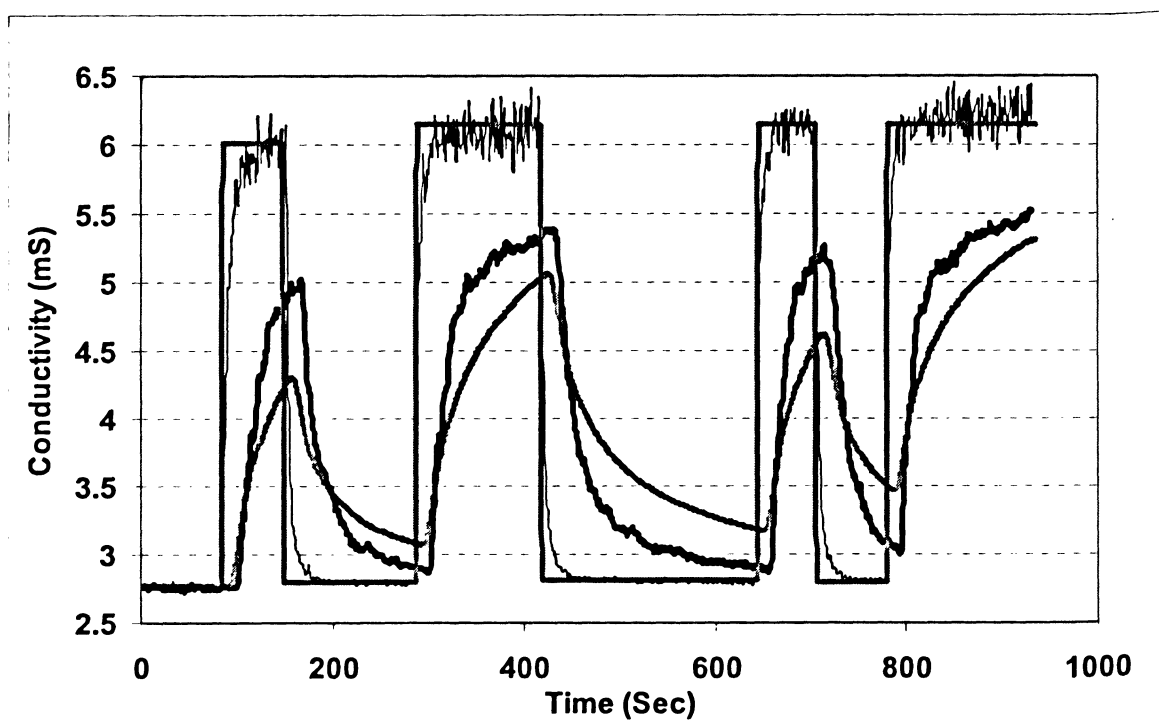
Figure (6.26) shows the effect of changing impellers on the dynamic response predicted by CFD. Table (6.9) compares channeling and $V_{\text{fully mixed}}/V$ ratio between experimental and CFD predictions for different impellers used.

A through review of the literature suggests that little effort has been spent investigating the effect of impeller blade geometry on impeller efficiency. The efficiency calculations presented in section 6.3.1.4 indicate that A320 impeller exhibited superior performance in the mixing vessel compared to the other impellers.

It is believed that the performance of an impeller depends on many factors related to impeller design, including blade width, blade height, blade twist, blade angle, blade thickness, and number of blades. The impellers used in this work have different blade widths and shapes. Accordingly, impeller performance is directly related to blade width and shape. Table (6.10) outlines the maximum blade width and shape for all impellers utilized in this study.



(a)- 227 L/hr, 50 rpm, 0.5% xanthan gum, A310 Impeller




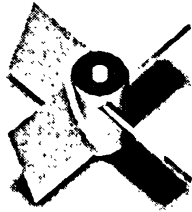

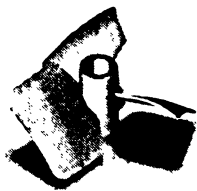
(b)- 227 L/hr, 50 rpm, 0.5% xanthan gum, A100 Impeller

Figure (6.26) Effect of Impeller Type on CFD Dynamic Response
Experimental Data in Black and CFD Data in Gray

Table (6.9) Effect of Impeller Type on Dynamic Model Parameters Estimation from Experimental and CFD Data, 897L/hr, 0.5% Xanthan Gum

Dynamic Parameters	Experimental	CFD	Experimental	CFD
	<u>150 rpm</u>		<u>400 rpm</u>	
<u>A100</u>				
f	0.540	0.443	0.173	0.130
$V_{\text{fully mixed}}/V$	0.38	0.48	0.91	0.98
<u>A200</u>				
f	0.590	0.477	0.195	0.154
$V_{\text{fully mixed}}/V$	0.33	0.44	0.88	0.93
<u>A310</u>				
f	0.499	0.396	0.153	0.098
$V_{\text{fully mixed}}/V$	0.42	0.48	0.97	0.98
<u>A320</u>				
f	0.462	-	0.122	-
$V_{\text{fully mixed}}/V$	0.45	-	0.99	-

Table (6.10) Width and Shape of Impellers Blades

	A100	A200	A310	A320
Maximum Blade Width (mm)	71	35.6	28	90
Blade Shape				

The motion of an impeller in fluid can induce two forces: lift and drag. Lift is the net force perpendicular or normal to the flow direction, while drag is the net force acting in the flow direction. Two forms of resistance contribute to the total drag force: surface drag (or skin friction) and form (or profile, pressure) drag. Surface drag arises from the friction of the fluid against the skin of the impeller and form drag arises due to the shape or form of the object (impeller) (Durgaiah, 2006). An optimal impeller blade design can be achieved by increasing lift force and decreasing drag force.

Many factors affect lift force. Blade shape can greatly affect lift, because the amount of lift force generated depends on flow “turning” produced by the blades. The higher the flow turning, the greater the lift generated. Streamlined (A320), sleek twisted (A310) and contoured-shaped (A100) blades can give rise to high lift force compared with the straight and sharp blades of A200. Convex blades (only A320) have the tendency to deflect the flow over impeller surface. Such blades do not let flow continue in a straight-line motion. This will decrease pressure on the side of impeller normal to the direction of flow and consequently increasing lift force (Coanda Effect, Bertin, 2002).

The amount of lift force generated also depends on the size of blades because lift force is directly proportional to blade area. A320 has the greatest width among all other impellers used, giving rise to big blade areas and consequently high lift force. Power dissipated in the impeller region was found to be increase with increasing blade projected area (increasing blade width), resulting in an increasing power number (Patwardhan & Joshi, 1999, Kunciewicz & Pietrzykowski, 2001, Kumaresan, et al., 2006, Wu and Pullum, 2000). Pumping effectiveness, on the other hand, was found to increase with increasing impeller projected area, leading to an increase in flow and circulation numbers (Patwardhan & Joshi, 1999, Kunciewicz & Pietrzykowski, 2001, Kumaresan, et al., 2006, Wu and Pullum, 2000).

Blade geometry has a large effect on the amount of drag generated by the impeller. Streamlined blades (A320), sleeked twisted (A310) and contoured-shaped (A100) blades produce small form drag compared to sharp plat-like blades (A200). As with lift, the drag

depends linearly on the size of the blades. Airfoil-type blades (A320, A310 & A100) can also reduce skin friction compared to plate-type blades. The noticeable efficiency of A310 can be attributed to its blade twist angle that can increase flow and circulation number (increase lift force) and reduce form drag and skin friction.

6.4 Cavern Region & Flow Pattern in the Mixing Vessel

Analyzing system flow patterns can provide insight on the mixing process. Flow pattern can be used as a first indication to qualify impeller suitability for a particular mixing operation.

Flow fields generated by CFD were analyzed to estimate cavern dimensions and flow patterns. Dynamic model parameters were then related to the flow patterns.

6.4.1 Cavern Region in the Mixing Vessel

Motion in viscoplastic fluids possessing yield stress ceases when shear stresses imparted by an impeller fail to exceed yield stress of the fluid. This leads to the formation of a well mixed region, called cavern, around the impeller with the remaining fluid stagnant. CFD velocity contours made at different cuts in the vessel, as depicted in Figure (6.27) shows the formation of a well mixed region close to the impeller.

CFD flow fields depicted the formation of a cylindrical cavern around the impeller. Cavern diameters were measured on vertical planes cutting the impeller surface. Cavern boundary is usually defined by the locus of points where the local velocity magnitude is equal to 1% of the impeller tip speed (Hirata et al., 1994, Hirata and Asohima, 1996 & 1995). Cavern heights were estimated on planes parallel to the shaft, and perpendicular to the impeller. The effect of impeller speed, xanthan gum concentration, and impeller type on cavern dimension is shown in Figure (6.28), Figure (6.29), and Figure (6.30), respectively.

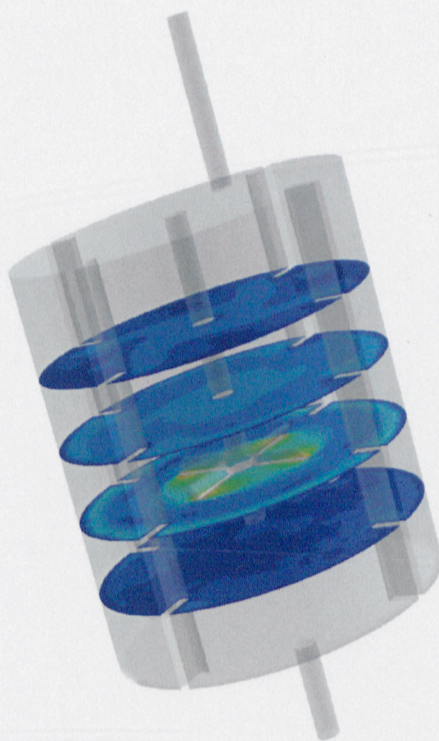


Figure (6.27) Vertical Velocity Contours in m/s showing Cavern Formation
1.5% Xanthan, 500 rpm

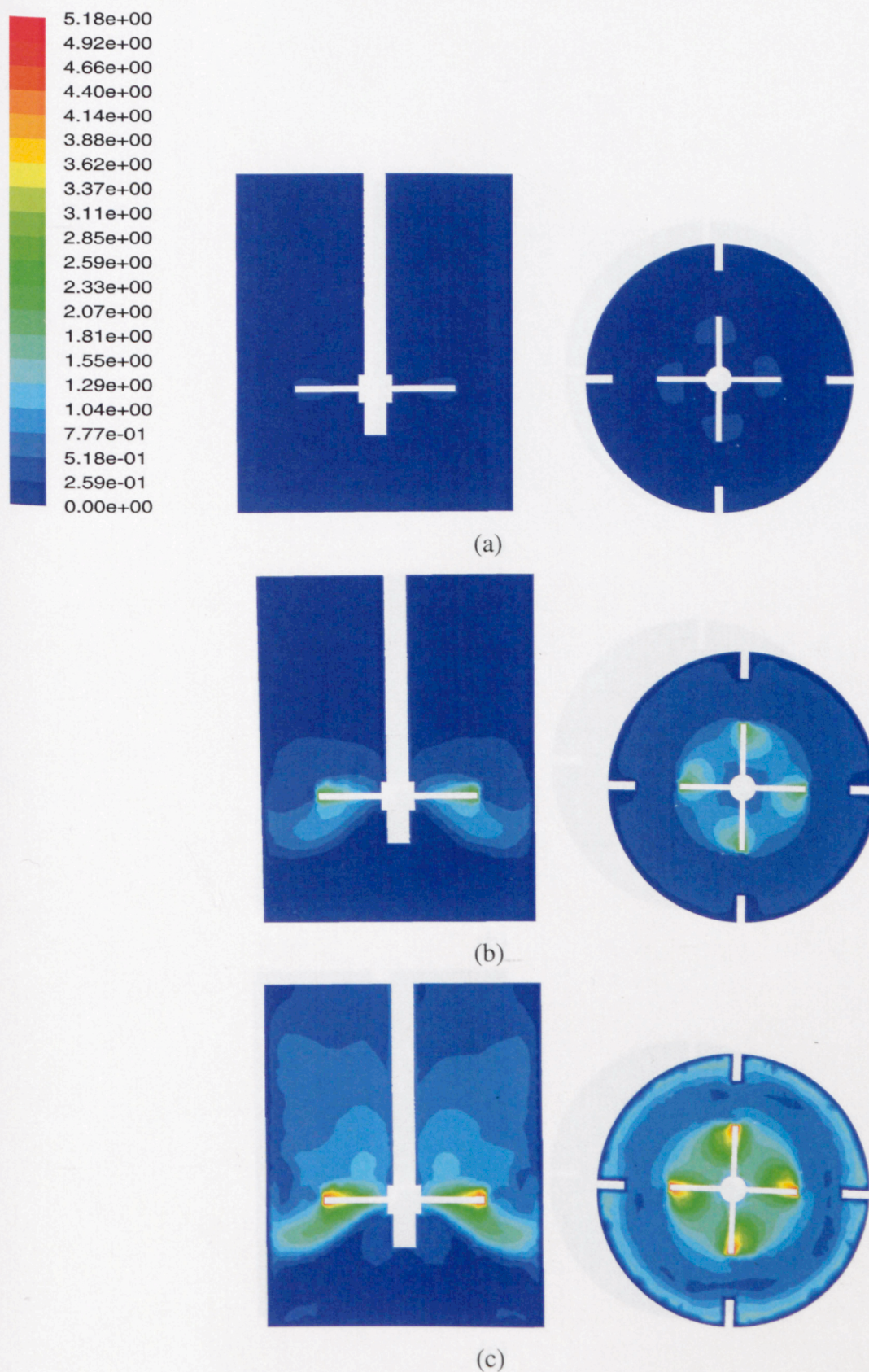


Figure (6.28) Velocity Contours in m/s showing the Effect of Impeller Speed on Cavern Growth, 1.5% Xanthan Gum, (a) 50, (b) 250, (c) 500 rpm

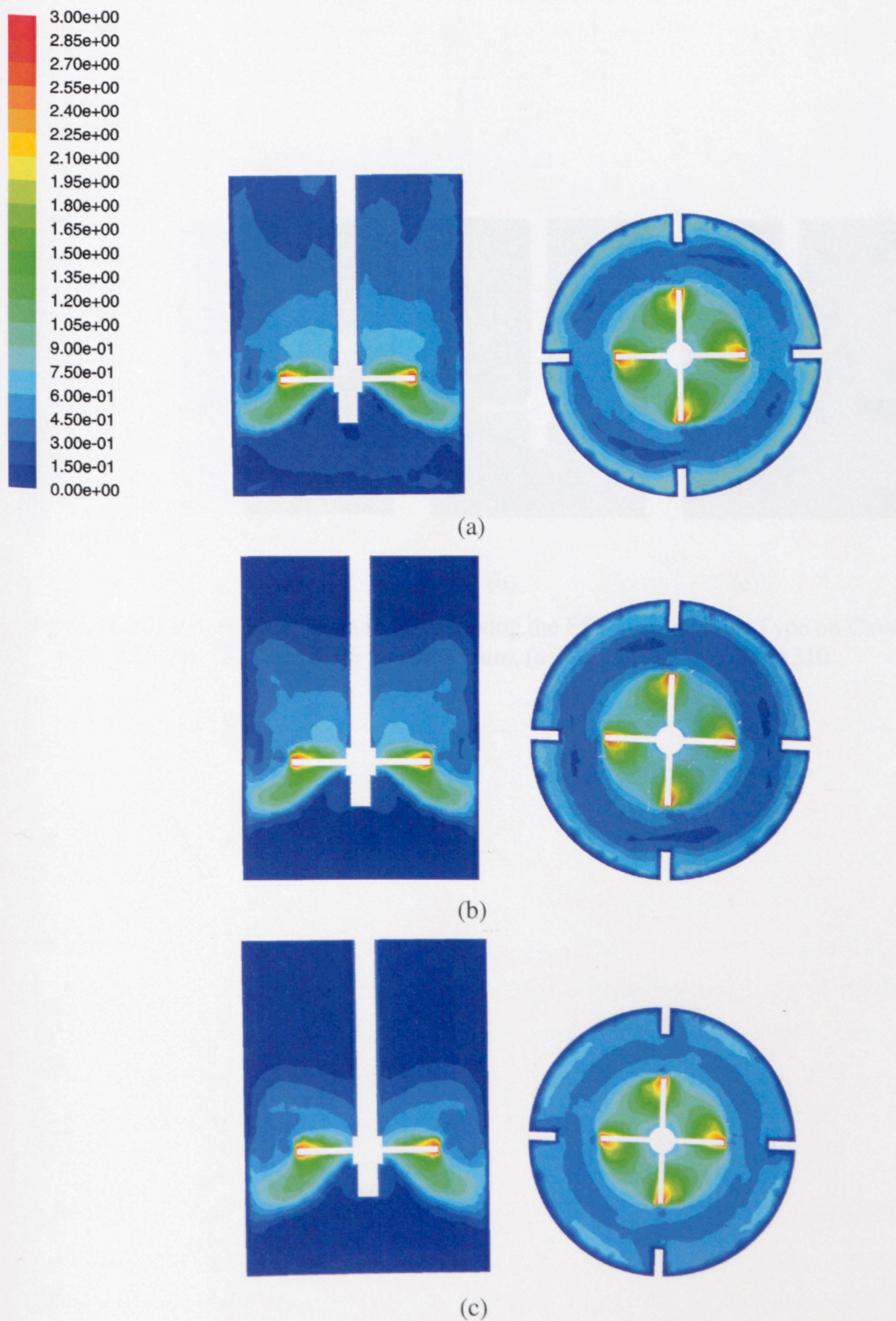


Figure (6.29) Velocity Contours in m/s showing the Effect of Xanthan Gum Concentration on Cavern Growth, 300 rpm, (a) 0.5%, (b) 1.0%, (c) 1.5% xanthan gum

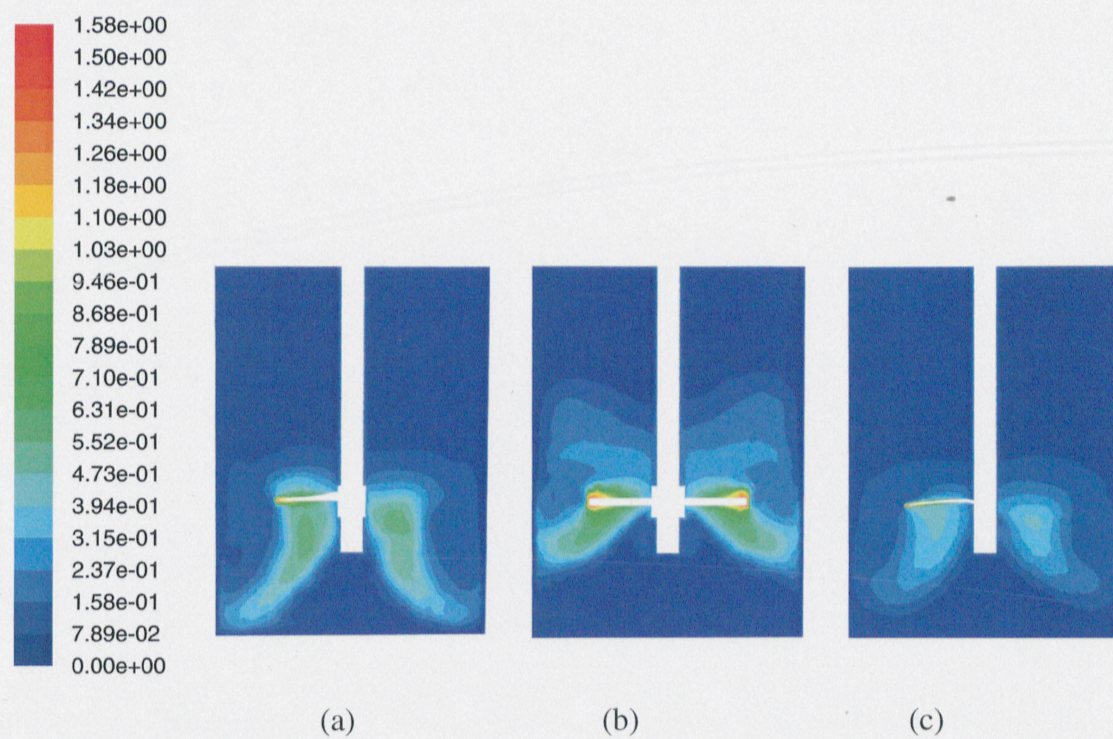


Figure (6.30) Velocity Contours in m/s showing the Effect of Impeller Type on Cavern Growth, 150 rpm, 0.5% Xanthan Gum, (a) A100, (b) A200, (c) A310

Cavern diameters and heights were calculated from CFD flow fields. The results are tabulated in Table (6.11).

Table (6.11) Cavern Diameter and Height in cm– A200 Impeller

Impeller Speed (rpm)	Xanthan Gum Concentration (%)	0.5		1.0		1.5	
		D_c	H_c	D_c	H_c	D_c	H_c
50		26.37	14.98	22.86	12.81	21.98	12.22
100		32.91	18.43	29.89	16.44	26.37	14.77
150		40	26.22	37.8	20.41	35.16	19.34
200		40	33.22	40	26.12	40	24.75
250		40	39.21	40	31.92	40	30.07
300		40	41	40	37.14	40	34.91
400		40	41	40	41	40	41

Cavern size found to increase with increasing impeller speed where regions with significant fluid motion were growing. With respect to xanthan gum concentration, however cavern size was found to decrease. This can be attributed to the effect of yield stress; as increasing xanthan gum concentration increases yield stress, more stagnant regions are formed in the mixing vessel where shear stress fails to exceed yield stress. Cavern size continued to grow to the point where cavern diameter touched the vessel wall. Cavern region then gained vertical circulation and increased in height until it filled the whole vessel. These observations were reported by many investigators for cavern growth in transition and turbulent flow region, including: (Elson, 1990 A & B, Hirata et al., 1991 & 1994, Galindo and Nienow, 1992, Galindo et al., 1996).

Following CFD predictions, cavern diameter was compared with Elson's model (1988), which describes the formation of a cylindrical cavern centered upon the impeller assuming that shear stress at the cavern boundary equals fluid yield stress. This model estimates cavern diameter as follows:

$$\left(\frac{D_c}{D}\right)^3 = \frac{P_{ot} \cdot Re_y}{\left(\frac{H_c}{D_c} + \frac{1}{3}\right)\pi^2} \quad (6-11)$$

where P_{ot} is impeller turbulent power number, Re_y is Reynolds yield stress ($=\rho \cdot N^2 \cdot D^2 / \tau_y$), D_c is cavern diameter and H_c is cavern height.

A plot of dimensionless cavern diameter, D_c/D , versus dimensionless stress (Reynolds yield stress defined using P_{ot}) should give a slope of 1/3. CFD data are plotted for all xanthan gum concentrations in Figure (6.31). The slope of D_c/D -versus- $P_{ot} \cdot Re_y$ line was 0.24, lower than the slope expected from Elson's model (1988). Galindo and Nienow (1992) reported a value of 0.25 for the slope of D_c/D -versus- $P_{ot} \cdot Re_y$ line for A315 axial flow impeller. Elson's (1988) was derived for radial flow impellers, assuming the formation of an exact-shaped circular cylindrical cavern. Before touching the vessel wall, however, cavern may take an ovoidal shape, as indicated by Galindo and Nienow (1992).

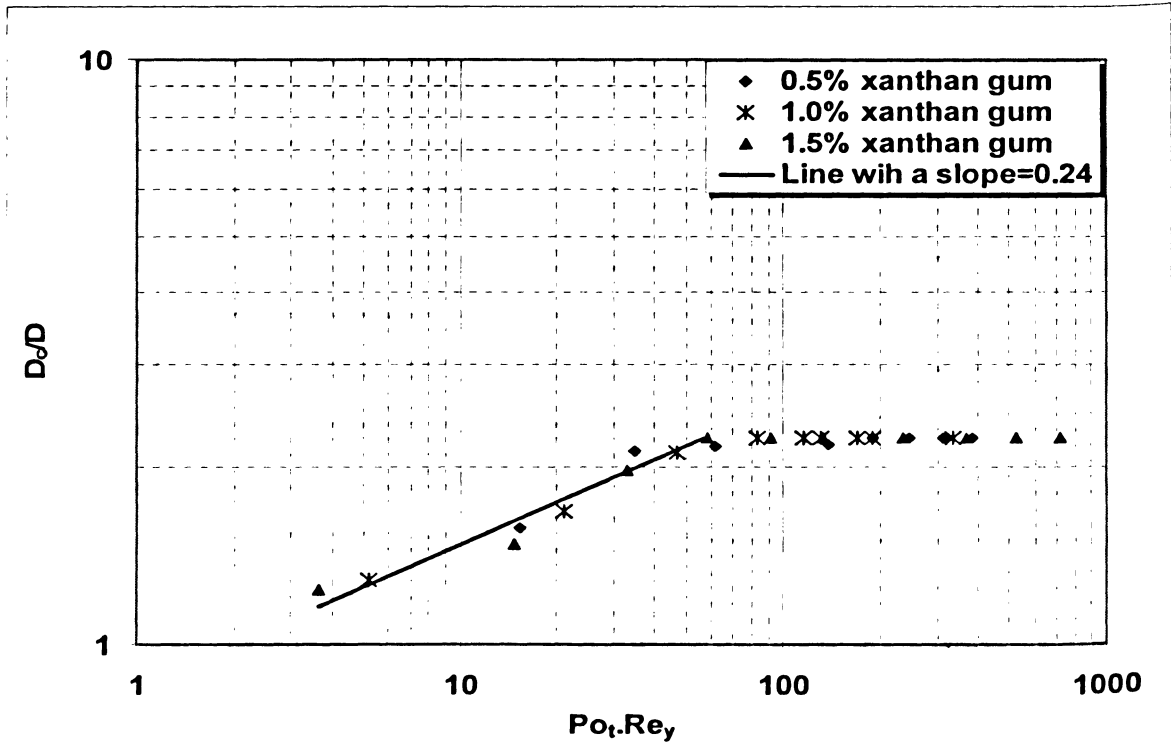


Figure (6.31) D_c/D versus $P_{ot} \cdot Re_y$ – A200 Impeller

Cavern height become proportional to impeller speed after reaching the vessel wall as depicted in the following equation:

$$\frac{H_c}{D_c} \propto N^p \quad (6-12)$$

where p varies from 0.4 for radial-flow impellers to 0.75 for axial flow impellers (Elson, 1988) as indicated in Table (6.12).

Table (6.12) Summary of Cavern Dimensions for Axial Flow Impellers

Impeller Type	Mean H_c/D_c	P	Reference
A200	0.55 ± 0.10	0.86	Solomon et al., 1981 Elson, 1988
A100	0.75 ± 0.05	0.76	Elson, 1990 A
A315	0.58 ± 0.05	0.53	Galindo and Nienow, 1992

Cavern height and diameter were increased with increasing impeller speed. The ratio of H_c/D_c remained constant at 0.55 ± 0.10 for all concentrations of xanthan gum. Once cavern reaches the vessel wall, cavern height became proportional to impeller speed, with a slope of 0.86 ± 0.10 . Data for all xanthan gum concentrations are presented in Figure (6.32).

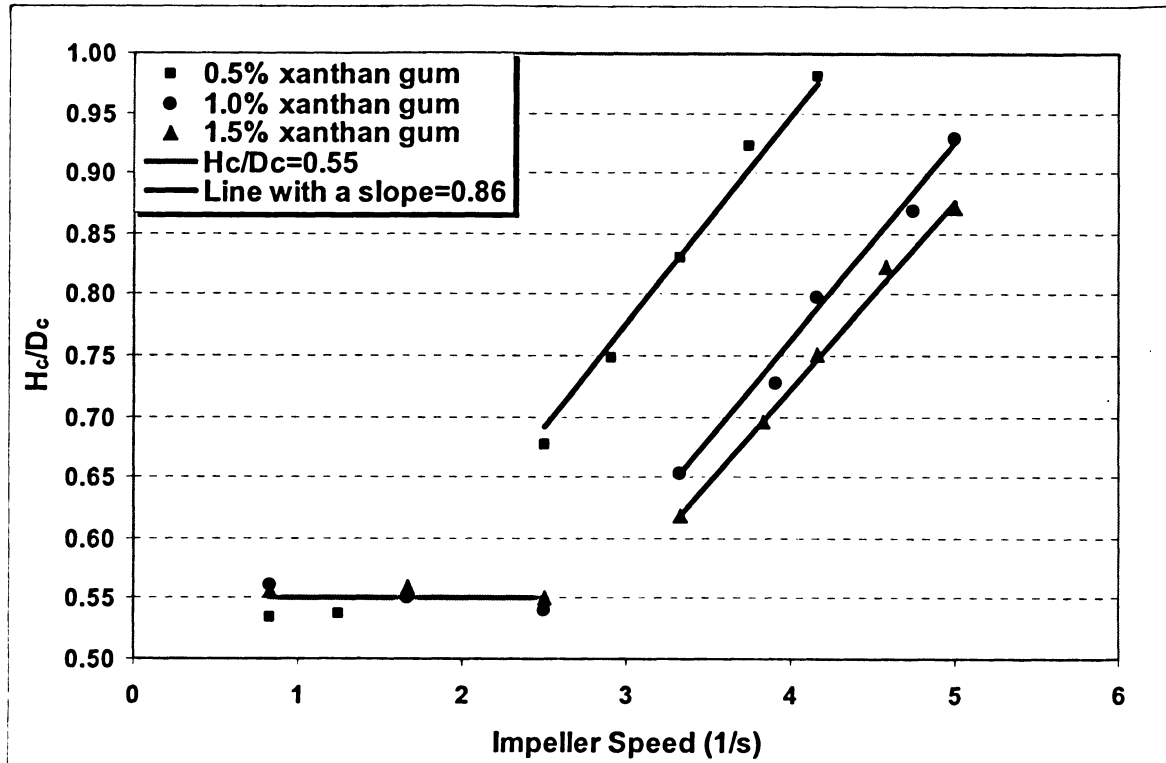
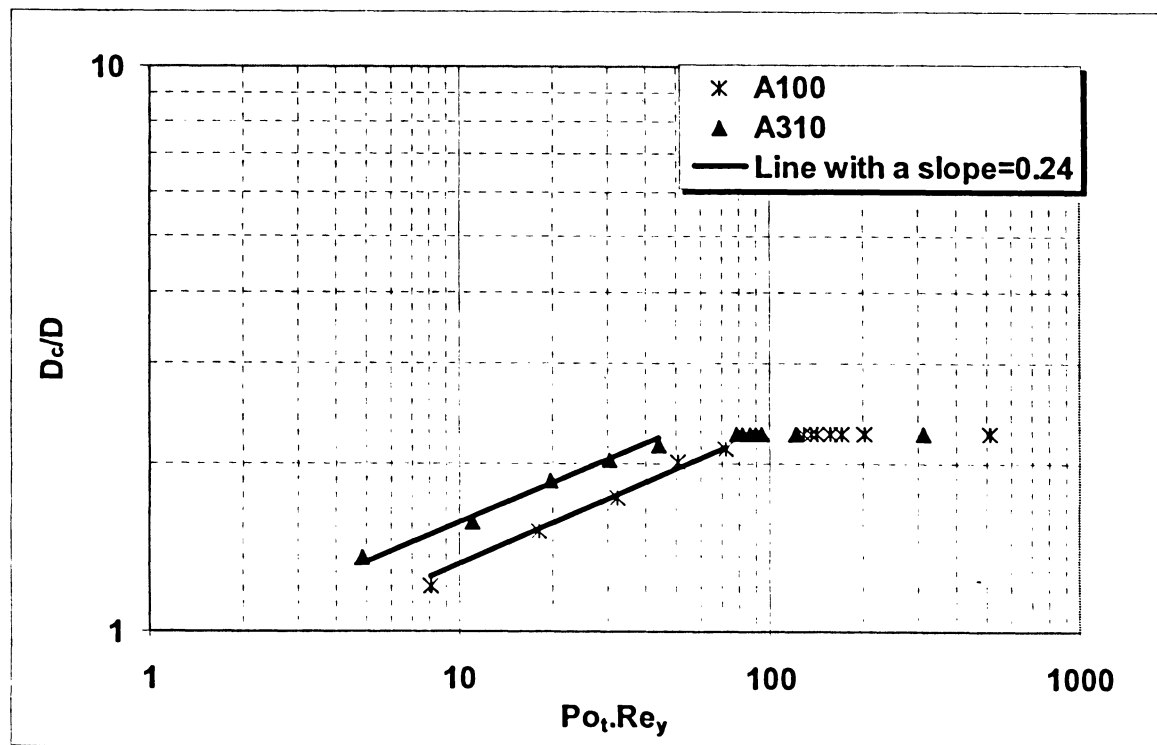


Figure (6.32) H_c/D_c versus Impeller Speed for A200 Impeller

Similar calculations were performed for A100 and A310. Table (6.13) compares cavern diameter and height for three examined impeller types. Cavern diameter was also compared with Elson's model (1988) for A100 and A310 at 0.5% xanthan gum solution. Figure (6.33) indicates that cavern growth in A310, expressed as D_c/D , was greater than that for A100 and A200. Line slope of D_c/D versus dimensionless stress Reynolds yield stress defined using Po_t is 0.24 for A100 and A310.

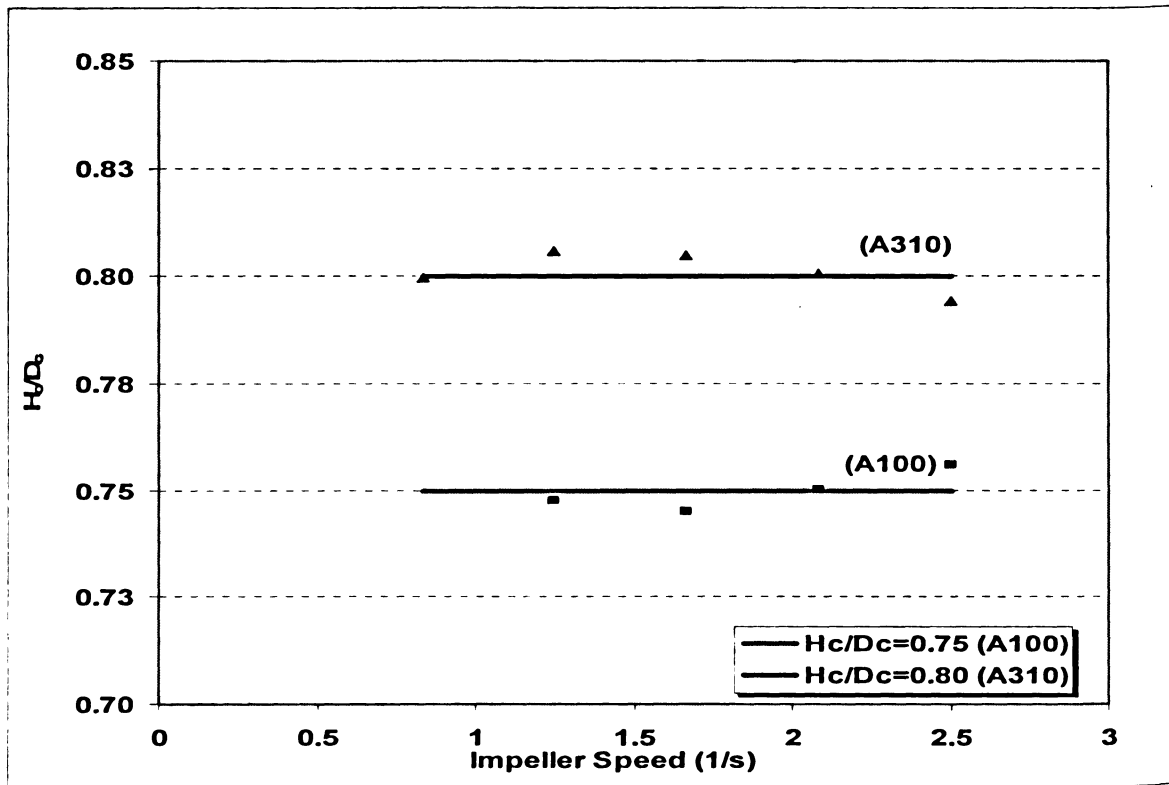
Table (6.13) Cavern Diameter and Height in cm – A100, A200 & A310 Impellers

Impeller Speed (rpm)	A100		A200		A310	
	D_c	H_c	D_c	H_c	D_c	H_c
50	25.50	19.37	26.37	14.98	23.98	19.18
100	30.19	22.65	32.91	18.43	33.13	26.87
150	37.80	28.73	40	26.22	38.24	30.21
200	40	35.85	40	33.22	40	36.65
210	40	37.11	40	34.67	40	38.23
220	40	38.04	40	36.72	40	39.52
250	40	41	40	39.21	40	41
400	40	41	40	41	40	41

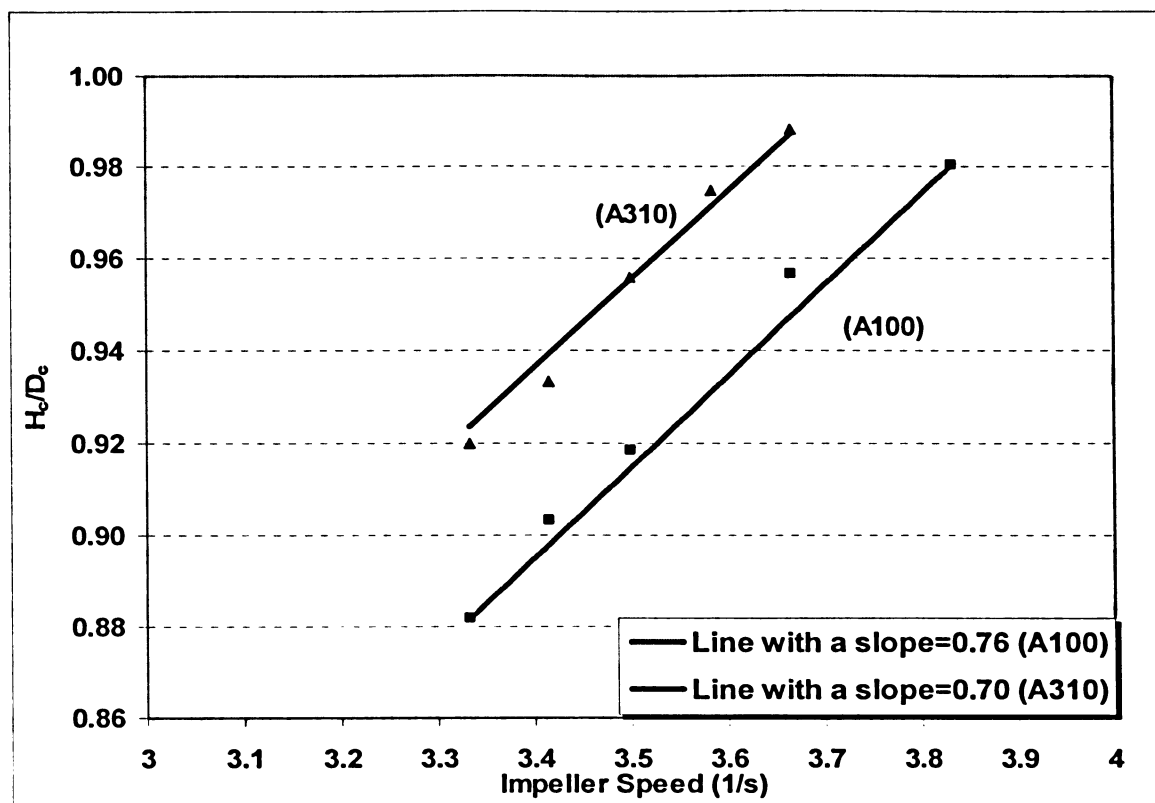
Figure (6.33) D_c/D versus $Po_1.Re_y$ for A100 and A310 Impellers

The ratio of H_c/D_c remained constant at 0.55 and 0.80 for A100 and A310, respectively. These ratios are in agreement with those reported for A100, as indicated in Table (6.12). No value of H_c/D_c was found for A310. Once cavern reached the vessel wall, cavern

height became proportional to impeller speed with a slope of 0.76 and 0.70 for A100 and A310, respectively. Corresponding data for all impellers are presented in Figure (6.34).



(a)- H_c/D_c versus impeller speed when $D_c < D$



(b)- H_c/D_c versus impeller speed when $D_c > D$

Figure (6.34) H_c/D_c versus impeller speed for A100 and A310 Impellers

Figure (6.33) and Figure (6.34) indicate that the ratio of D_c/D and H_c/D_c for A310 are greater than these for A200 and A100. The noticeable ability of A310 to enhance vessel dynamics (observed by decreasing channelling and increasing fully mixed volume) is related to the formation of cavern.

An overall picture of mixing can thus be described. Once the fluid enters the vessel, operation conditions can either enhance or deteriorate the overall performance of the process. Low impeller speed, high solution flowrate, or high solution concentration will form a cavern around the impeller. Stagnant (dead) zones will occupy the vessel and material from the inlet will not have the potential to go into the well mixed region close to the impeller. Instead, the material will take the short-cut (or short circuit) to the outlet.

Ein-Mozaffari et al. (2005) found that the size of the cavern generated around the impeller has a significant effect on the extent of non-ideal flow in continuous mixing of

fluids with yield stress. As the impeller speed increases, the cavern surface moves towards the tank wall and the fluid surface within the mixing vessel. When the cavern does not reach the vessel wall and fluid surface, a high percentage of the feed stream would be channeled easily to the exit without being entrained in the impeller flow. Thus, the continuous mixing system is prone to a high level of non-ideal flow.

6.4.2 Flow Pattern in the Mixing Vessel

The suitability of a particular impeller for any given mixing process depends on its capability to induce the fluid contents in the vessel into vigorous circulation, avoiding situations where regions of the fluid(s) are poorly mixed or not mixed at all. It is therefore necessary to determine, for each type of impeller, the flow pattern induced in the vessel. Flow pattern gives a first indication of agitator suitability for a particular application.

The flow fields generated by Mixsim 2.2 were used to depict the flow pattern generated in the vessel. Data are collected to show the effect of impeller speed, xanthan gum solution concentration and impeller type.

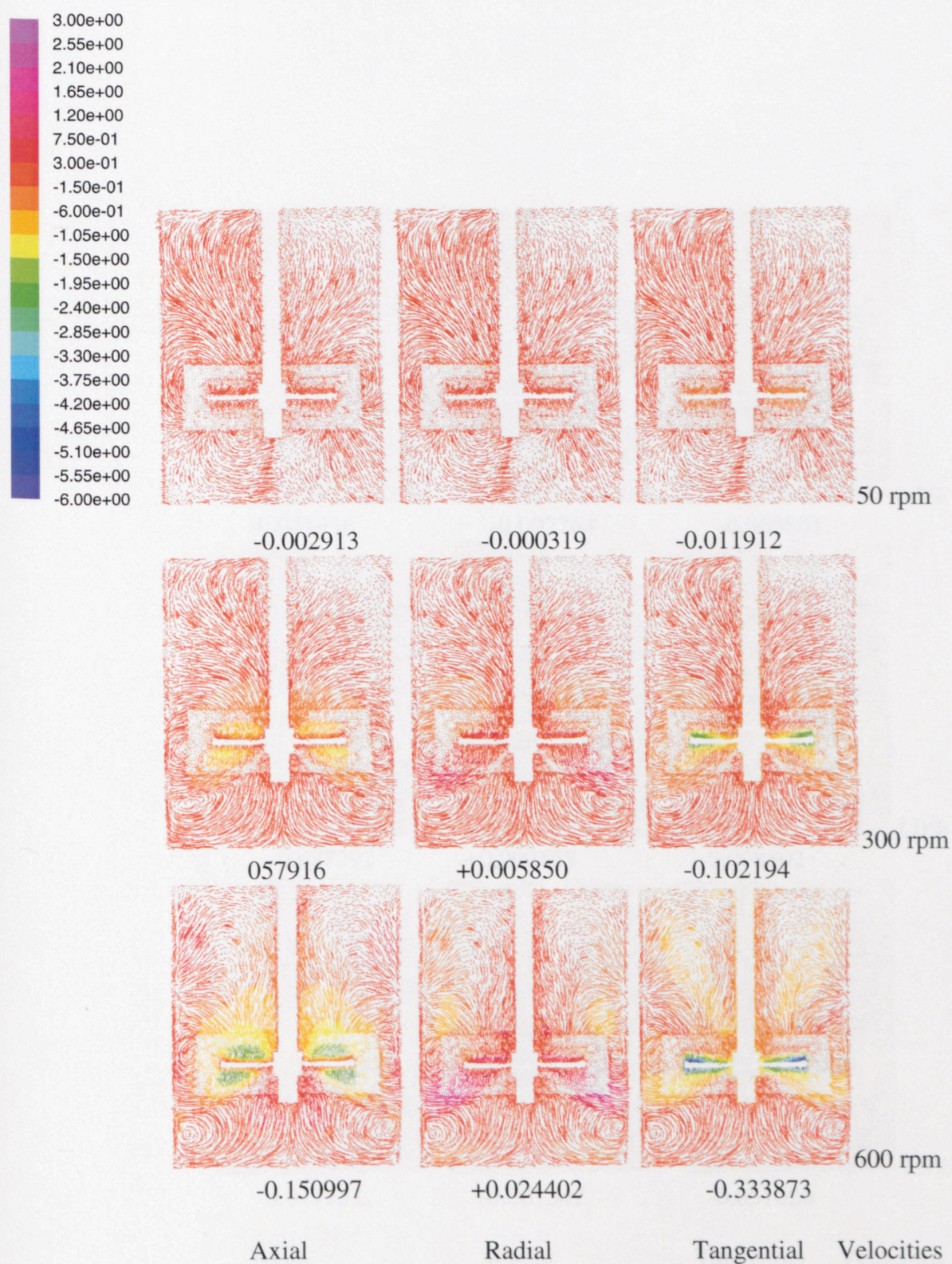


Figure (6.35) Effect of Impeller Speed on Flow Pattern, 1.5% Xanthan Gum
(Numbers indicate area weighted average velocity in m/s)

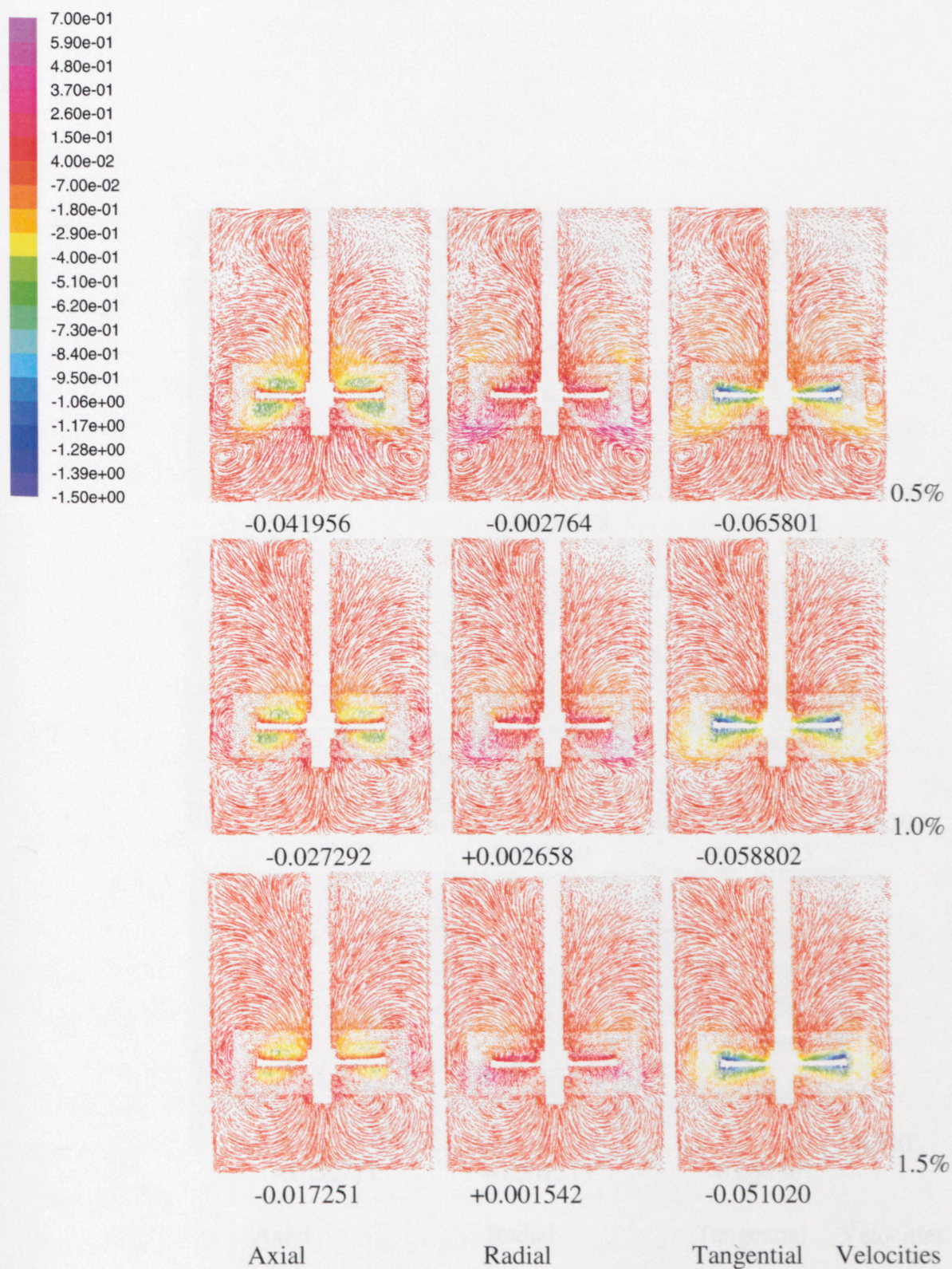


Figure (6.36) Effect of Xanthan Gum Concentration on Flow Pattern, 150 rpm
(Numbers indicate area weighted average velocity in m/s)

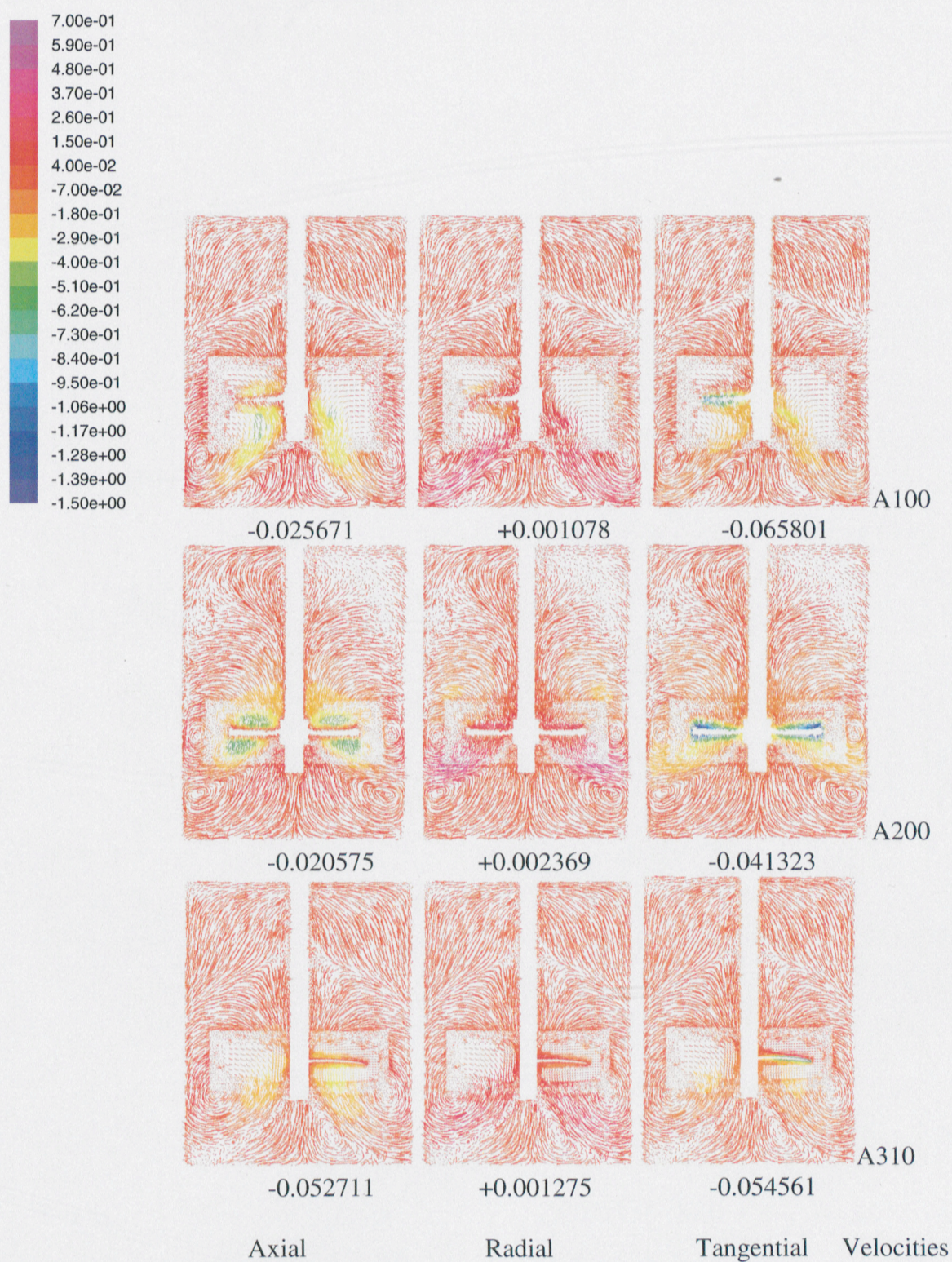


Figure (6.37) Effect of Impeller Type on Flow Pattern, 150 rpm, 0.5% Xanthan Gum
(Numbers indicate area weighted average velocity in m/s)

Axial flow impellers pumping downward develop high jet flow in the downward direction below the impeller. These jets entrain fluid and the velocity gradients become less sharp as they approach the tank bottom. After striking the tank bottom, the fluid moves along the bottom up to the wall where it turns upward. Most of this up-flowing liquid returns to the impeller from the impeller top surface after taking a 'U' turn at the top of the surface (Mavros et al., 1996, Ranade and Dommeti, 1996, Aubin et al., 2001).

Vectorial maps presented in Figure (6.35), Figure (6.36) and Figure (6.37) show that high velocities exist only below the impeller, and low velocities prevail elsewhere in the vessel, giving rise to poor mixing conditions. In the outflow of the impeller, the fluid is discharged axially. Once the high speed, down-flowing jet imparted by the impeller encounters the vessel bottom, fluid moves along the bottom and up the vessel wall. Due to the low pressure regions behind impeller blades, most of the fluid is taken in at the top of the impeller swept volume, with some fluid being drawn into vessel side.

This overall qualitative picture is confirmed by many investigators, including Ranade and Joshi, 1989, Rewatkar et al., 1990, Jaworski et al., 1991, Rewatkar & Joshi, 1991, Ranade et al., 1992, Fokema et al., 1994, Moore and Cossor 1995, Sahu and Joshi, 1995, Armenante and Chou, 1996, Mavros et al., 1996, Armenante et al., 1997, Joshi et al., 1998, Sahu et al., 1998, Brucato et al., 1998, Sheng et al., 1998, Fangary et al., 2000, Wu and Pullum, 2000, Aubin et al., 2001, Kunciewicz and Pietrzykowski, 2001, Wu et al., 2001, Jaworski et al., 2001, Bugay et al., 2002, Chapple et al., 2002, Aubin et al., 2004, Kukukova et al., 2005, and Lanchlan et al., 2006.

Considering the axial velocity component, the maximum down-flowing velocities occur in the impeller discharge region. In the upper part of the vessel, axial velocities are small, generally flowing downwards. The radial velocity component is high in the planes above and below the impeller only and tangential velocities are localized in the rest of the vessel. At the free liquid surface, velocity magnitudes diminished, except at very high impeller speed. Axial velocity below the impeller remained higher than that above the impeller due to the influence of impeller jet expansion. Area weighted average velocity

was calculated and is presented in Figure (6.35), Figure (6.36) and Figure (6.37). Axial, radial and tangential velocities are negative downward towards tank bottom, inward towards shaft, and clockwise with impeller rotation, respectively. Axial and tangential velocities were found to be consistently larger than radial velocities, indicating the existence of fluid swirling in the vessel. High impeller speeds gave a more tangentially directed discharge and axially downward pumped flow.

Increasing xanthan gum concentration resulted in decreasing all velocity components. However, the decrease in axial velocity was larger than that in tangential velocity, indicating that increasing xanthan gum concentration affects impeller pumping more than impeller circulation. With increasing xanthan gum concentration, regions of axially upward velocities disappeared, and a region of axially upward velocities was established beneath the impeller hub. Regions of high tangential velocities shrunk slightly and moved closer to the impeller. Swirling action reduced when xanthan gum solution increased as values of tangential velocities became smaller both above and below the impeller.

A100 & A200 impellers produced more tangentially than axially directed flow, whereas the A310 impeller was capable of producing an axially and tangentially balanced flow. The axial down flow induced by A100 was only 25% greater than that induced by A200. However, the axial flow induced by A310 was 156% greater than that induced by A200. Tangential velocities induced by A100 and A200 were larger than that induced by A310. The main difference in flow patterns generated by the different impellers occurred between the impeller zone and the vessel bottom. Although all impellers generated axial flow directly below them, A100 produced a flow that was more directed to the vessel wall (Dickey and Fasano, 2004). Both A100 and A310 produced a flow that was more directed downward than A200.

7. Conclusions & Recommendations for Future Work

7.1 Conclusions

- High impeller speed disturbs the fluid in the vessel, resulting in reduced dead zones and channeling. Increasing xanthan gum flowrate reduces mean residence time in the vessel, forcing the material to leave the vessel faster and hence increasing channeling and reducing fully mixed volume. As xanthan gum concentration increases, channeling and dead zones in the vessel increase because energy delivered by the impeller is dissipated in the more concentrated solution without producing enough mixing in the vessel. Relocating the exit location to the side of the mixing vessel increases channeling and decreases fully mixed volume because a large percentage of the material will exit without being drawn into the mixing zone.
- CFD prediction of system dynamic response was in good agreement with the response measured experimentally, especially at high impeller speed, low xanthan gum flowrate and low xanthan gum concentration. CFD was unable to predict the severe channeling occurring in the mixing vessel, quantified by the sudden bump (sharp increase in dynamic response curves). However, pathlines generated by CFD were able to distinguish the presence of channeling and dead zones in the vessel.
- Impeller type can affect the performance of the mixing process. The following impellers are ranked from the best performance to the worst in the vessel: A320>A310>A100>A200. The efficiency of an impeller depends on the lift force and drag force. Impellers which can produce high lift and small drag can be very efficient. Streamlined (A320), sleek twisted (A310) and contoured-shaped (A100) blades can give rise to high lift force compared with the straight and sharp blades of A200. Convex blades (A320) have the tendency to deflect the flow over

impeller surface. Such blades do not let the flow continue in a straight-lined motion, resulting in decreasing pressure on the side of impeller normal to the direction of flow and consequently increasing lift force (Coanda Effect, Bertin, 2002). A320 has the greatest width among all other impellers used, giving rise to high lift force. Streamlined blades (A320), sleeked twisted (A310) and contoured-shaped (A100) blades produce small form drag compared with sharp plate-like blades (A200). The ratio D_c/D and H_c/D_c for A310 is bigger than those for A200 and A100. The noticeable performance of A310 in enhancing vessel dynamics observed by decreasing channelling and increasing fully mixed volume can be related to this impeller's ability to induce more motion in the vessel.

- The performance of continuous mixed vessels can be improved by increasing the impeller speed, decreasing the feed flow rate, and decreasing the yield stress (by reducing the solution mass concentration). However, decreasing feed flow rate and solution mass concentration is likely not a viable solution because a reduction in production capacity would result. Increasing the impeller speed may require modification to the motor, and higher impeller speeds can cause air entrainment. Therefore, other remedies such as relocating the feed and/or exit locations and using the correct impeller must be taken into consideration. The results show that the extent of non-ideal flow was reduced using the bottom output and flow efficiency in the vessel was enhanced using an A320 impeller.
- An overall picture of mixing in continuous-flow mixers can thus be depicted as follows: once the fluid enters the vessel, operation conditions can either enhance or deteriorate the overall performance of the process. Low impeller speed, high solution flowrate, or high solution concentration will form a cavern around the impeller. The stagnant fluid in the vessel will contribute to channeling in the vessel. Material from the inlet will not have the potential to go to the well mixed region close to the impeller instead material will take a short-cut to the outlet.

NOMENCLATURE

a	Linearized coefficient of Φ
A	Control volume surface area, m^2
a_1, a_2	Model parameters in discrete time domain
b	Impeller number of blades
C	Impeller clearance off vessel bottom, m
C_m	Solution mass concentration
C'_m	Deviation in solution mass concentration, $C'_m = C_m - C_{m,ss}$
$C_{m,in}$	Inlet solution mass concentration
$C_{m,out}$	Inlet solution mass concentration
$C_{m,ss}$	Solution mass concentration at steady state conditions
d	Inlet pipe diameter, m
D	Impeller diameter, m
d_1, d_2	Model parameters in discrete time domain
D_c	Cavern diameter, m
de	Momentum conductance, $kg/m.s^2$
De	Impeller equivalent diameter, m
$D_{i,m}$	Diffusion coefficient of spices i in mixture m , m/s^2
E_1	Impeller pumping efficiency
E_2	Impeller circulation efficiency
e_t	White noise signal
e_t^f	Filtered white noise signal
f	Percentage of channeling, fraction
$F(\Phi)$	A function that incorporates any spatial discretization
F_a	Axial force imparted by the impeller, N
Fe	Strength of convection, $kg/m^2.s$
g	Gravitational acceleration, m/s^2
G_1	Transfer function for channeling zone
G_2	Transfer function for mixing zone
$G_{\text{mixing vessel}}$	Continuous-time domain mixing vessel transfer function
$\hat{G}(q)$	Discrete time domain mixing vessel transfer function
H	Impeller head, m
H_c	Cavern height, m
J_N	Cost function
K	Consistency index, $Pa.s^n$

K_R	Power number at Reynolds number equals 1 in Zappenfeld and Mersmann (1988) correlation (Table 2-3)
k_s	Proportionality constant in Metzner and Otto relationship
l	Impeller blade length, m
L	Length of input-output data
Le	Impeller equivalent height, m
M	Torque, N.m
n	Power law index
N	Impeller rotational speed, rpm
N_{faces}	Number of faces enclosing the cell
N_s	Effective number of blade edge
p	Impeller blade pitch, m
P	Power, W
q	Backward shift operator
Q	Solution flowrate, m ³ /s
Q_c	Overall liquid circulation generate in impeller swept volume , m ³ /s
Q_P	Impeller pumping flowrate generate in impeller swept volume, m ³ /s
Q_p	Impeller pumping capacity, m ³ /s
R	Percentage of recirculation, fraction
r, θ, z	Cylindrical coordinate
R^Φ	Unscaled residual
R_c^Φ	Scaled residual
s	Ratio of impeller diameter to vessel diameter
S_Φ	Source term in general transport equation
\bar{S}_Φ	Volume average source term in general transport equation
t	Time, sec
T	Vessel diameter, m
T_1	Time delay for channeling zone, s
T_2	Time delay for mixing zone, s
t_m	Mixing time in a batch mixing vessel, sec
t_s	Sampling time, sec
U	Impeller speed, m/s
u	Input signal
u_t^b	Frequency modulated, random binary input signal
V	Solution volume, m ³
$V_{\text{fully mixed}}$	Volume of fully mixed region, m ³

w	Impeller blade width, m
x, y, z	Rectangular coordinate
y	Output signal
y_t^b	Frequency modulated, random binary output signal
Z	Liquid depth in mixing vessel, m

Greek Letters

$\dot{\gamma}_{avg}$	Average Shear rate, s^{-1}
$\dot{\gamma}$	Shear rate, s^{-1}
α	Under relaxation factor
Γ_Φ	Diffusion coefficient of Φ , m/s^2
δ	Distance between nodes or faces, m
Δt	Time step, sec
Δw	Vessel wall proximity factor in Calderbank and Moo-Young equation (Table 2-3)
ζ_{av}	Power input per unit mass of material, W/kg
η	Apparent (non-Newtonian) viscosity, $N.s/m^2$
η_∞	Viscosity at infinite shear rate, $N.s/m^2$
η_c	Average circulation rate per unit power consumption
η_o	Viscosity at zero shear rate, $N.s/m^2$
η_p	Average pumping rate per unit power consumption
μ	Fluid viscosity, $N.s/m^2$
μ_o	Fluid yielding viscosity, $N.s/m^2$
ξ	Constant in Yasuada and Ellis rheological model (Table 1-2)
ρ	Fluid density, Kg/m^3
$\rho_1, \rho_2, \dots, \rho_9$	Model parameters in discrete time domain
τ	Shear stress, N/m^2
τ_1	Time constant for channeling, s
$\tau_{1/2}$	Shear stress at which viscosity drops to half its zero shear value, N/m^2
τ_2	Time constant for mixing zone, s
τ_m	Mean residence time in mixing vessel, s^{-1}
τ_y	Yield stress, N/m^2
ω	Frequency, rad/s

ω_{a1}	Frequency at which the magnitude of Bode plot of the partial derivative of the dynamic model with respect to a_1 is maximum, rad/s
ω_{a2}	Frequency at which the magnitude of Bode plot of the partial derivative of the dynamic model with respect to a_2 is maximum, rad/s
ω_f	Frequency at which the magnitude of Bode plot of the partial derivative of the dynamic model with respect to f is maximum, rad/s
ω_R	Frequency at which the magnitude of Bode plot of the partial derivative of the dynamic model with respect to R is maximum, rad/s

Mathematical Operations

$\frac{\partial}{\partial t}$	Partial derivative
\int_{CV}	Integration on control volume
\int_A	Integration on control volume area
∇	Del or nabla operator
div	Divergence of vector field
grad	Gradient of a scalar field
$q-1$	Backward shift operator

Dimensionless Numbers

Fl	Primary flow number
Fl_c	Secondary flow number
Fr	Froude number
N_f	Axial force number
Pe	Peclet number
Po	Power number
Po_t	Impeller turbulent power number
Re	Reynolds number
Re_y	Yield Stress Reynolds number

Vectors, Matrices & Tensors

$(\nabla\Phi)_n$	Magnitude of $\nabla\Phi$ normal to face f
\vec{r}	Displacement vector pointed from upstream cell center to the face midpoint (center)
$\overline{\overline{D}}$	Rate of deformation (or strain) tensor
\mathbf{g}	Gravitational acceleration vector
\mathbf{I}	Identity matrix
J_i	Concentration gradient diffusion flux of species i .
\mathbf{p}	Fluid pressure vector
R_i	Net rate of production of species i by chemical reaction
S_i	Rate of creation by addition from the dispersed phase plus any other sources
\mathbf{u}	Velocity vector
Y_i	Local mass fraction of species i
$\rho\mathbf{u}$	Mass velocity vector
$\rho\mathbf{u}\mathbf{u}$	Connective momentum tensor
$\boldsymbol{\tau}$	Shear stress tensor
Φ	General transport property

Subscripts

axial	Axial velocity
f	Cell face
i	Species in a mixture
m	Mixture
nb	Neighbor cells
new	New value of Φ obtained after using under relaxation factor
old	Old value of Φ obtained before using under relaxation factor
p	Node P in Figure (5.2) Grid Notation
radial	Radial velocity
tangential	Tangential velocity

Superscripts

\rightarrow	Vector of transport property
m	Value of any scalar quantity Φ at the corresponding time step

REFERENCES

Abbot, M. B. and Basco, D.R., "Computational Fluid Dynamics – An Introduction for Engineers", Longman Scientific & Technical, England, 1989.

Adams, L.W. and Barigou, M., "CFD Analysis of Caverns and Pseudo-Caverns Developed during Mixing of non-Newtonian Fluids", 12th European Conference on Mixing, Bologna, Italy, 27-30 June 2006.

Agricola, G., "De Re Metallica" (originally published in 1556), translated by H.C. Hoover and L.H., Hoover, Dover Publications, New York, 299-300, 1950.

AIChE Equipment Testing Procedure, "Mixing Equipment (Impeller Type)", American Institute of Chemical Engineers, 2001.

Amanullah, A., Hjorth., S.A., Nienow, A.W., "A New Mathematical Model to Predict Cavern Diameters in Highly Shear Thinning, Power Law Liquids using Axial Flow Impeller", Chem. Eng. Sci., 53, 3, 455-469, 1998.

Amanullah, A., Hjorth., S.A., Nienow, A.W., "Cavern Sizes Generated in Highly Shear Thinning Viscous Fluids by Scaba 3SHP1 Impellers", Food and Bioproducts Processing, 75, 232-238, 1997.

Armenante, P. M. and Chou, C. C., "Velocity Profiles in a Baffles Vessel with Single or Double Pitched-Blade Turbine", AIChE J., 42(1), 42-54, 1996.

Armenante, P. M., Luo, C., Chou, C.C, Fort, I., and Medek, J., "Velocity Profiles in a Closed, Unbaffled Vessel: Comparison between Experimental LDV Data and Numerical CFD Predictions", Chem. Eng. Sci., 52(20), 3483-3492, 1997.

- Arratia, P.E., Kukura, J., Lacmobe, J., Muzzio, F.J., "Mixing of Shear-Thinning Fluids with Yield Stress in Stirred Tanks", *AIChE J.*, 52(7), 2310, 2322, 2006.
- Aubin, J., Fletcher, D. F., and Xuereb, C., "Modeling Turbulent Flow in Stirred Tanks with CFD: The Influence of the Modeling Approach, Turbulent Model and Numerical Scheme", *J. Exp. Thermal Fluid Sci.*, 28, 431-445, 2004.
- Aubin, J., Kresta, S.M., Bertrand, J., Xuereb, C., and Fletcher, D.F., "Alternate Operating Methods for Improving the Performance of Continuous Stirred Tank Reactors", *Chem. Eng. Res. Des.*, 84, 569-582, 2006.
- Aubin, J., Mavros, P., Fletcher, D.F., Bertrand, J., Xuereb, C., "Effect of Axial Agitator Configuration (Up-Pumping, Down Pumping, Reverse Rotation) on Flow Patterns Generated in Stirred Vessels", *Chem. Eng. Res. Des.* 79, 845-856, 2001.
- Bakker, A. and Fasano, J.B., "A Computational Study of the Flow Pattern in an Industrial Paper Pulp Chest with a Side Entering Impeller", *AIChE Symposium Series*, 89(293), 118-124, 1993.
- Bakker, A., and Gates, L.E., "Properly Choose Mechanical Agitators for Viscous Liquids", *Chem. Eng. Prog.*, 91(12), 25-34, 1995.
- Barakat, H.Z. and Clark, J.A., "Analytical & Experimental Study of Transient Laminar Natural Convention Flows in a partially Filled Containers", *Proc. 3rd Int. heat, Transfer. Conf., Chicago*, Vol. II, Paper 57, 1966.
- Barnes, H.A., "A Handbook of Elementary Rheology", University of Wales, Institute of non-Newtonian Fluid Mechanics, 2000.
- Barnes, H.A., Hutton, J.F. and Walters, K. "An Introduction to Rheology", Elsevier Science Pub. Co., 1989.

Barth, T.J. Jespersen, D.C., "The Design and Application of Upwind Schemes on Unstructured Meshes", AIAA-89-0366, 1-12, 27th Aerospace Sciences Meeting, Reno, Nevada, 1989.

Bates, R.L., "Agitators", in "Encyclopedia of Chemical Progress Equipments", Reinhold Publishing Corp., 1-22, 1964.

Bertin J.J., "Aerodynamics for Engineers", Upper Saddle River, N.J., Prentice Hall, 2002.
Bittorf, K.J. and Kresta, S. M., "Active Volume of mean Circulation for Stirred tanks Agitated with Axial Impellers", Chem. Eng. Sci., 55, 1325-1335, 2000.

Blasinski, H. and Ryzski, E., "Mixing of non-Newtonian Fluids with Turbine, Propellers, and Paddle Agitators", Int. Chem. Eng., 16(4), 751-754, 1976.

Blazek, J., "Computational Fluid Dynamics: Principles and Applications", Elsevier Science Pub. Co., 2005.

Brid, R.B., Stewart, W.E., Lightfoot, E.N., "Transport Phenomena", John Wiley, 2002.

Brucato, A., Ciofalo, M., Grisafi, F., and Micale, G., "Numerical Prediction of Flow Fields in Baffled Vessels: A Comparison of Alternative Modeling Approaches", Chem. Eng. Sci., 53(21), 3653-3684, 1998.

Bubbico, R., Cave, D., Mazzarotta, B., "Influence of Solid Concentration and Type of Impeller on the Agitation of Large PVC Particles in Water", Récents Progrès en Génie des Procédés, 11(52), 81-88, 1997.

Bugay, S., Escudie, R., Line, A., "Experimental Analysis of Hydrodynamics in Axially Agitated Tank", AIChE J., 48(3), 463-475, 2002.

Bujalski, W., Jaworski, Z., Nienow, A.W.” CFD Study of Homogenization with Dual Rushton Turbines - Comparison with Experimental Results: Part II: The Multiple Reference Frame”, Chem. Eng. Res. Des., 80(1), 97-104, 2002.

Calderbank, P. H. and Moo-Young, M. B., “The Power Characteristics of Agitator for the Mixing of Newtonian & non-Newtonian Fluids”, Chem. Eng. Res. Des., 39, 337-347, 1961.

Calderbank, P. H. and Moo-Young, M. B., “The Prediction of Power Consumption in the Agitation of non-Newtonian Fluids”, Chem. Eng. Res. Des., 37, 26-33, 1959.

Caretto, L.S., Gosman, A.D., Patankar, S.V., Spalding, D.B., “Two Calculation Procedures for Steady, Three-Dimensional Flows with Recirculation”, Proc. 3rd Conf. Numerical Methods in Fluid Dynamics, Paris, Vol. II, 6-67, 1972.

Carrington, S., Odell, J., Fisher, L., Mitchell, J., Hartley, L., “Polyelectrolyte Behaviour of Dilute Xanthan Solutions: Salt Effects on Extensional Rheology”, Polymer 37, 2871–2875, 1996.

Casson, N., “Rheology of Disperse Systems”, Pergamon Press, 1959.

Chapple, D., Kresta, S.M., Wall, A., Afacan, A., “The Effect of Impeller and Tank Geometry on Power Number for a Pitched Blade Turbine”, Chem. Eng. Res. Des., 80, 364-372, 2002.

Chhabra, R. P. and Richardson, J. F., “Non-Newtonian Flow in the Process Industries: Fundamentals and Engineering Applications”, Butterworth Heinemann, 1999.

Chung, T.J., “Computational Fluid Dynamics”, Cambridge University Press, 2002.

Corpstein, R.R., Dove, R.A., and Dickey, D.S., "Stirred Tank Reactor Design", Chem. Eng. Prog., 75(2), 66-74, 1979.

Courant, R., Isaacson, E., and Ress, M., "On the Solution of Non-Linear Hyperbolic Differential Equations by Finite Difference", Comm. Pure. Appl. Math., 5, 243-248, 1952.

Cross, M.M., "Polymer Systems. Deformation and Flow", Macmillan, 1968.

Darwish, M., Asmar, D., Moukalled, F., "A Comparative Assessment within a Multigrid Environment of Segregated Pressure-Based Algorithms for Fluid Flow at All Speeds", Num. Heat Trans., Part B, 45, 49-74, 2004.

Daskopoulos, P. and Harris, C.K., "Three Dimensional CFD Simulations of Turbulent Flow in Baffled Stirred Tanks: An Assessment of the Current Position", IChemE Symposium Series No. 140, 1-8, 1996.

Date, A.W., "Introduction to Computational Fluid Dynamics", Cambridge University Press, 2005.

Deglon, D.A. and Meyer, C.J., "CFD Modeling of Stirred Tanks: Numerical Considerations", Minerals Eng., 19(10), 1059-1068, 2006.

Dickey, D.S. and Fenic J. G., "Dimensional Analysis for Fluid Agitation Systems", Chem. Eng. J, 5, 7-13, 1976.

Doraiswamy, D., Grenville. R. K. and Etchells III A.W., "Two-Score Years of the Metzner-Otto Correlation", Ind. Eng. Chem. Res., 33 (10), 2253-2258, 1994.

Ducla, J.M., Desplanches, H., and Chevalier, J.L., "Effective Viscosity of non-Newtonian Fluids in a Mechanically Stirred Tank", Chem. Eng. Commun., 21, 29-36, 1983.

- Durgaiiah, R.D., "Fluid Mechanics and Machinery", New Age International, New Delhi, India, 2006.
- Edgar, T.F., Himmelblau, D.M., and Lasdon, L.S., "Optimization of Chemical Processes", McGraw-Hill, New York, Second Edition, 2001.
- Edward, L. P., Atiemo-Obeng, V.A., and Kresta, S. M., "Handbook of Industrial Mixing Science & Practice", Wiley-Interscience, 2004.
- Ein-Mozaffari, F., "Macorscale Mixing & Dynamic Behavior of Agitated Pulp Stock Chests", PhD Thesis, University of British Columbia, 2002.
- Ein-Mozaffari, F., Bennington, C.P.J, Dumont, G.A., "Performance & Design of Agitated Pulp Stock", Appita J., 56(2), 127-133, 2003.
- Ein-Mozaffari, F., Bennington, C.P.J, Dumont, G.A., "Suspension Yield Stress and the Dynamic Response of Agitated Pulp Chests", Chem. Eng. Sci., 60(8-9), 2399-2408, 2005.
- Ein-Mozaffari, F., Kammer, L.C., and Bennington, C.P.J., "Performance and Design of Agitated Pulp Stock Chests", PACEWST Conference, Whistler, BC, Paper No. 3B6,1-8, 2001.
- Ein-Mozaffari, F., Kammer, L.C., Dumont, G.A., and Bennington, C.P.J., "Dynamic Modeling of Agitated Pulp Stock Chests", Control System Conference, Stockholm, Sweden, 194-195, 2002 A.
- Ein-Mozaffari, F., Kammer, L.C., Dumont, G.A., and Bennington, C.P.J., "Design Criteria for Dynamic Behavior of Agitated Pulp Stick Chests", PACEWST Conference, Jasper, Alberta, Paper No. 2B2, 1-9, 2002 B.

Ein-Mozaffari, F., Kammer, L.C., Dumont, G.A., and Bennington, C.P.J., "The Effect of Operating Conditions and Design Parameters on the Dynamic Behaviour of Agitated Pulp Stock Chests", *Can. J. Chem. Eng.*, 82(1), 154-161, 2004.

Elson, T. P., "Mixing of Fluids Possessing a Yield Stress", *Proc. 6th European Conf. on Mixing*, Pavia, Italy, 458-492, 1988.

Elson, T. P., "X-ray Flow Visualization of Flow Patterns during the Mixing of Yield Stress, Newtonian and Dilatant Fluids", *Chem. Eng. Comm.*, 94, 143-158, 1990 A.

Elson, T. P., "The Growth of Caverns Formed around Rotating Impellers during the Mixing of Yield Stress Fluids", *Chem. Eng. Comm.*, 96, 303-319, 1990 B.

Elson, T. P., Cheesman, D. J., and Nienow, A. W., "X-Ray Studies of Cavern Sizes and Mixing Performance with Fluids Possessing a Yield Stress", *Chem. Eng. Sci.*, 41(10), 2555-2562, 1986.

Elson, T.P., "Mixing of Fluids Possessing a Yield Stress", *6th European Conference on Mixing*, Pavia, Italy, 485-492, 24-26 May, 1988.

Etchells, A.W., Ford, W.N., and Short, D.G.R., "Mixing of Bingham Plastics on an Industrial Scale", *Fluid Mixing III, IChE Symposium Series*, No. 108, 271-285, 1987.

Fangary, Y.S., Barigoi, M., Seville, J.P.K., Parker, D.J., "Fluid Trajectories in a Stirred Vessel of non-Newtonian Liquid Using Positron Emission Particle Tracking", *Chem. Eng. Sci.*, 55, 5969-5979, 2000.

Fasano, J.B., Miller, J.L., and Pasley, S.A., "Consider Mechanical Design of Agitators", *Chem. Eng. Prog.*, 91 (8), 60-71, 1995.

Ferguson, J. and Kemblowski, Z., "Applied Fluid Rheology", Elsevier Applied Science, London and New York, 1991.

Fletcher C. A. J., "Computational Techniques for Fluid Dynamics", Springer-Verlag, Berlin, Heidelberg, 1991.

Fletcher, R., "Practical Methods of Optimization", John Wiley Sons, Chichester, UK, Second Edition, 1987.

Fluent 6.3, User's Guide Documentation, Fluent Inc., 2006.

Fokema, M.D., Kretsa S.M. and Wood P.E., "Importance of Using Correct Impeller Boundary Conditions for CFD Simulations of Stirred Tanks", Can. J. Chem. Eng., 72, 177-183, 1994.

Ford, C, Ein-Mozaffari, F., Bennington, C.P.J, Taghipour, F., "Simulation of Mixing Dynamics in Agitated Pulp Stock Chests Using CFD", AIChE J., 52(10), 3562-3569, 2006.

Ford, C. "CFD Simulation of Mixing Dynamics in Agitated Pulp Stock Chests", M.Sc. Thesis, University of British Columbia, 2004.

Foresti, R. and Liu, T., "Agitation of non-Newtonian Liquids", Ind. Eng. Chem., 51(7), 860-864, 1959.

Galindo, E., and Nienow, A.W., "Mixing of Highly Viscous Simulated Xanthan Fermentation broths with the Lightnin A315 Impeller", Biotechnol. Prog., 8, 233-239, 1992.

Galindo, E., and Nienow, A.W., "Performance of the Scaba 6SRGT Agitator in Mixing of Simulated Xanthan Gum Broths", Chem. Eng. Technol., 16, 102-108, 1993.

Galindo, E., Arguello, M.A., Velasco, D., Albiter, V., Martinez, A., "A Comparison of Cavern Development in Mixing a Yield Stress Fluid by Rushton and Intemig Impellers", Chem. Eng. Technol., 19, 315-323, 1996.

Galindo, E., Nienow, A.W., and Badham, R.S., "Mixing of Simulated Xanthan Gum Broths", Proceeding 2nd International Conference on Bioreactor Fluid Dynamics", Cranfield, UK, 65, 78, 1988.

Galindo, E., Torrestiana, B, and Garcia-Rejon, A., "Rheological Characterization of Xanthan Fermentation Broths and their Reconstructed Solutions", Bioprocess Eng., 4, 113-118, 1989.

Garcia-Ochoa, F and Casas, J.A., "Apparent Yield Stress in Xanthan Gum Solutions at Low Concentrations", The Chemical Engineering Journal, 53, B41-B46, 1994.

Gentry, R. A., Martin, R.E., and Daly, B.J., "An Eulerian Differencing Method for Unsteady Compressible Flow Problems", J. Compu. Phys. 1, 87-94, 1966.

Greenbaum, A., "Iterative Methods for Solving Linear Systems", SIAM (Society of Industrial & Applied Mathematics), 1997.

Harlow, F.H. and Welch, J.E., "Numerical Calculation of Time-Dependent Viscous Incompressible Flow of Fluid with Free Surface", Phys. Fluids, 8, 2182-289, 1965.

Harnby, N., Edwards, M.F., and Nienow, A.W., "Mixing in Process Industry", Butterworth Heinemann, 1997.

Harvey, A. D., Wood, S.P., Leng, D.E., "Experimental and Computational Study of Multiple Impeller Flows", Chem. Eng. Sci., 52(9), 1479-1491, 1997.

Hirata, Y. and Aoshima, Y., "Flow Characteristics and Power Consumption in an Agitated Shear Thinning Plastic Fluid", IChemE Symposium Series No. 136, Fluid Mixing VIII, Cambridge UK, 415-422, 1995.

Hirata, Y. and Aoshima, Y., "Formation and Growth of Cavern in Yield Stress Fluids Agitated under Baffled and Non-Baffled Conditions", Chem. Eng. Res. Des., 74, 438-444, 1996.

Hirata, Y., Nienow, A. W., and Moore, I. P. T., "Estimation of Cavern Sizes in a Shear Thinning Plastic Fluids Agitated by a Rushton Turbine based on LAD Measurements", J. Chem. Eng. Japan., 27(2), 235-237, 1994.

Hirata, Y., Nienow, A. W., and Moore, I. P. T., "LDA Studies of Velocity Distributions and Cavern Sizes in a Yield Stress Fluid Agitated by a Rushton Turbine", Proc. 7th European Conf. on Mixing, UK, London, Vol.1, 167-172, 1991.

Holland, F.A., and Chapman, F.S., "Liquid Mixing and Processing in Stirred Tanks", Reinhold Publishing Corp., 1966.

Honnote, M., Flores, F., Torres L, and Galindo, E., "Apparent Yield Stress Estimation in xanthan Gum Solutions and Fermentation Broths using a Low-Cost Viscometer", The Chem. Eng. J., 45, B49-B56, 1991.

Houcine, I., Plasari, E., and David, R., "Effects of the Stired Tank's Design on Power Consumption and Mixing Time in liquid Phase", Chem. Eng. Technol., 23(7), 605-613, 2000.

Ibrahim, S. and Nienow, A.W., "Power Curves and Flow Patterns for a Range of Impellers in Newtonian Fluids $40 < Re < 5 \times 10^5$ ", Chem. Eng. Res. Des., 485-491, 1995.

Ihejirika, I and Ein-Mozaffari, F., "Using CFD and Ultrasonic Velocimetry to Study the Mixing of Pseudoplastic Fluids with a Helical Ribbon Impeller", *Chem. Eng. Technol.*, 30(5), 606-614, 2007.

Iranshahi, A., Heniche, M., Bertrand, F., Tanguy, P.A., "Numerical Investigation of the Mixing Efficiency of the Ekato Paravisc Impeller", *Chem. Eng. Sci.*, 61, 2609-2617, 2006.

Issa, R.I., "Solution of the Implicitly Discretised Fluid Flow Equations by Operator-Splitting", *J. Comput. Phys.*, 62, 40-65, 1986.

Jang, D.S., Jetli, R, and Acharya, S., "Comparison of the PISO, SIMPLER and SIMPLEC Algorithms for the Treatment of the Pressure-Velocity Coupling in Steady Flow Problems", *Num. Heat Trans.*, 10, 209-228, 1986.

Jansson, P. E., Kenne, L., Lindberg, B., "Structure of the Extracellular Polysaccharide from *Xanthomonas Campestris*", *Carbohydr. Res.*, 45, 275-282, 1975.

Jaworski, Z., Dyster, K. N., Nienow, A.W., "The Effect of Size, Location and Pumping Direction of Pitched Blades Turbine Impellers on Flow Patterns: LDA Measurements & CFD Predictions", *Chem. Res. Des.*, 79, 887-894, 2001.

Jaworski, Z., Nienow, A.W., Dyster, "An LDA Study of Turbulent Flow in Field in a Baffled Vessel Agitated by an Axial, Down Pumping Hydrofoil Impeller", *Can. J. Chem. Eng.*, 74, 3-15, 1996.

Jaworski, Z., Nienow, A.W., Koutsakos, E., Dyster, K., Bujalski, W., "An LDA Study of Turbulent Flow in Baffled Vessel Agitated by a Pitched Blade Turbine", *Chem. Eng. Res. Des.*, 69, 313-320, 1991.

- Jian, M., Zhengming, G., Litian, S., "CFD Simulation of Mixing in a Stirred Tank with Multiple Hydrofoil Impellers", *Chinese J. Chem. Eng.*, 13 (5), 583-588, 2005.
- Johnson, D.N., and Hubbard, D.W., "Mixing by Impeller Agitation in Continuous Flow Systems Containing Polysaccharide Solutions", *Biotech and Bioeng*, 16(9), 1283-1297, 1974.
- Joshi, J. B., Sahu, A. K., Kumar, P., "LDA Measurements and CFD Simulations of Flow Generated by Impellers in Mechanically Agitated Reactors", *Sadhana*, 23, Parts 5&6, 505-539, 1998.
- Kammer, L.C., Ein-Mozaffari, F., Dumont, G.A., Bennington, C.P.J. "Identification of Channeling and Recirculation Parameters of Agitated Pulp Stock Chests", *J. Process Control*, 15(1), 31-38, 2005.
- Katzbauer, B., "Properties and Application of Xanthan Gum", *Polymer Degradation and Stability*, 59, 81-84, 1998.
- Kelly, W. and Gigas, B., "Using CFD to Predict the Behavior of Power law Fluids near Axial- Flow Impellers Operating in the Transitional Flow Regime", *Chem. Eng. Sci.*, 58, 2141-2152, 2003.
- Kelly, W.J. and Humphrey, A.E., "Computational Fluid Dynamics Model for Predicting Flow of Viscous Fluids in a Large Fermentor with Hydrofoil Flow Impellers and Internal Cooling Coils", *Biotchnol. Prog.*, 14, 248-258, 1998.
- Kennedy, J. F. and Bradshaw, I. J. "Production, Properties and Applications of Xanthan", *Prog. Ind. Microbiol.*, 19, 319-371, 1984.
- Kerdouss, F., Bannari, A., Proulx, P. "CFD Modeling of Gas Dispersion and Bubble Size in a Double Turbine Stirred Tank", *Chem. Eng. Sci.*, 61(10), 3313-3322, 2006.

- Khopkar, A.R., Kasat, G.R., Pandit, A.B., Ranade, V.V., "Computational Fluid Dynamics Simulation of the Solid Suspension in a Stirred Slurry Reactor", *Ind. Eng. Chem. Res.*, 45(12), 4416-4428, 2006.
- Khopkar, A.R., Mavros, P., Ranade, V.V., and Bertrand, J., "Simulation of Flow Generated by an Axial Flow Impeller-Bath and Continuous Operation", *Chem. Eng. Res Des.*, 82,737-751, 2004.
- King, R., "Fluid Mechanics of Mixing: Modeling, Operations, and Experimental Techniques", Kluwer Academic Publishers, 1992.
- King, R.L., Hiller, R.A., and Tatterson, G.B., "Power Consumption in a Mixer", *AIChE J.*, 34(3), 506-509, 1988.
- Knoch, A., "Influence of non-Newtonian Flow Behavior on Mixing Process Characteristics", *Chem. Eng. Technol.*, 22(2), 112-118, 1999.
- Koutsakos, E., Nineow A.W., and Dyster, K.N., "Laser Anemometry Study of Shear Thinning Fluids Agitated by a Rushton Turbine", *ICheE Symposium Series*, No. 121, "Fluid Mixing IV", Bradford, UK, 51-73, 1990.
- Kresta, S.M. and Wood, P.E., "The Mean Flow Field Produced by a 45° Pitched Blade Turbine: Changes in Circulation Pattern due to Off Bottom Clearance", *Can. J. Chem. Eng.*, 71, 42-53, 1993.
- Kubera, P.M. and Oldshue, J.Y., "Advanced Impeller Technologies Match Mixing Performance to Process Needs", *Randol Gold Forum*, Vancouver, Canada, 1992.

- Kukukova, A., Mostek, M., Jahoda, M., and Machon, V., "CFD Prediction of Flow and Homogenization in a Stirred Vessel: Part I Vessel with One and Two Impellers", Chem. Eng. Technol. 28 (10), 1125-1133, 2005.
- Kumaresan, T. and Joshi, J.B., "Effect of Impeller Design on the Flow Pattern and Mixing in Stirred Tanks", Chem. Eng. J., 115, 173-193, 2006.
- Kumaresan, T., Nere, N.K., Joshi, J.B., "Effect of Internals on the Flow Pattern and Mixing in Stirred Tanks", Ind. Eng. Chem., 44, 9951-9961, 2005.
- Kunczewicz, C. and Pietrzykowski, M., "Hydrodynamic Model of a Mixing Vessel with Pitched-Blade Turbine", Chem. Eng. Sci., 56, 4659-4672, 2001.
- Lanchlan, J.W., Graham, L. J., Nyuyen, B., Mehidi, M.N.N., "Energy Efficiency Study on Axial Flow Impellers", Chem. Eng. Processing, 45, 625-632, 2006.
- Lane, G.L., Schwarz, M.P., Evans, G.M., "Numerical Modeling of Gas-Liquid Flow in Stirred Tanks", Chem. Eng. Sci., 60(8-9), 2203-2214, 2005.
- Leonard, B.P., "A Stable and Accurate Convective Modeling Procedure Based on Quadratic Upstream Interpolation", Comput. Methods. Appl. Mech. Eng., 19, 59-98, 1979.
- Leonard, B. P., Mokhtari, S., "Beyond First-Order Upwinding: The Ultra-Sharp Alternative for Non-oscillatory Steady-State Simulation of Convection", Int. J. Num. Method. Eng., 30, 729-766, 1990.
- Levenspiel, O., "Chemical Reaction Engineering", John Wiley and Sons, 3 rd edition, 1988.
- Lighnin Mixing Equipment Co. Inc., "A 310 Versus 1.0 Pitch Ratio Propeller – Comparison Portable Mixers", Lighnin Mixing Equipment Co. Inc, 1985.

Lighnin Mixing Equipment Co. Inc., "A310 Impeller for Flow Controlled Applications", Technical Report, Lighnin Mixing Equipment Co. Inc, 1981.

Ljung, L., "System Identification: Theory for the User" 3rd Edition, PTR Prentice Hall, USA, 1999.

Luo, J.Y., Gosman, A.D., Issa, R.I., Middleton, J.C., Fitzgerald, M.K., "Full Flow Filed Computation of Mixing in Baffle Stirred Vessels", Chem. Eng. Res. Des., 71, 342-344, 1993.

Luo, J.Y., Gosman, A.D., Issa, R.I., "Prediction of Impeller-Induced Flows in Mixing Vessels using Multiple Frames of Reference", Inst. Chem. Eng. Sympo. Ser., 136, 549-556, 1994.

Macosko, C. W., "Rheology: Principles, Measurements, and Applications", Advances in Interfacial Engineering Series, New York: VCH, 1994.

Malkin, A. Y. and Isayev, A. I., "Rheology. Concepts, Methods, and Applications", ChemTec Publishing, 2006.

Malkin, A. Y., "Rheology Fundamentals", Fundamental Topics in Rheology Series, ChemTec Publishing, 1994.

Marshall, E.M.Y, Tayalia, Y., Oshinowo, L., Weetman, R., "Comparison of Turbulence Models in CFD Predictions of Flow Number and Power Draw in Stirred Tanks", Section No. 7.26, Mixing XVII, Banff, Alberta, Canada, 1999.

Mavros, P., Naude, I., Xuereb, C., and Bertrand, J., "Laser Doppler Velocimetry in Agitated Vessels: Effect of Continuous Liquid Stream on Flow Patterns", Chem. Eng. Res. Des., 75, 763-776, 1997.

Mavros, P., Xubereb, C., and Bertrand, J., "Determination of 3-D Flow Fields in Agitated Vessels by Laser-Doppler Velocimetry. Effect of Impeller Type and Liquid Viscosity on Liquid Flow Patterns", Chem. Eng. Res. Des., 74, 658-668, 1996.

Mavros, P., Xuereb, C., Fort, I., and Bertrand, J., "Investigation of Flow Patterns in Continuous-Flow Stirred Vessels by Laser Doppler Velocimetry", Can. J. Chem. Eng., 80, 591-600, 2002 A.

Mavros, P., Xuereb, C., Fort, I., and Bertrand, J., "Investigation by laser Doppler Velocimetry of the Effects of Liquid Flow Rates and Feed Positions on the Flow Patterns Induced in a Stirred Tank by an Axial-flow Impeller", Chem. Eng. Sci., 57, 3939-3952, 2002 B.

McCabe, W.L., Smith J. C., Harriott, P., "Unit Operations of Chemical Engineering", McGraw-Hill, 7th Edition, 2005.

McDonough, R.J., "Mixing for the Process Industries", Van Nostrand Reinhold, New York, 1992.

Medek, J. and Fort, I., "Mixing in Vessel with Eccentric Mixer", Proceedings 5th European Conference on Mixing, Paper 27, Würzburg, Germany, 263-271, 1985.

Metzner, A. B. and Otto, R. E., "Agitation of non-Newtonian Fluids", AIChE J., 3(1), 3-10, 1957.

Metzner, A.B., Feehs, R.H., Ramos, H.L., Otto, R.E., and Tuthill, J.D., "Agitation of Viscous Newtonian and Non- Newtonian Fluids", AIChE J., 7(1), 3-9, 1961.

Mishra, V.P., Dyster, K.N., Jaworski, Z., Nienow, A.W., Mckemmie, J., "A Study of an Up- and a Down-Pumping Wide Blade Hydrofoil Impeller: Part I. LAD Measurements", Can. J. Chem. Eng., 76, 577-588, 1998.

- Mmbaga, J.P., "The Use of Mixing-Sensitive Chemical Reactions to Characterize Mixing in The Liquid Phase of Fibre Suspensions", PhD Thesis, University of British Columbia, 1999.
- Moilanen, P., Laakkonen, M., and Aittamäa, J., "Modeling Aerated Fermenters with Computational Fluid Dynamics", *Ind. Eng. Chem. Res.*, 45(25), 8656-8663, 2006.
- Morre, I.P.T. and Cossor, G., "Velocity Distributions in a Stirred tank Containing a Yield Stress Fluid", *Chem. Eng. Sci.*, 50(15), 2467-2481, 1995.
- Morrison, F. A., "Understanding Rheology", Oxford University Press, 2001.
- Moukalled, F. and Darwish, M., "A Comparative Assessment of the Performance of Mass Conservative-Based Algorithms for Incompressible Multiphase Flows", *Num. Heat. Trans., Part B*, 42, 259-283, 2002.
- Moukalled, F. and Darwish, M., "Pressure-Based Algorithm for Multifluid Flows at All Speeds- Part I: Mass Conservation Formulation", *Num. Heat. Trans., Part B*, 45, 495-522, 2004 A.
- Moukalled, F. and Darwish, M., "The Performance of Geometric Conservation-Based Algorithms for Incompressible Multifluid Flow", *Num. Heat. Trans., Part B*, 45, 343-368, 2004 B.
- Muller C., Anrhouch, M., Lecourtier, J., and Chaveteau, G., "Salt Dependence of the Conformation of a Single-Stranded Xanthan", *Int. J. Biol. Macromol.*, 8, 167-172, 1986.
- Naude, I., Xuereb, C., Bertrand, J., "Direct Prediction of the Flows Induced by a Propeller in an Agitated Vessel using an Unstructured Mesh", *Can. J. Chem. Eng.*, 76(3), 631-640, 1998.

- Nienow, A.W., "Agitators for Mycelial Fermentations", Trends. Biotechnol., 8, 224-233, 1990.
- Nienow, A.W., "Hydrodynamics of Stirred Bioreactors", App. Mech. Rev., 51(1), 3-32, 1998.
- Nienow, A.W., "Mixing Studies of High Viscosity Fermentation Processes Xanthan Gum", The World Biotechnology Report, Vol. I, London, UK, 293-304, 1984.
- Nienow, A.W., and Elson, T.P., "Aspects of Mixing in Rheologically Complex Fluids", Chem. Eng. Res. Des., 66, 5-15, 1988.
- Nouri, J.M. and Hockey, R.M., "Power Number Correlation between Newtonian and non-Newtonian Fluids in a Mixing Vessel", J. Chem. Eng. Japan, 31(5), 848-852, 1998.
- Oldshue, J.Y. and Todd, D.B., "Mixing and Blending", in "Encyclopedia of Chemical Technology", Vol. 15, 604-637, John Wiley & Sons Inc, 1981.
- Oldshue, J.Y., "Fluid Mixing in 1989", Chem. Eng. Prog., 85, 33-38, 1989.
- Oldshue, J.Y., "Fluid Mixing Technology", McGraw Hill Publications Co., New York, 1983.
- Oldshue, J.Y., "Let's Understand Mixing", Chem. Tech., 11, 554-561, 1981.
- Oldshue, J.Y., Weetman, R. J., Coyle, C.K., Hoing, J.L., "Mixing with Open Impellers in Higher Viscosity Fluids", Visctech Proceedings, 1989.
- Patankar, S.V., "A Calculation Procedure for Two-Dimensional Elliptic Situations", Num. Heat. Transfer, 4, 409-425, 1981.

Patankar, S.V., "Numerical Heat Transfer and Fluid Flow", Hemisphere Publishing Corporation, Taylor & Francis Group, New York, 1980.

Patankar, S.V., "Numerical Prediction of Three-Dimensional Flows", in Launder, B.E., Studies in Convection: Theory, Measurements and Applications, Vol. I, Academic, New York, 1975.

Patankar, S.V., and Spalding, D.B., "A Calculation Procedure for Heat, Mass and Momentum Transfer in Three-dimensional Parabolic Flows", Int. J. Heat Mass Transfer, 15 (10), 1787-1806, 1972.

Patwardhan, A.W. and Joshi, J.B., "Relation between Flow Pattern and Blending in Stirred Tanks", Ind. Eng. Chem. Res., 38, 3131-3143, 1999.

Perry, R.H., and Green, D.W., "Perry's Chemical Engineers' Handbook", McGraw-Hill, 7th Edition, 1997.

Podolsak, A.K., Tiu, C., Saeki, T., Usui, H., "Rheological Properties and Some Applications for Rhamsan and Xanthan Gum Solutions", Polymer International, 40, 155-167, 1996.

Ramsey, W. D. and Zoller, G.C., "How the Design of Shafts, Seals and Impellers Affects Agitator Performance", Chem. Eng., 30, 52-59, 1976.

Ranade, V.V. and Dommeti, M.S., "Computational Snapshot of Flow Generated by Axial Impellers in Baffled Stirred Vessels", Chem. Eng. Res. Des., 74, 476-484, 1996.

Ranade, V.V. and Joshi, J.B., "Flow Generated by Pitched Blade Turbines I: Measurements using Laser Doppler Anemometer", Chem. Eng. Commun., 81, 197-224, 1989.

Ranade, V.V., "An Efficient Computational Model for Simulating Flow in Stirred Vessels: A Case of Rushton Turbine", *Chem. Eng. Sci.*, 52(24), 4473-2284, 1997.

Ranade, V.V., "Computational Flow Modeling for Chemical Reactor Engineering", Academic Press, 2002.

Ranade, V.V., Mishra, V.P., Saraph, V.S., Deshpande, G.B., Joshi, J.B., "Comparison of Axial Flow Impellers Using a Laser Doppler Anemometer", *Ind. Eng. Chem. Res.*, 31, 2370-2379, 1992.

Renaud, M, Belgacem , M.N., Rinaudo, M., "Rheological Behaviour of Polysaccharide Aqueous Solutions", *Polymer*, 46, 12348–12358, 2005.

Rewatkar, V.B. and Joshi, J.B., "Effect of Impeller Design on Liquid Phase Mixing in Mechanically Agitated Reactors", *Chem. Eng. Commun.*, 102, 1-33, 1991.

Rewatkar, V.B., Raghava Rao, K.S.M.S., and Joshi, J.B., "Power Consumption in Mechanically Agitated Contactors using Pitched Blades Turbine Impellers", *Chem. Eng. Commun.*, 88, 69-90, 1990.

Roberg, K.E., "Numerical Simulations of the Flow of Fiber Suspension in a Side-Entering Mixers", *Récents Progrès en Génie des Procédés*, 11(51), 203-210, 1997.

Rocheffort, W.E. and Middleman, S., "Rheology of Xanthan Gum: Salt, Temperature, and Strain Effects in Oscillatory and Steady Shear Experiments", *J. Rheology*, 31(4), 337-368, 1987.

Rudolph, L., Schaefer, M., Atiemo-Obeng, V., Kraume, M., "Mixing of High Viscosity Fluids: Experimental and Numerical Explorations of Co-Axial Mixers", 12th European Conference on Mixing, Bologna, Italy, 2006.

Runchal, A.K. and Wolfshtein, M., "Numerical Integration Procedure for the Steady State Navier-Stokes Equations", J. Mech. Eng. Sci., 11, 445-452, 1969.

Rushton, J.H., "Design and Utilization of Internal Fittings for Mixing Vessels", 43(12), 649-658, 1947.

Rushton, J.H. and Oldshue J.Y., "Mixing of Liquids" in Chemical Eng. Symposium Series "Reaction Kinetics and Unit Operation", 55(25), 181-198, 1959.

Rushton, J.H. and Oldshue, J.Y., "Mixing - Present Theory and Practice Part I", Chem. Eng. Prog. 49 (4), 161- 168, 1953.

Sahu, A. K. and Joshi, J. B., "Simulation of Flow in Stirred Vessels with Axial Flow Impellers: Effects of Various Numerical Schemes and Turbulence Mode Parameters", Ind. Eng. Chem., 34, 626-639, 1995.

Sahu, A.K., Kumar, P., Joshi, J.B., "Simulation of Flow in Stirred vessel with Axial Flow Impeller: Zonal Modeling and Optimization of Parameters", Ind. Eng. Chem. Res., 37, 2116-2130, 1998.

Sahu, A.K., Kumar, P., Patwardhan, A.W., and Joshi, J.B., "CFD Modeling and Mixing in Stirred Tanks", Chem. Eng. Sci., 54, 2285-2293, 1999.

Samaras, K., Mavros, P., Zamboulis, D., "Effect of Continuous Stream and Agitator Type on CFSTR Mixing State", Ind. Eng. Chem., 45, 4805-4815, 2006 A.

Samaras, K., Mavros, P., Zamboulis, D., "Operability Limits of Continuous-Flow Stirred Tanks", 12 th European Conference on Mixing, Bologna, 2006 B.

Seborg, D.F, Edgar, T.F., and Mellichamp, D.A., "Process Dynamics and Control", John Wiley and Sons, 1989.

Serraano-Carreón, L. and Galindo, E., "Studies on Cavern Development in Mixing a Yield Stress Fluid in a Pilot Scale Proto Fermenter", *Récents Progrès en Génie des Procédés*, 11 (51), 161-168, 1997.

Shekhar, S.M. and Jayanti, S., "Mixing of Power-Law Fluids using Anchors: Metzner-Otto Concept Revisited", *AIChE J.*, 49(1), 30-40, 2003.

Shekhar, S.M. and Jayanti, S., "Mixing of Pseudoplastic Fluid using Helical Ribbon Impellers", *AIChE J.*, 49(11), 2768-2772, 2003.

Sheng, J., Meng, H. and Fox, R., "Validation of CFD Simulations of a Stirred Tank Using Particle Image Velocimetry Data", *Can. J. Chem. Eng.*, 76, 611-625, 1998.

Skelland, A.H.P., "Mixing and Agitation of non-Newtonian Fluids" Chapter 7, 179-209", in Cheremisinoff N.P. and Gupta, R., "Handbook of Fluids in Motion", Ann Arbor Science, 1983.

Smolka, L.B. and Belmonte, A., "Charge Screening Effects on Filament Dynamics in Xanthan Gum Solutions", *J. non-Newtonian Fluid Mech.*, 137, 103-109, 2006.

Solomon, J., Elson, T.P., and Nienow, A. W., "Cavern Sizes in Agitated Fluids with a Yield Stress", *Chem. Eng. Commun.*, 11, 143-164, 1981.

Sommerfeld, M. and Decker, S., "State of the Art and Future Trends in CFD Simulation of Stirred Vessel Hydrodynamics", *Chem. Eng. Technol.*, 27(3), 215-224, 2004.

Sue, Y.S. and Holland, F.A., "Agitation and Mixing of non-Newtonian Fluids", *Chem. Process Eng.*, 63, 110-120, 1968.

Tanner, R.I., "Engineering Rheology", Second Edition, Oxford University Press, 2000.

Tatterson, G.B., "Fluid Mixing & Gas Dispersion in Agitated Tanks", McGraw Hill Inc., 1991.

Tatterson, G. B., "Scale up & Design of Industrial Mixing Processes", McGraw Hill Inc, 1994.

Torres, L.G., Flores, F., and Galindo, E., "Apparent Yield Stress of Xanthan Solutions and Broths", Bioprocess Eng., 12, 41-46, 1995.

Torres, L.G., Nienow, A. W., Sanchez, A., Galindo, E., "The Characterization of Viscoelasticity Parameter and Other Rheological Properties of Various Xanthan Gum Fermentation Broths and Solutions", Bioprocess Eng., 9, 231-237, 1993.

Torrez, C. and Andre, C., "Power Consumption of a Rushton Turbine Mixing Viscous Newtonian and Shear-thinning Fluids: Comparison between Experimental and Numerical Results", Chem. Eng. Techno., 21(7), 599-604, 1998.

Torrez, C. and Andre, C., "Simulation of a Rushton Turbine Mixing Yield Stress Fluids: Application of the Metzner-Otto Concept", Chem. Eng. Technol., 22(8), 701-706, 1999.

Uhl., V.W. and Gary, J. B., "Mixing Theory and Practice", Academic Press, New York, 1966.

Ulbrecht, J.J., and Patterson, G.K., "Mixing of Liquids by Mechanical Agitation", Gordon and Brach Science Publishers, 1985.

Upreti, S.R. and Ein-Mozaffari, F., "Identification of Dynamic Characterization Parameters of Agitated Pulp Chests Using Hybrid Genetic Algorithm", Chem. Eng. Res. Des., 84, 221-230, 2006.

Van Doormal, J.P., Raithby, G.D., "Enhancements of the SIMPLE Method for Predicting Incompressible Fluid Flows", Numer. Heat Transfer., 7, 147-163, 1984.

Versteeg, H.K., & Malalasekera, W., "An Introduction to Computational Fluid Mechanics – The Finite Volume Method", Longman Scientific and Technical, 1995.

Versteeg, H.K., & Malalasekera, W., "An Introduction to Computational Fluid Mechanics – The Finite Volume Method", Second Edition, Pearson Prentice Hall, 2007.

Vlaev, D.D., Nikov, I., and Martinov, M., "Shear and Skin Friction on Particles in Power-Law Fluids Agitated by Flat-Blade and Fluid Foil Impellers", Chem. Eng. Sci, 61, 5455-5467, 2006.

Vlaev, S.D., Nikov, I., and Martinov, M., "Shear and Skin Fraction on Particles in Power-Law Fluids Agitated by Flat-Blade and Fluid Foil Impellers", Chem. Eng. Sci., 61, 5455-5467, 2006.

Vlaev, S.D., Staykov, P., and Popov, R., "Pressure Distribution at Impeller Blades of Some radial Flow Impellers in Saccharose and Xanthan Gum Solutions. A CFD Visualization Approach", Food and Bioproducts Processing, 82, 13-20, 2004.

Weetman, R. J., Coyle, C.K., "The Use of Fluidfoil Impellers in Viscous Mixing Application", AIChE Annual Meeting, California, USA, 1989.

Weetman, R. J., Oldshue, J.Y., "Power, Flow and Shear Characteristics of Mixing Impellers", 6th European Conference on Mixing, Italy, 1988.

Wesseling, P., "Principles of Computational Fluid Dynamics", Springer, 2001.

Westra, J.G., "Rheology of (Carboxymethyl) Cellulose with Xanthan Gum Properties", Macromolecules 22, 367-370, 1989.

Whitcomb, P.J. and Macosko, C.W., "Rheology of Xanthan Gum", *J. Rheol.*, 22, 493-496, 1978.

Wilkins, R.J., Miller, J.D., Dietz, D.C., and Myers, K.J. "New Technique for Measuring and Modeling Cavern Dimensions in a Bingham Plastic Fluid", *Chem. Eng. Sci.*, 60 5269-5275, 2005.

Wikstrom, T. and Rasmuson, A., "The Agitation of Pulp Suspensions with a Jet Nozzle Agitator", *Nordic Pulp and Paper Research J.*, 13(2), 88-94, 1998.

Witchterle, K. and Wein, O., "Threshold of Mixing of Non Newtonian Liquids", *Int. Chem. Eng.*, 21, 116-120-1981.

Witchterle, K., and Wein, O., "Agitation of Concentrated Suspension", Congress CHISA, Prague, Czechoslovakia, Paper B 4.6, 1975.

Wu, J. and Pullum, L., "Performance Analysis of Axial-Flow Mixing Impellers", *AIChE J.*, 46(3), 489-498, 2000.

Wu, J., Graham J., and Mehdi N.N., "Estimation of Agitator Flow Shear Rate", *AIChE J.*, 52(7), 2323-2332, 2006.

Wu, J., Graham, L.J., and Mehdi N.N., "Performance Estimator of Agitator Flow Shear Rate", *AIChE J.*, 52(7), 2323-2332, 2006 A.

Wu, J., Graham, L.J., Nguyen, B., and Mehdi, N.N., "Energy Efficiency Study on Axial Flow Impellers", *Chem. Eng. Process.*, 45, 625-632, 2006 B.

Wu, J., Zhu, Y., and Pullum, L., "Impeller Geometry Effect on Velocity and Solid Suspension", *Chem. Eng. Res. Des.*, 79, 989-997, 2001.

Wyczalkowski, W., "How Fluid Properties Affect Mixer & Impeller Design", Chem. Eng., 43-47, 2004.

Xu, H. and Zhang, C. "Study of the Effect of Non-Orthogonality for Non-Staggered Grids- The Results", Int. J. Numer. Meth. Fluids, 29, 625-644, 1999.

Xu, Z, Xin, L, Dexiang, G, Wei, Z, Tong, Z, and Yonghong, M, "Rheological Models for Xanthan Gum", J. Food Eng. 21, 203-209, 1996.

Yue-Lan, S., Zheng-Ming, G., Zhi-Peng, L., "Experimental Study and Numerical Simulation of Gas-Liquid Flow in a Stirred Tank with a New Multiple Impeller", Chinese J. Process Eng., 7(1), 24-28, 2007.

Zannoud, N., Giraud, P., Costes, J., and Bertrand, J., "Local Laser Measurements of Velocities and Concentration in Two Continuous Systems: A Tubular Jet-Stirred Reactor and a Stirred Vessel", 7th European Conference on Mixing, Brugge, 173-180, 1991.

Zeng, M. and Tao, W.Q., "A Comparison Study of the Convergence Characteristics and Robustness for Four Variants of SIMPLE-Family at Fine Grids", Eng. Comp., 20(3), 320-340, 2003.

Zeppenfeld, R., and Mersmann, A.B., "A New Fluid Dynamics Model for Mixing of Newtonian and Power-law Liquids in the Transient Regime", Chem. Eng. Technol., 11, 162-170, 1988.

Zhou, G. and Kresta, S.M., "Distribution of Energy Between Convective and Turbulent Flow for Three Frequently Used Impellers", Chem. Eng. Res. Des., 74, 379-389, 1996.

Zlokarnik, M, "Stirring: Theory and Practice", Wiley-VCH, Weinheim, 2001.

Appendix Experimental & CFD Data

Channeling and $V_{\text{fully mixed}}/V$ for A200, Configuration 1

0.5% xanthan gum, experimental data

Impeller Speed (rpm) \ Flowrate (L/hr)	Torque (N.m)	227		603		896	
		f	$V_{\text{fully Mix}}/V$	f	$V_{\text{fully Mix}}/V$	f	$V_{\text{fully Mix}}/V$
50	0.0285	0.629	0.31	0.649	0.24	0.687	0.21
100	0.1002	0.535	0.34	0.578	0.29	0.650	0.23
150	0.2455	0.476	0.45	0.528	0.41	0.590	0.33
200	0.4584	0.368	0.57	0.426	0.49	0.480	0.45
250	0.8161	0.244	0.74	0.286	0.70	0.406	0.58
300	1.1400	0.196	0.82	0.244	0.77	0.272	0.74
400	2.0500	0.089	0.97	0.135	0.95	0.195	0.88
500	3.2700	0.012	1.00	0.041	0.96	0.093	0.91

0.5% xanthan gum, CFD data

Impeller Speed (rpm) \ Flowrate (L/hr)	Torque (N.m)	227		603		896	
		f	$V_{\text{fully Mix}}/V$	f	$V_{\text{fully Mix}}/V$	f	$V_{\text{fully Mix}}/V$
50	0.0275	0.485	0.46	0.547	0.42	0.580	0.33
100	0.0970	0.432	0.49	0.491	0.44	0.534	0.37
150	0.2334	0.390	0.57	0.431	0.51	0.477	0.44
200	0.4405	0.310	0.72	0.358	0.64	0.411	0.52
250	0.7725	0.229	0.79	0.284	0.73	0.316	0.68
300	1.0593	0.180	0.89	0.213	0.84	0.240	0.77
400	1.8952	0.073	0.99	0.115	0.98	0.154	0.93
500	3.0054	0.006	1.00	0.031	0.98	0.073	0.94

1.0% xanthan gum, experimental data

Impeller Speed (rpm)	Flowrate (L/hr)	Torque (N.m)	227		603		896	
			f	$V_{\text{fully Mix}}/V$	f	$V_{\text{fully Mix}}/V$	f	$V_{\text{fully Mix}}/V$
50		0.0451	0.656	0.25	0.696	0.22	0.730	0.18
100		0.1185	0.597	0.30	0.626	0.26	0.656	0.20
150		0.2202	0.511	0.38	0.595	0.31	0.627	0.29
200		0.4178	0.428	0.54	0.498	0.44	0.530	0.38
250		0.6677	0.349	0.68	0.405	0.64	0.434	0.55
300		1.0038	0.242	0.79	0.279	0.73	0.310	0.68
400		1.9500	0.136	0.91	0.167	0.87	0.221	0.83
500		3.0900	0.067	0.97	0.086	0.93	0.111	0.87
600		4.4900	0.009	0.99	0.021	0.96	0.047	0.92

1.0% xanthan gum, CFD data

Impeller Speed (rpm)	Flowrate (L/hr)	Torque (N.m)	227		603		896	
			f	$V_{\text{fully Mix}}/V$	f	$V_{\text{fully Mix}}/V$	f	$V_{\text{fully Mix}}/V$
50		0.0442	0.574	0.40	0.600	0.33	0.634	0.28
100		0.1110	0.518	0.44	0.547	0.37	0.595	0.29
150		0.2171	0.450	0.51	0.484	0.44	0.552	0.36
200		0.4057	0.367	0.62	0.414	0.56	0.481	0.46
250		0.6400	0.280	0.75	0.338	0.67	0.378	0.61
300		0.9594	0.216	0.84	0.253	0.78	0.285	0.71
400		1.8008	0.123	0.96	0.160	0.93	0.189	0.86
500		2.8683	0.040	1.00	0.066	0.95	0.103	0.89
600		4.1761	0.005	1.00	0.021	0.98	0.045	0.93

1.5% xanthan gum, experimental data

Impeller Speed (rpm)	Flowrate (L/hr)	Torque (N.m)	227		603		896	
			f	$V_{\text{fully Mix}}/V$	f	$V_{\text{fully Mix}}/V$	f	$V_{\text{fully Mix}}/V$
50		0.0689	0.715	0.23	0.736	0.18	0.766	0.14
100		0.1286	0.642	0.26	0.678	0.20	0.711	0.16
150		0.2510	0.594	0.31	0.633	0.26	0.669	0.22
200		0.4412	0.492	0.49	0.534	0.38	0.564	0.34
250		0.6390	0.409	0.63	0.444	0.57	0.487	0.49
300		0.9589	0.336	0.73	0.373	0.65	0.393	0.62
400		1.8100	0.188	0.85	0.243	0.81	0.283	0.78
500		2.9800	0.117	0.91	0.151	0.88	0.178	0.83
600		4.3600	0.028	0.98	0.059	0.94	0.093	0.89
700		6.0000	0.003	1.00	0.023	0.97	0.040	0.90

1.5% xanthan gum, CFD data

Impeller Speed (rpm)	Flowrate (L/hr)	Torque (N.m)	227		603		896	
			f	$V_{\text{fully Mix}}/V$	f	$V_{\text{fully Mix}}/V$	f	$V_{\text{fully Mix}}/V$
50		0.0682	0.612	0.32	0.643	0.28	0.680	0.22
100		0.1234	0.567	0.35	0.589	0.29	0.640	0.23
150		0.2383	0.500	0.43	0.526	0.38	0.591	0.30
200		0.4222	0.419	0.54	0.456	0.50	0.510	0.41
250		0.6093	0.330	0.70	0.369	0.63	0.422	0.56
300		0.9010	0.265	0.80	0.307	0.74	0.339	0.67
400		1.6998	0.170	0.89	0.216	0.86	0.260	0.81
500		2.7650	0.080	0.95	0.124	0.91	0.148	0.87
600		4.0578	0.018	0.98	0.040	0.95	0.074	0.91
700		5.5333	0.001	1.00	0.012	0.95	0.028	0.92

Channeling and $V_{\text{fully mixed}}/V$ for A100, Configuration 1896 L/hr, 0.5% xanthan gum, experimental data

Impeller Impeller Speed (rpm)	Torque (N.m)	A100	
		f	$V_{\text{fully Mix}}/V$
150	0.0202	0.540	0.38
250	0.1050	0.370	0.68
400	0.2470	0.173	0.91

896 L/hr, 0.5% xanthan gum, CFD data

Impeller Impeller Speed (rpm)	Torque (N.m)	A100	
		f	$V_{\text{fully Mix}}/V$
150	0.0198	0.443	0.48
250	0.0971	0.289	0.73
400	0.2323	0.130	0.98

Channeling and $V_{\text{fully mixed}}/V$ for A310, Configuration 1896 L/hr, 0.5% xanthan gum, experimental data

Impeller Speed (rpm) \ Impeller	Torque (N.m)	A310	
		f	$V_{\text{fully Mix}}/V$
150	0.1050	0.499	0.42
250	0.2420	0.343	0.68
400	0.5630	0.153	0.97

896 L/hr, 0.5% xanthan gum, CFD data

Impeller Speed (rpm) \ Impeller	Torque (N.m)	A310	
		f	$V_{\text{fully Mix}}/V$
150	0.0971	0.396	0.48
250	0.2323	0.260	0.73
400	0.5398	0.098	0.98

Channeling and $V_{\text{fully mixed}}/V$ for A320, Configuration 1896 L/hr, 0.5% xanthan gum, experimental data

Impeller Impeller Speed (rpm)	Torque (N.m)	A320	
		f	$V_{\text{fully Mix}}/V$
150	0.0820	0.462	0.45
250	0.1976	0.313	0.71
400	0.4886	0.122	0.99

Channeling and $V_{\text{fully mixed}}/V$ for A200, Configuration 2227 L/hr, 0.5% xanthan gum, experimental data

Impeller Impeller Speed (rpm)	Torque (N.m)	A200	
		f	$V_{\text{fully Mix}}/V$
150	0.2455	0.580	0.39
200	0.4584	0.448	0.51
250	0.8161	0.307	0.68
400	2.0500	0.145	0.91

227 L/hr, 0.5% xanthan gum, CFD data

Impeller Impeller Speed (rpm)	Torque (N.m)	A200	
		f	$V_{\text{fully Mix}}/V$
150	0.2334	0.513	0.50
200	0.4405	0.390	0.62
250	0.7725	0.295	0.72
400	1.8952	0.126	0.94